

AD 682201

Bulletin 38
Part 1
(of 3 Parts)

THE SHOCK AND VIBRATION BULLETIN

AUGUST 1968

A Publication of
THE SHOCK AND VIBRATION
INFORMATION CENTER
Naval Research Laboratory, Washington, D.C.



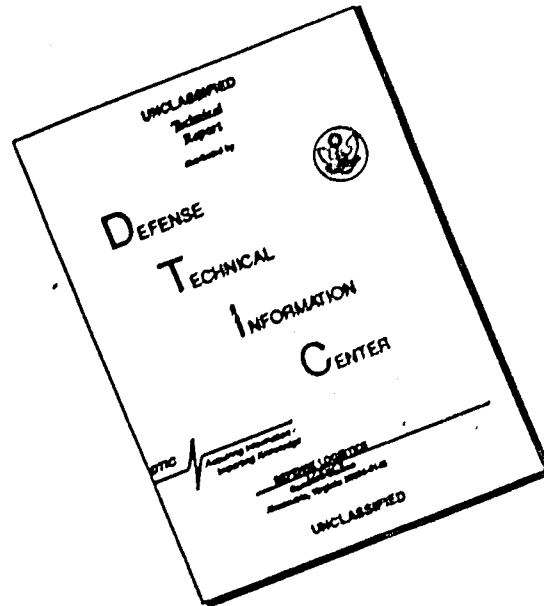
Office of
The Director of Defense
Research and Engineering

Reproduced by the
CLEARINGHOUSE
for Federal Scientific & Technical
Information Springfield Va 22151

This document has been approved for public release and sale; its distribution is unlimited.

142

DISCLAIMER NOTICE



THIS DOCUMENT IS BEST QUALITY AVAILABLE. THE COPY FURNISHED TO DTIC CONTAINED A SIGNIFICANT NUMBER OF PAGES WHICH DO NOT REPRODUCE LEGIBLY.

Bulletin 38
Part 1
(of 3 Parts)

THE SHOCK AND VIBRATION BULLETIN

AUGUST 1968

**A Publication of
THE SHOCK AND VIBRATION
INFORMATION CENTER
Naval Research Laboratory, Washington, D.C.**

The 38th Symposium on Shock, Vibration and Associated Environments was held in St. Louis, Missouri, on 1-2 May 1968.

**Office of
The Director of Defense
Research and Engineering**

CONTENTS :

PART 1

Vibration Analysis

VIBRATION RESPONSES OF SIMPLE CURVED PANELS TO HIGH INTENSITY RANDOM AND DISCRETE FREQUENCY NOISE ;	1
C. E. Rucker, NASA Langley Research Center, Hampton, Virginia	
RANDOM VIBRATION USING FINITE ELEMENT APPROACH	7
K. K. Kapur, Ching-U Ip and E. P. Howard, Aerospace Corporation, San Bernardino, California	
FREQUENCY ANALYSIS OF REPETITIVE BURSTS OF RANDOM VIBRATION	17
W. E. Noonan, McDonnell Company, St. Louis, Missouri	
SIMPLIFIED RANDOM VIBRATION COMPUTATIONS ;	27
LaVerne W. Root and A. S. Henry, Collins Radio Company, Cedar Rapids, Iowa	
CONCENTRATED MASS EFFECTS ON THE VIBRATION OF CORNER SUPPORTED RECTANGULAR PLATES ;	37
R. L. Barnoski, Measurement Analysis Corporation, Los Angeles, California, and T. D. Schoessow, Aerospace Corporation, El Segundo, California	
VIBRATION OF ECCENTRICALLY STIFFENED PLATES ;	45
B. R. Long, Defence Research Establishment Suffield, Ralston, Alberta, Canada	
CRACK DETECTION IN A STRUCTURAL BEAM THROUGH CROSS- CORRELATION ANALYSIS	55
F. Baganoff, Baganoff Associates, Inc., St. Louis, Missouri, and D. Baganoff, Stanford University, Stanford, California	
A THEORETICAL MODAL STUDY FOR THE LATERAL VIBRATIONS OF BARS HAVING VARIABLE CROSS SECTION AND FREE END CONDITION,	67
A. F. Witte, Sandia Corporation, Albuquerque, New Mexico	
*VARIABLE RESONANT VIBRATION GENERATOR FOR EXPERIMENTAL VIBRATIONAL ANALYSIS OF STRUCTURES	
H. Soulant and S. Lee, Naval Ship Research and Development Center, Washington, D.C.	
*THE PREDICTION OF INTERNAL VIBRATION LEVELS OF FLIGHT VEHICLE EQUIPMENT	
R. W. Sevy and D. L. Earls, Air Force Flight Dynamics Laboratory, Wright-Patterson AFB, Ohio	
SATURN V COMPONENT VIBRATION TESTS USING SEGMENTED SHELL SPECIMENS	87
C. Hwang, Northrop Corporation, Norair Division, Hawthorne, California, and C. E. Lifer, NASA, Marshall Space Flight Center, Huntsville, Alabama	
AN APPLICATION OF FLOWGRAPHS TO THE FREE VIBRATION OF STRUCTURES	99
P. M. Wright, University of Toronto, Toronto, Canada, and C. C. Feng, University of Colorado, Boulder, Colorado	
DUAL SPECIFICATIONS IN VIBRATION TESTING	109
W. B. Murfin, Sandia Corporation, Albuquerque, New Mexico	
SUBSTITUTE ACOUSTIC TESTS	115
T. D. Scharon and T. M. Yang, Bolt Beranek and Newman Inc., Van Nuys, California	

*This paper appears in Shock and Vibration Bulletin 38, Supplement.

SIMPLIFIED METHOD OF CALCULATING NATURAL FREQUENCIES AND
 NORMAL MODES OF VIBRATION FOR SHIPS; 125
 H. B. Ali and H. F. Alma, Naval Ship Research and Development Center,
 Washington, D.C.

RESPONSE SPECTRA FOR SWEEPING SINUSOIDAL EXCITATIONS 133
 D. L. Cronin, TRW Systems Group, Redondo Beach, California

PAPERS APPEARING IN PART 2

Structural Analysis

- AN OVERALL VIEW OF STRUCTURAL DYNAMICS**
 R. M. Mains, Washington University, St. Louis, Missouri
- DYNAMIC SUBSTRUCTURES METHOD FOR SHOCK ANALYSIS**
 M. Pakstys, Jr., General Dynamics, Electric Boat Division, Groton, Connecticut
- IDENTIFICATION OF COMPLEX STRUCTURES USING NEAR-RESONANCE TESTING**
 J. P. Raney, NASA Langley Research Center, Hampton, Virginia
- PROPAGATION OF LONGITUDINAL STRESS WAVES IN A COMPLEX
 BAR TYPE STRUCTURE**
 D. L. Block, Martin Marietta Corporation, Orlando, Florida
- ALSEP SYSTEM STRUCTURAL DYNAMICS STUDY**
 M. M. Bahn, Aerospace Systems Division, The Bendix Corporation,
 Ann Arbor, Michigan
- REDUCING THE NUMBER OF MASS POINTS IN A LUMPED PARAMETER SYSTEM**
 M. T. Soifer and A. W. Bell, Dynamic Science, Monrovia, California
- LATERAL DYNAMIC RESPONSE OF LARGE SUBSYSTEMS DURING
 LAUNCH TRANSIENT CONDITIONS**
 J. S. Gaffney and P. E. Campos, Atlantic Research Corporation, Costa Mesa, California
- A NEW APPROACH TO THE INTERACTION PROBLEMS OF FLUID-FILLED
 ELASTIC MEMBRANE SHELLS**
 C. L. Tai and S. Uchiyama, Space Division, North American Rockwell Corporation,
 Downey, California
- STRUCTURAL AND VIBRATION ANALYSIS OF NAVY CLASS H.I. MEDIUMWEIGHT
 SHOCK TEST**
 W. P. Welch and P. D. Saunders, Westinghouse Electric Corporation,
 Sunnyvale, California
- TRANSIENT RESPONSES OF A LINEAR MECHANICAL SYSTEM BY USE OF EXPERIMENTALLY
 DETERMINED UNIT IMPULSE RESPONSES**
 V. P. Warkulwiz, General Electric Company, Valley Forge Space Technology Center,
 Pennsylvania
- A MOMENT TECHNIQUE FOR SYSTEM PARAMETER IDENTIFICATION**
 F. Kozin and C. H. Kozin, Midwest Applied Science Corporation,
 West Lafayette, Indiana
- REINFORCED CONCRETE BEAM RESONANCES**
 F. G. Krach, Barry Controls Division, Barry Wright Corporation,
 Watertown, Massachusetts
- STRUCTURAL DYNAMIC ANALYSIS OF THE MARINER MARS '69 SPACECRAFT**
 H. J. Holbeck, Jet Propulsion Laboratory, Pasadena, California, and
 T. D. Arthurs and W. J. Gaugh, Northrop Systems Laboratory,
 Northrop Corporation, Hawthorne, California
- LINE SOLUTION TECHNOLOGY AS A GENERAL ENGINEERING APPROACH TO THE
 STATIC, STABILITY, AND DYNAMIC RESPONSE OF STRUCTURAL MEMBERS
 AND MECHANICAL ELEMENTS**
 W. D. Pilkey, IIT Research Institute, Chicago, Illinois, and
 R. Nielsen, Jr., Department of Transportation, Washington, D.C.

**UPPER AND LOWER BOUNDS TO BENDING FREQUENCIES OF NONUNIFORM SHAFTS,
AND APPLICATIONS TO MISSILES**

N. Rubinstein, V. G. Sigillito and J. T. Stadter, Applied Physics Laboratory,
The Johns Hopkins University, Silver Spring, Maryland

**DAMAGE PREDICTION FOR OPEN FRAME STRUCTURES SUBJECT TO LIQUID
PROPELLANT EXPLOSIONS**

G. C. Kao and V. M. Conticelli, Wyle Laboratories, Huntsville, Alabama, and M. J.
Rosenfield, U.S. Army Corps of Engineers, Ohio River Division Laboratories,
Cincinnati, Ohio

SIMPLIFIED DYNAMICS OF HARDENED BURIED BUILDINGS

J. V. Poppitz, Bell Telephone Laboratories, Inc., Whippany, New Jersey

INFLUENCE COEFFICIENT MATRIX QUICK CHECK PROCEDURE

G. W. Bishop, Bishop Engineering Company, Princeton, New Jersey

Mechanical Impedance

**DETERMINATION OF FIXED BASE NATURAL FREQUENCIES OF DUAL FOUNDATION
SHIPBOARD EQUIPMENTS BY SHAKE TESTS**

L. P. Petak and G. J. O'Hara, Naval Research Laboratory, Washington, D.C.

***VIBRATION TRANSMISSION METHODS FOR FOUNDATION STRUCTURES**

E. V. Thomas, Annapolis Division, Naval Ship Research and Development Center,
Annapolis, Maryland

VIBRATION ANALYSIS OF A STRUCTURAL FRAME USING THE METHOD OF MOBILITY

J. Verga, Hazeltine Corporation, Little Neck, New York

APPLICABILITY OF MECHANICAL ADMITTANCE TECHNIQUES

D. U. Noiseux and E. B. Meyer, Bolt Beranek and Newman Inc.,
Cambridge, Massachusetts

**APPLICATION OF THE MECHANICAL RECEPTANCE COUPLING PRINCIPLE TO
SPACECRAFT SYSTEMS**

E. Heer, Jet Propulsion Laboratory, Pasadena, California, and L. D. Lutes,
Rice University, Houston, Texas

**A VERIFICATION OF THE PRACTICALITY OF PREDICTING INTERFACE DYNAMICAL
ENVIRONMENTS BY THE USE OF IMPEDANCE CONCEPTS**

F. J. On, NASA, Goddard Space Flight Center, Greenbelt, Maryland

**EXPERIMENTAL TECHNIQUE FOR DETERMINING FIXED-BASE NATURAL FREQUENCIES
OF STRUCTURES ON SINGLE NONRIGID ATTACHMENT POINTS**

G. M. Remmers, Naval Research Laboratory, Washington, D.C.

DETERMINATION OF MODAL MASS FROM TEST DATA

I. P. Vatz, Brown Engineering, A Teledyne Company, Huntsville, Alabama

PAPERS APPEARING IN PART 3

Damping

DESIGN OF A DAMPED MACHINERY FOUNDATION FOR HIGH SHOCK LOADING

E. V. Thomas, Annapolis Division, Naval Ship Research and Development Center,
Annapolis, Maryland

CONSTRAINED LAYER DAMPING WITH PARTIAL COVERAGE

D. S. Nokes and F. C. Nelson, Tufts University, Medford, Massachusetts

**THE EFFECTS OF ROTATORY INERTIA AND SHEAR DEFORMATION ON THE FLEXURAL
VIBRATIONS OF A TWO-LAYERED VISCOELASTIC-ELASTIC BEAM**

T. Nicholas, Air Force Materials Laboratory, Wright-Patterson AFB, Ohio

*This paper appears in Shock and Vibration Bulletin 38, Supplement.

- METHODS OF DAMPING VERY STIFF STRUCTURAL MEMBERS**
H. T. Miller, Lord Manufacturing Company, Erie, Pennsylvania
- THE OPTIMUM DESIGN OF FIVE-PLY VISCOELASTIC ISOLATION FLEXURES FOR POINT INERTIA LOADING**
D. A. Frohrib, University of Minnesota, Minneapolis, Minnesota
- APPLICATION OF DAMPING DEVICE FOR CRITICAL SPEED CONTROL**
J. F. Mullen and M. R. Kulina, Curtiss-Wright Corporation, Wood-Ridge, New Jersey
- DEVELOPMENT OF PRACTICAL TUNED DAMPERS TO OPERATE OVER A WIDE TEMPERATURE RANGE**
A. D. Nashif, University of Dayton Research Institute, Dayton, Ohio
- MULTIFREQUENCY RESPONSE OF VISCOELASTIC DAMPERS**
R. K. Newman and D. C. Kraft, University of Dayton, Dayton, Ohio
- THE CRITICAL DAMPING CALCULATOR AND A COMPARISON OF SELECTED STRUCTURAL DAMPING EVALUATION SYSTEMS**
B. E. Douglas, Annapolis Division, Naval Ship Research and Development Center, Annapolis, Maryland
- FORCED RESPONSE OF LUMPED PARAMETER SYSTEM WITH APPLICATIONS TO MISSILE DYNAMICS**
J. D. Sowers, Chrysler Corporation Space Division, New Orleans, Louisiana
- A NON-FLUID VELOCITY DAMPER**
W. G. Flannely, Kaman Aircraft Division, Kaman Corporation, Bloomfield, Connecticut
- THE DYNAMIC RESPONSE OF LINEARLY VISCOELASTIC CYLINDRICAL SHELLS TO PERIODIC OR TRANSIENT LOADING**
E. A. Fitzgerald, Missile and Space Systems Division, McDonnell Douglas Corporation, Santa Monica, California
- DAMPING OF MULTISPAN STRUCTURES BY MEANS OF VISCOELASTIC LINKS**
D. I. G. Jones, Air Force Materials Laboratory, Wright-Patterson AFB, Ohio
- DAMPING MEASUREMENTS ON SOFT VISCOELASTIC MATERIALS USING A TUNED DAMPER TECHNIQUE**
C. M. Cannon and A. D. Nashif, University of Dayton, Dayton, Ohio, and D. I. G. Jones, Air Force Materials Laboratory, Wright-Patterson AFB, Ohio
- AIRCRAFT STRUCTURAL RESPONSE DUE TO GROUND IMPACT**
J. D. Weber, Convair Division of General Dynamics, San Diego, California
- EFFECT OF TEMPERATURE ON THE VISCOELASTIC HIGH POLYMER MATERIALS**
J. M. Ohno, Aerospace Systems Division, The Bendix Corporation, Ann Arbor, Michigan
- "BROAD BAND" EXTENSIONAL DAMPING MATERIALS**
D. R. Blenner and T. J. Dudek, Lord Manufacturing Company, Erie, Pennsylvania
- A SINUSOIDAL PULSE TECHNIQUE FOR ENVIRONMENTAL VIBRATION TESTING**
J. T. Howlett and D. J. Martin, NASA Langley Research Center, Hampton, Virginia
- A STUDY OF THE PERFORMANCE OF AN OPTIMUM SHOCK MOUNT**
K. T. Cornelius, Naval Ship Research and Development Center, Washington, D.C.
- AN INVESTIGATION OF THE PERFORMANCE OF GAS-BEARING MACHINERY SUBJECTED TO LOW-FREQUENCY VIBRATION AND SHOCK**
P. W. Curwen and A. Frost, Mechanical Technology Inc., Latham, New York
- AN EXPERIMENTAL INVESTIGATION OF AN ACTIVE VIBRATION ABSORBER**
T. D. Dunham, Southwest Research Institute, San Antonio, Texas, and D. M. Egle, University of Oklahoma, Norman, Oklahoma
- INTEGRATED SHOCK AND ACOUSTIC MODULAR DESIGN CONCEPT FOR SUBMARINES**
M. Pakstys, Jr. and G. A. Ziegler, Electric Boat Division of General Dynamics, Groton, Connecticut

**CYCLIC DEFORMATION CREW ATTENUATOR STRUTS FOR THE APOLLO
COMMAND MODULE**

D. L. Platus, Mechanics Research, Inc., El Segundo, California

**DEVELOPMENT OF THE KINEMATIC FOCAL ISOLATION SYSTEM FOR
HELICOPTER ROTORS**

R. W. Balke, Bell Helicopter Company, Fort Worth, Texas

A TOOL FOR PARAMETRIC ANALYSIS OF COMPLEX ISOLATION SYSTEMS

B. J. Jones and F. A. Smith, Martin Marietta Corporation, Denver, Colorado

AN ACTIVE STABILIZATION SYSTEM FOR VEHICLES AND OTHER MASSIVE BODIES

T. H. Putman, Westinghouse Research Laboratories, Pittsburgh, Pennsylvania

CRASH CONSIDERATIONS IN THE DESIGN OF THE NEW YORK STATE SAFETY SEDAN

S. Davis and N. B. Nissel, Fairchild Hiller, Republic Aviation Division,
Farmingdale, L.I., New York

VIBRATION ANALYSIS

VIBRATION RESPONSES OF SIMPLE CURVED PANELS TO HIGH-INTENSITY RANDOM AND DISCRETE FREQUENCY NOISE

Carl E. Rucker
NASA Langley Research Center
Langley Station, Hampton, Va.

Unexpectedly short times-to-failure for curved panels under acoustic loading led to detailed studies of their dynamic response characteristics to determine the reasons for such short times-to-failure. Non-linear response characteristics involving significant low-frequency motions due to buckling were observed. Such behavior resulted in a much higher percentage of large strain amplitudes than would have been predicted for a normal strain amplitude distribution. The acquisition of joint strain-sound pressure distributions for significant time durations was facilitated by the use of a pulse height analyzer which digitized, classified, stored, and displayed large amounts of information.

INTRODUCTION

The responses of aircraft or spacecraft structures to complex noise inputs involve such important variables as the structural materials, the fabrication techniques, and the related environmental conditions. Analytical procedures, generally, have not been adequate for predicting such responses, and hence, much reliance has been placed on experiments.

As part of a series of basic research studies of panel responses to noise, the effects of panel curvature have been documented. This paper has two purposes: (1) to present some of the recent panel test analysis results, and (2) to describe briefly a unique method of collecting statistical data.

SONIC FATIGUE FAILURES

Sonic fatigue data are shown in Fig. 1 for three different panel curvatures for comparison. Root-mean-square strain for a strain gage near the panel edge is plotted as a function of time-to-failure in minutes. The excitation was a broadband random noise from an air jet.

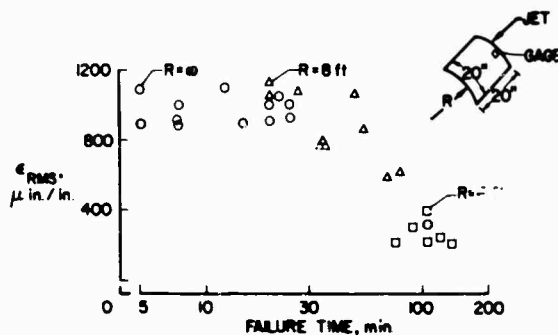


Fig. 1. Time-to-failure for 0.020-inch-thick aluminum-alloy panels of three curvatures in a random noise field having an overall sound-pressure level of 160 db

Its overall sound pressure level was 155 db and the spectrum peaked sharply at about 100 Hz (see Refs. 1 and 2). Identical 20- by 20-inch sheets of material were formed to curved fixtures with lap attachments. A&N bolts (3/16-inch diam.) with nuts tightened to a given torque were spaced around the periphery, 5/16 inch in from the edge and 1-1/2 inches on center.

This was done in an attempt to minimize the edge-attachment condition differences for the test panels.

One of the main results of the above study was the relatively short time-to-failure of the 4-foot-radius panels even though the measured strain levels were markedly lower than for the other curvatures. It was originally suggested that significantly different stress concentration factors may have existed. This paper, however, contains results of other studies relating to the dynamic behavior of the 4-foot-radius panel and which may also be significant in causing shorter times-to-failure.

Figure 2 shows a panel which failed due to sonic fatigue while formed into a 4-foot-radius configuration. It is believed that this failure resulted from test conditions for which the panel was buckled. Since buckling is a strong indicator of nonlinear behavior, the panel response was studied for other evidence of nonlinearities.

STRAIN RESPONSES

A series of dynamic response studies involving different intensities of acoustic loading were conducted, and some representative results are presented in Fig. 3. Overall root-mean-square strains are plotted as a function of discrete driving frequency for sound-pressure levels of 115 and 125 db impinging on the lower surface of the panel. At the lower excitation level, the panel appeared to be responding generally as a linear system. At the higher level, however, there was definite evidence of nonlinear response. The skewness of

the response peaks toward lower frequencies represents a soft spring effect; that is, the panel becomes less stiff at large vibration amplitudes.

The mode shape sketches in Fig. 3 illustrate qualitatively the modal pattern variation for these two levels of excitation. The sketch at the top suggests a buckling condition such that the center portion of the panel experiences relatively large amplitude motions at frequencies other than the driving frequency.

Both analytical and experimental studies have been made for the modal response of this panel, and the results are presented in Fig. 4. Frequency in Hz is shown for various modal numbers (number of antinodes). Theoretical calculations assuming both clamped and simply supported boundary conditions (Ref. 3) are represented by the solid and dashed curves, respectively. Experimental data obtained using discrete frequency excitation are represented by the circle points. They seem to fall close to the simply supported values at low modal numbers and close to the clamped values at high modal numbers. Note that the frequency for the fundamental mode corresponds closely to that of the sixth mode. As indicated in Fig. 3, the sixth mode was excited at a level of about 115 db, whereas at a 120-db level, and higher, the panel snapped into a buckled condition for which the fundamental and sixth modes are superimposed (see upper sketch of Fig. 3).

Additional panel response data for high levels of noise excitation are presented in Figs. 5 and 6. In Fig. 5 the mean square bending strains are shown as a function of frequency. The discrete frequency excitation (at a 145-db



Fig. 2. Aluminum-alloy panel (0.020-inch thick, 4-foot radius) after sonic fatigue failure due to siren excitation

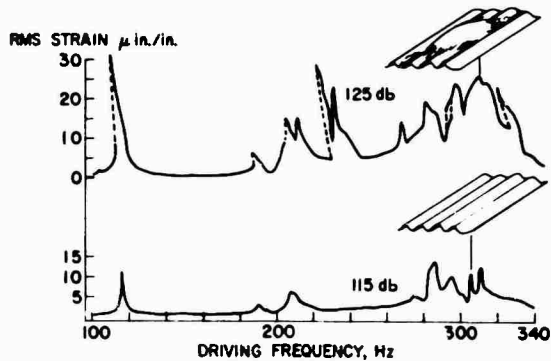


Fig. 3. Overall strain responses of a panel (4-foot radius) as a function of driving frequency for two different levels of discrete frequency excitation

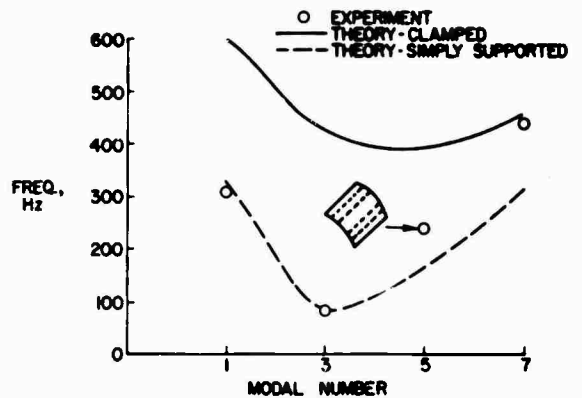


Fig. 4. Some modal responses of curved aluminum panel (4-foot radius) excited by discrete frequency noise

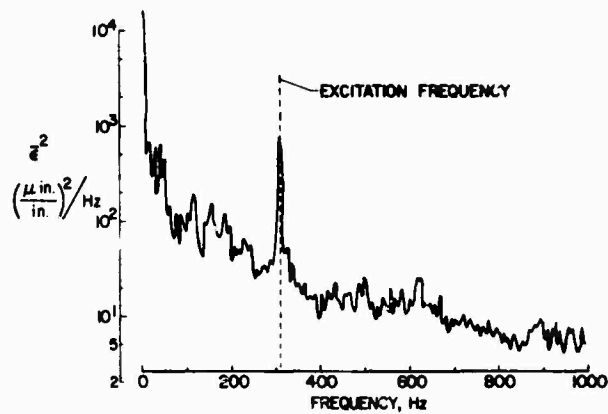


Fig. 5. Spectrum of bending strain response of curved panel (4-foot radius) due to discrete frequency excitation at 145-dB sound-pressure level

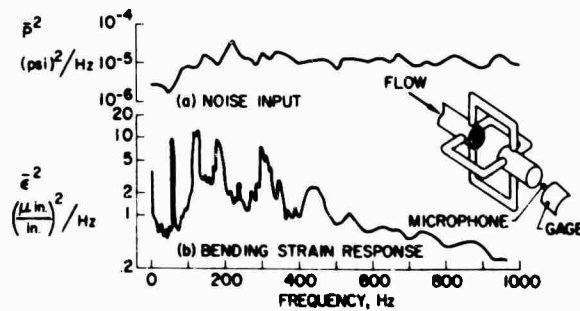


Fig. 6. Bending strain response spectrum of a panel (4-foot radius) due to random noise input from a four-branch airjet noise source

level) was provided by a siren for which the harmonic content was at least 40 db lower in level than the excitation frequency of the figure. The data shown were obtained by means of a 15-second tape loop and narrow-band filters. Note that relatively strong responses of the panel occur at frequencies lower than the exciting frequency.

The response of the panel to broadband noise is shown in Fig. 6. Again, mean-square bending strain per unit bandwidth is plotted as a function of frequency. The spectrum shape of the 150-db level random noise is shown at the top. Note that this nearly flat random noise spectrum was generated by a unique jet turbulator nozzle represented by the sketch at the right. A number of relatively strong responses are observed at the low frequencies, even in the range where the input spectrum tends to drop off. These latter response data are thus consistent with those of Fig. 5.

AMPLITUDE DISTRIBUTIONS

In order to study the statistical behavior of the panel, a unique method was used to collect and analyze appropriate sound pressure and associated strain data. Figures 7 and 8 illustrate the method used, and Fig. 9 contains the main results.

Included in Fig. 7 are schematic representations of the root-mean-square sound pressure and total panel strain time histories. In the course of this study the amplitude distributions were obtained at several arbitrary input noise loading levels. Such a procedure could be accomplished by the reading of oscillograph records at the proper times, as indicated

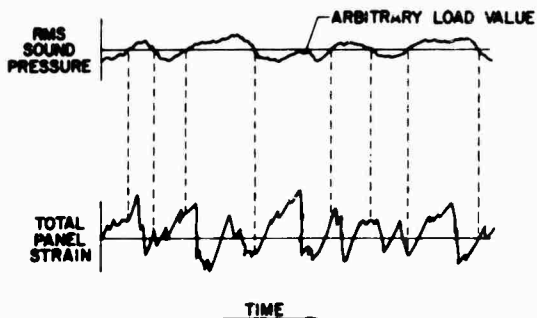


Fig. 7. Time histories of the root-mean-square sound pressure and associated total panel strain. Vertical dashed lines indicate points at which strain values were determined for an arbitrary sound-pressure load value.



Fig. 8. Enlarged sectional view of oscilloscope display of a pulse-height analyzer used for accumulation of joint probability data

schematically in Fig. 7. In order to automate the process of accumulating data of this type, however, a pulse-height analyzer was used in the manner suggested by the diagrams of Fig. 8. Records such as those of Fig. 7 were digitized about 300 times per second for their 80-minute durations (time-to-failure of the panel). The analyzer operates in such a way that all strain values associated with a given sound pressure are grouped together. Thus, it is possible to determine amplitude distribution directly from the analyzer.

Such a display is illustrated in Fig. 8 which contains a cathode ray oscilloscope presentation of the strain and sound-pressure data. The abscissa represents panel strain, the zero value being in the center and the negative and positive values being to the left and right, respectively. The ordinate is root-mean-square sound pressure; the vertical coordinate represents the number of measurements for given values of sound pressure and panel strain. Thus, at a given sound-pressure value, the display indicates the number of strain samples at each strain value for the entire time of the data recording. The type of display illustrated in the figure is useful qualitatively, but the numerical data are obtained directly from the tabulation circuits.

Sample strain amplitude distribution data, as measured with the pulse-height analyzer, are presented in Fig. 9 for the 4-foot-radius panel. The distribution shown is for a sound-pressure level of 157 db and contains over 79,000 samples. Also shown is a solid curve representing a normal or gaussian distribution. The probability of being equal to or less than a given value of strain is plotted on the vertical scale for various multiples of standard deviation (σ). It can be seen that the measured data

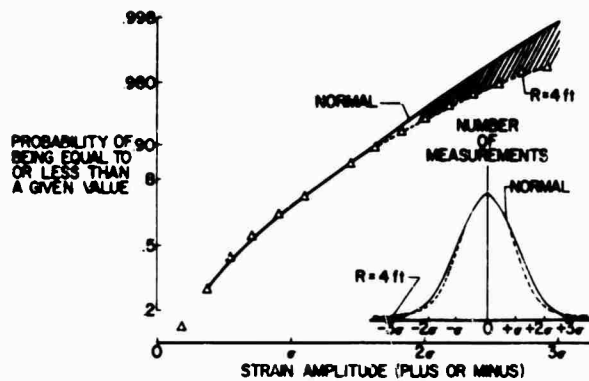


Fig. 9. Total strain amplitude distribution for a panel (4-foot radius) due to random noise loading compared to a normal distribution

generally follow the normal distribution curve up to nearly 2σ and then deviate from the normal distribution curve at higher values. This result implies that a greater percentage of the panel lifetime is spent at strain values above 3σ than would be the case for a normal distribution of strain amplitudes. Although not shown on the figure, similar data for the other two panel curvatures of Fig. 1 fell generally along the gaussian curve at the higher σ values. The implication from these data is that the 4-foot curvature panel, probably because of its nonlinear behavior characteristics, experienced an abnormally high number of high strain values.

These strain peaks may account for the shorter time-to-failure of these panels.

CONCLUDING REMARKS

Unexpectedly short times-to-failure for curved panels under acoustic loading led to detailed studies of their dynamic response characteristics. Nonlinear response characteristics involving significant low-frequency motions due to buckling were observed. Such behavior resulted in a much higher percentage of large strain amplitudes than would have been predicted for a normal strain amplitude distribution.

REFERENCES

1. C. E. Rucker, "Some Experimental Effects of Curvature on Response of Simple Panels to Intense Noise," A paper presented at the 67th Meeting of the Acoustical Society of America, which was held in New York in May 1964
2. P. M. Edge, Jr. and C. E. Rucker, "Response-to-Noise Studies of Some Aircraft and Spacecraft Structures," *Acoustical Fatigue in Aerospace Structures* (W. S. Trapp and D. M. Forney, Jr., eds.) (Syracuse Univ. Press, New York) 1965, pp. 404-408
3. J. L. Sewall, "Vibration Analysis of Cylindrically Curved Panels With Simply Supported or Clamped Edges and Comparisons With Some Experiments," NASA TN D-3791, Table IVb, p. 38, and Fig. 5, p. 49, 1967

DISCUSSION

S. Davis (Fairchild Hiller): Can you tell me where the strain gage was located and why the particular location was chosen? Obviously, the strain measurement you take would vary at different locations on the panel depending upon the particular mode shape being excited.

G. Brooks (NASA) (for C. E. Rucker): Well, of course, quite a study went into determining

the best locations for these gages. They had strain gages located on all four edges out about 1/2 inch from the bolt line. In addition to this there were also strain gage bridges located near the center of the panel in some cases. These strain gage locations were selected on the basis of the experience of the survey of the panels to find out where the strains were usually the largest.

J. Rice (Goodyear Aerospace Corp.): Was your acoustic excitation normal, grazing, or in a reverberant room?

G. Brooks: It was normal. The acoustic excitation was provided by a horn which was placed below the panel so that the panels were excited from the bottom, or the center of the radius of curvature.

* * *

RANDOM VIBRATION USING FINITE ELEMENT APPROACH

K. K. Kapur, Ching-U Ip, and E. P. Howard
Aerospace Corporation
San Bernardino, California

The finite element method of structural analysis is extended to determine the response of complex structures to multiple random loadings. The method is used to calculate the output power spectral densities and mean square values of deflections and internal forces. The method is illustrated by a number of examples.

INTRODUCTION

The finite element method is one of the most effective tools for analyzing static and dynamic problems in structural mechanics, and many authors [1-5] have contributed to its development. The approach has been used for vibrations [6], acoustics [7], seepage [8], heat conduction [9], wave propagation [10], and stability [11] problems. In this paper, a consistent matrix formulation for the response of any structure to multiple random loads is presented using this approach.

Using exact mathematical formulation, several authors have discussed the response of linear elastic systems to various types of random excitations [12,13]. Because of the difficulties encountered in analyzing multiple random inputs using exact differential equations, most authors have analyzed beam and plate random vibration problems due to single random inputs or completely uncorrelated inputs [14-16]. The results are of academic interest and have some application to physical problems. The difficulties encountered in analyzing the response of a structure to multiple random excitation can be overcome, however, if the structure is divided into finite elements, thus reducing a continuous structure with infinite degrees of freedom to a structure with a finite number of degrees of freedom. The method used is illustrated by several examples.

It is assumed throughout that the random process is stationary and ergodic.

DEVELOPMENT OF BASIC THEORY

The general procedure of the finite element method is used to divide the total structure into a number of elements. These elements are connected at their corners or nodal points. When a typical three-dimensional element n is being considered, the displacements are given by

$$\underline{u}(x, y, z, t) = \underline{A}(x, y, z) \underline{v}_n(t), \quad (1)$$

where the elements of \underline{u} are components of the displacement vector and \underline{A} is a transformation matrix giving displacements \underline{u} in terms of \underline{v}_n , the generalized coordinates or nodal displacements for the n th element. The kinetic energy, T , the strain energy, U , and the dissipation function, F , can be written as

$$T = 1/2 \int_V m \dot{\underline{u}}^t \dot{\underline{u}} \, dv,$$

$$U = 1/2 \int_V \underline{\epsilon}^t \underline{\sigma} \, dv,$$

and

$$F = 1/2 \int_V c \dot{\underline{u}}^t \dot{\underline{u}} \, dv.$$

These can also be written as

$$T = 1/2 \dot{\underline{v}}_n^t \underline{M}_n \dot{\underline{v}}_n,$$

$$U = 1/2 \underline{v}_n^t \underline{K}_n \underline{v}_n.$$

and

$$F = 1/2 \dot{v}_n^t C_n \dot{v}_n,$$

where

$$M_n = \int_v m A^t A dv,$$

$$K_n = \int_v B^t D B dv,$$

and

$$C_n = \int_v c A^t A dv = \frac{c}{m} M_n.$$

Here, $B(x, y, z)$ is a transformation matrix giving strains in terms of v_n , and the D matrix consists of appropriate material constants giving stresses in terms of strains. The mass matrix M for the assembled structure can be obtained by applying the Boolean transformation of Ref. 1 in the form

$$v = a r. \quad (2)$$

Thus,

$$M = a^t m a.$$

Similarly,

$$K = a^t k a$$

and

$$C = a^t c a,$$

where m , k , and c are diagonal matrices, the n th elements of which are the matrices M_n , K_n , and C_n , respectively. When the generalized forces corresponding to the generalized displacements r are denoted by R , the equations of motion for the complete structure can be written as

$$M \ddot{r} + K r + C \dot{r} = R. \quad (3)$$

The displacements r can be expressed in terms of the normal coordinates q as

$$r = \phi q(t), \quad (4)$$

where ϕ is a matrix of normal modes. By substituting (4) in (3) and premultiplying by ϕ^t ,

$$[M'_n] \ddot{q} + [C'_n] \dot{q} + [K'_n] q = \phi^t R, \quad (5)$$

where

$$[M'_n] = \phi^t M \phi,$$

$$[C'_n] = \phi^t C \phi = \frac{c}{m} [M'_n],$$

and

$$[K'_n] = \phi^t K \phi.$$

The response of the above system to a sinusoidal loading $R = R_0 e^{i\omega t}$ can now be found. By using the notation

$$K'_n/M'_n = \omega_n^2, C'_n/\sqrt{K'_n M'_n} = 2\zeta_n,$$

the equations of motion are of the form

$$\ddot{q} + [2\zeta_n \omega_n] \dot{q} + [\omega_n^2] q = [M'_n]^{-1} \phi^t R_0 e^{i\omega t}. \quad (6)$$

Therefore,

$$q = [Z_n(\omega)]^{-1} \phi^t R_0 e^{i\omega t} \quad (7)$$

where

$$\begin{aligned} Z_n(\omega) &= M'_n(-\omega^2 + \omega_n^2 + 2i\zeta_n \omega_n \omega) \\ &= M'_n(-\omega^2 + \omega_n^2 + c\omega/mi), \end{aligned} \quad (8)$$

and is known as the impedance matrix for the normal coordinates. Finally, the displacements r can be written as

$$\begin{aligned} r &= \phi [Z_n]^{-1} \phi^t R_0 e^{i\omega t} \\ &= H(\omega) R_0 e^{i\omega t}, \end{aligned} \quad (9)$$

where

$$H(\omega) = \phi [Z_n(\omega)]^{-1} \phi^t, \quad (10)$$

and is known as the matrix of complex response functions. The complex response function $H_{ij}(\omega)$, which is the ij element of $H(\omega)$, is defined as the displacement produced at i due to a unit force at j having the same direction as $e^{i\omega t}$. Equation (10) may also be written in terms of the frequency f (in cycles per second). Thus,

$$H(f) = \phi [Z_n(f)]^{-1} \phi^t \quad (11)$$

where

$$Z_n(f) = 4\pi^2 M'_n(-f^2 + f_n^2 + 2i\zeta_n f_n f). \quad (12)$$

If the forces R are random, the cross-correlation matrix $R_{R_i}(\tau)_{R_j}$ may be defined as

$$\begin{aligned} \underline{R}_{R_i R_j}(\tau) &= \lim_{T \rightarrow \infty} \frac{1}{T} \int_{-T/2}^{T/2} \underline{R}(t) \underline{R}^t(t+\tau) dt \\ &= \langle \underline{R}(t) \underline{R}^t(t+\tau) \rangle, \end{aligned} \quad (13)$$

where $\langle \rangle$ represents the time average.

The i, j element of $\underline{R}_{R_i R_j}$ matrix gives the cross-correlation the loadings R_i and R_j for $i \neq j$ and the autocorrelation function otherwise. The input power spectral density matrix $\underline{S}_I(f)$ of the excitation forces \underline{R} is defined as

$$\underline{S}_I(f) = 2 \int_{-\infty}^{\infty} \underline{R}_{R_i R_j}(\tau) e^{-i2\pi f \tau} d\tau. \quad (14)$$

The output power spectral density matrix $\underline{S}_O(f)$ of the response displacements \underline{r} can similarly be written as

$$\underline{S}_O(f) = 2 \int_{-\infty}^{\infty} \underline{R}_{r_i r_j}(\tau) e^{-i2\pi f \tau} d\tau \quad (15)$$

where

$$\begin{aligned} \underline{R}_{r_i r_j}(\tau) &= \lim_{T \rightarrow \infty} \frac{1}{T} \int_{-T/2}^{T/2} r(t) r^t(t+\tau) dt \\ &= \langle r(t) r^t(t+\tau) \rangle. \end{aligned} \quad (16)$$

Denoting by $h(t)$ the matrix of impulse response functions, the i, j element of which gives the response at i due to a unit impulse at j , the displacements $\underline{r}(t)$ can be written as

$$r_i(t) = \int_0^{\infty} h_{ij}(\tau) R_j(t-\tau) d\tau. \quad (17)$$

By substituting this value in Eq. (16),

$$\begin{aligned} \underline{R}_{r_i r_j}(\tau) &= \int_0^{\infty} \int_0^{\infty} \left[h_{i1}(\theta_1) \underline{R}(t-\theta_1) \underline{R}^t(t+\tau-\theta_2) h_{j2}^t(\theta_2) \right. \\ &\quad \left. \times d\theta_2 d\theta_1 \right] \end{aligned}$$

or

$$\begin{aligned} \underline{R}_{r_i r_j}(\tau) &= \int_0^{\infty} \int_0^{\infty} \left[h_{i1}(\theta_1) \underline{R}_{R_i R_j}(\tau+\theta_1-\theta_2) \right. \\ &\quad \left. \times h_{j2}^t(\theta_2) d\theta_2 d\theta_1 \right]. \end{aligned} \quad (18)$$

By substituting this value of $\underline{R}_{r_i r_j}(\tau)$ in Eq. (15),

$$\begin{aligned} \underline{S}_O(f) &= 2 \int_{-\infty}^{\infty} e^{-i2\pi f \tau} \left[\int_0^{\infty} \int_0^{\infty} h_{i1}(\theta_1) \underline{R}_{R_i R_j}(\tau+\theta_1-\theta_2) \right. \\ &\quad \left. \times h_{j2}^t(\theta_2) d\theta_2 d\theta_1 \right] d\tau \\ &= 2 \int_0^{\infty} h_{i1}(\theta_1) e^{i2\pi f \tau} \\ &\quad \times \left[\int_{-\infty}^{\infty} \underline{R}_{R_i R_j}(\tau+\theta_1-\theta_2) e^{-i2\pi f(\tau+\theta_1-\theta_2)} d\tau \right] \\ &\quad \times \left[\int_{-\infty}^{\infty} h_{j2}^t(\theta_2) e^{-i2\pi f \theta_2} d\theta_2 \right] \\ &= \underline{H}^*(f) \times \left[2 \int_{-\infty}^{\infty} \underline{R}_{R_i R_j}(\tau) e^{-i2\pi f \tau} d\tau \right] \underline{H}(f) \\ &= \underline{H}^*(f) \underline{S}_I(f) \underline{H}(f), \end{aligned} \quad (19a)$$

where $\underline{H}^*(f)$ is the complex conjugate of $\underline{H}(f)$. Similarly,

$$\underline{S}_O(\omega) = \underline{H}^*(\omega) \underline{S}_I(\omega) \underline{H}(\omega). \quad (19b)$$

The diagonal elements of the matrix $\underline{S}_O(f)$ give the spectral densities of the responses, while the off-diagonal elements give the cross-spectral densities of the responses. The mean square of the i th response r_i can be obtained from the ii element of the matrix $\underline{S}_O(f)$. Thus,

$$\langle r_i^2(t) \rangle = \int_0^{\infty} S_{Oii}(f) df = \int_0^{\infty} S_{Oii}(\omega) d\omega. \quad (20)$$

It is clear from Eq. (20) that

$$S_{Oii}(f) = 2\pi S_{Oii}(\omega).$$

Numerically, the integrations in Eq. (20) can be performed by calculating $S_{Oii}(\omega)$ at various values of ω and then applying the trapezoidal formula for area calculation.

For manipulations on an electronic computer, Eq. (19) can be written in a slightly different form by decomposing $\underline{S}_I(f)$ into real and imaginary parts. Let

$$\underline{S}_I(f) = \underline{p} + i\underline{q}. \quad (21)$$

where \underline{p} is a symmetric matrix and \underline{q}' is a skew symmetric matrix. Also, let

$$[\underline{Z}_n]^{-1} = \underline{E}_n + i \underline{D}_n,$$

where

$$\underline{E}_n = \left(-f^2 + f_n^2 \right) / 4\pi^2 M_n \left[\left(f_n^2 - f^2 \right)^2 + 4\zeta_n^2 f_n^2 f^2 \right]$$

and

$$\underline{D}_n = -2\zeta_n f_n f / 4\pi^2 M_n \left[\left(f_n^2 - f^2 \right)^2 + 4\zeta_n^2 f_n^2 f^2 \right].$$

Then,

$$\underline{H}(f) = \underline{\phi} \underline{E}_n \underline{\phi}^t + i \underline{\phi} \underline{D}_n \underline{\phi}^t \quad (22)$$

and

$$\underline{H}^*(f) = \underline{\phi} \underline{E}_n \underline{\phi}^t - i \underline{\phi} \underline{D}_n \underline{\phi}^t. \quad (23)$$

By substituting Eqs. (21) through (23) in Eq. (19), the real part of $\underline{S}_o(f)$ is determined as

$$\begin{aligned} & \underline{\phi} \underline{E}_n \underline{\phi}^t \underline{p} \underline{\phi} \underline{E}_n \underline{\phi}^t + \underline{\phi} \underline{D}_n \underline{\phi}^t \underline{q}' \underline{\phi} \underline{E}_n \underline{\phi}^t \\ & - \underline{\phi} \underline{E}_n \underline{\phi}^t \underline{q}' \underline{\phi} \underline{D}_n \underline{\phi}^t + \underline{\phi} \underline{D}_n \underline{\phi}^t \underline{p} \underline{\phi} \underline{D}_n \underline{\phi}^t. \end{aligned} \quad (24)$$

Similarly, the imaginary part of $\underline{S}_o(f)$ is

$$\begin{aligned} & \underline{\phi} \underline{E}_n \underline{\phi}^t \underline{q}' \underline{\phi} \underline{E}_n \underline{\phi}^t - \underline{\phi} \underline{D}_n \underline{\phi}^t \underline{p} \underline{\phi} \underline{E}_n \underline{\phi}^t \\ & + \underline{\phi} \underline{E}_n \underline{\phi}^t \underline{p} \underline{\phi} \underline{D}_n \underline{\phi}^t + \underline{\phi} \underline{D}_n \underline{\phi}^t \underline{q}' \underline{\phi} \underline{D}_n \underline{\phi}^t. \end{aligned} \quad (25)$$

If required, the mean square values of the internal forces in the structure can also be obtained. The internal forces \underline{P} can be written as

$$\underline{P} = \underline{k} \underline{v} \quad (26)$$

or

$$\underline{P} = \underline{k} \underline{a} \underline{r}.$$

The complete cross-correlation matrix for the output forces \underline{P} is given by

$$\begin{aligned} \underline{R}_{P_i P_j} &= \langle \underline{P}(t) \underline{P}^t(t + \tau) \rangle \\ &= \underline{k} \underline{a} \langle \underline{r}(t) \underline{r}^t(t + \tau) \rangle \underline{a}^t \underline{k}^t. \end{aligned} \quad (27)$$

Similarly to Eq. (19), the output power spectral density matrix $\underline{S}_{P_o}(f)$ for the forces \underline{P} can be shown to be given by

$$\underline{S}_{P_o}(f) = \underline{k} \underline{a} \underline{H}^*(f) \underline{S}_r(f) \underline{H}(f) \underline{a}^t \underline{k}^t$$

or

$$\underline{S}_{P_o}(f) = \underline{k} \underline{a} \underline{S}_o(f) \underline{a}^t \underline{k}^t. \quad (28)$$

To calculate the mean square values of the forces, only the real part of the output power spectral density matrix $\underline{S}_o(f)$ for the generalized displacements \underline{r} , given by Eq. (24), should be substituted in Eq. (28).

An automatic computer program was set up to calculate the output power spectral densities and mean square values of the displacements and internal forces from the initial data in its simplest form. The program has the option of either automatically generating the stiffness, mass, and damping matrices or obtaining these as input data. A set of spectral matrices and their associated frequencies to describe the power and cross-spectral density functions is required as input. The program calculates the natural frequencies, mode shapes, and output power spectral densities at the desired frequencies. In addition, it performs numerical integration to obtain the mean square values of displacements or internal forces. Equations (24) and (25) are used to calculate the real and imaginary parts of the output power spectral density matrix \underline{S}_o . If only the mean square values of the responses are desired, then only the real part of the matrix \underline{S}_o is computed.

TYPICAL EXAMPLES AND RESULTS

A few typical cases have been solved here to show the accuracy obtained using the finite element approach as well as to demonstrate its versatility. In all cases the damping coefficient, c , is assumed to be equal to $0.1 \sqrt{EI_m/L^4}$. The cases solved are for the following:

1. A simply supported beam subjected to a uniformly distributed load such that there is no cross correlation between loading intensities. Thus,

$$S_I(w, x_A, x_B) = S_I(w, x_A) \delta(x_A - x_B).$$

(The δ -function has zero value except when $x_A = x_B$.)

This problem was solved by dividing the beam into eight equal parts. The mass and stiffness matrices for a beam element can be obtained from Ref. 3. The uniformly distributed load is assumed to be acting at the node points. The generalized displacements used and the corresponding loads are shown in Fig. 1, while stiffness and mass matrices for the uniform simply supported beam are illustrated

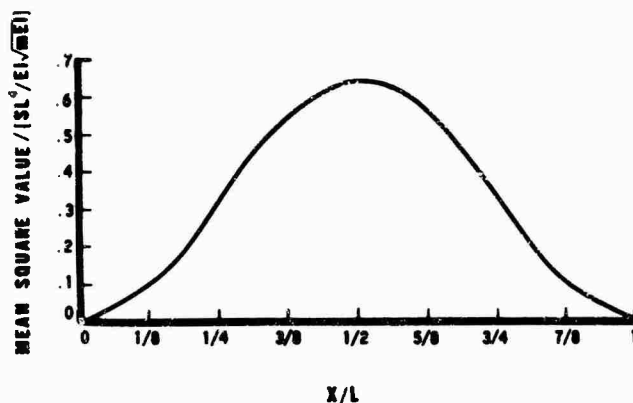


Fig. 5. Mean square values of displacements due to a random concentrated load at the center

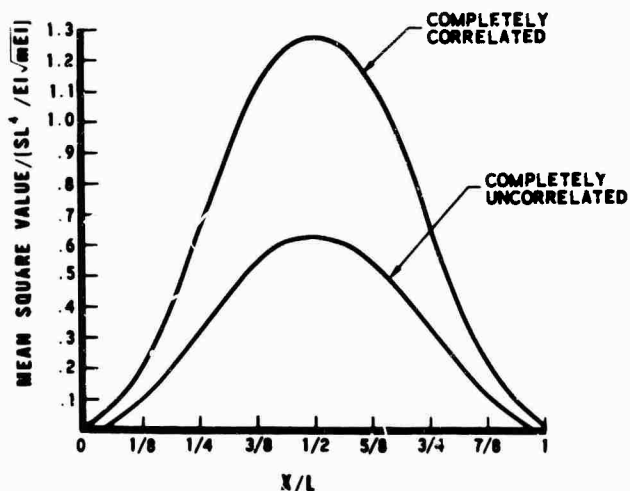


Fig. 6. Mean square values of displacements due to two random loads

where

$$w_1 = 10.0 \frac{\sqrt{EI}}{mL^4}$$

This is shown in Fig. 7. The mean square values of the displacement along the beam are shown in Fig. 8. By using Eq. (28), the mean square values of the internal moments were computed and are shown in Fig. 9.

SUMMARY AND CONCLUSIONS

A general method for the determination of the response of a structure to multiple input random vibrations is outlined; the finite element method was used to characterize the structure. To illustrate the method, the response of a uniform beam with various end

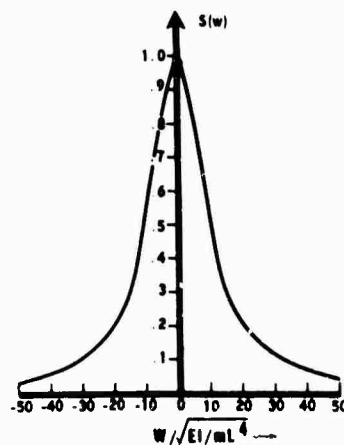


Fig. 7. Input power spectral density for the cantilever beam

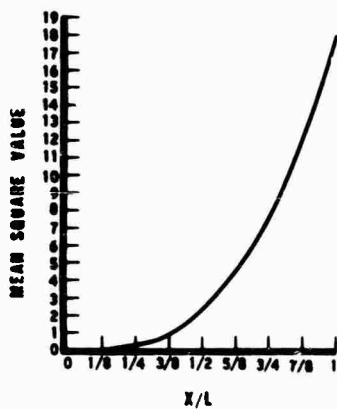


Fig. 8. Mean square values of the displacements for a cantilever beam due to a concentrated load

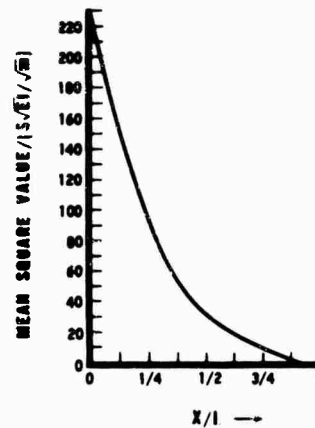


Fig. 9. Mean square values of the displacement for a cantilever beam due to a concentrated load

constraints was determined when the beam was subjected to multiple random inputs. It is believed that these examples are sufficiently complex to illustrate the method. Shear and rotary inertia effects could have been included in the examples chosen by making use of the Timoshenko beam element developed in Ref. 6, but this would only have served to make the computations more tedious. The method is applicable to nonuniform, nonsymmetrical beams as well as to plates, shells, or any other structure that can be reasonably subdivided into finite elements; moreover, the method can handle a fully populated input power spectral density

matrix, and is completely general with respect to geometry and material properties.

Mathematically, it can be shown that the method converges to the exact solution as the number of elements is increased; therefore, any desired degree of accuracy can be obtained, depending on computer and formulation time expended. Care should be used when numerical integration is used to calculate the mean square values of the displacements or stresses. For instance, near the natural frequencies, the integration interval to be used should be small in order to incorporate the peaks in the output power spectral densities correctly.

REFERENCES

1. J. H. Argyris, "Continua and Discontinua - An Apercu of Recent Developments of the Matrix Displacement Method," paper presented at the Air Force Conference on Matrix Methods in Structural Mechanics at Wright Patterson Air Force Base, Dayton, Ohio, October 1965
2. M. J. Turner, H. C. Martin, and R. C. Weikel, "Further Development and Applications of the Stiffness Method," paper presented at the AGARD Structures and Materials Panel in Paris, July 1962
3. J. S. Archer, "Consistent Matrix Formulation for Structural Analysis Using Finite Element Techniques," *J. Am. Inst. Aeron. and Astron.* 3:1910-1917 (1965)
4. R. J. Melosh, "Basis for Derivation of Matrices for the Direct Stiffness Method," *J. Am. Inst. Aeron. and Astron.* 1:1631-1637 (1963)
5. R. W. Clough and Y. R. Rashid, "Finite Element Analysis of Axisymmetric Solids," *J. Eng. Mech. Div., ASCE*, 91:71-86 (1965)
6. K. K. Kapur, "Vibrations of a Timoshenko Beam Using Finite Element Approach," *J. Acoust. Soc. Am.* 40:1058-1064 (1966)
7. G. M. L. Gladwell, "A Finite Element Method for Acoustics," *Proceedings 5th Int. Congr. Acoust. Paper L.33*, 1965
8. O. C. Zienkiewicz, P. Mayer, and Y. K. Cheung, "Solution of Anisotropic Seepage

- by Finite Elements," J. Eng. Mech. Div., ASCE, 92:111-120 (1966)
9. E. L. Wilson and R. E. Nickell, "Application of the Finite Element Method to Heat Conduction Analysis," Nuclear Engineering and Design, 4:276-286 (1966)
 10. R. E. Jones, et al., "Wave Propagation Analysis in Elastic Structures by Use of Finite Element Models," paper presented at the 5th U.S. National Congress of Applied Mechanics, Minneapolis, June 1966
 11. K. K. Kapur and B. J. Hartz, "Stability of Plates Using the Finite Element Approach," J. Eng. Mech. Div., ASCE, 92:177-195 (1966)
 12. S. H. Crandall, "Random Vibrations" (The MIT Press, Massachusetts), Vol. 1, 1958, and Vol. 2, 1963
 13. W. T. Thomson and M. V. Barton, "The Response of Mechanical Systems to Random Excitation," J. Appl. Mech., ASME (June 1957), pp. 248-251
 14. A. C. Eringen, "Response of Beams and Plates to Random Loads," J. Appl. Mech., ASME (1957), pp. 46-52
 15. J. L. Bogdonoff and J. E. Goldberg, "On the Bernoulli-Euler Beam Theory with Random Excitation," J. Aero Space Sciences, 27:371-376 (1960)
 16. S. H. Crandall and A. Yildiz, "Random Vibrations of Beams," J. Appl. Mech., ASME (1962), pp. 267-275
 17. J. D. Robson, An Introduction to Random Vibration (Elsevier Publishing Co., New York), 1966, pp. 71-73

Appendix

NOTATION

The following symbols have been adopted for use in this paper. Underlines indicate that the symbol represents a matrix.

- | | |
|--|---|
| \underline{a} = Boolean transformation matrix | \underline{h} = the matrix of impulse response functions |
| \underline{A} = transformation matrix giving displacements \underline{u} in terms of \underline{v}_n | \underline{H} = matrix of complex response functions |
| c = damping constant | \underline{k} = diagonal stiffness matrix, the n th element of which is \underline{K}_n |
| \underline{B} = transformation matrix giving strains in terms of \underline{v}_n | \underline{K} = stiffness matrix for the complete structure |
| \underline{c} = diagonal damping matrix, the n th element of which is \underline{C}_n | \underline{K}_n = stiffness matrix for the n th element |
| \underline{C} = damping matrix for the complete structure | $[\underline{K}'_n] = \underline{\phi}^t \underline{K} \underline{\phi}$ |
| \underline{C}_n = damping matrix for the n th element | L = length of the beam element |
| $[\underline{C}'_n] = \underline{\phi}^t \underline{C} \underline{\phi}$ | m = mass per unit volume; for beams, mass per unit length |
| D = matrix giving stresses in terms of strains | \underline{m} = diagonal mass matrix, the n th element of which is \underline{M}_n |
| f = frequency in cycles per second | \underline{M}_n = mass matrix for the n th element |
| F = dissipation function | $[\underline{M}'_n] = \underline{\phi}^t \underline{M} \underline{\phi}$ |
| | \underline{p} = real part of input power spectral density matrix |
| | \underline{P} = internal forces |

- \underline{q} = normal coordinates
 \underline{q}' = imaginary part of input power spectral density matrix
 \underline{r} = generalized displacements for the whole structure
 \underline{R} = generalized forces for the whole structure
 $\underline{R}_{r_i r_j}$ = matrix of cross correlation functions for displacements r_i
 $\underline{R}_{R_i R_j}$ = matrix of cross correlation functions for forces R_i
 \underline{S}_i = input power spectral density matrix
 \underline{S}_o = output power spectral density matrix
 \underline{S}_{P_o} = output power spectral density matrix for internal forces P
- t = time
 T = kinetic energy
 U = strain energy
 \underline{v}_n = nodal displacements for the n th element
 ω = frequency in radians per second
 ω_n = n th natural frequency
 x, y, z = rectangular coordinates
 $\underline{\phi}$ = matrix of normal modes
 $2\zeta_n = C'_n / \sqrt{K'_n M'_n}$
 τ = time variable
 $[]$ = diagonal matrix
 $\langle \rangle$ = time average

* * *

FREQUENCY ANALYSIS OF REPETITIVE BURSTS OF RANDOM VIBRATION

W. E. Noonan
McDonnell Company
St. Louis, Missouri

An investigation was conducted to determine the applicability of using an analog harmonic analyzer to determine the frequency spectrum of transients or signals that consist of a series of pulses or bursts. The analysis was based on the application of standard Fourier techniques for transient functions to obtain an amplitude function independent of time. The Fourier amplitude spectrum was obtained by applying the energy function relating time and frequency.

This investigation indicated that the harmonic analyzer must be able to perform the functions of filtering, true squaring, and true integration. An analyzer with these capabilities can determine the Fourier amplitude spectrum of transient functions or the power spectral density of randomly occurring pulses or bursts. The technique presented in this paper provides an accurate, economical method for analyzing data that previously required the use of a digital computer.

INTRODUCTION

The analysis of periodic and stationary random functions has been extensively detailed in the literature. Many investigations have been conducted in the industry to develop equipment capable of producing, controlling, and analyzing periodic and continuous random data. Frequency decomposition harmonic analysis is commonly used for periodic functions and power spectral density analysis of continuous random functions. Occasionally vibration data is encountered that does not fall into either of the above categories. An example of such a signal is the vibration generated by a rocket motor or thruster that is fired intermittently for short periods but otherwise remains inactive. The purpose of this paper is to present a method for processing such data and to describe the use of a harmonic analyzer for implementation of this method.

The analysis to be described is based on the well-known Fourier transform for mapping transient time function into the frequency domain [1]:

$$F(f) = \int_{-\infty}^{\infty} f(t) e^{-j\omega t} dt. \quad (1)$$

Application of the Fourier transform requires the integral of the data to be absolutely convergent. The integral,

$$\int_{-\infty}^{\infty} |f(t)| dt, \quad (2)$$

must be finite.

A theoretical study of the Fourier transform as related to a transient function is reviewed, and its relation to the energy and power spectrum is shown. The analysis of data consisting of short-duration bursts is described, and the achievement of power spectral density for the environment, using transient analysis techniques, is demonstrated. Methods of performing the Fourier transform using an analog harmonic analyzer are presented, and the analysis of stylized pulses is included.

FOURIER ANALYSIS

Fourier Transform - Transient Function

The Fourier transform (defined by Eq. (1)) for a transient function is obtained from the Fourier series for periodic function:

$$f(t) = \sum_{n=-\infty}^{\infty} e^{jn\omega_0 t} \frac{1}{T_0} \int_{-T_0/2}^{T_0/2} f(\sigma) e^{-jn\omega_0 \sigma} d\sigma. \quad (3)$$

As $1/T_0$ is equal to f_0 , Eq. (3) is rewritten,

$$f(t) = \sum_{n=-\infty}^{\infty} e^{jn\omega_0 t} f_0 \int_{-T_0/2}^{T_0/2} f(\sigma) e^{-jn\omega_0 \sigma} d\sigma. \quad (4)$$

Now, if the period T_0 grows without limit, the periodic function $f(t)$ tends to an aperiodic (transient) function, and Eq. (4), therefore, approaches the limiting form,

$$f(t) = \int_{-\infty}^{\infty} e^{j\omega t} df \int_{-\infty}^{\infty} f(\sigma) e^{-j\omega \sigma} d\sigma, \quad (5)$$

where $T_0 \rightarrow \infty$, $f_0 \rightarrow df$, and $nf_0 \rightarrow f$.

The Fourier integral (Eq. (5)) for transient functions can be written as the transform pair:

$$F(f) = \int_{-\infty}^{\infty} f(t) e^{-j\omega t} dt \quad (6)$$

and

$$f(t) = \int_{-\infty}^{\infty} F(f) e^{j\omega t} df. \quad (7)$$

The transform pair in Eqs. (6) and (7) can be written in terms of angular frequency (ω) by substituting $2\pi/\omega_0$ for T_0 in Eq. (3). For this case the transform pair is expressed as

$$F(\omega) = \frac{1}{2\pi} \int_{-\infty}^{\infty} f(t) e^{-j\omega t} dt \quad (8)$$

and

$$f(t) = \int_{-\infty}^{\infty} F(\omega) e^{j\omega t} d\omega. \quad (9)$$

The $F(f)$ and $F(\omega)$ functions can be written in terms of amplitude and phase spectrums:

$$F(f) = |F(f)| e^{j\phi(f)} \quad (10)$$

and

$$F(\omega) = |F(\omega)| e^{j\phi(\omega)}. \quad (11)$$

The functions $|F(f)|$ and $|F(\omega)|$ are amplitude-density functions and have the dimensions of amplitude/hertz and amplitude/radian/second. The amplitude density is not a measure of the amplitude characteristics of $f(t)$ because the amplitudes of the sinusoidal in Eq. (7), $F(f) df$, are infinitesimal. The amplitude density is a characteristic that shows relative magnitude only.

Equation (6) is the relation that maps the transient function from the time-to-frequency domain. It is the performance of this operation that will be discussed using analog techniques.

The energy relation for the time and frequency function will now be discussed. Returning to the periodic function, the average power is expressed as

$$\frac{1}{T_0} \int_{-T_0/2}^{T_0/2} f^2(t) dt = \sum_{n=-\infty}^{\infty} |V(n)|^2. \quad (12)$$

where

$$V(n) = \frac{1}{T_0} \int_{-T_0/2}^{T_0/2} f(t) e^{-jn\omega_0 t} dt.$$

The energy in one fundamental period is

$$\int_{-T_0/2}^{T_0/2} f^2(t) dt = T_0 \sum_{n=-\infty}^{\infty} |V(n)|^2. \quad (13)$$

Letting the period approach infinity for the transient function, the energy can be expressed as

$$\lim_{T_0 \rightarrow \infty} \sum_{n=-\infty}^{\infty} |V(n)|^2 T_0$$

$$= \lim_{T_0 \rightarrow \infty} \sum_{n=-\infty}^{\infty} \left| \frac{1}{T_0} \int_{-T_0/2}^{T_0/2} f(t) e^{-jn\omega_0 t} dt \right|^2 T_0 \quad (14)$$

and

$$\lim_{T_0 \rightarrow \infty} \sum_{n=-\infty}^{\infty} |V(n)|^2 T_0$$

$$= \lim_{T_0 \rightarrow \infty} \sum_{n=-\infty}^{\infty} \left| \int_{-T_0/2}^{T_0/2} f(t) e^{-jn\omega_0 t} dt \right|^2 \frac{1}{T_0}. \quad (15)$$

Applying this to Eq. (13), the energy relation for the time and frequency transient function is expressed as

$$\int_{-\infty}^{\infty} f^2(t) dt = \int_{-\infty}^{\infty} |F(f)|^2 df. \quad (16)$$

The above expression in terms of angular frequency is

$$\int_{-\infty}^{\infty} f^2(t) dt = 2\pi \int_{-\infty}^{\infty} |F(\omega)|^2 d\omega. \quad (17)$$

As the total energy of a transient is finite, the average power over an infinite period is infinitesimal. The integral square of the function over an infinite interval is finite, but the mean square over the same infinite interval is an infinitesimal quantity.

Some discussion of the one-sided spectrum [2] should be included. With reference to Eq. (16), it should be noted that a negative frequency spectrum has little physical meaning. The spectrum $|F(f)|^2$ is an even function, and Eq. (16) could be rewritten as

$$\int_{-\infty}^{\infty} f^2(t) dt = 2 \int_0^{\infty} |F(f)|^2 df. \quad (18)$$

If we let $|F'(f)| = \sqrt{2} |F(f)|$, then

$$\int_{-\infty}^{\infty} f^2(t) dt = \int_0^{\infty} |F'(f)|^2 df. \quad (19)$$

The spectrum $|F'(f)|$ is the function that the analog analyzer is calibrated to display.

Fourier Transform and Power Spectral Density

Certain random environments involve multiple, short-duration pulses or bursts. These functions can be a randomly occurring repetition of the same pulse or an ensemble of statistically independent random bursts with equal power spectral densities. A pulse is defined as a single excursion from the zero base line, while the burst consists of a complex waveform having a number of plus and minus excursions from the zero base line. Both the pulse and burst ensembles differ from the transient, as the ensemble has finite power.

The power spectral density of the ensemble is related by a weighting factor to the squared

Fourier amplitude spectrum of the individual pulse or burst. The weighting factor is the average number of occurrences per second. Additional restraints, which depend on the sequence of positive and negative occurrences, affect the spectrum of the ensemble near zero frequency. These restraints will be discussed in detail in a later section.

The analysis of an ensemble of independent bursts is conducted in a manner similar to the transient analysis. The squared Fourier amplitude spectrum is computed for each pulse or burst, summed, and then averaged over the time sample.

$$G(f) = \frac{\sum_{n=1}^N |F_n(f)|^2}{T}, \quad (20)$$

where

$G(f)$ = power spectrum ensemble

N = number of pulses in time T

T = length of time sample.

If it is assumed that the Fourier amplitude spectrum is the same for each function, then Eq. (20) can be rewritten as

$$G(f) = \frac{N}{T} |F(f)|^2, \quad (21)$$

where N/T = weighting factor — average number of bursts per second.

A discussion of Eq. (21), including verification by experimental measurements, is presented in a later section.

ANALOG ANALYSIS

The analog analysis of transient data consists of the basic operations of filtering, squaring, and integrating. The result of these operations is the amplitude spectrum, $|F(f)|$, of the Fourier transform. The filtered output of the transient, $f_0(t)$, can be expressed as a summation from the beginning, a , to the time, t , of the input transient, $f_1(t)$, and the unit impulse response of the filter, $h(t)$:

$$f_0(t) = \int_a^t h(t-\tau) f_1(\tau) d\tau. \quad (22)$$

Mapping Eq. (22) from the time-to-frequency domain results in an expression

containing the Fourier spectrums and the frequency response function of the filter:

$$|F_0(f)| = |H(f)| |F_1(f)|, \quad (23)$$

where

$$|H(f)| \begin{cases} 1, & f_c - \Delta f/2 < f < f_c + \Delta f/2 \\ 0, & \text{elsewhere} \end{cases}$$

where f_c = filter center frequency, and Δf = filter bandwidth.

The filtered time function contains only that part of the total energy of $f_1(t)$ in the filter's narrow frequency band. The energy of the filtered output is the integral square of the time function and is expressed as

$$\int_{-\infty}^{\infty} f_0^2(t) dt. \quad (24)$$

As $f_0(t)$ has nonzero values over some finite time, T , Eq. (24) can be rewritten as:

$$\int_0^T f_0^2(t) dt. \quad (25)$$

Returning to the time-to-frequency relation for the energy (see Eq. (18)),

$$\int_0^T f_0^2(t) dt = 2 \int_0^{\infty} |F_0(f)|^2 df. \quad (26)$$

As the characteristics of the filter are such that only energy in the bandpass is transmitted with unity gain, the limit of integration can be restricted to the filter bandpass, and the output Fourier amplitude spectrum can be replaced by the input spectrum:

$$\int_0^T f_0^2(t) dt = 2 \int_{f_c - \Delta f/2}^{f_c + \Delta f/2} |F_1(f)|^2 df. \quad (27)$$

If the bandpass of the filter is small, so that the amplitude spectrum of the data is assumed constant within the frequency band, Eq. (27) is rewritten as

$$\int_0^T f_0^2(t) dt = 2 |F_1(f)|^2 \Delta f. \quad (28)$$

The Fourier amplitude spectrum is therefore shown to be

$$|F_1(f)| = \left[\frac{1}{2\Delta f} \int_0^T f_0^2(t) dt \right]^{1/2}. \quad (29)$$

The $|F'(f)|$ spectrum defined by Eq. (19) is expressed as

$$|F_1'(f)| = \left[\frac{1}{\Delta f} \int_0^T f_0^2(t) dt \right]^{1/2}. \quad (30)$$

Equation (30) is the function which describes the analog analyzer. The analyzer must perform the basic required functions of filtering, true squaring, and true integration. True squaring and true integration are mandatory operations, and it is these operations which enable the harmonic analyzer (see Fig. 1) to perform analog analysis of a transient. The output of the integrator is proportional to $|F'(f)|^2$. By displaying the function in logarithmic format, the analyzer can easily display the absolute value of the Fourier spectrum or the power spectral density. The power spectral density is obtained by normalizing the function, $|F'(f)|^2$, with respect to the length of the time record, T . When analyzing an ensemble of pulses or bursts, the function, $|F'(f)|^2$, represents the squared Fourier transform of the entire ensemble.

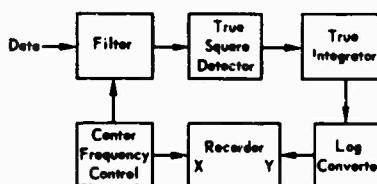


Fig. 1. Analog analyzer

The procedure for the analog analysis is to transcribe the transient onto a magnetic tape loop. Included on this loop is a trigger signal for the integrator which starts the integration function prior to the beginning of the transient. The integrator is set to integrate all nonzero values of the squared, filtered output. The process is repeated as the center frequency is stepped through the frequency range in bandwidth increments. This results in a value of the Fourier amplitude spectrum at each filter center frequency.

Analog Analysis - Stylized Pulses

Analog analysis was conducted on a single pulse and on an ensemble of 54 pulses all having positive magnitude. For the multiple-pulse case, the time duration between the beginning of each pulse varied linearly but was repeated once for each incremental change. This resulted in 27 different time spacings for the ensemble of 54 pulses. The time spacing for this ensemble varied from 32.32 to 320 ms in 12.32 ms increments. The pulse amplitude was unity, and the pulse width was 20 ms.

The single pulse, which was analyzed on the harmonic analyzer, is presented in Fig. 2. The Fourier amplitude spectrum resulting from the analog analysis is compared with a spectrum which is mathematically derived from the time function. Figure 3 verifies the applicability of the harmonic analyzer in determining Fourier amplitude spectrums for transient time functions.

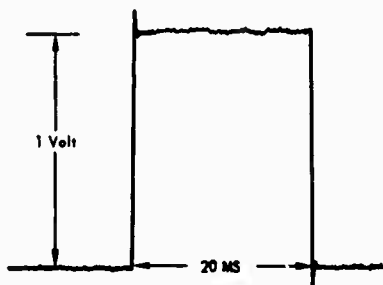


Fig. 2. Analog analysis, stylized pulse - time function

The power spectral density for the time-variant ensemble was approximated using Eq. (21). Although the time-variant ensemble is not a random process consisting of independent occurrences, the mathematical representation using Eq. (21) will be shown to be valid except at certain discrete frequencies. The discrete frequencies are a function of the time dependency between pulses.

Before discussing the applicability of Eq. (21), more general cases will be considered. These cases will be based on the application of unit impulses. The first case is the randomly occurring, Poisson-distributed unit impulses that have equal probability of positive or negative occurrence. The autocorrelation and power spectral density are presented in Figs.

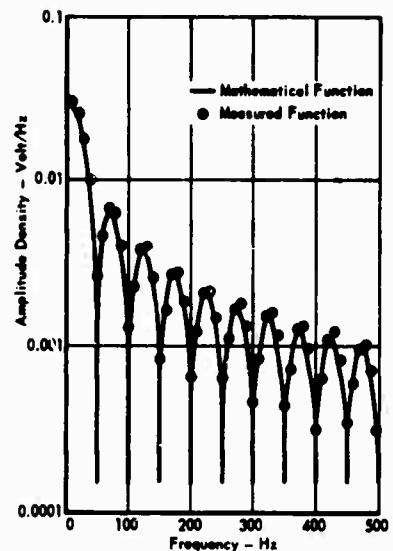


Fig. 3. Analog analysis, stylized pulse - frequency function Fourier amplitude spectrum

4 and 5 [3]. The only value for the autocorrelation is at zero time displacement ($\tau = 0$). The value at zero τ is a weighted unit impulse. The weighting factor is the average number of impulse occurrences per second. Equations (31) and (32) are expressions for the autocorrelation and power spectral density.

$$R(\tau) = \frac{N}{T} u(\tau) \quad (31)$$

and

$$G(f) = \frac{N}{T}, \quad (32)$$

where

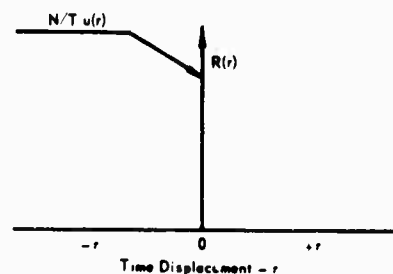


Fig. 4. Random Poisson-distributed unit impulses (equal probability of positive or negative occurrences) - autocorrelation

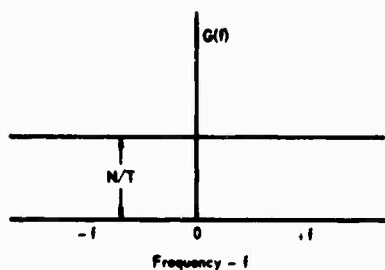


Fig. 5. Random Poisson-distributed unit impulses (equal probability of positive or negative occurrences) — power spectral density

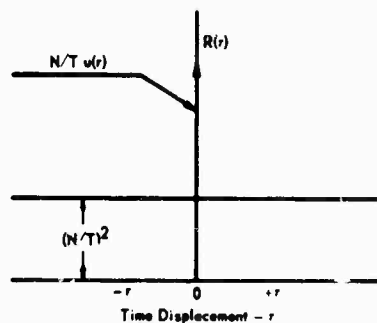


Fig. 6. Random Poisson-distributed unit impulses (positive occurrence only) — autocorrelation

$R(\tau)$ = autocorrelation

$G(f)$ = power spectral density

N/T = weighting factor — average number of impulses per second

N = number of impulses in time record, T

$u(\tau)$ = unit impulse.

If the randomly occurring, Poisson-distributed unit impulses are restricted to only positive occurrences, the autocorrelation and power spectral density for this ensemble of unit impulses (see Figs. 6 and 7) are expressed as [3]

$$R(\tau) = \left(\frac{N}{T}\right)u(\tau) + \left(\frac{N}{T}\right)^2 \quad (33)$$

and

$$G(f) = \left(\frac{N}{T}\right) + \left(\frac{N}{T}\right)^2 u(f) \quad (34)$$

The effect on the power spectrum of restricting the ensemble to only positive occurrences is to introduce a weighted unit impulse $[(N/T)^2 u(f)]$ at zero frequency. This zero frequency component can be verified using the following expression relating the power spectrum and the Fourier amplitude spectrum:

$$G(f) = \frac{|F(f)|^2}{T} \quad (35)$$

At zero frequency, the Fourier amplitude is equal to the integral (area) of the time function. The power spectrum at zero frequency for the positive occurring unit impulses is expressed as

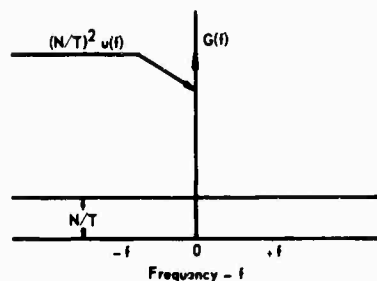


Fig. 7. Random Poisson-distributed unit impulses (positive occurrence only) — power spectral density

$$G(0) = \frac{|F(0)|^2}{T} = \frac{N^2}{T} \quad (36)$$

If the time (T) grows without limit, Eq. (36) can be rewritten as

$$G(0) = \left(\frac{N}{T}\right)^2 u(f) \quad (37)$$

Equation (37) corresponds to the second term of Eq. (34).

The general case for the time-variant ensemble of Fig. 10 would be positive unit impulses occurring at the start of each square pulse. An exact mathematical solution for this case was not considered necessary, as general trends established sufficient information to verify experimental results. The autocorrelation and power spectral density for this time-variant ensemble of unit impulses are presented in Figs. 8 and 9. The autocorrelation of this time-variant ensemble of unit impulses is similar to the autocorrelation of the

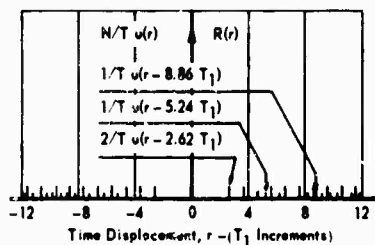


Fig. 8. Time-variant unit impulses -- autocorrelation

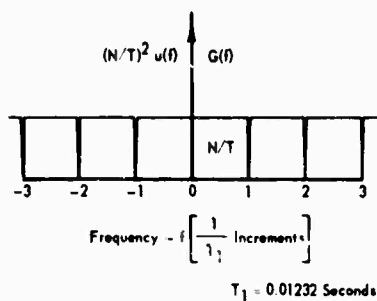


Fig. 9. Time-variant unit impulses -- power spectral density

Poisson-distributed, positive impulses. The primary difference is that the constant, $(N/T)^2$, in the random ensemble is replaced by a series of weighted unit impulses, spaced periodically in time, with weighted values ranging from $1/T$ to $2/T$. These periodic impulses only affect the power spectrum at zero frequency, the fundamental frequency, and harmonics. The fundamental frequency for this case is the reciprocal of the incremental time spacing, $1/0.01232$ or 81 Hz.

At zero frequency, the power spectrum for the time-variant case approximates the zero frequency value for the Poisson-distributed, positive pulses and is expressed as

$$G(0) = \frac{N^2}{T} \approx \left(\frac{N}{T}\right)^2 u(f) \quad (38)$$

The magnitude of the power spectrum at the fundamental frequency and the first seven harmonics was numerically calculated and was found to be approximately zero. The power spectral density of the time-variant ensemble of unit impulses can now be expressed as

$$G(f) = \frac{N}{T} + \left(\frac{N}{T}\right)^2 u(f) \begin{cases} f \neq m 81 \\ m = 1, 2, 3, \dots, 7 \end{cases} \quad (39)$$

$$G(f) = \dots \quad f = m 81. \quad (40)$$

The power spectral density of the ensemble of square pulses (see Fig. 10) was determined, based on linear system relations and the power spectral density of the time-variant unit impulses. It was assumed that a theoretical system could be constructed such that the assumed system's unit impulse response would be equal to the individual square pulse in the time-variant ensemble. The input-output relation for this assumed theoretical system can be expressed as

$$f_{out}(t) = \int_{-\infty}^{\infty} h(t-\tau) f(\tau) d\tau, \quad (41)$$

where

Theoretical System

$$f_{in}(t) \longrightarrow [h(t)] \longrightarrow f_{out}(t)$$

where $h(t)$ = unit impulse response -- square pulse, 20-ms wide, unit amplitude.



Fig. 10. Analog analysis, stylized multiple pulses -- time function

The Fourier transform of the unit impulse response is the system function, $H(f)$, for the theoretical system. For this case the system function would correspond to the Fourier transform, $F(f)$, of the individual square pulse. In a linear system, the output power spectral density is a function of the input power spectral density and the system function, and is expressed as

$$G_{out}(f) = |H(f)|^2 G_{in}(f). \quad (42)$$

For the particular theoretical system described here, the input-output power spectral density is expressed as

$$G_{out}(f) = |F(f)|^2 G_{in}(f). \quad (43)$$

The three cases discussed previously, involving the random and time-variant unit impulses, will now be applied to this theoretical system. The output of this system would be a repetition of the 20-ms square pulses. The occurrence of the square pulses would be a function of the occurrence of the unit impulses. The power spectral density for the output of this theoretical system, resulting from the application of the random and time-variant unit impulses, can be expressed as follows:

(1) Poisson-distributed unit impulses, with equal probability of plus or minus occurrence:

$$G(f) = \frac{N}{T} |F(f)|^2. \quad (44)$$

(2) Poisson-distributed unit impulses with only positive occurrence:

$$G(f) = \frac{N}{T} |F(f)|^2 + \left[\frac{N}{T} F(0) \right]^2 u(f). \quad (45)$$

(3) Time-variant unit impulses:

$$G(f) = \frac{N}{T} |F(f)|^2 + \left[\frac{N}{T} F(0) \right]^2 u(f) \begin{cases} f \neq m 81 \\ m = 1, 2, 3, \dots, 7 \end{cases} \quad (46)$$

$$G(f) = 0, \quad f = m 81. \quad (47)$$

Equations (46) and (47) give the solution for the time-variant ensemble of square pulses. A comparison of these solutions with data obtained from an analysis on a harmonic analyzer is presented in Fig. 11. This comparison verifies the suitability of the harmonic analyzer to perform frequency analysis of pulse data.

It should be noted that the power spectral density, presented by Eqs. (46) and (47), only applies to the time-variant ensemble in question. Any variation in the time spacing would affect the magnitude of the periodic components. The extreme case would be a constant time spacing between pulses (periodic pulse train). For this case, the values at the fundamental and harmonics would predominate, and the values at all other frequencies would become insignificant.

Some mention should be made of the multiple-burst case. This case consists of short-duration, complex waveform signals. If the multiple-burst signal was constructed by taking short-duration, random samples from a

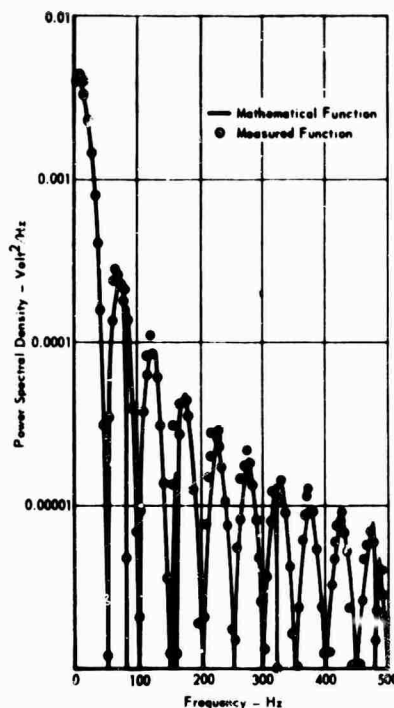


Fig. 11. Analog analysis, stylized multiple pulses — frequency function

continuous, stationary random function, the power spectral density for the burst function, $S_B(f)$, is expressed as

$$S_B(f) = \frac{N}{T_1} |F(f)|^2. \quad (48)$$

where $F(f)$ = Fourier transform of individual burst and N = number of bursts in time record, T_1 .

If it is assumed that each burst has the same power spectral density, then the power spectral density of the continuous function, $S_C(f)$, would be equal to the power spectral density of the individual burst. The relation between the power spectral density of the continuous function and the multiple-burst function is expressed as

$$S_C(f) = \frac{T_1}{N t_0} S_B(f) = \frac{|F(f)|^2}{t_0}, \quad (49)$$

where t_0 = burst duration.

Equation (49) is the basic operation performed by analog harmonic analyzers to determine power spectral density for continuous, stationary random processes.

Figure 12 presents a comparison between the power spectral densities of continuous and burst functions. Both functions were analyzed on a harmonic analyzer. The burst function was obtained from a burst vibration test and represents the input acceleration spectrum for a qualification test specimen. The burst occurrence corresponded to the time-variant case discussed previously, and the burst duration was 20 ms. The periodic components, which were discussed previously, were masked by the analysis bandwidth. The sharp peak in the burst spectrum at 900 Hz was attributed to a structural resonance of the vibration system. This resonance was excited by transients induced into the system by the abrupt starting and stopping of the burst signal.

CONCLUSIONS

It was shown that the analog analyzer described in this paper determines the absolute value squared of the Fourier transform, $|F(f)|^2$. Depending on the signal to be analyzed, the amplitude of the Fourier transform or the power spectral density can be determined.

The analog techniques suggested in this paper present an accurate and economical method for analyzing data which previously required the use of a digital computer. Analog

harmonic analyzers are admittedly slower than digital computers but are less expensive when analyzing random data that requires statistical confidence.

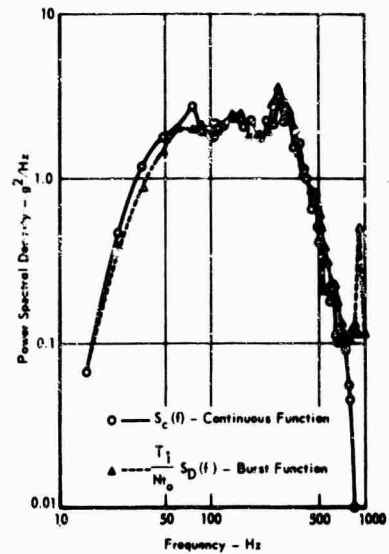


Fig. 12. Acceleration power spectral density comparison test, continuous vs burst function

REFERENCES

1. R. Legros and A. V. S. Martin, Transform Calculus for Electrical Engineers (Prentice-Hall, Inc.), 1961, pp. 38-61
2. J. S. Bendat and A. G. Piersol, Measurement and Analysis of Random Data (John Wiley & Sons, Inc.), 1966, pp. 81-85
3. Y. W. Lee, Statistical Theory of Communication (John Wiley & Sons, Inc.), 1964, pp. 240-248

DISCUSSION

H. Saunders (G.E. Co.): What type of harmonic analyzer did you use?

Mr. Noonan: We used a Honeywell Model 9300, but any harmonic analyzer which had capabilities of performing filtering, true squaring and true integration could be used. That was the primary factor.

Mr. Saunders: One of the problems with a spectral analyzer is the limited amount of continuous data available. The tape splice frequency usually tends to mask some of the data. Have you given any thought to using the digital approach called the Cooley-Tukey method?

Mr. Noonan: We have used that at McDonnell. The only problem is that it takes such a large volume of data or sample to describe this type of function. For instance, these bursts varied linearly with time, occurring over a 10-1/2 second period. The frequency response went up past 2 kHz so, considering the sample rate and sample duration, a very large storage capacity would be required in the digital computer. This is very expensive. We could do this on a harmonic analyzer at a lower cost.

Mr. Saunders: I did not refer to the conventional or Blackman-Tukey method. I meant the fast Fourier transform technique which is

the Cooley-Tukey method. In fact, the shorter amount of time you have for a data burst, the better results you can get using this approach. It is much more accurate than the analog type.

Mr. Noonan: The sample that we are looking at is 10-1/2 seconds. There are the data we want to analyze. We do not want to analyze 1/2 second of this. We want to analyze 10-1/2 seconds. I understand that this technique employs a method by which one can process these data very rapidly, but I can't understand how this can be decreased. You have 10-1/2 seconds data and you have to sample at a certain rate. That is fixed.

Mr. Saunders: Are you considering the 10-1/2 seconds of data to be stationary and ergodic or nonstationary?

Mr. Noonan: No, it is considered as a transient. The whole approach was made using one burst or one sample. It ended after 10-1/2 seconds and it began at zero. It was not continuous.

Mr. Saunders: I think if you go through the Cooley-Tukey approach, you can save a lot, both in computing time and in accuracy.

* * *

SIMPLIFIED RANDOM VIBRATION COMPUTATIONS

LaVerne W. Root and Allen S. Henry
Collins Radio Company
Cedar Rapids, Iowa

A complete set of simplified formulas for mean-square amplitude has been derived for those broadband random processes which satisfy two assumptions: The process is stationary and the spectral density of the process may be represented by straight line segments on log-log coordinates. These formulas are exact and are simpler to use for both hand and machine computations than the formulas presently available in the literature.

Given acceleration spectral density, velocity spectral density, or displacement spectral density, one can compute mean-square acceleration, mean-square velocity, or mean-square displacement in terms of any of the spectral density quantities, using the tables of formulas provided in this paper. Also included in this paper are most of the formulas and definitions used in discussing random vibration test spectrums.

INTRODUCTION

This paper presents formulas for the calculation of the mean-square amplitudes associated with a broadband random spectrum. These formulas are simpler to use for both hand and machine calculations than the formulas previously presented in the literature. Though simple to use, the formulas presented herein are exact when the random vibration spectrum is represented by straight line segments on log-log coordinates. Therefore, these simplified formulas have a broad application since virtually all random vibration test spectrums are represented by straight line segments on log-log coordinates, and all random spectrums can be approximated to any required degree of accuracy by straight line segments on log-log coordinates.

A convenient reference for the formulas and definitions commonly used in discussing random vibration spectrums is also provided in this paper. The formulas and definitions are given as they are used in deriving the formulas for the mean-square amplitudes.

Tables 1 through 3 (acceleration spectral density, velocity spectral density, and displacement spectral density) give the formulas for computing mean-square acceleration, velocity,

and displacement in terms of the specified spectral density. Other important formulas are indicated by numbers in the text. Appendix A presents a numerical example that illustrates the use of several of the formulas.

NOMENCLATURE

a	acceleration (g)
A(f)	acceleration spectral density (g^2/Hz)
d	displacement (in.)
d_{p-p}	double amplitude displacement (in.)
D(f)	displacement spectral density ($in.^2/Hz$)
f	frequency (Hz)
K_i	number of octaves between f_i and f_{i+1}
m	db change in root-mean-square amplitude
M	db change in spectral density

- $p(t), q(t), r(t)$ general random functions
- $P(f), Q(f), R(f)$ general spectral density functions
- q_{rms} root-mean-square amplitude of general function
- t time (sec)
- v velocity (in./sec)
- $V(f)$ velocity spectral density (in.²/sec²/Hz)
- \ln logarithms to base e
- \log logarithms to arbitrary base unless base is specified
- α dimensionless slope
- θ slope in db per octave
- σ standard deviation

DERIVATION OF MEAN-SQUARE AMPLITUDE FORMULAS

Assume that $q(t)$ is a stationary random process; two common parameters used to describe the process are the mean-square

amplitude, $\overline{q^2}$, and the spectral density, $Q(f)$ [1]. The following is the general equation for calculating the mean-square amplitude from the spectral density [2]:

$$\overline{q^2} = \int_0^{\infty} Q(f) df \quad (1)$$

The root-mean-square amplitude, q_{rms} , is given by [2]

$$q_{rms} = [\overline{q^2}]^{1/2} \quad (2)$$

The purpose of this paper is to derive formulas for $\overline{q^2}$ and q_{rms} , using Eqs. (1) and (2), when $Q(f)$ is represented by a set of straight line segments on log-log coordinates.

We shall suppose that $Q(f)$ is represented by N straight line segments (Fig. 1) and that the initial and terminal points of each segment have the coordinates (f_i, Q_i) and (f_{i+1}, Q_{i+1}) ; $i = 1, 2, \dots, N$ respectively. Since only straight line segments are used in representing $Q(f)$, a general equation may be written which is applicable to each segment. In terms of the i -th line segment, the equation is

$$Q(f) = C_i f^{\alpha_i} \quad f_i \leq f \leq f_{i+1} \quad (a)$$

where the dimensionless slope, α_i , is given by

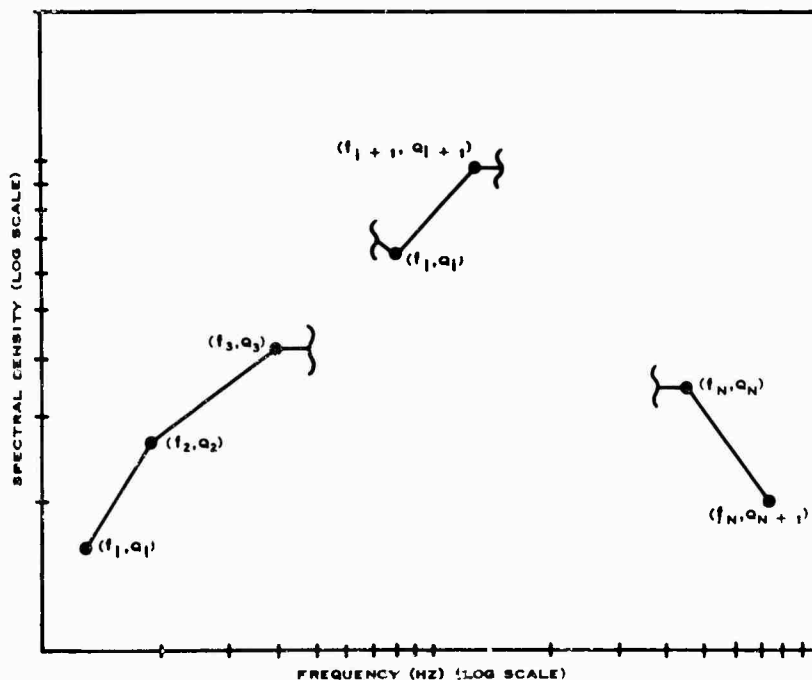


Fig. 1. Typical spectral density plot

$$\alpha_i = \frac{\log(Q_{i+1}/Q_i)}{\log(f_{i+1}/f_i)}, \quad (3)$$

and the constant, C_i , is given by

$$C_i = \frac{Q_i}{f_i^{\alpha_i}} = \frac{Q_{i+1}}{f_{i+1}^{\alpha_i}}. \quad (b)$$

By substituting Eq. (b) into Eq. (a) one obtains

$$Q(f) = Q_i \left(\frac{f}{f_i}\right)^{\alpha_i} = Q_{i+1} \left(\frac{f}{f_{i+1}}\right)^{\alpha_i}. \quad (4)$$

Substituting Eq. (a) into Eq. (1) yields

$$(\overline{q^2}) = \sum_{i=1}^N \int_{f_i}^{f_{i+1}} C_i f^{\alpha_i} df. \quad (c)$$

The preceding equation shows that $(\overline{q^2})$ is simply the sum of N individual integrals, each extending over a single line segment; that is

$$(\overline{q^2}) = \sum_{i=1}^N (\overline{q^2})_i, \quad (5)$$

where

$$(\overline{q^2})_i = \int_{f_i}^{f_{i+1}} C_i f^{\alpha_i} df. \quad (d)$$

To evaluate $(\overline{q^2})_i$, it suffices to derive equations for the evaluation of a typical term $(\overline{q^2})_i$. Note that even though the i -th line segment, as shown in Fig. 1, has a positive slope ($\alpha_i > 0$), it is generally possible for the slope of the i -th segment to be zero ($\alpha_i = 0$) or negative ($\alpha_i < 0$).

Integrating as indicated in Eq. (d) and using Eq. (b) yields the two equivalent expressions

$$\left. \begin{aligned} (\overline{q^2})_i &= \frac{Q_{i+1}}{\alpha_i + 1} \left[f_{i+1} - f_i \left(\frac{f_i}{f_{i+1}}\right)^{\alpha_i} \right] \\ &= \frac{Q_i}{\alpha_i + 1} \left[f_{i+1} \left(\frac{f_{i+1}}{f_i}\right)^{\alpha_i} - f_i \right] \end{aligned} \right\} (e)$$

provided that $\alpha_i \neq -1$. In the event $\alpha_i = -1$, Eqs. (b) and (d) lead to

$$\left. \begin{aligned} (\overline{q^2})_i &= Q_{i+1} f_{i+1} \ln(f_{i+1}/f_i) \\ &= Q_i f_i \ln(f_{i+1}/f_i) \end{aligned} \right\} (6)$$

Formulas (e) and (6) for $(\overline{q^2})$ are those most commonly presented in the literature [3,4,5,6]. However, Formula (e) is time consuming and awkward to use in performing manual calculations because it is necessary to evaluate either $(f_i/f_{i+1})^{\alpha_i}$ or $(f_{i+1}/f_i)^{\alpha_i}$. Computer programs using Formula (e) must incorporate checks to assure that the magnitude of these quantities does not exceed the allowable range of the computer.

Formula (e) can be replaced by a much simpler formula by noting that from Eq. (b),

$$(f_{i+1}/f_i)^{\alpha_i} = (Q_{i+1}/Q_i). \quad (f)$$

By substituting (Q_{i+1}/Q_i) for $(f_{i+1}/f_i)^{\alpha_i}$ in Eq. (e), one obtains the result that if $\alpha_i \neq -1$, then

$$(\overline{q^2})_i = \frac{1}{\alpha_i + 1} [Q_{i+1} f_{i+1} - Q_i f_i]. \quad (7)$$

This formula, which can be used in performing either manual or machine calculations, does not have the disadvantages of Formula (e) as previously cited.

As α_i approaches minus one, Eqs. (7) and (e) approach the indeterminate form (0/0) which causes computational difficulties. Equation (6) is modified as discussed in Appendix B for use when α_i is close or equal to minus one. The modified formula is given as Eq. (B-1), which consists of averaging the two formulas given in Eq. (6). It should be noted that Eq. (B-1) reduces to Eq. (6) for $\alpha_i = -1$ and that the error ($\alpha_i \neq -1$) from using Eq. (B-1) is considerably less than would be obtained from using either of the formulas from Eq. (6).

ALTERNATE FORMULAS

In many cases the slopes of the line segments representing a spectrum are given in terms of decibels/octave. If θ_i is the slope expressed in decibels/octave, then there is a simple relation between θ_i and α_i . Let K_i be the number of octaves between f_i and f_{i+1} , and let M_i be the decibel change between Q_i and Q_{i+1} . Then

$$K_i = \log_2 (f_{i+1}/f_i) = \frac{\log_{10} (f_{i+1}/f_i)}{\log_{10} 2} \quad (8)$$

$$M_i = 10 \log_{10} (Q_{i+1}/Q_i) \quad (9)$$

Now $\theta_i = M_i/K_i$, or using Eq. (3)

$$\theta_i = 10 (\log_{10} 2) \alpha_i \quad (g)$$

For all practical purposes Eq. (g) may be replaced with

$$\theta_i = 3\alpha_i \quad (10)$$

therefore Eq. (7) can be rewritten in terms of θ_i as

$$(\overline{q^2}) = \frac{3}{\theta_i + 3} [Q_{i+1} f_{i+1} - Q_i f_i] \quad (11)$$

for $\theta_i \neq -3$. If $\theta_i = -3$, then Eq. (B-1) should be used.

EXTENSION OF FORMULAS

Often one is given $Q(f)$ corresponding to $q(t)$, and it is necessary to compute either $(\overline{p^2})$ or $(\overline{r^2})$ where $p(t)$, $q(t)$, and $r(t)$ are related as follows:

$$p(t) = \frac{dq}{dt}, \quad r(t) = \int q dt \quad (h)$$

If $P(f)$ and $R(f)$ are the spectral densities associated with $p(t)$ and $r(t)$ respectively, then the following relations may be obtained from general theory [1]:

$$P(f) = (2\pi f)^2 Q(f) \quad (12)$$

$$R(f) = Q(f)/(2\pi f)^2 \quad (13)$$

Therefore, the quantities $(\overline{p^2})_i$ and $(\overline{r^2})_i$ can be expressed in terms of Q_i and α_i using Eqs. (12), (13), and the simplified formulas for $(\overline{p^2})_i$ and $(\overline{r^2})_i$ analogous to Eq. (7). That is,

$$(\overline{p^2})_i = \frac{(2\pi)^2}{\alpha_i + 3} [Q_{i+1} f_{i+1}^3 - Q_i f_i^3], \quad \alpha_i \neq -3 \quad (14)$$

$$\begin{aligned} (\overline{p^2})_i &= (2\pi)^2 Q_i f_i^3 \ln (f_{i+1}/f_i) \\ &= (2\pi)^2 Q_{i+1} f_{i+1}^3 \ln (f_{i+1}/f_i), \quad \alpha_i = -3 \quad (15) \end{aligned}$$

$$(\overline{r^2})_i = \frac{1}{(2\pi)^2 (\alpha_i - 1)} \left[\frac{Q_{i+1}}{f_{i+1}} - \frac{Q_i}{f_i} \right], \quad \alpha_i \neq 1 \quad (16)$$

$$\begin{aligned} (\overline{r^2})_i &= \frac{Q_i}{(2\pi)^2} \ln (f_{i+1}/f_i) \\ &= \frac{Q_{i+1}}{(2\pi)^2 f_{i+1}} \ln (f_{i+1}/f_i), \quad \alpha_i = 1 \quad (17) \end{aligned}$$

Successive applications of Eqs. (12) and (13) make it possible to express the mean-square amplitudes of higher derivatives or multiple integrals of $q(t)$ using the coordinate points (f_i, Q_i) and the slopes α_i .

DISCUSSION OF FORMULAS AND TABLES

Given any one of the spectral densities $A(f)$, $V(f)$, and $D(f)$ corresponding to acceleration a ; velocity v ; and displacement (single amplitude) d , one can compute the mean-square amplitudes $(\overline{a^2})$, $(\overline{v^2})$, and $(\overline{d^2})$ using the formulas derived previously. The formulas to be used for the mean-square amplitudes when the acceleration spectral density is known are given in Table 1. Tables 2 and 3 give similar formulas in terms of velocity and displacement spectral densities, respectively. In applying the formulas given in the tables, the following units must be used: $(\overline{a^2})$, g ; $A(f)$, g^2/Hz ; $(\overline{v^2})$, $(in./sec)^2$; $V(f)$, $(in./sec)^2/Hz$; $(\overline{d^2})$, $(in.)^2$; and $D(f)$, $(in.)^2/Hz$.

Once the mean-square values associated with the individual line segments have been computed, using the formulas from the tables, Eq. (5) is used to obtain the total mean-square value. The root-mean-square value is obtained using Eq. (2).

In addition to the assumption of stationarity, if one assumes that the random process is Gaussian with a mean value of zero, the root-mean-square value from Eq. (2) is the standard deviation or q_σ as it is occasionally designated. Frequently we are interested in $q_{3\sigma}$ which is given as

$$q_{3\sigma} = 3q_{rms} \quad (18)$$

In the case of displacement one may be interested in the three-sigma, peak-to-peak displacement, which is given by

$$d_{p-p} = 2d_{3\sigma} = 6d_{rms} \quad (19)$$

(in. double amplitude).

An additional equation, in terms of q_{rms} , is the decibel change, m , between two levels, which is given by

TABLE 2
Velocity Spectral Density - (in./sec)²/Hz

MEAN-SQUARE AMPLITUDE	DIMENSIONLESS SLOPE: a_v	SLOPE (db/OCTAVE): θ_v
Mean-square acceleration: g^2 $\overline{(a^2)} =$	$\frac{(2\pi)^2}{(a_v + 3)(386)^2} \left[v_2 f_2^3 - v_1 f_1^3 \right]$ $a_v \neq -3$	$\frac{3(2\pi)^2}{(\theta_v + 9)(386)^2} \left[v_2 f_2^3 - v_1 f_1^3 \right]$ $\theta_v \neq -9$
	$\frac{(2\pi)^2}{(386)^2} \left[\frac{v_2 f_2^3 + v_1 f_1^3}{2} \right] \ln(f_2/f_1)$ $a_v = -3$	$\ln(f_2/f_1)$ $\theta_v = -9$
Mean-square velocity: (in/sec) ² $\overline{(v^2)} =$	$\frac{1}{a_v + 1} \left[v_2 f_2 - v_1 f_1 \right]$ $a_v \neq -1$	$\frac{3}{\theta_v + 3} \left[v_2 f_2 - v_1 f_1 \right]$ $\theta_v \neq -3$
	$\frac{v_2 f_2 + v_1 f_1}{2} \ln(f_2/f_1)$ $a_v = -1$	$\ln(f_2/f_1)$ $\theta_v = -3$
Mean-square displacement: (in) ² $\overline{(d^2)} =$	$\frac{1}{(a_v - 1)(2\pi)^2} \left[\frac{v_2}{f_2} - \frac{v_1}{f_1} \right]$ $a_v \neq 1$	$\frac{3}{(\theta_v - 3)(2\pi)^2} \left[\frac{v_2}{f_2} - \frac{v_1}{f_1} \right]$ $\theta_v \neq 3$
	$\frac{1}{2(2\pi)^2} \left[\frac{v_2}{f_2} + \frac{v_1}{f_1} \right] \ln(f_2/f_1)$ $a_v = 1$	$\ln(f_2/f_1)$ $\theta_v = 3$

TABLE 3
Displacement Spectral Density - (in.)²/Hz

MEAN-SQUARE AMPLITUDE	DIMENSIONLESS SLOPE: α_d	SLOPE (db/OCTAVE): θ_d
Mean-square acceleration: g^2 $\overline{(a)^2} =$	$\frac{(2\pi)^4}{(\alpha_d + 5)(386)^2} (D_2 f_2^5 - D_1 f_1^5)$ $\alpha_d \neq -5$	$\frac{3(2\pi)^4}{(\theta_d + 15)(386)^2} (D_2 f_2^5 - D_1 f_1^5)$ $\theta_d \neq -15$
	$\frac{(2\pi)^4}{(386)^2} \left(\frac{D_2 f_2^5 + D_1 f_1^5}{2} \right) \ln(f_2/f_1)$ $\alpha_d = -5 \quad \theta_d = -15$	
Mean-square velocity: (in/sec) ² $\overline{(v)^2} =$	$\frac{(2\pi)^2}{\alpha_d + 3} (D_2 f_2^3 - D_1 f_1^3)$ $\alpha_d \neq -3$	$\frac{3(2\pi)^2}{\theta_d + 9} (D_2 f_2^3 - D_1 f_1^3)$ $\theta_d \neq -9$
	$(2\pi)^2 \left(\frac{D_2 f_2^3 + D_1 f_1^3}{2} \right) \ln(f_2/f_1)$ $\alpha_d = -3 \quad \theta_d = -9$	
Mean-square displacement: (in) ² $\overline{(d)^2} =$	$\frac{1}{\alpha_d + 1} (D_2 f_2 - D_1 f_1)$ $\alpha_d \neq -1$	$\frac{3}{\theta_d + 3} (D_2 f_2 - D_1 f_1)$ $\theta_d \neq -3$
	$\left(\frac{D_2 f_2 + D_1 f_1}{2} \right) \ln(f_2/f_1)$ $\alpha_d = -1 \quad \theta_d = -3$	

$$n = 20 \log_{10} (q_{rms, 2}/q_{rms, 1}) \quad (20)$$

Occasionally one or more line segments in a spectrum leaves the spectral density unknown at one end point of the segment and a slope is given instead. Equation (4) allows one to compute the unknown spectral density using the frequencies, the slope, and the known spectral density.

A numerical example is included in Appendix A to illustrate the use of several of the equations which have been presented.

CONCLUSIONS

A complete set of simplified formulas for mean-square acceleration, velocity, and

displacement has been derived. These equations are exact but are considerably simpler to use for both manual and machine computation than previously published formulas.

Additional formulas have been included in the paper in an attempt to have all formulas used in conjunction with a random vibration test spectrum in a single document.

ACKNOWLEDGMENT

The analysis upon which this paper is based has been sponsored by Collins Radio Company as a part of a continuing program to improve the environmental design of its products.

REFERENCES

1. S. H. Crandall and W. D. Mark, Random Vibration in Mechanical Systems, Ch. 1 (Academic Press, New York and London), 1963
2. C. T. Morrow and R. B. Muchmore, "Shortcomings of Present Methods of Measuring and Simulating Vibration Environments," *J. Appl. Mech.*, 22(3):367-371, Sept. 1955
3. "Sandia Corporation Standard Environmental Test Methods," SC4452D(M), June 1966
4. I. J. Sandler, "Techniques of Analysis of Random and Combined Random-Sinusoidal Vibration," *Shock, Vibration, and Associated Environments Bull.*, Part 3 (31):211-224, Apr. 1963
5. H. Himmelblau, "Graphical Method of Calculating RMS Values for Shaped Random Vibration Spectra," *Shock and Vibration Bull.*, Part 2 (34):225-237, Dec. 1964
6. W. Tustin, "Vibration Topics," *Test Engineering*, 12(5):16-17, 36-37, Nov. 1964

Appendix A

NUMERICAL EXAMPLE

To illustrate the use of the equations and tables given in the body of the paper we obtain a_{rms} and d_{rms} for the spectrum given in Fig. A-1. All of the coordinates of the end points of the line segments are known except the spectral density at f_1 . However, the slope is given as 6 db/octave. Equation (10) gives $\theta_1 = 3\alpha_1$ so that $\alpha_1 = (\theta_1/3) = 2$. Equation (4) is used to obtain the spectral density $A_1 = A_2(f_1/f_2)^2 = 0.0148 \text{ g}^2/\text{Hz}$. The dimensionless slopes are computed using Eq. (3):

$$\alpha_i = \frac{\log(Q_{i+1}/Q_i)}{\log(f_{i+1}/f_i)}$$

for example,

$$\alpha_3 = \frac{\log(A_4/A_3)}{\log(f_4/f_3)} = \frac{\log(0.06/0.1)}{\log(167/100)} = -1.$$

It is convenient to tabulate the calculated values as in Table A-1, as several steps are involved in the computations. As spectral density is g^2/Hz , we obtain the mean-square acceleration and displacement formulas from Table 1:

$$(\overline{a^2})_i = \begin{cases} \frac{1}{\alpha_i + 1} (A_{i+1} f_{i+1} - A_i f_i), & \alpha_i \neq -1 \\ \left(\frac{A_{i+1} f_{i+1} + A_i f_i}{2} \right) \ln(f_{i+1}/f_i), & \alpha_i = -1 \end{cases}$$

$$(\overline{d^2})_i = \begin{cases} \frac{(386)^2}{(2\pi)^4 (\alpha_i - 3)} \left(\frac{A_{i+1}}{f_{i+1}^3} - \frac{A_i}{f_i^3} \right), & \alpha_i \neq 3 \\ \frac{(386)^2}{2(2\pi)^4} \left(\frac{A_{i+1}}{f_{i+1}^3} + \frac{A_i}{f_i^3} \right) \ln(f_{i+1}/f_i), & \alpha_i = 3 \end{cases}$$

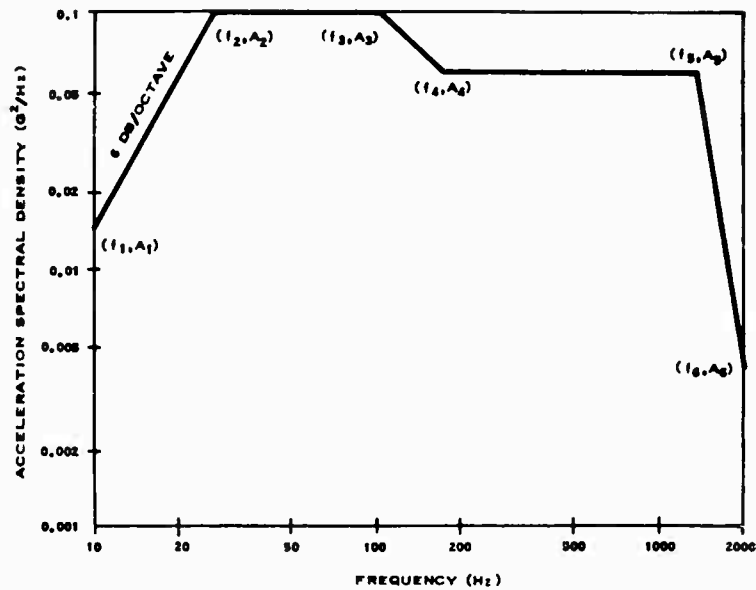


Fig. A-1. Typical acceleration spectrum for numerical example

By carrying out the arithmetic one obtains the entries in Table A-1. An intermediate step giving $A_i f_i$ and A_i/f_i^3 is performed prior to using the preceding equations. The columns $(\overline{a^2})_i$ and $(\overline{d^2})_i$ are totaled to give the total mean-square amplitude as given by Eq. (5):

$$(\overline{q^2}) = \sum_{i=1}^N (\overline{q^2})_i$$

The root-mean-square amplitudes are obtained using Eq. (2):

$$a_{rms} = [(\overline{a^2})]^{1/2} = 9.8 \text{ g.}$$

$$d_{rms} = [(\overline{d^2})]^{1/2} = 0.032 \text{ in.}$$

The three-sigma, double amplitude displacement may be obtained by using Eq. (19):

$$d_{p-p} = 6d_{rms} = 0.198 \text{ in. DA.}$$

TABLE A-1
Sample Calculations

i	α_i	f_i	A_i	$A_i f_i$	$(\overline{a^2})_i^a$	A_i/f_i^3	$(\overline{d^2})_i^b$
1	2	10	0.0148	0.15	0.82	14.79×10^{-6}	870×10^{-6}
2	0	26	0.1	2.60	7.40	5.69×10^{-6}	178×10^{-6}
3	-1	100	0.1	10.00	2.23	0.10×10^{-6}	2×10^{-6}
4	0	167	0.06	10.02	73.98	0.01×10^{-6}	~0
5	-7.58	1400	0.06	84.00	11.54	~0	~0
6	-	2000	0.004	8.00	-	~0	-

$$^a(\overline{a^2}) = 95.97.$$

$$^b(\overline{d^2}) = 1050 \times 10^{-6}.$$

Appendix B

EVALUATION OF INDETERMINATE FORMS

Associated with each equation for the mean-square, there is a value, let us say C , of the dimensionless slope α for which the equation reduces to an indeterminate (0/0) form. Therefore, when $\alpha = C$, an alternate equation is given. In a practical situation α may be close to C so that the basic equation is effectively indeterminate and yet the alternate equation is not exact. In these circumstances it is best to use the alternate equation in the form given in the tables and in Eq. (B-1) below:

Figure B-1 gives the error caused by using either of the alternate forms of Eq. (6) in terms of $|\alpha - C|$. Figure B-2 gives the error caused by using the alternate form as given by Eq. (B-1). It is clear from these figures that the use of Eq. (B-1), in instances where α is close to C , will yield fairly accurate results when the basic mean-square equation is, for practical purposes, an indeterminate form. Figure B-2 is applicable to all alternate equations given in Tables 1, 2, and 3.

$$(\bar{q}^2)_1 = \left(\frac{Q_{i+1} f_{i+1} + Q_i f_i}{2} \right) \ln (f_{i+1}/f_i) \quad (B-1)$$

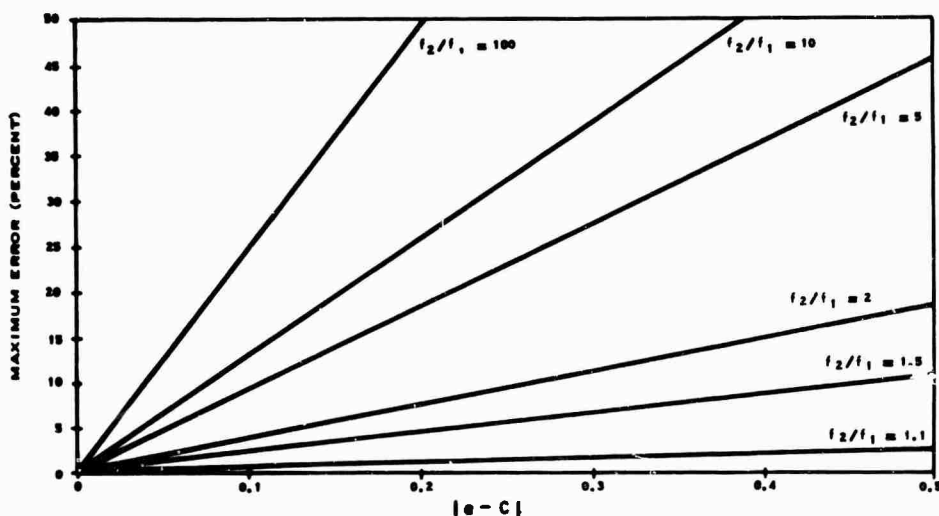


Fig. B-1. Maximum error from using Eq. (6) in place of Eq. (7)

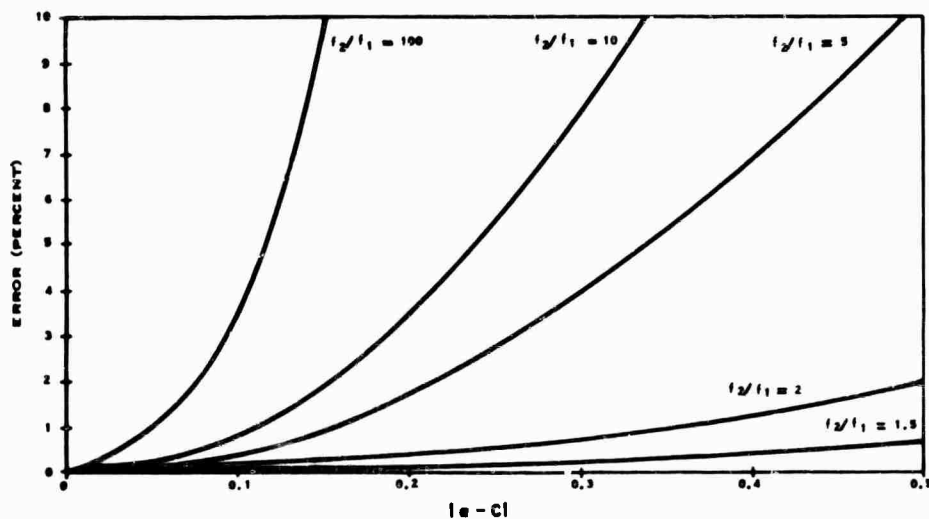


Fig. B-2. Error from using Eq. (B-1) in place of Eq. (7)

CONCENTRATED MASS EFFECTS ON THE VIBRATION OF CORNER-SUPPORTED RECTANGULAR PLATES

Richard L. Barnoski and Terry D. Schoessow*
Measurement Analysis Corporation
Los Angeles, California

For certain problems involving the shock and vibration isolation of panel-mounted electronic equipment, the physical system can be idealized as a corner-supported, rectangular plate with a geometrically centered, concentrated mass. This paper examines the variation of the fundamental frequency of this idealized configuration as a function of the plate dimensions, the boundary restraint at the corners, and the added mass. Three rectangular plates are considered with aspect ratios of $a/b = 1.0$, $a/b = 1.5$, and $a/b = 2.0$, and the boundary restraints are either simply supported or rigidly clamped. The added mass, expressed as a ratio of the plate mass, varies in discrete increments ranging from 0 (an unloaded uniform plate) to 4. Results obtained by analog simulation methods which have been experimentally verified are displayed graphically in parametric form and are suitable for use by designers.

INTRODUCTION

In the structural design of physical systems, problems which involve equipment mounted on a stud-supported panel are frequently encountered. A typical problem might involve shock and vibration isolation of a system in which the dynamic characteristics of the equipment-panel configuration are important. The fundamental modal frequency is often of primary interest. In partial response to this design problem, this paper considers the determination of the fundamental modal frequency of a corner-supported rectangular plate with a geometrically centered concentrated mass. The solutions are obtained by analog simulation methods and are presented in parametric form suitable for use by designers. The parametric variation includes the aspect ratio of the plates, the boundary restraint, and the added lumped mass. Such solutions are substantiated by results of laboratory experiments.

PROBLEM DESCRIPTION

The idealized model is assumed to be a homogeneous, thin, elastic plate of rectangular

geometry (see Fig. 1) with a lumped mass at the geometric center. The governing equation of motion is assumed to be of the form

$$D\nabla^2 \nabla^2 w + m\ddot{w} = f(x, y, t) \quad (1)$$

where w is the plate deflection from its static equilibrium position; m is the plate mass per unit area; and

$$\ddot{w} = \frac{d^2 w}{dt^2}$$

$$D = \frac{Eh^3}{12(1-\nu^2)}$$

and

$$\nabla^2 = \frac{\partial^2}{\partial x^2} + \frac{\partial^2}{\partial y^2}$$

The plate flexural rigidity D contains the Young modulus of the material E , the plate thickness h , and the Poisson ratio ν , while the del operator ∇ defines spatial derivatives involving rectangular geometry.

*Mr. Schoessow is now with the Aerospace Corp., El Segundo, Calif.

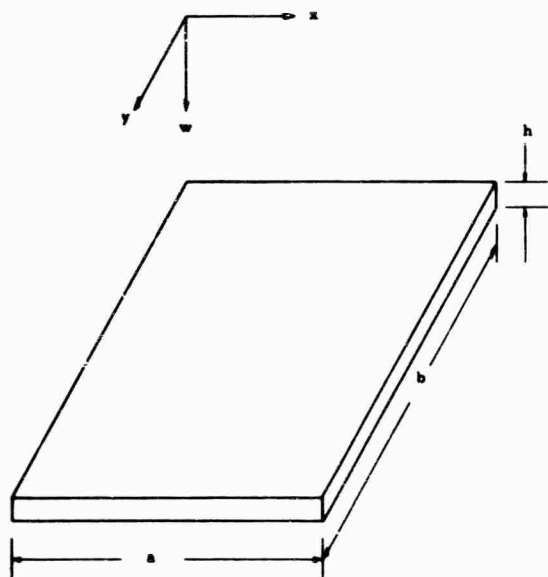


Fig. 1. Plate geometry

To calculate the desired modal frequencies, one seeks solutions to the characteristic equation for the homogeneous form of Eq. (1), noted as

$$\nabla^4 w + \frac{m}{D} \ddot{w} = 0 \quad (2)$$

subject to the boundary conditions

$$\left. \begin{aligned} w(0, 0, t) \\ w(0, b, t) \\ w(a, 0, t) \\ w(a, b, t) \end{aligned} \right\} = 0 \quad (3)$$

$$\left. \begin{aligned} M_{xx}(0, 0, t) \\ M_{xx}(0, b, t) \\ M_{yy}(a, 0, t) \\ M_{yy}(a, b, t) \end{aligned} \right\} = 0 \quad (4)$$

and the mass constraints

$$\begin{aligned} \Delta_m \ddot{w} \left(\frac{a}{2}, \frac{b}{2}, t \right) = & v_x \left(\frac{a}{2} - \frac{\Delta x}{2}, \frac{b}{2}, t \right) - v_x \left(\frac{a}{2} + \frac{\Delta x}{2}, \frac{b}{2}, t \right) \\ & + v_y \left(\frac{a}{2}, \frac{b}{2} - \frac{\Delta y}{2}, t \right) - v_y \left(\frac{a}{2}, \frac{b}{2} + \frac{\Delta y}{2}, t \right) \end{aligned} \quad (5)$$

Here, M_{xx} and M_{yy} define plate bending moments and Δ_m refers to the mass at the center of the plate which is distributed uniformly over the dimensions $\Delta x, \Delta y$. The boundary conditions quoted by Eqs. (3) and (4) are those for simply supported corner supports. For clamped corner supports, one requires the boundary conditions of Eq. (3) and those for the slope given by

$$\left. \begin{aligned} \theta_{xx}(0, 0, t) \\ \theta_{xx}(0, b, t) \\ \theta_{yy}(a, 0, t) \\ \theta_{yy}(a, b, t) \end{aligned} \right\} = 0 \quad (6)$$

METHOD OF SOLUTION

In this paper the modal frequencies are determined by electrically simulating the plate configuration and measuring the fundamental resonance. The network used is a passive analog simulation [1] which corresponds mechanically to a lumped parameter representation and mathematically to a finite-difference model. The difference grid is a uniformly spaced 9×9 mesh extending over the complete plate. Solutions considering finite difference models are discussed in Refs. 2 and 3; solutions involving an energy formulation are commented upon in Ref. 4.

The analog model physically consists of an interlacing rectangular grid of Bernoulli-Euler beams coupled by torque tubes with attached masses at the beam intersections. It is topologically similar to the physical configuration and assumes mechanical-electrical equivalences of force \approx current and velocity \approx voltage. These networks are such that mass \approx capacitance, flexibility \approx inductance, and viscous damping \approx resistance. The spatial geometry and the required spatial differentiations are accounted for by properly interconnecting multiwinding transformers. Boundary conditions are accounted for by opening or shorting the circuit at appropriate positions so that boundaries, at irregularly positioned support points, can be treated with ease. Since mass and stiffness properties are accounted for by the capacitors and inductors, nonuniform distributions likewise may be treated most efficiently if first-order difference approximations are acceptable.

PHYSICAL EXPERIMENTS

Laboratory experiments were performed on six aluminum plates with aspect ratios of

$a/b = 1.0$, $a/b = 1.5$, and $a/b = 2.0$. These plates had thicknesses of $h = 0.0625$ in. and $h = 0.125$ in. The corners of the plates were clamped for the first series of experiments and simply supported for the second series of experiments. The added mass Δ_m ranged over the interval $0 \leq \Delta_m/M \leq 4$, where M is the total mass of the basic plate. A total of 12 sets of data were taken for comparison with the analog results.

The plate dimensions were 9 in. sq, 9 in. by 13.5 in., and 9 in. by 18 in. Each plate size was tested in two thicknesses: 0.0625 in. and 0.125 in. The plates were made of 6061-T6 aluminum so that $E = 10.5 \times 10^6$ lb/in.², $\rho = 0.10$ lb/in.³ and $\nu = 0.3$. The concentrated mass loads were applied over a 1-sq-in. area in the centers of the plates and were secured to the plates with dental cement.

The clamped condition was accomplished by sandwiching the corners of the test plate between hardened aluminum blocks. The block-plate-block sandwich was clamped to "C" channel rails that were bolted to a heavy concrete foundation. This provided both zero deflection

and zero slope at the corner supports as required for clamped boundaries. This setup is shown in Fig. 2. The fundamental frequency of vibration of the panels showed a high degree of sensitivity to the clamping force. The procedure was to "tune" the unloaded panels to the theoretical natural frequency by adjusting the clamping forces, then leaving these forces undisturbed while adding the masses to the center of the panel.

The test setup for the simply supported corners was less involved and consisted of resting plates on the points of No. 6 finishing nails that had been driven through a predrilled piece of 1-in. plywood (see Fig. 3). The corners of the plates were center punched where the nail points made contact to ensure plate contact at these locations during the experiment. This arrangement precluded any attempt at tuning the fundamental modal frequency of the unloaded plate.

Figure 4 shows a block diagram of the instrumentation used to measure the fundamental mode of vibration of the plates. This instrumentation is listed in the Appendix. The test

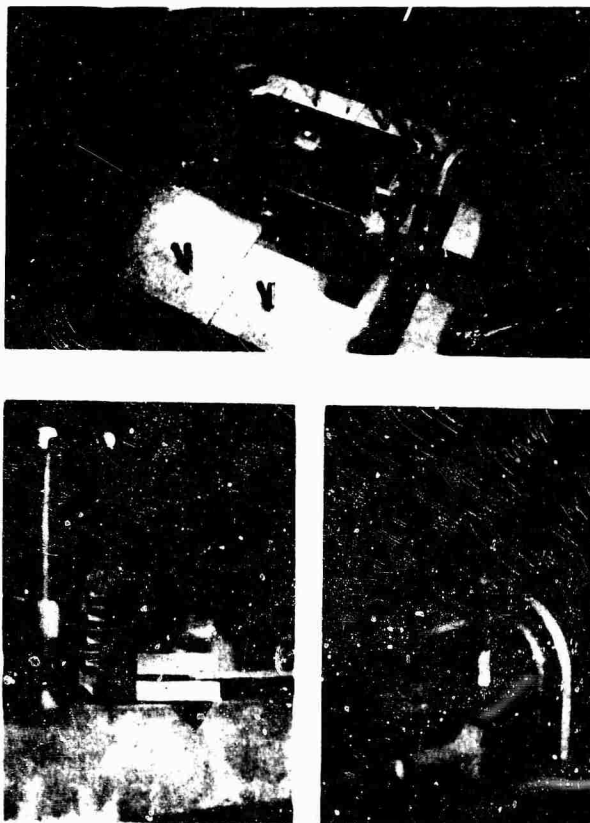


Fig. 2. Test setup for clamped corners

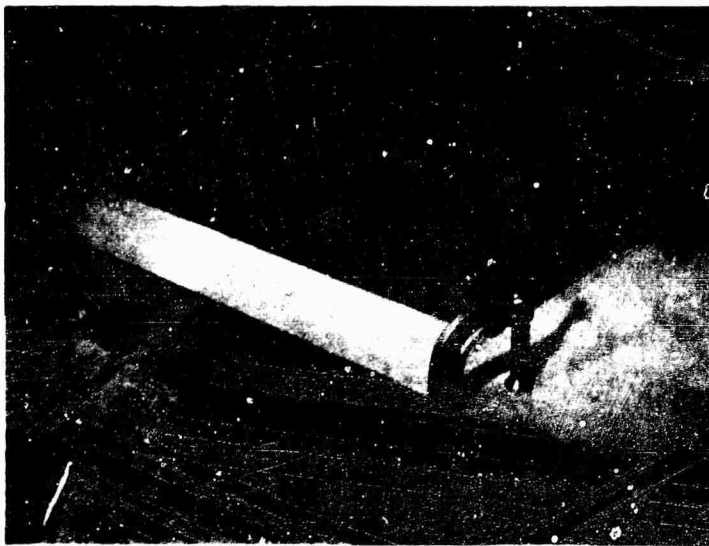


Fig. 3. Test setup for point-supported corners

oscillator controlled the horizontal sweep on the oscilloscope and the filtered output of the accelerometer supplied the vertical signal. The test plate was excited by gently tapping it with a soft rubber mallet; the frequency analyzer was set on its narrowest bandwidth (6 percent) and tuned for maximum output. This filtering operation eliminated all modes but the fundamental, as well as high frequency disturbances caused by striking the panel with the mallet.

To measure precisely the frequency of the fundamental mode of vibration, a test oscillator was connected to the horizontal input of the oscilloscope. A circular Lissajous pattern then was formed by adjusting the oscillator frequency until it coincided with that of the panel. Since

this pattern is a function of the relative amplitude and phase of the two signals, it reduces to a circle when the signals are of equal amplitude and either 90 or 270 degrees out of phase. In general, a line is formed when the signals are either in phase or 180 degrees out of phase, and an elliptical pattern is formed with other combinations of relative phase and amplitude.

RESULTS

The results of both the analog simulation and experimental studies are shown by Figs. 5 and 6. These figures are families of curves (in the aspect ratio a/b) plotted as a function of the frequency ratio f_{11}/f_{aa} vs the mass ratio $\Delta m/M$. The term f_{11} is the fundamental modal

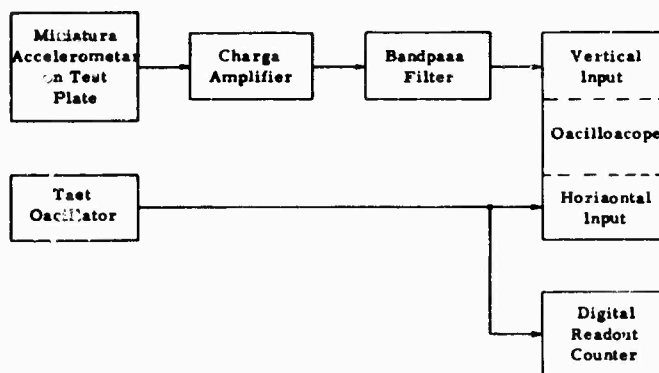


Fig. 4. Test instrumentation setup

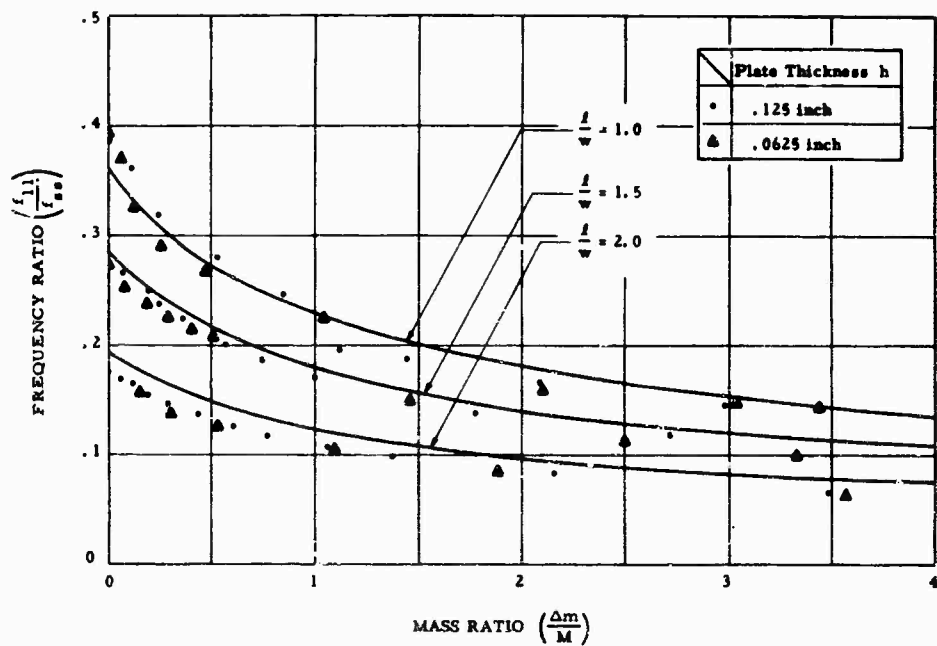


Fig. 5. Effect of a concentrated mass on the fundamental frequency of rectangular plates simply supported at the corners (analog results)

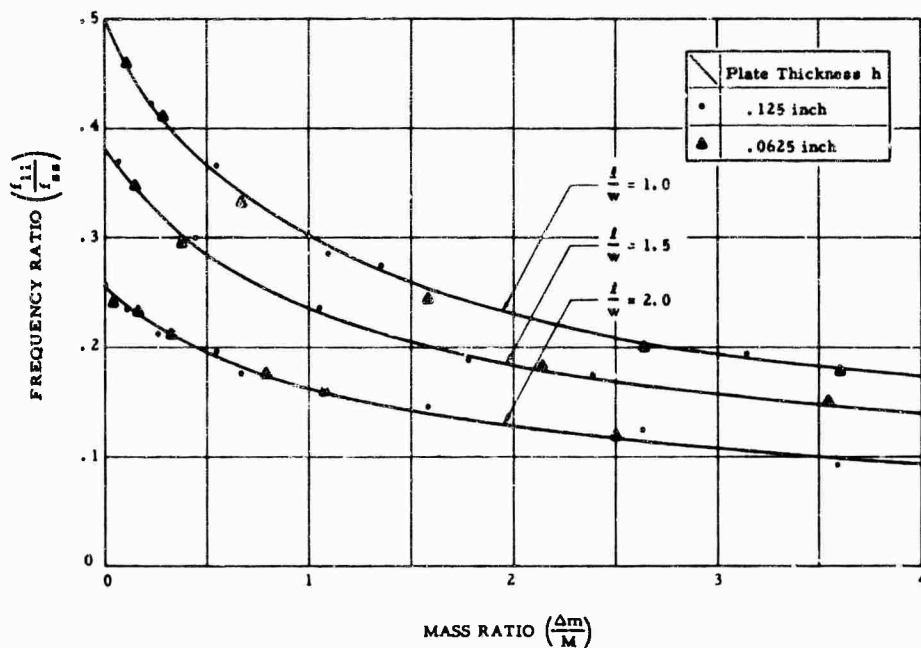


Fig. 6. Effect of a concentrated mass on the fundamental frequency of rectangular plates rigidly clamped at the corners (analog results)

frequency of the plate-mass configuration while the frequency f_{ss} is

$$f_{ss} = \frac{\pi}{2} \sqrt{\frac{D}{m}} \left[\left(\frac{r}{a}\right)^2 + \left(\frac{a}{b}\right)^2 \right] \text{ cps. } r = a = 1. \quad (8)$$

which is noted as the fundamental modal frequency of a uniform, rectangular plate simply supported at all edges. A comparison of the experimental and analog results shows close agreement; moreover, the results for the unloaded plate agree almost exactly with those shown in Ref. 2. The behavior of the plate-mass system over the range of masses added for both boundary restraints is as expected; that is, the fundamental frequency decreases with an increase in Δ_m .

For a given aspect ratio, f_{11}/f_{ss} appears to approach an asymptotic value as the ratio Δ_m/M grows larger. Such a value may be interpreted as that in which the distributed mass of the plate becomes unimportant relative to the added mass Δ_m , and the composite configuration behaves dynamically as a single-degree-of-freedom system. Experimental studies on clamped corner plates showed that additional masses ($5 \leq \Delta_m/M \leq 7$) caused an increase in the fundamental frequency. This suggests plate

membrane forces and/or large deflection phenomena are acting to stiffen the plate. Such results cannot be accounted for by the analog results as the networks are based upon Bernoulli-Euler theory implicit in Eq. (1).

Suppose, for example, one desires to estimate the fundamental frequency of a thin, uniform, aluminum plate of dimensions $a = b = 10$ in. with rigidly clamped corner supports, a geometrically centered mass with $\Delta_m/M = 1$, and a thickness $h = 0.0625$ in. From this data,

$$D = 235 \text{ lb-in.}$$

$$m = 1.625 \times 10^{-5} \text{ lb-sec}^2/\text{in.}^3$$

so that

$$f_{ss} = \frac{\pi}{2} \sqrt{\frac{D}{m}} \left[\left(\frac{1}{a^2}\right) + \left(\frac{1}{b^2}\right) \right] = 119 \text{ cps.}$$

From Fig. 6 where $a/b = 1.0$ and $\Delta_m/M = 1$,

$$\frac{f_{11}}{f_{ss}} = 0.3,$$

and

$$f_{11} = 0.3 \times 119 = 35.7 \text{ cps.}$$

REFERENCES

1. R. L. Barnoski, "Dynamic Characteristics of Square Plates by Passive Analog Simulation," NASA CR-866, Jan. 1967
2. H. L. Cox and J. Boxer, "Vibration of Rectangular Plates Point-Supported at the Corners," *The Aeronautical Quarterly*, Part 1, 11:41-50, Feb. 1960
3. D. J. Dawe, "A Finite Element Approach to Plate Vibration Problems," *J. Mech. Eng. Sci.*, 7(1):28-32, 1965
4. C. L. Kirk, "A Note on the Lowest Natural Frequency of a Square Plate Point-Supported at the Corners," *J. Roy. Aeron. Soc.*, Tech. Notes, 66:240-241, Apr. 1962

Appendix A

LIST OF TEST INSTRUMENTS

Oscilloscope:	Tektronix 545, CA plug-in	Accelerometer:	Unholtz Dickie Model 2E5
Test oscillator:	Hewlett Packard 200 CD	Frequency analyzer:	Brueel & Kjaer 2107
Charge amplifier:	Unholtz Dickie Model 11 Series	Counter:	Hewlett Packard 5216A

DISCUSSION

H. Saunders (G.E. Co.): In the analytical work, what method did you use to determine the frequencies?

Mr. Schoessow: I do not understand. We were comparing analog computer results to experimental results.

Mr. Saunders: Have you given any thought to getting an analytical solution and checking with the analog results?

Mr. Schoessow: I think that is what prompted the entire exercise. The analytical solution just is not easily obtainable.

Mr. Saunders: No, you would have to use the Rayleigh-Ritz or a similar method to obtain the solution and even then there would be problems.

Mr. Schoessow: Yes, it is an extremely complex thing. Dr. Barnoski did all the analog computer results and the theoretical analysis that led to that point. I conducted the experimental investigation, so that I personally have not gone through all of these trials. He said that it was certainly much easier to do on the analog computer. You can dial in varying masses very easily. All of these parameters are very easily adjustable since you have passive elements and they are all coupled with

transformers. You can get a very quick simulation and change parameters very easily.

Mr. Saunders: Have you given any thought to using other than a constant uniform thickness plate?

Mr. Schoessow: I have not worked this problem. I know there have been several papers presented here in the last few days that are well handled by digital approaches for complex structures or structures that vary over their areas.

D. Stewart (McDonnell Douglas Corp.): Is the concentrated mass uniformly distributed over the plate or lumped in the middle?

Mr. Schoessow: I am sorry I failed to mention that. The concentrated mass was assumed to be put in over one element of the plate. We had a 9 by 9 in. grid so it would be very close to attachment at a point or a very small area. The experimental results were also obtained by putting this over a 1-sq-in. area. We were using plates that were 9 by 9, 9 by 13-1/2 and 9 by 18 in.

Mr. Stewart: Are the results, then, for the mass located at different spots on the plate?

Mr. Schoessow: No, it is a centrally located mass, and it is only for the fundamental mode.

* * *

VIBRATION OF ECCENTRICALLY STIFFENED PLATES

B. R. Long
Defence Research Establishment Suffield
Defence Research Board
Ralston, Alberta, Canada

Analysis of plates with eccentric stiffening involves simultaneous solution of plate bending equations, plane stress equations, beam equations, and displacement compatibility equations. This solution does not seem possible in the general case; however, such a solution can be obtained for the free vibration dynamic behavior of stiffened rectangular plates having one set of parallel stiffeners and having two simply supported edges orthogonal to the stiffener direction. This solution allows direct comparison with frequencies and mode shapes obtained by other methods, such as the equivalent orthotropic plate approach.

In this paper, displacement functions are assumed in the stiffener direction, satisfying the simply supported boundary conditions. Application of the governing equations to each plate segment and to each stiffener leads to a set of homogeneous equations involving undetermined mode shape parameters. Coefficients of the equations contain the frequency parameter ω . As the determinant of these coefficients must be zero for nontrivial solutions, a computer search routine is used to find values of ω that cause singularities of the determinant.

Because of the large number of variables in the analysis, general quantitative results are not presented; however, calculated frequencies and mode shapes are shown for some specific examples. These results are compared with those obtained by orthotropic plate theory. Increasing stiffener eccentricity and spacing are found to increase the discrepancy between frequencies predicted by orthotropic theory and those predicted by the beam-plate theory, with the former being larger in the examples considered.

For a given plate configuration in which only the stiffener depth is varied, it is shown that certain frequencies are convergent, presumably because the corresponding mode shapes become identical in the limit.

INTRODUCTION

Stiffened plating forms a structural element of practical importance and has therefore been the subject of a number of investigations; however, exact analytical solutions have been obtained only for highly idealized situations. Theoretical considerations often involve treating the structure as an equivalent orthotropic plate that reflects the combined properties of plating and stiffeners. A primary objection to this approach is that it probably will not be valid for wide stiffener spacing. Other approaches involve treating an infinitely long panel or a panel with a single stiffener.

Statically loaded, rectangular plates stiffened in one direction and having two opposite edges simply supported were analyzed by Von

Karman [1] who neglected the bending rigidity of the plating. Investigations were carried out by Reissner [2] and Yamaki [3] on panels of infinite length. Clarkson [4] studied the case of a long rectangular panel with stiffeners in one direction and having a single concentrated load applied to one of the stiffeners. Smith [5] solved the problem of a statically loaded, rectangular panel with a finite number of stiffeners in one direction.

Among the earliest studies of the dynamics of stiffened plating were the investigations of Hoppmann, Huffington, and Magness [6]; Hoppmann and Magness [7]; and Huffington and Hoppmann [8]. These analyses used orthotropic plate theory based on experimentally derived rigidities as suggested by Hoppmann [9]. Kirk [10] used isotropic plate mode shapes with the

Rayleigh method to determine the frequencies of panels with many stiffeners or one stiffener. Wah [11] considered free vibrations of a rectangular plate having a finite number of stiffeners of zero eccentricity. Mikulas and McElman [12] investigated the dynamic behavior of a stiffened rectangular panel by "smearing out" the stiffener effects.

Within the limitations of small deflection elasticity theory, the aim, in this paper, is to develop an exact solution to the problem of free vibrations of a stiffened rectangular plate having two edges simply supported and having one set of eccentric stiffeners normal to the simply supported boundaries.

NOMENCLATURE

a, b	Plate segment dimensions
d	Half stiffener width
e _s	Stiffener eccentricity
f, m, s, Q	Stress resultants at edge of plate segment
h	Stiffener depth
t	Plate thickness
u, v, w	Plate displacements
$\bar{u}, \bar{v}, \bar{w}, \theta$	Beam displacements
x, y, z	Plate coordinates
$\bar{x}, \bar{y}, \bar{z}$	Beam coordinates
x ₀ , y ₀	Coordinates for entire panel
A_1, \dots, A_4 B_1, \dots, B_4	Coefficients in plate segment displacement expressions
D	Plate bending rigidity
EI _x , EI _y	Stiffener bending rigidities
J	Stiffener torsional rigidity
T	Time
U, V, X	Plate displacement functions
$\bar{U}, \bar{V}, \bar{X}, \Theta$	Beam displacement amplitudes
β, λ	Roots of characteristic equation for X

ν	Poisson's ratio
ρ	Plate mass per unit area
ρ_b	Stiffener mass per unit length
ω	Frequency parameter

DERIVATION OF EQUATIONS

Plate Equilibrium

A stiffened plate typical of the type to be considered in this paper is shown in Fig. 1. Each plate segment is assumed uniform and isotropic and, for simplicity, plate segments are assumed to be identical to each other. These comments apply to the stiffeners as well. Coordinates x, y, and z for plate elements and \bar{x} , \bar{y} , and \bar{z} for stiffeners are shown in Fig. 1, and corresponding displacements are denoted by u, v, and w for plates and \bar{u} , \bar{v} , and \bar{w} for stiffeners. Stiffener eccentricity is defined by $e_s = (h - t)/2$ where h is the stiffener depth and t is the plating thickness. Consideration of vertical equilibrium of plating leads to the well-known plate equation

$$\nabla^4 w + \frac{\rho}{D} \ddot{w} = 0, \quad (1)$$

where ρ is the mass per unit plate area, D is the plate bending rigidity, ∇^4 is the biharmonic operator, and a dot infers differentiation with respect to time. Noting that the boundaries

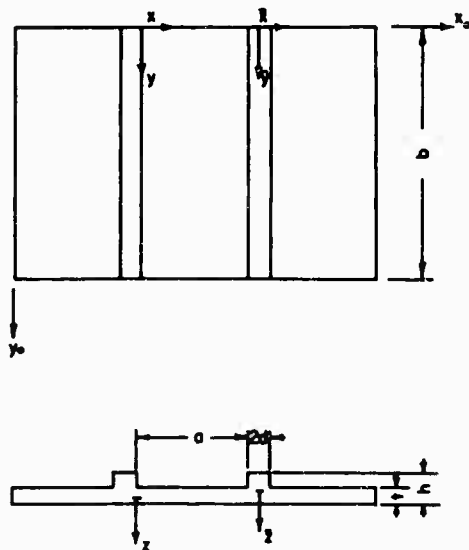


Fig. 1. Typical stiffened plate

$y = 0, b$ are simply supported, the free-vibration deflections are assumed in the form $w = X(x) \sin \alpha y e^{i\omega T}$, where $\alpha = m\pi/b$, and $m = 1, 2, \dots$.

Substitution in Eq. (1) leads to a general solution for X ; namely,

$$X = A_1 \cosh \lambda x + A_2 \sinh \lambda x + A_3 \cos \beta x + A_4 \sin \beta x \quad (2)$$

where

$$\lambda = \left(\omega \sqrt{\frac{\rho}{D}} + \alpha^2 \right)^{1/2}$$

and

$$\beta = \left(\omega \sqrt{\frac{\rho}{D}} - \alpha^2 \right)^{1/2}$$

Since only small deflections are considered, the in-plane plate motions can be considered separately from the bending. Equilibrium considerations lead to the governing equations

$$\frac{\partial^2 u}{\partial x^2} + \frac{1}{2}(1-\nu) \frac{\partial^2 u}{\partial y^2} + \frac{1}{2}(1+\nu) \frac{\partial^2 v}{\partial x \partial y} = 0 \quad (3)$$

$$\frac{\partial^2 v}{\partial y^2} + \frac{1}{2}(1-\nu) \frac{\partial^2 v}{\partial x^2} + \frac{1}{2}(1+\nu) \frac{\partial^2 u}{\partial x \partial y} = 0 \quad (4)$$

when in-plane inertia effects are ignored. Membrane displacements are assumed in the form

$$u = U(x) \sin \alpha y e^{i\omega T} \quad (5)$$

$$v = V(x) \cos \alpha y e^{i\omega T} \quad (6)$$

Substitution of Eqs. (3) and (4) into Eqs. (5) and (6) leads to general solutions for U, V as

$$U = B_1 \cosh ax + B_2 ax \cosh ax + B_3 \sinh ax + B_4 ax \sinh ax \quad (7)$$

$$V = (\gamma B_2 + B_3) \cosh ax + B_4 ax \cosh ax + (B_1 + \gamma B_4) \sinh ax + B_2 ax \sinh ax \quad (8)$$

where $\gamma = (3-\nu)/(1+\nu)$ and ν is Poisson's ratio.

Stiffener Equilibrium

Forces applied by the plating on a stiffener element (per unit length) are shown in Fig. 2. Here subscripts i refer to stress resultants

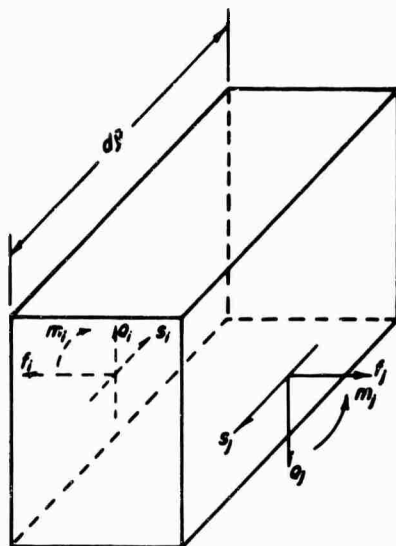


Fig. 2. Forces on stiffener element

along $x = 0$ in the i th plate segment and subscripts j refer to edge $x = a$ of the j th plate segment. The shearing stress resultants Q , normal stress resultant f , and bending moment m can be calculated from the plate displacements u, v , and w . Considering moment equilibrium in the $\bar{x}-\bar{z}$ plane force equilibrium in the \bar{x}, \bar{y} , and \bar{z} directions, four equations are obtained involving the stiffener displacements $\bar{u}, \bar{v}, \bar{w}$, and θ , where θ is the torsional displacement. From moment equilibrium

$$J \frac{\partial^2 \theta}{\partial y^2} + d(Q_j + Q_i) + e_s(f_j - f_i) + m_i - m_j = 0 \quad (9)$$

where J is beam torsional stiffness and $2d$ is the stiffener width.

Considering forces in the \bar{x} direction,

$$-EI_x \frac{d^4 \bar{w}}{dy^4} + f_j - f_i + d \left(\frac{ds_i}{dy} + \frac{ds_j}{dy} \right) = 0 \quad (10)$$

where EI_x represents the stiffener bending stiffness in the $\bar{x}-\bar{y}$ plane. Equilibrium in the \bar{y} direction requires

$$2d\bar{h}E \frac{d^2 \bar{v}}{dy^2} + (s_j - s_i) = 0 \quad (11)$$

Consideration of forces in the \bar{z} direction leads to

$$EI_y \frac{d^4 \bar{w}}{dy^4} + \rho_B \bar{w} + (Q_i - Q_j) + e_s \left(\frac{ds_i}{dy} - \frac{ds_j}{dy} \right) = 0 \quad (12)$$

where EI_y is the beam bending stiffness in the $X-Y$ plane and ρ_B is the mass of stiffener per unit length.

Beam displacements are assumed in a form satisfying the simple support boundary conditions, namely

$$\left. \begin{aligned} \bar{u} &= \bar{U} \sin ay \omega e^{i\omega T} \\ \bar{v} &= \bar{V} \cos ay \omega e^{i\omega T} \\ \bar{w} &= \bar{W} \sin ay \omega e^{i\omega T} \\ \theta &= \bar{\Theta} \sin ay \omega e^{i\omega T} \end{aligned} \right\} \quad (13)$$

Making the appropriate substitutions into Eqs. (9) to (12) and writing these equations for each of the N stiffeners leads to $4N$ homogeneous transcendental equations involving the constants A, B for each plate and the constants \bar{U}, \bar{V}, \dots for each stiffener.

Continuity of Displacements

Considering the edge $x=0$ of a plating segment, for continuity of deflection,

$$\left. \begin{aligned} u|_{x=0} &= \bar{u} - e_s \theta \\ v|_{x=0} &= \bar{v} - e_s \frac{\partial \bar{w}}{\partial y} - d \frac{\partial \bar{u}}{\partial y} \\ w|_{x=0} &= \bar{w} + d\theta \end{aligned} \right\} \quad (14)$$

and

$$\left. \begin{aligned} \frac{\partial w}{\partial x} \Big|_{x=0} &= \theta \end{aligned} \right\}$$

Similarly for the edge $x=a$,

$$\left. \begin{aligned} u|_{x=a} &= \bar{u} - e_s \theta \\ v|_{x=a} &= \bar{v} - e_s \frac{\partial \bar{w}}{\partial y} + d \frac{\partial \bar{u}}{\partial y} \\ w|_{x=a} &= \bar{w} - d\theta \end{aligned} \right\} \quad (15)$$

and

$$\left. \begin{aligned} \frac{\partial w}{\partial x} \Big|_{x=a} &= \theta \end{aligned} \right\}$$

These equations are applied to all edges of plate segments which terminate at a stiffener. At the right and left hand edges of the stiffened panel, boundary conditions must be applied to the plate deflections. Though others could be used, boundary conditions chosen for the first plate segment, are

$$\left. \begin{aligned} w|_{x=0} &= 0 \\ f|_{x=0} &= 0 \\ v|_{x=0} &= 0 \\ m|_{x=0} &= -K \frac{\partial w}{\partial x} \Big|_{x=0} \end{aligned} \right\} \quad (16)$$

and

where K is a constant describing the support stiffness. Identical conditions apply along the edge $x=a$ of the last plate segment, except that for the last condition,

$$m|_{x=a} = K \frac{\partial w}{\partial x} \Big|_{x=a} \quad (17)$$

Making the appropriate substitutions in Eqs. (14) to (17) results in a set of $8(N+1)$ homogeneous equations. Thus, for a plate with N stiffeners there are $4(3N+2)$ simultaneous equations in the coefficients A, B, V , etc.

Solution for Frequencies and Mode Shapes

Clearly, for a nontrivial solution, the determinant of the coefficient matrix must be zero. A crude but effective method of solving for the natural frequencies involves a trial and error computer solution. Essentially, ω , the frequency parameter, is plotted against $D(\omega)$, the determinant value, and zero values of $D(\omega)$ are looked for. This can be accomplished by plotting $D(\omega)$ for successively smaller increments of ω until singularities of the determinant have been isolated. Within these ranges, convergence on the frequencies is facilitated by a linear interpolation procedure. For the examples presented below, determinant values were found by the standard IBM subroutine MINV. For problems involving larger matrix orders, a more efficient approach should be sought, as the computer time required by this method would become prohibitive.

To find mode shapes corresponding to particular frequencies, one of the unknown (nonzero)

displacement parameters may be assumed arbitrarily and the others found in terms of this. Computer solution for the examples presented below used the standard IBM subroutine SIMQ.

Examples

Natural frequencies and mode shapes were found for three stiffened panels, each of which had outside dimensions of 10 in. by 15 in. All edges were taken as simply supported. The panels had either one, two, or three stiffeners uniformly spaced parallel to the short side. Stiffeners and plating were assumed to be mild steel ($E = 30 \times 10^6$ psi, $\nu = 0.3$) with the plating 0.1 in. thick. Stiffeners were taken as 0.25-in. wide and frequencies and mode shapes were calculated for various depths of stiffener, i.e., for varying eccentricity. In the following sections the mode frequencies are referred to as f_{nm} where m is the number of half sine waves in the y direction and n is the number of half sine waves in the x direction for an unstiffened panel.

Figure 3 shows the frequencies f_{11} , f_{21} , f_{12} and f_{22} for the panel with one stiffener. Figures 4 and 5 show these same results for panels with two and three stiffeners, respectively. Frequencies corresponding to those shown in these figures were calculated according to the orthotropic theory of Mikulas and McElman [12]. Figure 6 represents the discrepancy in these calculations, expressed as a

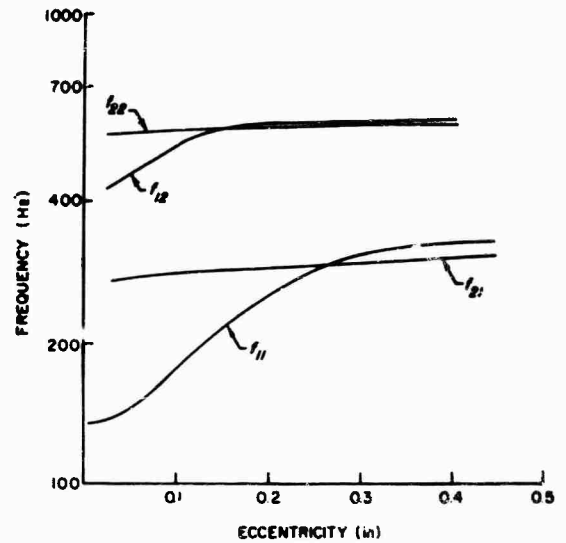


Fig. 3. Frequencies for plate with one stiffener

percent of the frequency by the current method, for the fundamental frequency of each of the panels.

The same comparison is made in Fig. 7 for four natural frequencies of the plate with two stiffeners. Figure 8 shows the variation in the f_{11} mode shape in the $x-z$ plane for the panel with two stiffeners.

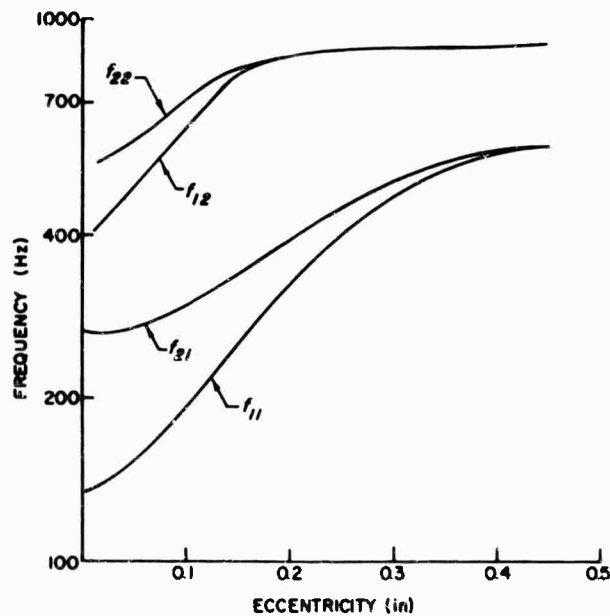


Fig. 4. Frequencies for plate with two stiffeners

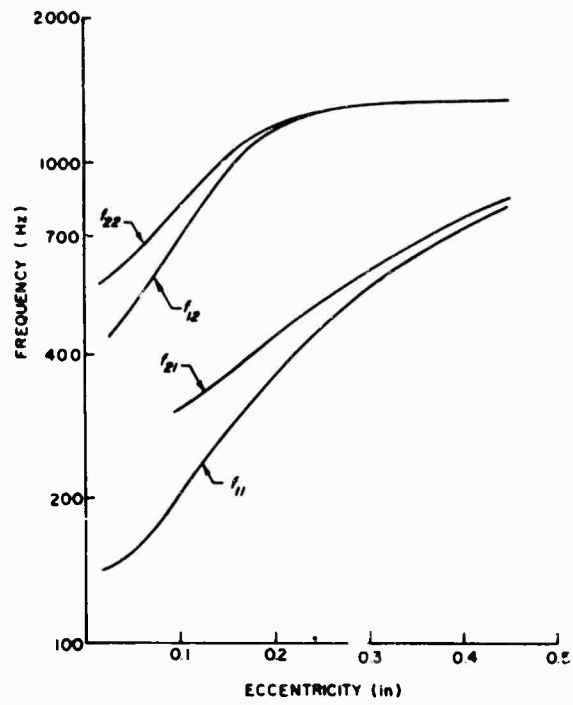


Fig. 5. Frequencies for plate with three stiffeners

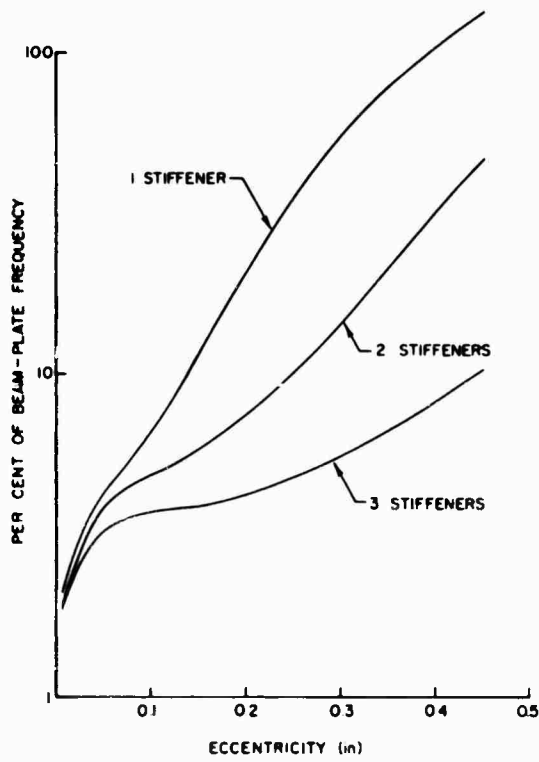


Fig. 6. Difference in fundamental frequencies found by orthotropic theory and beam-plate theory

CONCLUSIONS

The method outlined in this paper provides a straightforward approach to the determination of mode shapes and natural frequencies of a class of stiffened plates. Because of the large number of variables involved in the analysis, it is impossible to present general quantitative results; however, some general observations may be made:

1. Natural frequencies of modes with nodes at stiffener locations do not increase significantly with stiffener eccentricity. This can result in a frequency f_{im} greater than a frequency f_{jm} when $i < j$. For example, in Fig. 3, f_{11} becomes greater than f_{21} .

2. Certain of the natural frequencies tend to converge as stiffener eccentricity becomes large, as illustrated in Figs. 4 and 5.

3. Frequencies predicted by the orthotropic theory of Mikulas and McElman [12] differ greatly from those of the current beam-plate theory when the stiffener spacing and eccentricity are large. The same is true of mode shapes predicted by the orthotropic theory as these are sine functions in the x_0 coordinate.

4. For problems involving a panel with many stiffeners, it would be necessary to use a more efficient method to find the natural frequencies, as computer time required by the method described would become excessive.

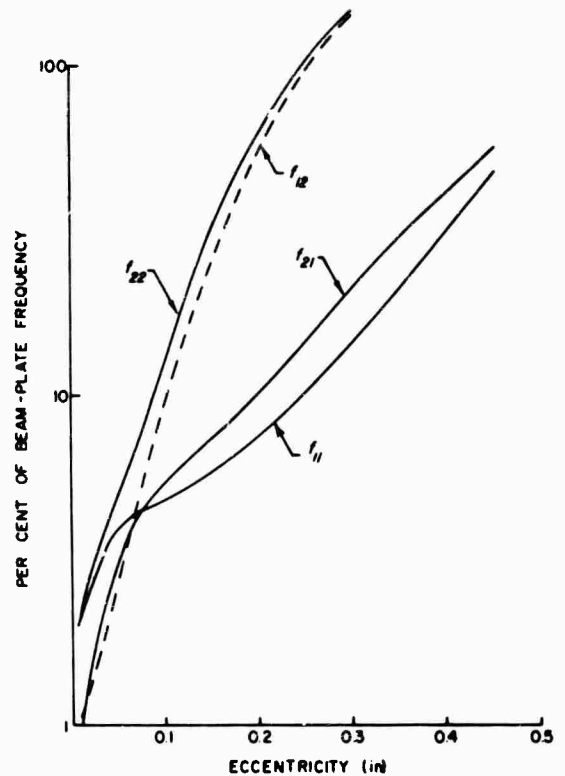


Fig. 7. Difference in frequencies found by orthotropic theory and beam-plate theory for plate with two stiffeners

Alternatively, reasonable approximations to the natural frequencies for this case might be obtained by assuming a plate of infinite length.

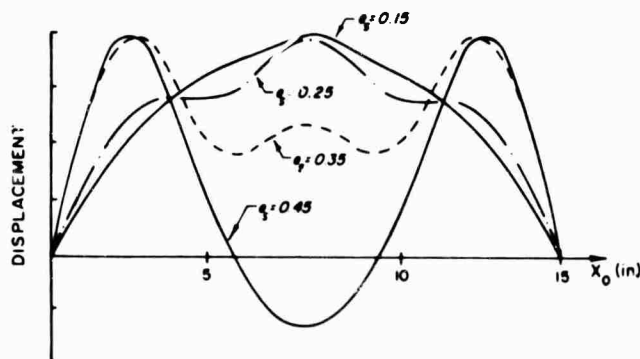


Fig. 8. Variation in f_{11} mode shape with eccentricity for plate with two stiffeners

REFERENCES

1. T. von Karman, "Beitrage zur Technischen Physik und Technischen Mechanik," Festschrift August Foppl, J. Springer, Berlin, 1923
2. E. Reissner, "Über die Berücksichtigung der Gurtsteifigkeit bei der Berechnung der 'mithagenden Breite'," Schweizerische Bauzeitung, 108, 1936
3. M. Yamaki, "Bending of Stiffened Plates Under Uniform Normal Pressure," Rept. 137, Inst. of High Speed Mech., Tohoku Univ., 1962
4. J. Clarkson, "Elastic Analysis of a Beam-Plating Structure Under a Single Concentrated Load," Proc. IX Internat. Cong. of Appl. Mech., 6, Brussels, 1957
5. C. S. Smith, "Elastic Analyses of Stiffened Plating Under Lateral Loading," Trans. RINA, 106(2), 1963
6. W. H. Hoppmann, II, N. J. Huffington, and L. S. Magness, "A Study of Orthogonally Stiffened Plates," J. Appl. Mech., 23, 1956
7. W. H. Hoppmann, II and L. S. Magness, "Nodal Patterns of the Free Flexural Vibrations of Stiffened Plates," J. Appl. Mech., 24, 1957
8. N. J. Huffington and W. H. Hoppmann, II, "On the Transverse Vibrations of Rectangular Orthotropic Plates," J. Appl. Mech., 25, 1958
9. W. H. Hoppmann, II, "Bending of Orthogonally Stiffened Plates," J. Appl. Mech., 22, 1955
10. C. L. Kirk, "Vibration Characteristics of Stiffened Plates," J. Appl. Eng. Sci., 2(3), 1960
11. T. Wah, "Vibration of Stiffened Plates," Aero. Quart., 15(3), 1964
12. M. M. Mikulas and J. A. McElmar, "On Free Vibrations of Eccentrically Stiffened Cylindrical Shells and Flat Plates," NASA TN D-3010, 1965

DISCUSSION

Mr. Forkois (NRL): Your sketch showed an integral stiffener. Will this method be applicable to bolted stiffeners, riveted stiffeners, welded stiffeners, or solid single stiffeners? I think there would be some differences.

Mr. Long: Yes, I think so too. I would expect that it may be reasonable for a welded stiffener, but certainly questionable for bolted or riveted stiffeners.

W. Wassman (NOL): I noted that the accuracy decreased with the eccentricity of the stiffeners and that the mode shapes changed with the eccentricity of the stiffeners. This leads me to suspect that the assumed mode shapes were leading to the loss of accuracy. Did you investigate the possibility of assuming a more complex mode shape?

Mr. Long: No. Of course, the reason one assumes the simple supports is to get these nice simple sine functions in the Y direction; otherwise it is difficult to satisfy the governing equations.

D. Egle (Univ. of Okla.): I have a question about the continuity conditions. You didn't mention just what they were. Do you use the continuity equations in which the normals in the plane and the normals in the beams remain normal to the plate? Do you assume a straight line distribution, essentially?

Mr. Long: Yes.

Mr. Egle: There has been some similar work on ring stiffened shells at Southwest Research Institute. They found, in essence, the same thing that you did — that the average smeared analysis was not valid for high end numbers or circumferential wave numbers. They made one interesting point which I wonder if you have tried. The frequencies when the rings are essentially infinitely rigid are very similar to the frequencies of a shell that is simply supported between two rings. Did you compare your frequencies for large eccentricities with the frequency of a simply supported plate, the width of which would be just the distance between two stiffeners?

Mr. Long: I have looked into this type of thing but I have not compared it to a fully simply supported plate. I looked into simple supports on three sides and a fixed edge on the other which, for example, is what the two outside panels in this example would effectively be. I

looked into the case of two edges built in and two edges simply supported which is what the inside panel here would be. You get something somewhere in between for the fundamental mode shape.

* * *

CRACK DETECTION IN A STRUCTURAL BEAM THROUGH CROSS-CORRELATION ANALYSIS

F. Baganoff
Baganoff Associates, Inc.
St. Louis, Missouri

and

D. Baganoff
Stanford University
Stanford, California

A new method for nondestructive structural testing is being developed, and when perfected, the modal vibrations of a simple primary structure, such as a torque box, will be monitored in response to broadband, mechanical force input. The resulting electrical signals, sensed at two or more preselected points, would be cross correlated to obtain computerized engineering curves. This study concludes that any changes due to fatigue that are introduced into the structure will produce corresponding changes in the stationary process and will be reflected in the fingerprint curves. This standard fingerprint will be stored for later comparison with test fingerprints obtained for structures with suspected structural fatigue. Further, it is expected that in the future an average curve obtained for a suitable number of production items may be used as a basis for qualification testing.

In a study that is to serve as a fundamental building block, the modal vibrations for a structural beam were both analyzed in the laboratory and modeled mathematically. Two identical beams were used in the experiments, but one of the beams had a cross-sectional crack placed in it. Mathematically, the fissured beam was modeled, as two "lightly coupled," second-order mechanical systems. The equations show that at one extreme, that is when the fissure is almost through the beam, each pair of symmetric and nonsymmetric modes about the crack approach each other in frequency. The cross correlation of the two response signals produces a characteristic "beat frequency" envelope on the time cross-correlation curve that becomes lower in frequency and amplitude, because of the influence of an exponentially decaying function, until it is nonexistent when the beam becomes broken in half. At the other extreme, when the fissure is very shallow, the ordered set of higher frequency, modal vibrations produces a time cross-correlation curve in which the envelope peaks in a uniform manner and then decays to zero.

The experimental results confirm the uniform peak predicted for the homogeneous beam and the predicted "beat frequency" envelope for the damaged beam. It may be noted that these radical departures were obtained for a very shallow crack. It will be shown that the cross-correlation function acts as a phase detector and is very sensitive to changes in the modal frequencies. To make these findings practical, cross-correlation functions with long averaging times will be necessary to insure data repeatability.

Continued investigations in this area will deal with the repeat of this basic experiment to try to evaluate the coefficients and to extend these methods to other structural shapes, such as "T" and "H" beams.

INTRODUCTION

This paper presents the results of research in a new computerized method for monitoring the structural integrity of a beam. Experimentally, a homogeneous beam was excited laterally

by a broadband point force and the resultant modal vibrations were sensed by two sensitive accelerometers. Previous experiments in other areas had shown that the time cross-correlation function for two random signals was particularly sensitive to relatively small

changes in component frequencies in the two signals. The parallel analytical study showed that a computerized computation as this would have to be used to detect the small changes in the modal frequencies of the vibrating beam as a result of the introduction of a small cross-sectional crack.

Both the experimental and theoretical results show that the time correlation function, because of its nature, is an ideal computerized output. For large time delays, this function acts as a phase sensitive detector. The method would be severely limited if it were not possible to compute the correlation points using averaging times in excess of 20 sec.

Although the structural beam chosen for analysis is fairly uncommon in useful structures, it represented a formidable problem for analytical study. The plan is to use the present results as a building block in the eventual understanding of the prediction of changes in more complex structures. It is expected that for complex structures the significance of changes in the time correlation function will have to be developed empirically.

Research is continuing to analytically predict the changes in the time cross-correlation function as related to where, along the beam, the crack is located, the extent of the fissure, and different end conditions on the beam. Further work is planned to develop a broader understanding for more complicated structures, such as "T" or "H" beam construction, or possibly a torque box configuration such as that found in an aircraft wing. However, it is doubtful that the onset of fatigue in typical built-up aircraft structures will be predictable in the time cross-correlation functions, except as developed empirically.

A computerized method for continuous surveillance of the structural integrity of transportation equipment has long been needed. With the recent advances in the passenger carrying capability of the coming commercial aircraft, structural surveillance of the airframe and jet engines requires greater emphasis on the development of this method. Other needs, such as the structural surveillance of bridges, building structures, Naval ships, and motor vehicles readily come to mind.

DEVELOPMENT APPROACH

The object of this investigation was to understand the phenomenon behind the cross-correlation functions as they pertain to the

cracked beam. In addition to the two major approaches, previously mentioned, a third and less important approach was also taken. In the latter case, cross-correlation functions were hand calculated using modal response data obtained with sinusoidal excitation. Throughout this work, the comparisons are based more on a qualitative than a quantitative nature.

Parallel experimentation on an aircraft stabilizer indicated that, analytically, a coupled modes approach would not be unreasonable. The cross-correlation functions, in this case, are approximately identical for both positive and negative time delays, indicating that a standing wave phenomenon probably exists. However, the curves are not perfectly symmetrical, suggesting that some traveling wave energy may also be present. Further, the imaginary envelope for these functions seems to indicate that a beating phenomenon is taking place for this typical built-up structure.

Because of practical limitations, there are obvious differences between the mathematical model and the experimental setup. The mass loading of the beam by the shaker and the two accelerometers was found not to be a factor. In the experimentation, it was found desirable to use a peaked broadband force to primarily excite the higher frequency modes. Also, utilization of a two-point force input was considered but found not to be a factor. The study proposes to show that the bunching of the modes at the higher frequencies causes the cross-correlation function to beat.

MODEL

In the case of the beam that is nearly severed, the resulting two vibration systems act almost independently of one another. Each system has a fundamental vibration mode with a frequency ω_0 , as the two beams are equal in length. The introduction of a small amount of spring coupling causes the two fundamental modes to become phase coherent, and thus, to generate two new frequencies, α and β , combining both systems into one. In one instance, the phase of the coupled force tends to increase the apparent bending stiffness so that ω_0 becomes β . Simultaneously, the component force that is out of phase tends to reduce the apparent bending stiffness and produce the asymmetric modal frequency, α . The concept of coupled modes is a very powerful analytical tool and permeates many branches of science.

Reference should be made to Fig. 1 for a drawing of the theoretical vibrating beam. The assumptions made are as follows:

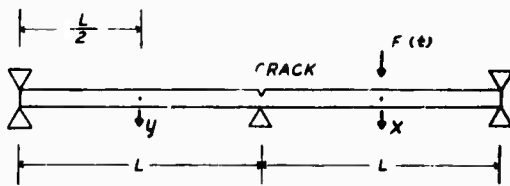


Fig. 1. Theoretical beam experiment

1. Assume symmetry on the two sides (easy algebra).
2. By placing the crack above a support, the solution will not degenerate to nonsense when the beam is completely severed.
3. Locate the two accelerometers at the points marked x and y .
4. Let the shaker be placed at point x and designate the forcing function by $F(t)$.
5. Let x and y represent the deflections of the beam at the two points shown.

The total deflection $x(\ell, t)$ for a beam with pinned ends can be expressed as the product of a function relating the distance along the beam ℓ and of a function expressing time as the variable [1].

$$x(\ell, t) = \sum_n \psi_n(\ell) \psi_n(t).$$

The total deflection can be approximated by the deflection of the fundamental mode $x(\ell, t)$ as the force is applied at the center of each vibrating system. If some higher mode is excited such as that which takes place in the experimentation, then $x(\ell, t)$ would represent this higher mode.

The approximate motion of the two systems can be described by the following two coupled equations:

$$\ddot{x} + 2\gamma\dot{x} + \omega_0^2(x + \epsilon y) = f(t), \quad (1)$$

$$\ddot{y} + 2\gamma\dot{y} + \omega_0^2(\epsilon x + y) = 0,$$

where

M = effective mass of beam of length L = $1/2$ true mass

K = effective spring constant = $48EI/L^3$

I = moment of inertia of the cross section

E = Young's modulus

aluminium: $E = 11 \times 10^6$ psi
steel: $E = 30 \times 10^6$ psi

ϵ = coupling term, where $0 \leq \epsilon \ll 1$, that is, $\epsilon \rightarrow 0$ for a severed beam

$$f(t) = F(t)/M$$

γ = damping coefficient, assume γ small, and

$$\omega_0^2 = K/M.$$

Define the operator D as follows:

$$D(x) = \left(\frac{\partial^2}{\partial t^2} + 2\gamma \frac{\partial}{\partial t} + \omega_0^2 \right) x. \quad (2)$$

Then the two equations become

$$D(x) + \epsilon \omega_0^2 y = f(t),$$

$$D(y) + \epsilon \omega_0^2 x = 0.$$

In a like manner, define the operator H as follows:

$$H(y) = \left[\left(\frac{\partial^2}{\partial t^2} + 2\gamma \frac{\partial}{\partial t} + \omega_0^2 \right)^2 - \epsilon^2 \omega_0^4 \right] y. \quad (3)$$

The two equations become simply

$$H[y(t)] = -\epsilon \omega_0^2 f(t), \quad (4)$$

$$D[y(t)] = -\epsilon \omega_0^2 x(t).$$

Using standard methods, the first equation of Eq. (4) gives the relation between the power spectrum of the input, $S_{ff}(\omega)$, and the power spectrum of the second coordinate, $S_{yy}(\omega)$, i.e.,

$$|H(i\omega)|^2 S_{yy}(\omega) = -\epsilon \omega_0^2 S_{ff}(\omega), \quad (5)$$

where from Eq. (3)

$$H(i\omega) = [(i\omega)^2 + 2\gamma(i\omega) + \omega_0^2]^2 - \epsilon^2 \omega_0^4.$$

The second equation of Eq. (4) yields

$$D^*(i\omega) S_{yy}(\omega) = -\epsilon \omega_0^2 S_{xy}(\omega), \quad (6)$$

where from Eq. (2)

$$D^*(i\omega) = (-i\omega)^2 + 2\gamma(-i\omega) + \omega_0^2.$$

$S_{xy}(\omega)$ is the cross power spectrum, i.e., the Fourier transform of the cross-correlation function $R_{xy}(\tau)$.

$$S_{xy}(\omega) = \int_{-\infty}^{\infty} e^{-i\omega\tau} R_{xy}(\tau) d\tau.$$

$R_{xy}(\tau)$ = ensemble mean of $[x(\tau)y(t+\tau)]$.

From Eqs. (5) and (6), $S_{yy}(\omega)$ can be eliminated to obtain

$$S_{xy}(\omega) = -\epsilon\omega_0^2 \frac{D^*(i\omega)}{|H(i\omega)|^2} S_{ff}(\omega). \quad (7)$$

$D^*(i\omega)$ and $|H(i\omega)|^2$ can be rearranged and written as

$$D^*(i\omega) = (\omega_0^2 - \omega^2) - 2i\gamma\omega,$$

$$|H(i\omega)|^2 = \left[(\omega_0^2 - \omega^2)^2 - \epsilon^2\omega_0^4 + 4\gamma^2\omega^2 \right]^2 + 16\gamma^2\epsilon^2\omega_0^4\omega^2. \quad (8)$$

For zero damping ($\gamma = 0$), the roots of the equation $|H(i\omega)|^2 = 0$ are given by

$$(\omega_0^2 - \omega^2) = \pm \epsilon\omega_0^2,$$

or $\omega^2 = \omega_0^2(1 \pm \epsilon)$, and $\omega = \pm \omega_0\sqrt{1 \pm \epsilon}$, (4 roots $\times 2$).

If small damping ($\gamma/\omega_0 \ll 1$) is assumed then it can be expected that the new roots will be only slightly perturbed away from the above eight roots. Using the assumption of small damping ($\gamma/\omega_0 \ll 1$), the roots are given by

$$\omega = \pm \sqrt{\alpha^2 \pm 2i\alpha\gamma}, \quad \pm \sqrt{\beta^2 \pm 2i\beta\gamma}, \quad (9)$$

where $\alpha = \omega_0\sqrt{1-\epsilon}$ and $\beta = \omega_0\sqrt{1+\epsilon}$ (i.e., the roots for zero damping).

In terms of the roots given by Eq. (9) $|H(i\omega)|^2$ can be expressed as

$$|H(i\omega)|^2 = (\alpha^2 - 2i\gamma\alpha - \omega^2)(\alpha^2 + 2i\gamma\alpha - \omega^2) \times (\beta^2 - 2i\gamma\beta - \omega^2)(\beta^2 + 2i\gamma\beta - \omega^2)$$

or

$$|H(i\omega)|^2 = (\alpha^4 + 4\gamma^2\alpha^2 - 2\gamma^2\omega^2 + \omega^4) \times (\beta^4 + 4\gamma^2\beta^2 - 2\gamma^2\omega^2 + \omega^4) \quad (10)$$

or

$$|H(i\omega)|^2 = [4\gamma^2\alpha^2 + (\alpha^2 - \omega^2)^2] [4\gamma^2\beta^2 + (\beta^2 - \omega^2)^2].$$

Equations (8) and (10) can be substituted into Eq. (7) to give

$$S_{xy}(\omega) = -\epsilon\omega_0^2 S_{ff}(\omega) \times \frac{(\omega_0^2 - \omega^2) - 2i\gamma\omega}{[4\gamma^2\alpha^2 + (\alpha^2 - \omega^2)^2] [4\gamma^2\beta^2 + (\beta^2 - \omega^2)^2]} \quad (11)$$

If the definitions for α and β are used, it can be shown by using partial fractions that Eq. (11) can be written as

$$S_{xy}(\omega) = S_{ff}(\omega) \left[\frac{-1/4}{4\gamma^2\alpha^2 + (\alpha^2 - \omega^2)^2} \times \frac{1/4}{4\gamma^2\beta^2 + (\beta^2 - \omega^2)^2} \frac{2\epsilon\gamma^2\omega_0^2 i 2\epsilon\gamma\omega_0^2 \omega}{(\alpha)(\beta) (\alpha)(\beta)} \right],$$

where $(\alpha)(\beta)$ stands for the product of the first two denominators. As the last two terms are of the order γ^2 and γ respectively, while the first two terms are of the order of unity, the last two terms can be ignored (as small damping is assumed) to write

$$S_{xy}(\omega) = \left[\frac{-1/4}{4\gamma^2\alpha^2 + (\alpha^2 - \omega^2)^2} \times \frac{1/4}{4\gamma^2\beta^2 + (\beta^2 - \omega^2)^2} \right] S_{ff}(\omega). \quad (12)$$

Assuming white noise for $S_{ff}(\omega)$, the Fourier transform of $S_{xy}(\omega)$ can be performed by using standard tables. The operation is laborious unless the simplifying assumption, $\gamma/\omega_0 \ll 1$, is utilized. The desired result simplifies to

$$R_{xy}(\tau) = \frac{1}{4\beta^3(\gamma)^2} e^{-\frac{\beta(\gamma)^2}{2(\beta)^2}\tau} \cos(\beta\tau) - \frac{1}{4\alpha^3(\gamma)^2} e^{-\frac{\alpha(\gamma)^2}{2(\alpha)^2}\tau} \cos(\alpha\tau) \quad (13)$$

Equation (13) represents the general solution to be compared in its present form with the experimental curves for the undamaged beam. Note that Eq. (13) has two terms: one involving the perturbed frequency β and the other α . Each term has a maximum value at

$\tau = 0$, but $R_{xy}(\tau)$ does not necessarily peak at $\tau = 0$ because of the minus sign preceding the second term. The minus sign can be interpreted as owing to the fact that α was designated as the asymmetric frequency, or in other words, the beam deflections x and y are 180 degrees out of phase. Conversely, since β is the symmetric frequency, the two deflections are in phase.

If more modes than just the fundamental mode are considered, then it is reasonable to expect that Eq. (13) will contain more of these terms. The principle of superposition should apply so long as there is no damping coupling of modes. In the synthesized cross-correlation curve based on modal response data, three such terms were considered and the resulting synthesized curve gave a good approximation to the experimentally derived curve.

Equation (13) for a large crack ($\epsilon \ll 1$) can best be investigated in another form. In this case, the exponential terms and the coefficients reduce to one another:

$$\alpha = \omega_0 \sqrt{1 - \epsilon} \rightarrow \omega_0, \quad \beta = \omega_0 \sqrt{1 + \epsilon} \rightarrow \omega_0.$$

However, the small terms in the two arguments must be retained:

$$\cos(\beta\tau) = \cos \omega_0 \sqrt{1 + \epsilon\tau} \rightarrow \cos \omega_0 \left(1 + \frac{\epsilon}{2}\right)\tau,$$

$$\cos(\alpha\tau) = \cos \omega_0 \sqrt{1 - \epsilon\tau} \rightarrow \cos \omega_0 \left(1 - \frac{\epsilon}{2}\right)\tau.$$

Thus Eq. (13) becomes

$$R_{xy} = \frac{1}{4\omega_0\gamma^2} e^{-\frac{\gamma^2}{2\omega_0}\tau} \left[\cos \omega_0 \left(1 + \frac{\epsilon}{2}\right)\tau - \cos \omega_0 \left(1 - \frac{\epsilon}{2}\right)\tau \right],$$

or

$$R_{xy} = \frac{-1}{2\omega_0\gamma^2} e^{-\frac{\gamma^2}{2\omega_0}\tau} \sin(\omega_0\tau) \sin\left(\frac{\epsilon}{2}\omega_0\tau\right). \quad (14)$$

Note that this result is for small damping ($\gamma/\omega_0 \ll 1$) and for a deep crack ($\epsilon \ll 1$). A schematic plot of this cross-correlation function is shown in Fig. 2.

The ac waveform $\sin(\omega_0\tau)$ of the function can be seen to be amplitude modulated by the term $\sin[(\epsilon/2)\omega_0\tau]$. As ϵ becomes smaller, the peak for the first half cycle moves further out in τ value. In the limit, the exponentially decaying function with the exponent $[-(\gamma/2)\omega_0\tau]$ keeps the envelope from ever peaking, and thus, the cross-correlation function is zero for all values of τ . This decaying term is present because α and β are really composed of narrow bands of frequency components owing to the broadband excitation. When the sensor located on the broken section is no longer responding to a force input, it would be expected that the cross-correlation function would be zero for all values of τ .

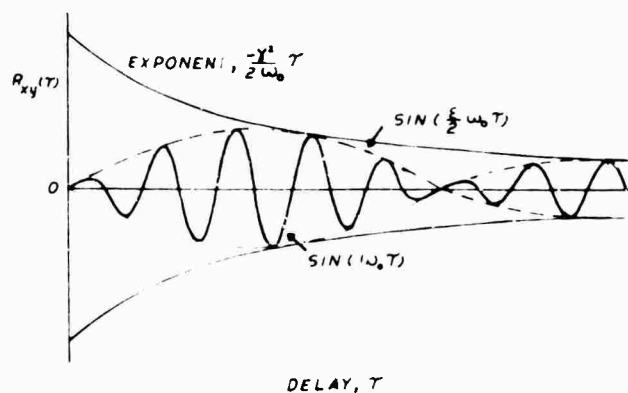


Fig. 2. Theoretical cross-correlation curves

EXPERIMENT

For both the homogeneous and the cracked beam, experimental cross-correlation functions were derived in the laboratory to be compared with the theoretical results discussed previously. The physical experiments differed in a number of respects from the theoretical model because of practical limitations. In each case the beams were excited laterally by a "peaked" broadband force derived from an electro-mechanical shaker physically mounted near one end. Two accelerometers, one mounted on each side of the crack, sensed the accelerations of the beam. The resulting two random signals were applied to a hybrid cross-correlation computer for near real-time analysis. A photograph of the experimental setup can be seen in Fig. 3.

The physical approximations that had to be made are given in the next few paragraphs. To begin with, cross-correlation functions were obtained and compared for the two beams, while still structurally intact, to check their dynamic responses at the higher modal frequencies. The mass loads on the beam by the shaker and the accelerometers were expected to distort the vibration modes. Certainly, there were other second-order effects, such as the static deflection of the beam owing to gravity, that were ignored in this series of experiments. The deflection signals seen on an oscilloscope were only slightly distorted probably also owing, in some part, to the local imperfections. The knife-edge supports at each end performed satisfactorily, judging from the same oscilloscope displays.

The fundamental mode frequency was experimentally determined to be approximately

4.1 Hz, which is consistent with the thinness of the beam. Their material was aluminum 0.5 by 1.0 in. in cross section and 6 feet in length. The extent of the crack can only be qualitatively defined as extending a combined distance from each side of approximately 20 percent of the cross-section distance. The vibration modes of interest in these experiments are for the abstract numbers ($n = 20$ through 25). The amplitude and frequencies of the responses obtained, using sinusoidal excitation, and for both the damaged and undamaged beams, can be found listed for reference in Table 1. As another piece of reference information, the bandwidth at the three decibel points was approximately 20 Hz, giving a damping coefficient (γ) of approximately 0.005. One may note that in the theoretical discussion it was concluded that a symmetric mode about the fissure would decrease in frequency and that an asymmetric mode would increase in frequency. By looking at Table 1 and Fig. 4 together, these general conclusions can be drawn.

The rim of the inertial shaker, which had a diameter of 4.5 in., was fastened at two points to the beam: 2.5 and 6.75 in. from the end. Whether these locations are nodes or antinodes for the various vibration modes can be learned from Fig. 4, which shows the locations for the forces, as well as for the two accelerometers superimposed on the mode shapes. The accelerometers were located 18 and 32 in. from the end, while the crack was introduced at a distance of 25 in. from the same point.

The broadband force had three predominant peaks with the largest one, by far, existing at 2000 Hz. The frequency response for the shaker can be seen in Fig. 5. This spectral shape is not unlike that found exciting a structural

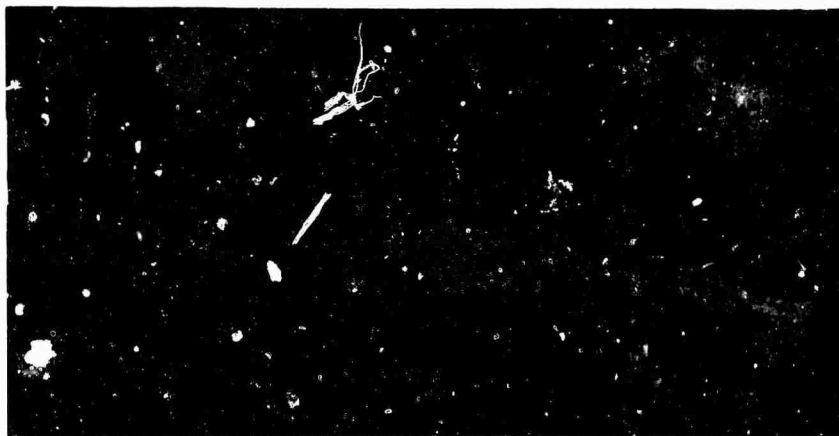


Fig. 3. Cracked beam experiment

TABLE 1
Homogeneous and Cracked Beams

Homogeneous Beam					Cracked Beam			
n	Freq. (Hz)	RMS _x	RMS _y	Phase (°)	Freq. (Hz)	RMS _x	RMS _y	Phase (°)
20		0	0		162.	2.3	0.9	0
21	1841	3.4	3.3	0	1788	1.6	0.9	0
22	1936	4.2	6.0	180		0	0	
23	2116	3.6	4.0	0	2177	1.9	2.9	180
24	2345	0.5	0.4	180	2496	0.7	0.5	180
25	2540	0.5	0.3	180	2482	1.6	0.6	180

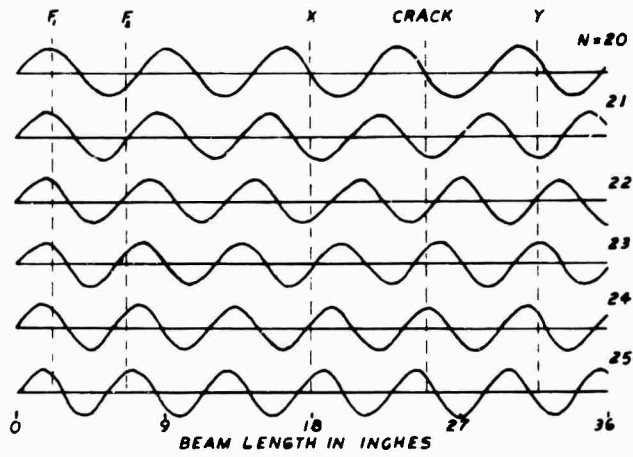


Fig. 4. Theoretical mode shapes

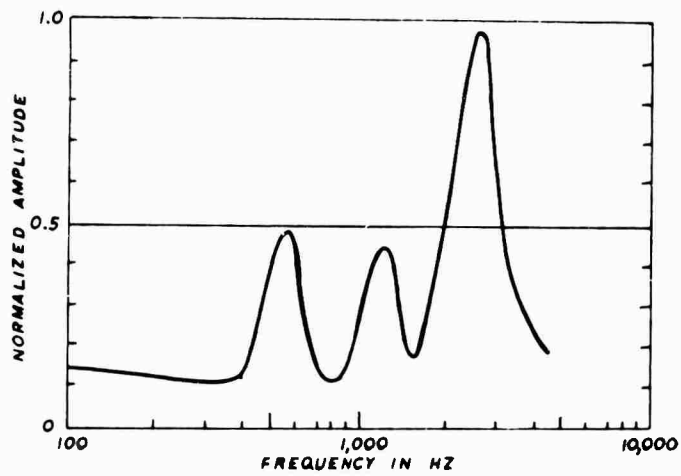


Fig. 5. Force frequency response

member in a practical situation. Different spectral shapes for the input force will produce different cross-correlation results, but this is of importance only analytically.

The two accelerometer signals were applied to a hybrid cross-correlation system and were cross correlated as defined by the equations [1]:

$$R_{xy}(\tau) = \lim_{T \rightarrow \infty} \frac{1}{T} \frac{1}{rms_x rms_y} \int_0^T y(t) x(t+\tau) dt. \quad (15)$$

where

$$(rms_x)^2 = \lim_{T \rightarrow \infty} \frac{1}{T} \int_0^T x(t)^2 dt.$$

This system is shown in the photograph in Fig. 6. As the force spectrum was peaked, only a select number of modes were excited; thus, the incoming response signals were amplified but not filtered any further. Should the occasion arise that the structural test member is excited by a flat broadband force, then the incoming signals could be filtered before they are cross correlated to see the results only for a select number of modes. For this purpose, the system has standard one-third octave and continuously tunable constant bandwidth analog filters.

A digital time delay unit in the system was utilized to delay signal $x(t)$ before $x(t) y(t)$ were multiplied together by a hybrid multiplier. This unit is automatically programmable in delay increments in multiples of 5 μ sec out to a τ maximum of 200,000 μ sec. The time delay

sector determined by the initial and final delay settings are selectable by digital switches. An analog-to-digital converter digitizes the incoming broadband signal. It is then time delayed the appropriate amount in magnetostriuctive lines and finally converted back to an analog signal by a digital-to-analog converter.

The averaging circuit located at the output of the multiplier employs operational amplifiers with various feedback networks that produce selectable averaging times of 2.5, 5, 15, 30, and 60 sec. Each computed point on the time correlation curves is a result of 30 sec averaging. Generally speaking for random signals, the longer the averaging time, the greater the repeatability of the points for repeated test data. Data repeatability for 30 sec averaging is within 5 percent of the reading.

In parallel with the multipliers, there are two true rms meters that produce rms_x and rms_y . The product of these two quantities is necessary, as shown in the above equation, to produce the normalized, cross-correlation function $R_{xy}(\tau)$. The normalized function has the advantage of being independent of the amplitude of the broadband force so long as its spectral distribution is not altered. The outputs from the averaging networks are digitized and the resulting digital readings are entered into a conventional digital computer. An extensive digital program corrects the data readings for instrumentation errors and computer system errors, and normalizes and scales the final results to the appropriate engineering units. The time correlation curves, shown in Fig. 7, are a direct product of this system.



Fig. 6. Cross-correlation system

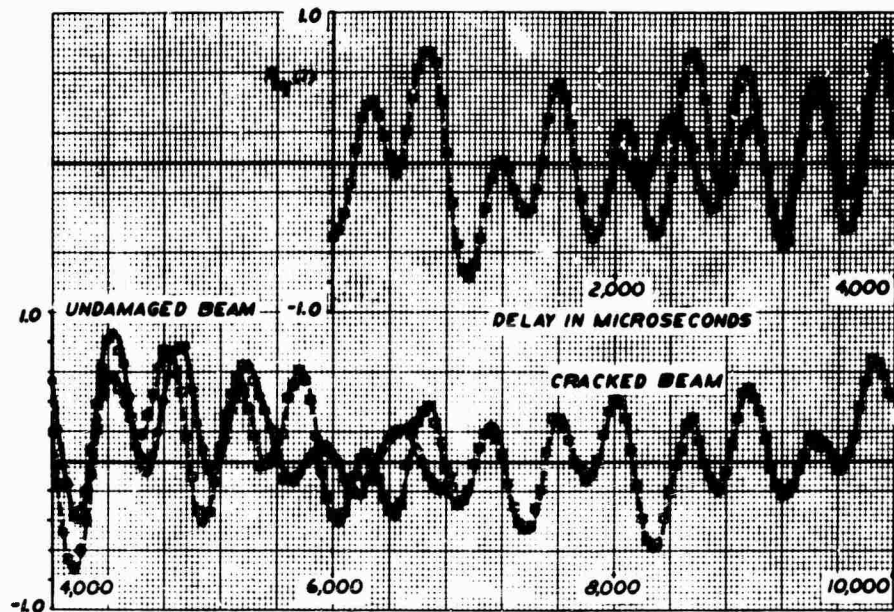


Fig. 7. Experimental cross-correlation curves

The resulting time cross correlation obtained for both the damaged and undamaged bar are shown superimposed in Fig. 7. The normalized function, which ranges from +1.0 to -1.0, is plotted along the vertical scale. The curves are faired lines through discrete points because signal $x(t)$ was delayed in time delay increments of 40 μsec . The heavy curve for the undamaged beam is assumed to be approximately zero in magnitude below 2000 μsec and above 6800 μsec . The imaginary envelope for the ac waveform peaks around 3900 μsec and then the curve is shown to be zero above 6800 μsec .

This waveform can best be understood by considering that the cross-correlation function for each mode, separately, would have the relationship below for sinusoidal excitation [1].

$$R_{xy_0}(\tau) = \frac{K}{r_{ms_x} r_{ms_y}} \sin \frac{n\pi \ell_1}{2L} \sin \frac{n\pi \ell_2}{2L} \cos (\omega_n \tau). \quad (16)$$

The constant, K, will have a mean-square value equal to the denominator, making the ratio 1.0. The two sine terms are bounded by values of ± 1.0 and are dependent upon the locations for the two transducers ℓ_1 and ℓ_2 . Thus, the function in Eq. (16) has a maximum at τ equals zero, but may be either a positive or negative number. The sum of three such terms for ($n = 21, 22,$ and 23) will be shown to approximate the curve in Fig. 7 for the undamaged

beam. Note that Eq. (16) with the additional terms can be compared with Eq. (13) which was derived for a broadband input.

The only plausible explanation for the cross-correlation function peaking at some other τ value besides zero seems to be a result of the beating of the separate cross-correlation functions. Then it should be possible to compute the τ_p at which the maximum occurred from other known data. The envelope maximum for the subtraction of two cosine functions occurs at

$$\frac{\omega_{n+1} - \omega_n}{2} \tau_p = \frac{\pi}{2},$$

or

$$\tau_p = \frac{1}{2(f_{n+1} - f_n)}. \quad (17)$$

Referring again to Table 1, the vibration modes beginning with $n = 21$ are an average 140 Hz apart in frequency. Substituting this value into Eq. (17), τ_p is calculated to be 3600 μsec . This compares favorably with the 3900 μsec obtained experimentally. The period for the axis crossings also agrees with the average period for the vibration modes ($n = 21, 22,$ and 23).

The heavy dashed curve shown in Fig. 7 is the time cross-correlation function obtained experimentally for the damaged beam. Referring

once again to Table 1, it can be seen that the modal frequencies for the damaged beam changed slightly, while the amplitudes changed substantially. In fact, vibration modes with $n = 21, 22,$ and 23 are replaced by vibration modes with $n = 20, 21, 23,$ and 25 . These results were derived empirically by driving the damaged beam with sinusoidal excitation and recording each of the response signals read on a true rms meter. The differences in the vibration modes are difficult to predict because, at these frequencies, they are highly dependent on irregularities in the beam and because the true input force is difficult to describe.

Bearing in mind the analytical discussion, a number of supporting observations can be made by looking at the dashed curve. The peaks of the ac waveform are much more irregular than for the solid curve, but an envelope drawn for the peak maximums would itself peak around $4000 \mu\text{sec}$ and would reach a minimum at approximately $6200 \mu\text{sec}$. Thereafter, the envelope would grow once more, much like the predicted theoretical curve. The axis crossings are a little more frequent, suggesting a slightly higher average frequency, ω_0 . This is borne out by the modal frequencies listed in Table 1. The irregular peaks indicate a faster beating or a wider separation of frequencies for the modal vibrations. Vibration mode $n = 20$ plays a predominant role in this respect. Equation (14) in the analytical discussion implied that the modal frequencies for a damaged beam would not be uniformly spaced in frequency. In contrast, for a homogeneous beam the modal frequencies increased with n^2 . The irregular curve obtained experimentally is thought to be a direct product of this analytical conclusion.

A further strengthening of the essential points made in this paper can be gained by constructing synthesized time cross-correlation curves from the sinusoidal, modal response data. Understandably, all the vibration modes up through $n = 25$ could not be taken into account because the hand calculations would reach a trying state. It further could be argued that the modes below $n = 100$, although small in response because of the input spectral shape, would only show up as a bias in $R_{xy}(\tau)$ plotted only on a τ scale out to $10,000 \mu\text{sec}$. For the remaining modes, either one or both of the response signals was small; consequently, only the modes between $n = 20$ and 25 will be considered.

The question of the effects on the time correlation function of a two-point force input also needs to be considered. Without complicating matters too much, the equations for the

deflections x and y at points l_1 and l_2 , respectively, and two force inputs at l_3 and l_4 , can be expressed as

$$x(l_1, t) = \sum_{n=20}^{25} \psi_n(l_1) [\xi_{n,l_3}(t) + \xi_{n,l_4}(t)],$$

(18)

and

$$y(l_2, t) = \sum_{n=20}^{25} \psi_n(l_2) [\xi_{n,l_3}(t) + \xi_{n,l_4}(t)],$$

where

$$\psi_n(l_1) = \sin \frac{nm l_1}{2L},$$

$$\xi_{n,l_3}(t) = \frac{F_{n1}}{|Z(\omega_n)|^2} \sin \frac{nm l_3}{2L} \cos \omega_n t,$$

$$\psi_n(l_2) = \sin \frac{nm l_2}{2L},$$

$$\xi_{n,l_4}(t) = \frac{F_{n2}}{|Z(\omega_n)|^2} \sin \frac{nm l_4}{2L} \cos (\omega_n t + \theta_n).$$

The quantities $\xi_{n,l_3}(t)$ and $\xi_{n,l_4}(t)$ are time-response functions for harmonic inputs with rms levels F_{n1} and F_{n2} . The familiar frequency dependent quantity is $Z(\omega_n)$, and a phase shift θ_n is included between the two forces.

The cross correlation of the equations in Eq. (18) can be written

$$\begin{aligned} R_{xy}(l_1, \tau) &= \frac{1}{T} \int_0^T \sum_{n=20}^{25} \psi_n(l_1) \xi_{n,l_3}(t) \psi_n(l_2) \xi_{n,l_3}(t) dt \\ &+ \frac{1}{T} \int_0^T \sum_{n=20}^{25} \psi_n(l_1) \xi_{n,l_4}(t) \psi_n(l_2) \xi_{n,l_4}(t) dt \\ &+ \frac{1}{T} \int_0^T \sum_{n=20}^{25} \psi_n(l_1) \xi_{n,l_3}(t) \psi_n(l_2) \xi_{n,l_4}(t) dt \\ &+ \frac{1}{T} \int_0^T \sum_{n=20}^{25} \psi_n(l_1) \xi_{n,l_4}(t) \psi_n(l_2) \xi_{n,l_3}(t) dt. \end{aligned}$$

(19)

Performing the indicated integrations, the final expression for $R_{xy}(l_1, l_2, \tau)$ can be expressed as

$$R_{xy}(l, \tau) = \sum_{n=20}^{25} \frac{\sin \frac{n\pi l_1}{2L} \sin \frac{n\pi l_2}{2L}}{2\pi |Z_n(\omega_n)|^2} \times \left[\cos \omega_n \tau \left\{ \frac{F_{n_1}^2}{2} \sin^2 \left(\frac{n\pi l_3}{2L} \right) + \frac{F_{n_2}^2}{2} \sin^2 \left(\frac{n\pi l_4}{2L} \right) \right. \right. \\ \left. \left. + (\cos \theta_n) \cos \omega_n \tau \left\{ F_{n_1} F_{n_2} \sin \frac{n\pi l_3}{2L} \sin \frac{n\pi l_4}{2L} \right\} \right] \quad (20)$$

Equation (20) in its present form assumes small damping ($\gamma \ll 1$), or in other words, no damping coupling between modes. This being the case, Eq. (20) indicates that the response contributions from each of the modes can be linearly summed. Further, it can be deduced that $R_{xy}(l_1, l_2, \tau)$ is an even function and that θ_n , the phase shift between the force inputs, does not cause this function to peak at some value other than $\tau = 0$.

Using the quantities for the rms accelerations found in Table 1, the two synthesized time cross-correlation curves shown in Fig. 3 were produced. The ac waveform for the undamaged beam increases in amplitude very similar to the experimental curve in Fig. 7. For the present example, the envelope maximum occurs at approximately 3800 μ sec and then begins to diminish in size. Overlapping of the two curves

will show that the axis crossings differ somewhat, becoming more pronounced for the larger values of τ . The sensitivity of the time correlation function at large τ 's to slight discrepancies in modal frequencies is planned to be used as an advantage in this process.

The synthesized curve for the damaged bar compares favorably in wave shape to that predicted analytically. The envelope for the peak maximums approximates a half sine wave with a maximum at 3600 μ sec and a minimum at approximately 5200 μ sec. Thereafter, the envelope begins to grow in amplitude again (beating phenomenon).

Admittedly, the comparisons between the analytical, experimental, and synthesized curves are more qualitative than quantitative in nature. Yet, the evidence that the peaks in the cross-correlation functions are a result of the bunching of vibration modes is considered fairly certain.

CONCLUSIONS

This paper proposes that cracks introduced into a structural beam cause slight changes in the frequencies and amplitudes of the modal vibrations. These small changes nevertheless produce significant changes in the time cross-correlation functions because of the beating of

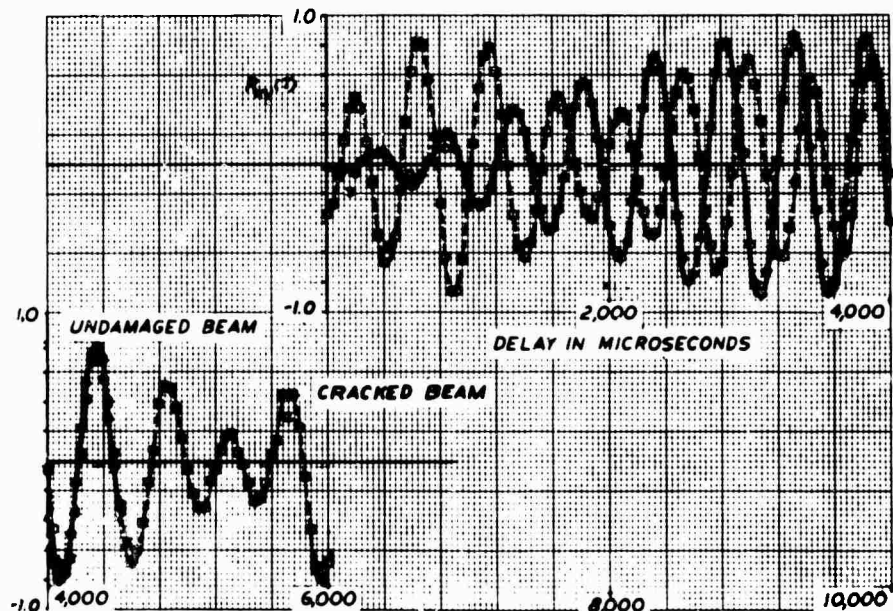


Fig. 8. Synthesized cross-correlation curves

the individual cross-correlation functions. At this time, the location of the crack along the beam would probably have to be determined empirically as, even for the simple beam, the analytical calculations would be extensive.

REFERENCE

1. S. H. Crandall, Random Vibrations, John Wiley & Sons, Inc., New York, 1958, pp. 187-229

DISCUSSION

R. Reed (NOL): Did you try any other approaches to the problem? Did you look into power spectral density or something like that? Also, I do not think you mentioned nonlinearities. You actually had a notch in your beam, as opposed to a crack, which is, I think, a nonlinearity. Did the cross spectral density indicate anything?

Mr. Baganoff: Let me answer your first question. Why would one go to cross-correlation analysis rather than power spectral density analysis? I firmly believe that PSD data, which is devoid of phase information, has its limitations. In other words, we are only looking at amplitude fluctuations as a function of frequency and I think that there is a lot of information wrapped up in phase. Instrumentation wise, it is probably ten times more difficult to preserve phase than it is amplitude just because there is so much information wrapped up in it. Regarding your second question, the nonlinearity was considered but we ran this experiment and got good correlation between the analytical and experimental approach. We want to look into these other aspects, but this is as far as we have progressed.

E. Sevin (ITT Research Institute): As I understand it, you are cross correlating the acceleration responses at two arbitrarily located points on the same beam. Could you comment just briefly on the physical principle being exploited here? I don't really appreciate what the lag really amounts to. What you are basically attempting to do is to run a confidence test on the stationarity of the process at any one point. Why wouldn't an autocorrelation at a given point really give you as much information?

Mr. Baganoff: Consider two of the modal vibrations. Suppose we have 2000 Hz and 2140 Hz. The point is that you are cross correlating both of these responses at the same time and they are 140 Hz apart. When you cross correlate them you get a certain shaped curve, as a function of tau. The lag, tau, allows the beating to take place between the cosine at 2000 Hz and a cosine at 2140 Hz. Then, when you introduce the fatigue or crack in the beam, the modal vibration at 2000 Hz no longer remains at 2000 Hz. It may change slightly, so that the separation is no longer 140 Hz. With the tau lag you can bring this out. You would not be able to get this from autocorrelation.

* * *

A THEORETICAL MODAL STUDY FOR THE LATERAL VIBRATIONS OF BARS HAVING VARIABLE CROSS SECTION AND FREE END CONDITIONS*

Arthur F. Witte
Sandia Corporation
Albuquerque, New Mexico

A considerable amount of interest has been generated in determining the normal bending modes of beams having a variable cross section and free end conditions. The practical applications of the problem became of interest in the early 1900's when applied to the free vibrations of a ship's hull. The problem has now become important when applied to the field of missiles and launch vehicles.

This paper contains a theoretical method that can be used to predict the normal bending modes of beams having variable cross section and free end conditions. The method outlined here works directly with the differential equation of motion

$$\frac{\partial^2}{\partial x^2} \left[EI(x) \frac{\partial^2 y}{\partial x^2} \right] + m(x) \frac{\partial^2 y}{\partial t^2} = 0,$$

where EI and m vary with x and where the bending moment and shear force are zero at each end. The effects of rotary inertia, shear, and material damping are not considered.

The method of solving the problem is basically one of transforming the partial differential equation and the boundary conditions into a system of linear algebraic equations with the use of finite difference approximations. The algebraic equations are written in matrix form and the problem becomes one of determining the eigenvalues and the eigenvectors of the matrix. However, the matrix must be inverted. Because of the free end conditions, the matrix is multiply degenerate and cannot be inverted until two degrees of freedom corresponding to rigid body translation and rigid body rotation are eliminated from the system of equations. Because of these two degrees of freedom, normal influence coefficient methods cannot be used when free end conditions are present.

This paper details the methods used, contains an operational FORTRAN II computer program for obtaining the first two normal bending modes, and compares the predicted results with experimental results obtained from a modal study on a small, high altitude research missile.

INTRODUCTION

Because the effects of rotary inertia, shear, and material damping have not been considered, the method of solution presented in this paper is not extremely complicated. Good engineering estimates of resonant frequencies and corresponding mode shapes of missile systems can be obtained where the wavelength of vibration is large compared with the lateral

dimensions of the system. Good estimates can generally be obtained for the first two normal bending modes.

The mathematics and computer program are such that with a little background in numerical methods of linear algebra and computer programming one can understand, without much difficulty, what is presented.

*This work was supported by the U.S. Atomic Energy Commission.

The method of solution can be summarized as follows:

1. Divide the bar into stations in such a manner as to accommodate the boundary conditions.

2. Use finite difference approximations to convert the partial differential equation

$$\frac{\partial^2}{\partial x^2} \left[EI(x) \right] \frac{\partial^2 y}{\partial x^2} + m(x) \frac{\partial^2 y}{\partial t^2} = 0$$

and the boundary conditions

$$EI(x) \frac{\partial^2 y}{\partial x^2} \Big|_{0,L} = 0$$

$$\frac{\partial}{\partial x} \left[EI(x) \frac{\partial^2 y}{\partial x^2} \right]_{0,L} = 0$$

to a set of ordinary differential equations.

3. Obtain a set of linearly dependent algebraic equations by assuming a solution of form

$$y_i = Y_i \sin(pt + \phi).$$

4. Write two equations which describe linear relations between the displacement of points on the bar corresponding to rigid body rotation and translation.

5. Obtain a set of linearly independent algebraic equations and write in matrix form.

6. Invert the matrix.

7. Determine the eigenvalues and corresponding eigenvectors which are the natural frequencies and corresponding mode shapes.

The method of solution described in this paper can be used for nonuniform bars with other end conditions; however, free-free end conditions create some difficulty not encountered when using other boundary conditions.

Results of an experimental modal study on a single stage Tomahawk high altitude research vehicle are compared with predicted results obtained using a FORTRAN II computer program which is listed in the Appendix.

NOMENCLATURE

\bar{A} Matrix A
 \bar{A}^{-1} \bar{A} inverse

\bar{B} Matrix B
 \bar{B}^{-1} \bar{B} inverse
 \bar{C} Matrix C
 \bar{D} Matrix D
E Modulus of elasticity
 EI_i Rigidity at stations i
I Area moment of inertia
 \bar{I} Identity matrix
L Length of the bar
 M_i Bending moment at station i
 \bar{P} Matrix P
 \bar{P}^{-1} \bar{P} inverse
 \bar{Q} Matrix Q
V Shear
 \bar{V} Vector V
 \bar{Y} Vector Y
Y A component of \bar{Y}
 \bar{Z} Vector Z
Z A component of \bar{Z}
 a_{ij} An element of \bar{A}
 b_{ij} An element of \bar{B}
 b'_{ij} An element of \bar{B}^{-1}
 c_{ij} An element of \bar{C}
 f_j The jth natural frequency in cycles per second (Hertz)
i An integer variable
j An integer variable
 m_i Mass per unit length of the bar at station i
n Number of stations or number of sections
 p_j The jth natural circular frequency in radians per second

q	Load intensity
t	Time
x	Distance along the bar from its left end
Δx	Distance between stations
y	Lateral displacement of the bar
β	Dominant eigenvalue of \bar{B}^{-1}
γ	Second eigenvalue of \bar{B}^{-1}
δ	Third eigenvalue of \bar{B}^{-1}
ϕ	A phase angle
ρ	Density
ζ	Damping factor C/C_{cr}

THE DIFFERENTIAL EQUATION OF MOTION AND BOUNDARY CONDITIONS

The following relationships hold for a bar, with a continuously varying rigidity, EI , subjected to a load of intensity, q , which may also vary continuously along the length of the bar:

y = deflection of the elastic curve

$\frac{dy}{dx}$ = slope of the elastic curve

$$EI \frac{d^2y}{dx^2} = -M \text{ (bending moment)} \quad (1)$$

$$\frac{d}{dx} \left[EI \frac{d^2y}{dx^2} \right] = -V \text{ (shear)}$$

$$\frac{d^2}{dx^2} \left[EI \frac{d^2y}{dx^2} \right] = q \text{ (load intensity).}$$

These relationships hold provided that the bar has a plane of symmetry and that bending occurs in that plane.

The principle of d'Alembert can be applied to a vibrating bar, and the load intensity, q , which varies along the length of the bar will be the reversed effective force given by

$$q = -m \frac{\partial^2 y}{\partial t^2} \quad (2)$$

The quantity m is the mass per unit length of the bar, which may vary continuously along the length of the bar. The expression for the reversed effective force is substituted into Eq. (1) and the equation for the lateral vibrations of a nonuniform bar becomes

$$\frac{\partial^2}{\partial x^2} \left[EI(x) \frac{\partial^2 y}{\partial x^2} \right] + m(x) \frac{\partial^2 y}{\partial t^2} = 0 \quad (3)$$

As y is now a function of both x and t , the equations in Eq. (1) become partial differential equations.

If the wavelength of the vibration is large compared with the lateral dimensions of the bar, the effects of rotary inertia and shear are considered negligible. Thus, for the lower modes of vibration of a bar whose lateral dimensions are small compared with its length, the effects of rotary inertia and shear may be neglected, and Eq. (3) adequately describes the motion of the bar if material damping is also neglected.

As a free-free bar is neither supported nor restrained at either end, the boundary conditions for each end are as follows:

1. The bending moment $EI(\partial^2 y / \partial x^2)$ is zero.

2. The shear force $(\partial / \partial x) [EI(\partial^2 y / \partial x^2)]$ is zero.

DETERMINATION OF THE FIRST NORMAL MODE

Consider the nonuniform bar of length L shown in Fig. 1. The bar is divided into n sections Δx in length where

$$\Delta x = \frac{L}{n} \quad (4)$$

The particular method of dividing the bar into sections is used to accommodate the boundary conditions.

As the deflection of a vibrating bar is a function of both x and t , the expression for the bending moment from Eq. (1) can be written as

$$EI \frac{\partial^2 y}{\partial x^2} = -M \quad (5)$$

This expression is put into Eq. (3) and the following equation of motion is obtained:

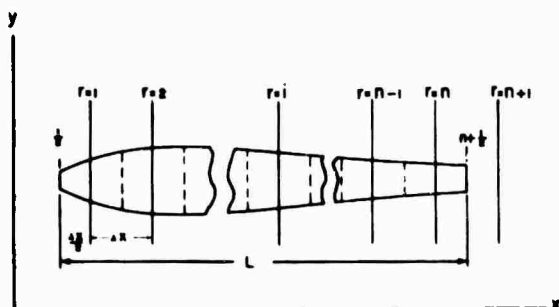


Fig. 1. Bar having a variable cross section and free end conditions

$$\frac{\partial^2(-M)}{\partial x^2} + m \frac{\partial^2 y}{\partial t^2} = 0. \quad (6)$$

If one assumes that the dependent variables y and M of Eqs. (5) and (6) can be adequately represented by second order polynomials in x ,* the following finite difference approximations for the first and second derivatives can be used:

$$\left. \begin{aligned} \frac{\lambda_1}{\partial x} \Big|_r &= \frac{u_{r+1} - u_{r-1}}{2\Delta x} \\ \frac{\partial u}{\partial x} \Big|_{r+1/2} &= \frac{u_{r+1} - u_r}{\Delta x} \\ \text{and} \\ \frac{\partial^2 u}{\partial x^2} \Big|_r &= \frac{u_{r+1} - 2u_r + u_{r-1}}{(\Delta x)^2} \end{aligned} \right\} \quad (7)$$

The quantity u is considered the dependent variable.

The approximation

$$u_{r+1/2} = \frac{u_{r+1} + u_r}{2} \quad (8)$$

will also be used when dealing with the boundary conditions. These approximations become more accurate as the number of sections into which the bar is divided is increased.

*This condition may be considered fulfilled provided the dependent variables may be adequately represented by a second order polynomial between at least three consecutive stations.

The second order difference approximations for $[\partial^2(-M)]/(\partial x^2)$ and $(\partial^2 y/\partial x^2)$ are substituted into Eqs. (5) and (6), resulting in the following ordinary differential equation for each station:

$$\frac{-(M_{r-1} - 2M_r + M_{r+1}))}{(\Delta x)^2} + m_r \frac{d^2 y_r}{dt^2} = 0 \quad (r=1, 2, 3, \dots, n), \quad (9)$$

where

$$M_r = -EI_r \frac{(y_{r-1} - 2y_r + y_{r+1}))}{(\Delta x)^2} \quad (r=1, 2, 3, \dots, n). \quad (10)$$

The boundary conditions for the bar shown in Fig. 1 are

$$M_{1/2} = 0, \quad V_{1/2} = \frac{\partial M}{\partial x} \Big|_{1/2} = 0$$

and

$$M_{n+1/2} = 0, \quad V_{n+1/2} = \frac{\partial M}{\partial x} \Big|_{n+1/2} = 0.$$

The boundary conditions can be written in finite difference form as

$$M_{1/2} = \frac{M_0 + M_1}{2} = 0$$

$$V_{1/2} = \frac{\partial M}{\partial x} \Big|_{1/2} = \frac{M_1 - M_0}{\Delta x} = 0$$

and

$$M_{n+1/2} = \frac{M_n + M_{n+1}}{2} = 0$$

$$V_{n+1/2} = \frac{\partial M}{\partial x} \Big|_{n+1/2} = \frac{M_{n+1} - M_n}{\Delta x} = 0.$$

Therefore

$$M_0 = M_1 = M_n = M_{n+1} = 0. \quad (11)$$

Equations (9), (10), and (11) are now used to form a set of ordinary differential equations that represent the original partial differential equation. These equations are of the form

$$\begin{aligned}
& \frac{-(M_0 - 2M_1 + M_2)}{(\Delta x)^2} + m_1 \frac{d^2 y_1}{dt^2} = 0 \\
& \frac{-(M_1 - 2M_2 + M_3)}{(\Delta x)^2} + m_2 \frac{d^2 y_2}{dt^2} = 0 \\
& \frac{-(M_2 - 2M_3 + M_4)}{(\Delta x)^2} + m_3 \frac{d^2 y_3}{dt^2} = 0 \\
& \dots \dots \dots \\
& \frac{-(M_{i-1} - 2M_i + M_{i+1})}{(\Delta x)^2} + m_i \frac{d^2 y_i}{dt^2} = 0 \\
& \dots \dots \dots \\
& \frac{(M_{n-2} - 2M_{n-1} + M_n)}{(\Delta x)^2} + m_{n-1} \frac{d^2 y_{n-1}}{dt^2} = 0 \\
& \frac{-(M_{n-1} - M_n + M_{n+1})}{(\Delta x)^2} + m_n \frac{d^2 y_n}{dt^2} = 0
\end{aligned} \tag{12}$$

where

$$\begin{aligned}
M_0 &= 0 \\
M_1 &= 0 \\
M_2 &= -EI_2 \frac{(y_1 - 2y_2 + y_3)}{(\Delta x)^2} \\
M_3 &= -EI_3 \frac{(y_2 - 2y_3 + y_4)}{(\Delta x)^2} \\
&\dots \dots \dots \\
M_i &= -EI_i \frac{(y_{i-1} - 2y_i + y_{i+1})}{(\Delta x)^2} \\
&\dots \dots \dots \\
M_{n-1} &= -EI_{n-1} \frac{(y_{n-2} - 2y_{n-1} + y_n)}{(\Delta x)^2} \\
M_n &= 0 \\
M_{n+1} &= 0
\end{aligned} \tag{13}$$

When a bar vibrates with one of its natural modes, the deflection of any point on the elastic curve varies harmonically with time, and a solution of the form

$$y_i = Y_i \sin (pt + \phi) \tag{14}$$

may be assumed for Eqs. (12) and (13). The quantity, p , is defined as the natural circular frequency of the vibrating bar. The equations in Eq. (13) may now be substituted into the

equations in Eq. (12) and the solution,

$$Y_i \sin (pt + \phi),$$

put into the resulting equations. A set of n linear algebraic equations can be obtained if one divides through each resulting equation by $\sin (pt + \phi)$. The n linear algebraic equations are

$$\begin{aligned}
& \frac{EI_2}{(\Delta x)^4} Y_1 - \frac{2EI_2}{(\Delta x)^4} Y_2 + \frac{EI_2}{(\Delta x)^4} Y_3 = m_1 p^2 Y_1 \\
& \frac{-2EI_2}{(\Delta x)^4} Y_1 + \frac{(4EI_2 + EI_3)}{(\Delta x)^4} Y_2 - \frac{2(EI_2 + EI_3)}{(\Delta x)^4} Y_3 \\
& \quad + \frac{EI_3}{(\Delta x)^4} Y_4 = m_2 p^2 Y_2 \\
& \dots \dots \dots \\
& \frac{EI_{i-1}}{(\Delta x)^4} Y_{i-2} - \frac{2(EI_{i-1} + EI_i)}{(\Delta x)^4} Y_{i-1} \\
& \quad + \frac{(EI_{i-1} + 4EI_i + EI_{i+1})}{(\Delta x)^4} Y_i - \frac{2(EI_i + EI_{i+1})}{(\Delta x)^4} Y_{i+1} \\
& \quad + \frac{EI_{i+1}}{(\Delta x)^4} Y_{i+2} = m_i p^2 Y_i \\
& \dots \dots \dots \\
& \frac{EI_{n-1}}{(\Delta x)^4} Y_{n-2} - \frac{2EI_{n-1}}{(\Delta x)^4} Y_{n-1} + \frac{EI_{n-1}}{(\Delta x)^4} Y_n = m_n p^2 Y_n
\end{aligned} \tag{15}$$

It should be noted that the general expression

$$\begin{aligned}
& \frac{EI_{i-1}}{(\Delta x)^4} Y_{i-2} - \frac{2(EI_{i-1} + EI_i)}{(\Delta x)^4} Y_{i-1} \\
& \quad + \frac{(EI_{i-1} + 4EI_i + EI_{i+1})}{(\Delta x)^4} Y_i - \frac{2(EI_i + EI_{i+1})}{(\Delta x)^4} Y_{i+1} \\
& \quad + \frac{EI_{i+1}}{(\Delta x)^4} Y_{i+2} = m_i p^2 Y_i
\end{aligned}$$

will hold for all stations provided the quantities EI_0 , EI_1 , EI_n , and EI_{n+1} are made zero.

The equations in Eq. (15) involve n equations and $n+1$ unknowns. The algebraic equation for each station can be divided through by the mass per unit length, m , at that station and a set of equations of the following form will be obtained:

$$\begin{aligned}
 a_{11}Y_1 + a_{12}Y_2 + a_{13}Y_3 &= p^2Y_1 \\
 a_{21}Y_1 + a_{22}Y_2 + a_{23}Y_3 + a_{24}Y_4 &= p^2Y_2 \\
 a_{31}Y_1 + a_{32}Y_2 + a_{33}Y_3 + a_{34}Y_4 + a_{35}Y_5 &= p^2Y_3 \\
 a_{42}Y_2 + a_{43}Y_3 + a_{44}Y_4 + a_{45}Y_5 + a_{46}Y_6 &= p^2Y_4 \\
 \dots & \\
 a_{n-2}Y_{n-2} + a_{n-1}Y_{n-1} + a_{nn}Y_n &= p^2Y_n
 \end{aligned}$$

The equations in Eq. (15) can be written in matrix form as

$$\begin{pmatrix}
 a_{11} & a_{12} & a_{13} & 0 & 0 & 0 & 0 & \dots & 0 \\
 a_{21} & a_{22} & a_{23} & a_{24} & 0 & 0 & 0 & \dots & 0 \\
 a_{31} & a_{32} & a_{33} & a_{34} & a_{35} & 0 & 0 & \dots & 0 \\
 0 & a_{42} & a_{43} & a_{44} & a_{45} & a_{46} & 0 & \dots & 0 \\
 \dots & \dots \\
 0 & \dots & \dots & 0 & a_{n-2} & a_{n-1} & a_{nn} & \dots & 0
 \end{pmatrix}
 \begin{pmatrix}
 Y_1 \\
 Y_2 \\
 Y_3 \\
 Y_4 \\
 \dots \\
 Y_n
 \end{pmatrix}
 = p^2
 \begin{pmatrix}
 Y_1 \\
 Y_2 \\
 Y_3 \\
 Y_4 \\
 \dots \\
 Y_n
 \end{pmatrix}
 \quad (16)$$

or

$$\bar{A}\bar{Y} = p^2\bar{Y} \quad (17)$$

The problem becomes one of finding the eigenvalues p^2 and the corresponding eigenvectors \bar{Y} of the matrix \bar{A} .

An iterative method of determining the largest eigenvalue of \bar{A} can be used provided the eigenvalue is real and unrepeated [1]. However, as the lowest natural frequency is of primary concern, Eq. (17) can be premultiplied by \bar{A}^{-1} . Thus, $\bar{A}^{-1}\bar{A}\bar{Y} = p^2\bar{A}^{-1}\bar{Y}$. But, $\bar{A}^{-1}\bar{A} = \bar{I}$ where \bar{I} is an identity matrix,

$$\bar{I} = \begin{pmatrix}
 1 & 0 & 0 & \dots & 0 \\
 0 & 1 & 0 & \dots & 0 \\
 \dots & \dots & \dots & \dots & \dots \\
 0 & 0 & 0 & \dots & 1
 \end{pmatrix}$$

The equation may now be written as $\bar{A}^{-1}\bar{Y} = \beta\bar{Y}$ where $\beta = 1/p^2$. The problem is then one of determining the largest eigenvalue β of \bar{A}^{-1} . However, the inverse of the square matrix \bar{A} can only be computed provided the matrix \bar{A} is nonsingular, i.e., provided the determinant of \bar{A} is not zero [2].

A free-free bar is capable of pure rotation, translation, or a combination of the two with a zero natural frequency, and $p^2 = 0$.

Equation (17) can be rewritten as

$$(\bar{A} - p^2\bar{I})\bar{Y} = 0.$$

For nontrivial solutions of \bar{Y} ,

$$|(\bar{A} - p^2\bar{I})| = 0.$$

if $p^2 = 0$, then $|\bar{A}| = 0$; the matrix \bar{A} is singular and cannot be inverted. The singularity of \bar{A} may be verified by the tedious expansion of the determinant of \bar{A} . The rows of \bar{A} are linearly connected by two relationships making \bar{A} multiply degenerate.

Two more equations can be written that describe the linear relations between the displacements of points on the bar.

Consider the vibrating bar, shown in Fig. 1, divided into n segments Δx in length. As an approximation, the centers of mass of the elements will be considered to be at stations $r = 1, 2, 3, \dots, n$. Again d'Alembert's principle can be applied to the vibrating bar; and the inertial force $m_i\Delta x(d^2y_i/dt^2)$ can be considered to be acting on each element through its center of mass. This approximation becomes more accurate as the number of segments into which the bar is divided is increased. As the bar is not supported or constrained in any manner in the plane of vibration, only the following inertial forces act on the bar:

$$\sum_{i=1}^n m_i\Delta x \frac{d^2y_i}{dt^2}$$

The following equations can be written

$$\sum F_y = 0$$

and

$$\sum M_{r=1/2} = 0.$$

These equations can be written as

$$\sum F_y = \sum_{i=1}^n m_i \Delta x \frac{d^2 y_i}{dt^2} = 0 \quad (18)$$

and

$$\sum M_{r=1/2} = \sum_{i=1}^n m_i \Delta x \frac{d^2 y_i}{dt^2} x_i = 0 \quad (19)$$

where

$$x_i = \frac{(2i-1)}{2} \Delta x.$$

It should be noted here that the effects of rotary inertia of the elements have again been neglected in writing Eq. (19). The assumed solution $y_i = Y_i \sin(pt + \phi)$ can be substituted into Eqs. (18) and (19) and the following equations result:

$$-p^2 \sin(pt + \phi) \Delta x \sum_{i=1}^n m_i Y_i = 0$$

and

$$-p^2 \sin(pt + \phi) \frac{(\Delta x)^2}{2} \sum_{i=1}^n (2i-1) m_i Y_i = 0.$$

For the nontrivial solution of p , the above equations can be written as

$$\sum_{i=1}^n m_i Y_i = 0$$

and

$$\sum_{i=1}^n (2i-1) m_i Y_i = 0.$$

Thus

$$m_1 Y_1 + m_2 Y_2 + m_3 Y_3 + \dots + m_n Y_n = 0 \quad (20)$$

and

$$m_1 Y_1 + 3m_2 Y_2 + 5m_3 Y_3 + \dots + (2n-1) m_n Y_n = 0. \quad (21)$$

Equation (20) may also be obtained by adding the n expressions of Eq. (15).

By means of Eqs. (20) and (21) one can eliminate two degrees of freedom in such a manner that $p^2 = 0$ is no longer a root of the frequency equation. The linearly dependent equations in Eq. (15) may be made linearly

independent by substituting Eqs. (20) and (21) for two of the original equations, let us say the first two. Terms involving Y_1 and Y_2 may be eliminated from the new set of linearly independent algebraic equations and a new vector equation of the form

$$\begin{pmatrix} b_{11} & b_{12} & \dots & b_{1n-2} \\ b_{21} & b_{22} & \dots & b_{2n-2} \\ \dots & \dots & \dots & \dots \\ b_{n-21} & b_{n-22} & \dots & b_{n-2n-2} \end{pmatrix} \begin{pmatrix} Y_3 \\ Y_4 \\ \vdots \\ Y_n \end{pmatrix} = p^2 \begin{pmatrix} Y_3 \\ Y_4 \\ \vdots \\ Y_n \end{pmatrix}$$

can be written. This vector equation can be written as

$$\bar{B} \bar{Y}' = p^2 \bar{Y}'. \quad (22)$$

Note that the matrix \bar{B} is now the new matrix of order $(n-2)$ by $(n-2)$ and \bar{Y}' is a vector the components of which are Y_3, Y_4, \dots, Y_n .

The inverse of the square matrix \bar{B} can now be computed, and Eq. (22) premultiplied by \bar{B}^{-1} . The resulting equation is $\bar{B}^{-1} \bar{B} \bar{Y}' = p^2 \bar{B}^{-1} \bar{Y}'$ which yields

$$\bar{B}^{-1} \bar{Y}' = \beta \bar{Y}' \quad (23)$$

where $\beta = 1/p^2$. The matrix \bar{B}^{-1} will be denoted by

$$B^{-1} = \begin{pmatrix} b'_{11} & b'_{12} & \dots & b'_{1n-2} \\ b'_{21} & b'_{22} & \dots & b'_{2n-2} \\ \dots & \dots & \dots & \dots \\ b'_{n-21} & b'_{n-22} & \dots & b'_{n-2n-2} \end{pmatrix}$$

The dominant eigenvalue of the matrix \bar{B}^{-1} can be computed by choosing some initial arbitrary vector \bar{Y}'_1 , let us say

$$\bar{Y}'_1 = \begin{pmatrix} 0 \\ 0 \\ 0 \\ \vdots \\ 1 \end{pmatrix}$$

This vector is premultiplied by \bar{B}^{-1} and a scalar quantity β is extracted from the new vector \bar{Y}'_2 in such a way as to reduce the last component of \bar{Y}'_2 to unity. In this manner the following sequence can be computed:

$$\bar{B}^{-1} \bar{Y}'_1 = \beta_1 \bar{Y}'_2$$

$$\bar{B}^{-1} \bar{Y}'_2 = \beta_2 \bar{Y}'_3$$

$$\dots$$

$$\bar{B}^{-1} \bar{Y}'_{i-1} = \beta_{i-1} \bar{Y}'_i$$

If \bar{Y}'_i approaches a limit \bar{Y}' the sequence will approach a limit and

$$\bar{B}^{-1} \bar{Y}' = \beta_1 \bar{Y}'$$

The scalar β_i will also approach a limit β which in general is the dominant eigenvalue of the matrix \bar{B}^{-1} and \bar{Y}' is the corresponding eigenvector [3]. The first natural frequency can be obtained by using $p_1 = \sqrt{\lambda/\beta}$ rps or $f_1 = p_1/2\pi$ Hz. The corresponding mode shape is given by

$$\bar{Y}'_1 = \begin{pmatrix} Y_{1,1} \\ Y_{1,2} \\ Y_{1,3} \\ \vdots \\ Y_{1,n} \end{pmatrix} = \begin{pmatrix} Y_{1,1} \\ Y_{1,2} \\ Y_{1,3} \\ \vdots \\ Y_{1,n} \end{pmatrix}^*$$

The values of $Y_{1,1}$ and $Y_{1,2}$ can be obtained with the use of Eqs. (20) and (21). The quantity $Y_{j,1}$ can be eliminated between the two equations and an equation for $Y_{j,2}$ can be written as

$$Y_{j,2} = - \sum_{i=3}^n (i-1) \frac{m_i}{m_2} Y_{j,i} \quad (24)$$

After the value of $Y_{j,2}$ has been calculated, $Y_{j,1}$ can be obtained using

$$Y_{j,1} = - \sum_{i=2}^n \frac{m_i}{m_1} Y_{j,i} \quad (25)$$

*Note that hereafter the mode shape corresponding to the j th natural frequency will be denoted as

$$\bar{Y}'_j = \begin{pmatrix} Y_{j,1} \\ Y_{j,2} \\ Y_{j,3} \\ \vdots \\ Y_{j,n} \end{pmatrix} = \begin{pmatrix} Y_{j,1} \\ Y_{j,2} \\ Y_{j,3} \\ \vdots \\ Y_{j,n} \end{pmatrix}$$

DETERMINATION OF THE SECOND NORMAL MODE AND THE MODES NEXT IN LINE

As the iterative process previously described can only be used to obtain the dominant eigenvalue and corresponding eigenvector of the matrix \bar{B}^{-1} , a new method of calculating the eigenvalue and corresponding eigenvector next in line must be used.

A similarity transformation will be used to construct a matrix which is similar to the matrix \bar{B}^{-1} . From this similar matrix the second eigenvector can be obtained as well as the corresponding eigenvalue [4].

A similarity transformation can be used to obtain a reduced matrix \bar{C} from the original matrix \bar{B}^{-1} , both of which have identical eigenvalues.

The eigenvector \bar{Y}'_1 corresponding to the first eigenvalue β can be used to construct a square matrix of the form

$$\bar{P} = \begin{pmatrix} Y_{1,3} & 0 & 0 & \dots & 0 \\ Y_{1,4} & 1 & 0 & \dots & 0 \\ Y_{1,5} & 0 & 1 & 0 & \dots & 0 \\ \dots & \dots & \dots & \dots & \dots & \dots \\ Y_{1,n} & 0 & 0 & \dots & 0 & 1 \end{pmatrix}$$

and its inverse

$$\bar{P}^{-1} = \begin{pmatrix} \frac{1}{Y_{1,3}} & 0 & 0 & \dots & 0 \\ -\frac{Y_{1,4}}{Y_{1,3}} & 1 & 0 & \dots & 0 \\ -\frac{Y_{1,5}}{Y_{1,3}} & 0 & 1 & 0 & \dots & 0 \\ \dots & \dots & \dots & \dots & \dots & \dots \\ -\frac{Y_{1,n}}{Y_{1,3}} & 0 & 0 & \dots & 0 & 1 \end{pmatrix}$$

Let

$$\bar{Q} = \bar{P}^{-1} \bar{B}^{-1} \bar{P}$$

The matrix \bar{Q} is similar to \bar{B}^{-1} and has identical eigenvalues [5]. The following expression is obtained by performing the matrix multiplication $\bar{P}^{-1} \bar{B}^{-1} \bar{P}$:

$$\bar{P}^{-1} \bar{B}^{-1} \bar{P} =$$

$$\begin{pmatrix} \beta & \frac{b'_{1,2}}{Y_{1,3}} & \dots & \frac{b'_{1,n-2}}{Y_{1,3}} \\ 0 & b'_{2,2} - \frac{Y_{1,4}}{Y_{1,3}} b'_{1,2} & \dots & b'_{2,n-2} - \frac{Y_{1,4}}{Y_{1,3}} b'_{1,n-2} \\ \dots & \dots & \dots & \dots \\ 0 & b'_{n-2,2} - \frac{Y_{1,n}}{Y_{1,3}} b'_{1,2} & \dots & b'_{n-2,n-2} - \frac{Y_{1,n}}{Y_{1,3}} b'_{1,n-2} \end{pmatrix}$$

This expression may be written as

$$\bar{Q} = \begin{pmatrix} \beta & \frac{b'_{1,2}}{Y_{1,3}} & \dots & \frac{b'_{1,n-2}}{Y_{1,3}} \\ 0 & & & \\ \vdots & & \bar{C} & \\ 0 & & & \end{pmatrix}$$

Consider the equation

$$\bar{Q} \bar{Z} = \gamma \bar{Z} \quad (26)$$

where γ is the eigenvalue of \bar{Q} and \bar{Z} the corresponding eigenvector. The equation may be rewritten as $(\bar{Q} - \gamma \bar{I}) \bar{Z} = \bar{0}$.

For nontrivial solutions of \bar{Z} ,

$$|(\bar{Q} - \gamma \bar{I})| = 0$$

where

$$|(\bar{Q} - \gamma \bar{I})| = (\beta - \gamma) |(\bar{C} - \gamma \bar{I})| = 0.$$

Thus if $\beta \neq \gamma$, then $|(\bar{C} - \gamma \bar{I})| = 0$. One can now write the following expression:

$$\bar{C} \bar{Z}' = \gamma \bar{Z}' \quad (27)$$

where \bar{Z}' is a vector the components of which are Z_2, Z_3, \dots, Z_{n-2} .

$\bar{C} =$

$$\begin{pmatrix} b'_{2,2} - \frac{Y_{1,4}}{Y_{1,3}} b'_{1,2} & \dots & b'_{2,n-2} - \frac{Y_{1,4}}{Y_{1,3}} b'_{1,n-2} \\ \dots & \dots & \dots \\ b'_{n-2,2} - \frac{Y_{1,n}}{Y_{1,3}} b'_{1,2} & \dots & b'_{n-2,n-2} - \frac{Y_{1,n}}{Y_{1,3}} b'_{1,n-2} \end{pmatrix} \quad (28)$$

The iterative procedure for determining the dominant eigenvalue and the corresponding

eigenvector previously described can be performed on the matrix \bar{C} to yield the dominant eigenvalue γ and the corresponding eigenvector \bar{Z}' .

The value of Z_1 must now be computed. Equation (26) can be rewritten as

$$\begin{pmatrix} \beta Z_1 + \frac{b'_{1,2}}{Y_{1,3}} Z_2 + \frac{b'_{1,3}}{Y_{1,3}} Z_3 + \dots + \frac{b'_{1,n-2}}{Y_{1,3}} Z_{n-2} \\ \dots \\ \dots \end{pmatrix} = \gamma \begin{pmatrix} Z_1 \\ \bar{Z}' \end{pmatrix} \quad (29)$$

From this equation, one can write

$$\beta Z_1 + \frac{b'_{1,2}}{Y_{1,3}} Z_2 + \frac{b'_{1,3}}{Y_{1,3}} Z_3 + \dots + \frac{b'_{1,n-2}}{Y_{1,3}} Z_{n-2} = \gamma Z_1$$

Therefore

$$Z_1 = \frac{b'_{1,2} Z_2 + b'_{1,3} Z_3 + \dots + b'_{1,n-2} Z_{n-2}}{(\gamma - \beta) Y_{1,3}} \quad (30)$$

and

$$\bar{Z} = \begin{pmatrix} Z_1 \\ Z_2 \\ Z_3 \\ \vdots \\ Z_{n-2} \end{pmatrix}$$

The eigenvalue γ and the corresponding eigenvector \bar{Z} of the matrix \bar{Q} have been obtained. Determination of the eigenvector of the similar matrix \bar{B}^{-1} is now required.

Consider the equation

$$\bar{B}^{-1} \bar{Y}'_2 = \gamma \bar{Y}'_2 \quad (31)$$

and Eq. (26), which can be written as

$$\bar{P}^{-1} \bar{B}^{-1} \bar{P} \bar{Z} = \gamma \bar{Z} \quad (32)$$

Premultiplying Eq. (32) by \bar{P} , one obtains

$$\bar{P} \bar{P}^{-1} \bar{B}^{-1} \bar{P} \bar{Z} = \gamma \bar{P} \bar{Z}$$

which is

$$\bar{B}^{-1} \bar{F} \bar{Z} = \gamma \bar{F} \bar{Z} \quad (33)$$

Therefore

$$\bar{V}_2' = \bar{F} \bar{Z} \quad (34)$$

or

$$\begin{pmatrix} Y_{2,3} \\ Y_{2,4} \\ Y_{2,5} \\ \vdots \\ Y_{2,n} \end{pmatrix} = \begin{pmatrix} Y_{1,3} Z_1 \\ Y_{1,4} Z_1 + Z_2 \\ Y_{1,5} Z_1 + Z_3 \\ \dots \\ Y_{1,n} Z_1 + Z_{n-2} \end{pmatrix} \quad (35)$$

The second natural frequency can be obtained by using $p_2 = \sqrt{I/\gamma}$ rps or $f_2 = p_2/2\pi$ Hz.

The values of $Y_{2,3}$ and $Y_{2,1}$ may be obtained by using Eqs. (24) and (25), respectively. The mode shape then becomes

$$\bar{V}_2 = \begin{pmatrix} Y_{2,1} \\ Y_{2,2} \\ \bar{V}_2' \\ Y_{2,n} \end{pmatrix} = \begin{pmatrix} Y_{2,1} \\ Y_{2,2} \\ Y_{2,3} \\ \vdots \\ Y_{2,n} \end{pmatrix}$$

The procedure previously described can again be used to obtain a third reduced matrix from which the third natural frequency and corresponding mode shape can be obtained. Again, a fourth reduced matrix can be obtained. The error in calculated frequencies and mode shapes becomes greater the further the original matrix is reduced. The amount of error can be reduced by originally using a greater number of stations.

THE COMPUTER PROGRAM

The program, listed in the Appendix, is written in FORTRAN II for the CDC-3600 Digital Computer for calculating the first and second natural frequencies and the corresponding mode shapes of uniform and nonuniform bars with free end conditions. The program utilizes the methods described previously and is capable of handling a bar divided into as many as one hundred stations.

The input data required by the program are as follows:

1. The number of stations n into which the bar is divided.
2. The length of the bar L in inches.
3. The rigidity of the bar EI at each station, in $\text{lb}_f \text{in.}^2$
4. The mass per unit length of the bar m at each station, in $\text{lb}_f \text{sec}^2 \text{per in.}^2$

As shown in Fig. 1, the first station, $r = 1$, must be $(\Delta x)/2$ from the end of the bar, the second station $r = 2$, at $3/2 \Delta x$, etc. Thus the n th station, $r = n$, must be located at $[(2n-1)/2]\Delta x$ from the end of the bar.

The output of the program is:

1. The data, L , n , and EI at each station, and m at each station.
2. The first and second natural circular frequencies, p_1 and p_2 , in radians per second.
3. The first and second natural frequencies, f_1 and f_2 , in Hertz.
4. The mode shapes corresponding to the first and second natural frequencies.
5. The number of iterations required for the recursion process previously described to converge to the dominant eigenvalues, β and γ .

The program is written so that the computer using the given data can form an $(n-2)$ by $(n-2)$ array which is matrix \bar{B} . This array is formed with the use of Eqs. (15), (20), and (21).

The matrix \bar{B} is inverted by using a cooperative subroutine subprogram that is listed after the main program.

The dominant eigenvalue β of \bar{B}^{-1} and the corresponding eigenvector \bar{V}_1' are determined by the iterative process previously described. An initial vector is assumed that has the numerical value of all its components, except the last, equal to zero. The last component of the assumed initial vector is unity.

During the iterative procedure, the scalar quantity β is extracted from the vector \bar{V}_1' in such a manner as to reduce the last component of \bar{V}_1' to unity. It should be noted here that the mode shape \bar{V}_1 always has the last component equal to unity. The test for convergence of the iterative process is made on the eigenvalue β .

The numerical values of $Y_{1,2}$ and $Y_{1,1}$ are then computed with the use of Eqs. (24) and (25), respectively.

The reduced $(n-3)$ by $(n-3)$ matrix \bar{C} is formed with the use of the following expression developed from Eq. (28):

$$C_{ij} = b'_{i+1,j+1} - \frac{Y_{1,i+3}}{Y_{1,3}} b'_{i,j+1} \quad (36)$$

where

$$i = 1, 2, 3, \dots, n-3$$

$$j = 1, 2, 3, \dots, n-3$$

Again the iterative procedure previously described is used to determine the dominant eigenvalue γ of the matrix \bar{C} , the value of p_2 , and the corresponding eigenvector \bar{Z}' . The numerical value of Z_1 is then calculated with the use of Eq. (30). A linear transformation, Eq. (35), is then made on \bar{Z} to determine \bar{Y}'_2 . Values of $Y_{2,2}$ and $Y_{2,1}$ are again calculated with the use of Eqs. (24) and (25), respectively. The mode shape \bar{Y}_2 , corresponding to the second natural frequency, is formed in such a manner that the last component is unity.

It should be noted that comment cards have been liberally distributed throughout the program for definition of nomenclature and to facilitate understanding of the procedures used.

The input data deck takes the following form:

1. The first card of the deck has the number of stations punched in the first three columns. The number of stations is an integer number and the input format is I3.
2. The second card has the bar length punched in the first nine columns. The input format is F9.4.
3. The next group of cards contains EI data. Data for up to five stations can be punched in the first 60 columns of a card. The input format is E12.5. Data for up to 100 stations can be read into the computer. Note that values of EI for the first and last stations must be read as zero, 0.00000E 00.
4. The last group of cards in the data deck contains mass distribution data. Again, data for up to five stations can be punched in the first 60 columns of a card. The input format is E12.5. Data for up to 100 stations can be read into the computer.

MODAL STUDY OF SINGLE-STAGE TOMAHAWK HIGH ALTITUDE RESEARCH VEHICLE

The previously outlined procedure and computer program were used to predict the first two bending modes of a single-stage Tomahawk High Altitude Research Vehicle. The EI and mass distribution curves for this vehicle are shown in Figs. 2 and 3, respectively.

An experimental modal study was also performed on the vehicle. The test vehicle was supported in a free-free configuration using a low frequency suspension system of 3/4-in. shock cord. The effect of the supports and their location on the free end conditions of the test vehicle was of some concern at the start of the study. It was later determined, by changing the locations of the supports several times, that the support locations had no perceptible effects on the test results. Ten accelerometers were placed along the length and on the outside surface of the test vehicle to define the mode shapes. A small exciter weighing less than 2 lb, with a force output of approximately 1 lb, was rigidly attached to one end of the test vehicle. The exciter served as a zero impedance source that did not effect the dynamic characteristics of the test vehicle. Bending modes were easily identified because the small shaker supplied only enough energy to excite the normal bending modes. Inherent mechanical filtering of the system yielded clean acceleration signals 90 degrees out of phase with the input force. The resulting predicted and experimentally determined first and second bending modes for the test vehicle are shown in Figs. 4 and 5. Damping factors, $\zeta = (C/C_{cr})$, were determined for the first and second modes, using the method of logarithmic decrement [6]. Values of ζ for the first and second modes were determined to be 9.6×10^{-4} and 19.1×10^{-4} , respectively. The errors in the predicted frequencies for the first and second modes, as compared with the experimentally obtained values, were 8.9 percent and 12.9 percent for the first and second modes, respectively.

CONCLUSIONS

Errors in the predicted modes depend on the following parameters:

1. The shape of the EI curve.
2. The shape of the mass distribution curve.
3. The number of stations into which the bar is divided.

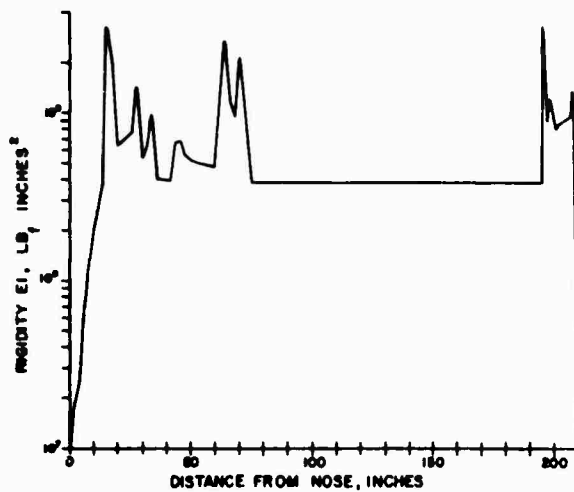


Fig. 2. EI distribution for high altitude research vehicle

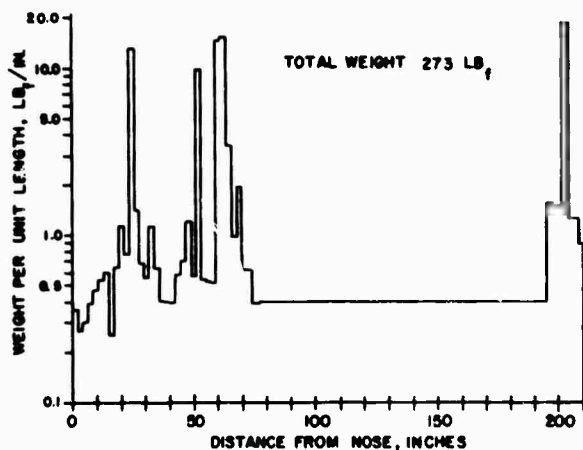
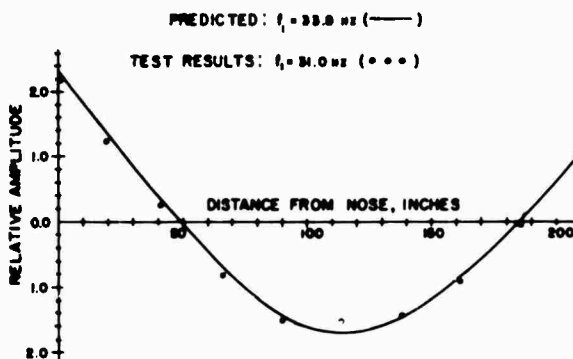


Fig. 3. Weight distribution for high altitude research vehicle

Fig. 4. First bending mode for high altitude research vehicle



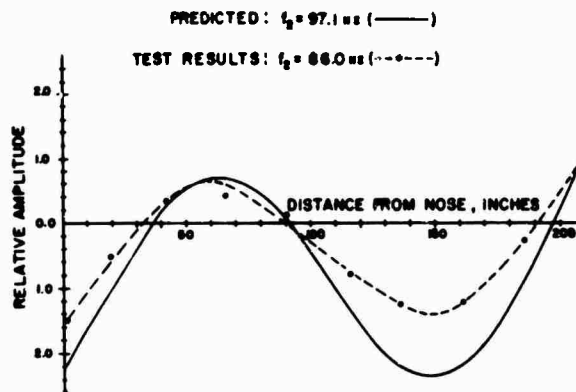


Fig. 5. Second bending mode for high altitude research vehicle

4. The mode in question.
5. The effect of material damping.

The number of stations or sections which should be used is dependent on the EI curve, the mass distribution curve, and the mode in question. EI and mass distribution curves with severe fluctuations require a large number of stations to reduce the calculated error. Higher modes require a larger number of stations than lower modes. This can be verified

by calculating the bending modes of a uniform bar using several values of n .

The theoretical methods and computer program outlined in this paper can provide good engineering estimates of at least the first two bending modes for small, relatively "uncomplicated" missile systems or free-flight bodies where the lateral dimensions are small compared with the length (a ratio of 1:10 can be used as a "rule of thumb").

REFERENCES

1. R. G. Stanton, Numerical Methods for Science and Engineering (Prentice-Hall, New Jersey), 1961, p. 181
2. V. N. Faddeeva, Computational Methods of Linear Algebra (Dover Publications, New York), 1959, p. 11
3. Stanton, op. cit., p. 181
4. Faddeeva, op. cit., p. 230
5. Ibid., p. 17
6. C. M. Harris and C. E. Crede, Shock and Vibration Handbook (McGraw-Hill, New York), 1961, p. 2-5

Appendix
PROGRAM LISTING

PROGRAM BARVIBF

```
C A PROGRAM FOR DETERMINING THE FIRST AND SECOND NATURAL FREQUENCIES
C AND THE CORRESPONDING MODE SHAPES FOR THE LATERAL VIBRATIONS
C OF A NON UNIFORM FREE-FREE BAR
```

```
C DEFINITION OF NOMENCLATURE
```

```
C R(I,J) MATRIX B
C BETA DOMINANT EIGENVALUE OF MATRIX B INVERSE
C RL LENGTH OF BAR (IN.)
C RM(I) MASS PER UNIT LENGTH OF THE BAR AT STATION I
C (LBF SECXSEC/IN.XIN.)
C C(I,J) MATRIX C
C EI(I) RIGIDITY OF THE BAR AT STATION I (LBF IN.XIN.)
C F(1) FIRST NATURAL FREQUENCY (CYC/SEC)
C F(2) SECOND NATURAL FREQUENCY (CYC/SEC)
C GAMMA DOMINANT EIGENVALUE OF MATRIX C
C H DELTA X, DISTANCE BETWEEN STATIONS (IN.)
C ITER NUMBER OF ITERATIONS REQUIRED TO CONVERGE TO THE
C DOMINANT EIGENVALUES
C N NUMBER OF STATIONS
C P(1) FIRST NATURAL CIRCULAR FREQUENCY (RAD/SEC)
C P(2) SECOND NATURAL CIRCULAR FREQUENCY (RAD/SEC)
C X(I) DISTANCE FROM LEFT END OF BAR TO STATION I (IN.)
C Y(I,J) EIGENVECTOR OF MATRIX B, OR MODE SHAPE
C Z(I,J) EIGENVECTOR OF MATRIX C
```

```
C REMARKS
```

```
C N MUST NOT EXCEED 100
```

```
C EI(1) AND EI(N) ARE READ INTO THE PROGRAM AS ZERO
C STATEMENT 29 AND PRECEEDING STATEMENT ARE FOR 43 DATA ONLY
```

```
C START OF PROGRAM
```

```
DIMENSION FI(101), RM(100), R(100, 100), Y(2, 100), A(100), IROW(1
101), ICOL(100), P(2), X(100), Z(2, 99), C(97, 97), F(2), ITS(100,2)
```

```
999 READ INPUT TAPE 5, 5, N
5 FORMAT(I3)
```

```
C CLEAR ARRAYS
```

```
FI(N+1) = 0.0
DO 10 I = 1, N
RM(I) = 0.0
FI(I) = 0.0
Y(1,I) = 0.0
Y(2,I) = 0.0
Z(1,I) = 0.0
Z(2, I) = 0.0
A(I) = 0.0
DO 10 J = 1, N
10 R(I, J) = 0.00
```

```
C ENTER DATA
```

```
READ INPUT TAPE 5, 20, RL, (FI(I), I = 1, N)
```

```

20 FORMAT (F9.4 / (5E12.5))
   READ INPUT TAPE 5, 25, (RM(I), I = 1, N)
25 FORMAT (5E12.5)
C CALCULATE DELTA X

   RN = N
   H = RL/DN

C LOAD THE ARRAY R(I,J)

   DO 30 I = 1, N
   R(1, I) = RM(I) / RM(1)
   AI = I
   H4 = H*H*H*H
30 R(2, I) = (AI - 1.) * RM(I) / RM(1)
   DO 40 I = 3, N
   R(1, I-2) = FI(I-1) / (H4 * RM(1))
   R(1, I-1) = -2. * (FI(I-1) + FI(I)) / (H4 * RM(1))
40 R(1, I) = (FI(I-1) + 4. * FI(I) + EI(I+1)) / (H4 * RM(1))
   M = N - 1
   DO 50 I = 3, M
50 R(1, I+1) = -2. * (FI(I) + EI(I+1)) / (H4 * RM(1))
   L = N - 2
   DO 60 I = 3, L
60 R(1, I+2) = FI(I+1) / (H4 * RM(1))

C ELIMINATE TERMS INVOLVING Y(1,1)

   DO 70 I = 2, N
   R(1, I) = B(1, I) + B(3, 1)
70 R(3, I) = H(3, I) - B(1, I)

C ELIMINATE TERMS INVOLVING Y(1,2)

   DO 80 I = 3, N
   A(I) = B(2, I) + R(3, 2)
   R(3, I) = H(3, I) - A(I)
   R(2, I) = B(2, I) + B(4, 2)
80 R(4, I) = B(4, I) - R(2, I)

C UPPER LEFT JUSTIFY THE REDUCED MATRIX R FOR INVERSION SUBROUTINE

   DO 90 I = 3, N
   DO 90 J = 3, N
90 R(I-2, J-2) = B(I, J)

C INVERT THE MATRIX B USING THE SUBROUTINE MATINV

   CALL MATINV ( R, L, 100, ARRA, 0, ICCL, IROW, ITS, DETERM)

C DETERMINE THE DOMINANT EIGENVALUE BETA OF THE MATRIX B AND THE
C CORRESPONDING EIGENVECTOR Y(1,J) AND CALCULATE P(1)

180 STORF = 0.0
   ITER = 0

C ASSUME AN ARBITRARY INITIAL VECTOR, Y(1,I) WHOSE LAST COMPONENT IS
C UNITY

   Y(1, N) = 1.0
190 DO 200 I = 1, L
   DO 200 J = 1, L
200 Y(2, I+2) = Y(2, I+2) + R(I, J) * Y(1, J+2)
   ITER = ITER + 1

C EXTRACT A SCALAR QUANTITY, BETA, AS TO REDUCE THE LAST COMPONENT OF

```

```

C   Y(1, I) TO UNITY
-----
      BETA = Y(2,N)
      DO 210 I = 3, N
      Y(1,I) = Y(2,I) / Y(2,N)
210  Y(2,I) = 0.0
-----
C   TEST BETA FOR CONVERGENCE
-----
      TEST = ABSF ( BETA - STORE )
      STORE = BETA
      IF ( TEST - 1.0E-13 ) 215, 190, 190
-----
C THE FIRST NATURAL CIRCULAR FREQUENCY P(1) IS THE SQUARE ROOT OF
C   1 / BETA (RAD / SEC)
-----
215  P(1) = SORTF( ABSF( 1.0 / BETA ) )
-----
C CALCULATE THE VALUES OF Y(1,2) AND Y(1,1)
-----
220  DO 230 I = 3, N
      AI = I
230  Y(1,2) = Y(1,2) + (AI - 1.) * (BM(I) / BM(2)) * Y(1,1)
      DO 240 I = 2, N
240  Y(1,1) = Y(1,1) + (BM(I) / BM(1)) * Y(1,1)
-----
C CALCULATE VALUES OF X FOR EACH STATION
-----
      X(1) = H/2.
      DO 250 I = 2, N
      BI = I
250  X(I) = X(1) + (BI - 1.) * H
-----
CALCULATE THE VALUE OF THE FIRST NATURAL FREQUENCY F(1) (CYC/SEC)
-----
      F(1) = P(1) / (2. * 3.14159)
-----
C WRITE OUT DATA
-----
      WRITE OUTPUT TAPE 6, 300, BL, N, (I, EI(I), I, BM(I), I = 1, N)
300  FORMAT (1M1, 57X, 5H DATA /19X, 17H BAR LENGTH, BL = , F10.4, 24X,
1 24H NUMBER OF STATIONS, N = , 13 // 18X, 30H RIGIDITY, EI, AT E
1ACH STATION, 21X, 42H MASS PER UNIT LENGTH, BM, AT EACH STATION / (
325X, 3H EI, 12, 2H =, E12.5, 10H LBF INXIN, 23X, 3H BM, 12, 2H =,
4E12.5, 18H LBF SECXSEC/INXIN)
-----
C WRITE OUT ANSWERS
-----
      WRITE OUTPUT TAPE 6, 310, P(1), F(1), (I, X(I), I, Y(1, I), I = 1, N)
310  FORMAT (/ 55X, 8H ANSWERS // 49X, 22H FUNDAMENTAL FREQUENCY
1// 36X, 4H P1 =, F10.4, 8H RAD/SEC, 3X, 4H F1 =, F10.4, 8H CYC/SEC
2// 54X, 11H MODE SHAPE /142X, 2H X, 12, 2H =, F10.5, 3H IN, 4X,
3 2H Y, 12, 2H =, F10.5))
      WRITE OUTPUT TAPE 6, 320, ITER
320  FORMAT (/ 41X, 27H THE NUMBER OF ITERATIONS =, 16)
-----
C IF ONLY THE FIRST NATURAL FREQUENCY IS REQUIRED THE FOLLOWING MAY
C   BE OMITTED AND THE COMPUTER SENT BACK TO STATEMENT 999
-----
C LOAD THE MATRIX C
-----
400  KL = N-3
      DO 700 I = 1, KL
      DO 700 J = 1, KL
      C(I, J) = B(I+1, J+1) + (Y(1, I+3) / Y(1, 3)) * B(1, J+1)
700  CONTINUE

```

```

C DETERMINE THE DOMINANT EIGENVALUE GAMMA OF THE MATRIX C AND THE
C   CORRESPONDING EIGENVECTOR Z(1,J) AND CALCULATE P(2)

      STORE = 0.0
      ITER = 0

C ASSUME AN ARBITRARY INITIAL VECTOR, Z(1,1), WHOSE LAST COMPONENT IS
C   UNITY

      Z(1, N-2) = 1.0
720 CONTINUE
      DO 760 I = 1, KL
      DO 740 J = 1, KL
      Z(2, I+1) = Z(2, I+1) + C(I,J) * Z(1, J+1)
760 CONTINUE
      ITER = ITER + 1

C EXTRACT A SCALAR QUANTITY, GAMMA, AS TO REDUCE THE LAST COMPONENT OF
C   Z(1, 1) TO UNITY

      GAMMA = Z(2, N-2)
      DO 780 I = 2, L
      Z(1,I) = Z(2,I) / Z(2,N-2)
780 Z(2, I) = 0.0

C TEST GAMMA FOR CONVERGENCE

      TEST = ABSF ( GAMMA - STORE )
      STORE = GAMMA
      IF ( TEST - 1.0E-13 ) 790, 720,720

C THE SECOND NATURAL CIRCULAR FREQUENCY P(2) IS THE SQUARE ROOT
C   OF 1/GAMMA (RAD/SEC)

790 P(2) = SQRTF( ABSF( 1.0 / GAMMA ))

CALCULATE THE VALUE OF Z(1, 1)

      R00 SUM = 0.0
      DO 820 I = 2, L
      R20 SUM = SUM + R(1,I) * Z(1,I) / Y(1,3)
      Z(1,1) = SUM / (GAMMA * BETA)

CALCULATE THE VALUES OF Y(2,1)

      DO 825 I = 1, N
      R25 Y(2,1) = 0.0
      Y(2,3) = Y(1,3) * Z(1,1)
      DO 830 I = 4, N
      R30 Y(2,1) = Y(1,1) * Z(1,1) + Z(1,I-2)
      DO 845 I = 3, N
      R35 Y(2,1) = Y(2,1) / Y(2,N)
      DO 840 I = 3, N
      A1 = 1
      R40 Y(2,2) = Y(2,2) - (A1 - 1) * (BM(I) / BM(2)) * Y(2,1)
      DO 860 I = 2, N
      R60 Y(2,1) = Y(2,1) - (RM(I) / BM(1)) * Y(2,1)

CALCULATE THE VALUE OF THE SECOND NATURAL FREQUENCY F(2) (CYC/SEC)

      F(2) = P(2) / (2.0 * 3.14159)

C WRITE OUT ANSWERS

      WRITE OUTPUT TAPE 6, 880, P(2), F(2), (I, X(I), I, Y(2,1)), I=1, N)

```

```

880 FORMAT ( / 49X, 25H SECOND NATURAL FREQUENCY
1// 36X, 4H P20, F10,4, 8H RAD/SEC, 3Y, 4H F20,F10,4, 8H CYC/SEC
2// 54X, 11H MODE SHAPE /(42X, 2H X,12, 2H =,F10,5, 3H IN, 4X,
3 2H Y,12, 2H =, F10,5))
WRITE OUTPUT TAPE 6, 900, ITER
900 FORMAT ( / 41), 27H THE NUMBER OF ITERATIONS = , 16)

```

```

C GO BACK TO START OF PROGRAM.

```

```

GO TO 999

```

```

END

```

```

SUBROUTINE MATINV( A, N, NMAX, B, M, PIVOT, IPIVOT, INDEX, DETERM)

```

```

C MATRIX INVERSION WITH ACCOMPANYING SOLUTION OF LINEAR EQUATIONS

```

```

DIMENSION IPIVOT(N), A(NMAX,NMAX), B(NMAX,1), INDEX(N,2), PIVOT(N)

```

```

C INITIALIZATION

```

```

10 DETERM = 1.0
15 DO 20 J = 1, N
20 IPIVOT(J) = 0
30 DO 50 I = 1, N

```

```

C SEARCH FOR PIVOT ELEMENT

```

```

40 AMAX = 0.0
45 DO 105 J = 1, N
50 IF ( IPIVOT(J) = 1) 60, 105, 60
60 DO 100 K = 1, N
70 IF (IPIVOT(K) = 1) 80, 100, 70
80 IF (ABS(A(J,K)) = ABS(A(J,K))) 85, 100, 100
85 IROW = J
90 ICOLUM = K
95 AMAX = A(J,K)
100 CONTINUE
105 CONTINUE
110 IPIVOT(ICOLUM) = IPIVOT(ICOLUM) + 1

```

```

C INTERCHANGE ROWS TO PUT PIVOT ELEMENT ON DIAGONAL

```

```

130 IF (IROW = ICOLUM) 140, 260, 140
140 DETERM = -DETERM
150 DO 200 L = 1, N
160 SWAP = A(IROW,L)
170 A(IROW, L) = A(ICOLUM, L)
200 A(ICOLUM, L) = SWAP
205 IF(M) 260, 260, 210
210 DO 250 L = 1, M
220 SWAP = B(IROW, L)
230 B(IROW, L) = B(ICOLUM, L)
250 B(ICOLUM, L) = SWAP
260 INDEX(I, 1) = IROW
270 INDEX(I, 2) = ICOLUM
310 PIVOT(I) = A(ICOLUM, ICOLUM)
320 DETERM = DETERM * PIVOT(I)

```

```

C DIVIDE PIVOT ROW BY PIVOT ELEMENT

```

```

330 A(ICOLUM, ICOLUM) = 1.0
340 DO 350 L = 1, N
350 A(ICOLUM, L) = A(ICOLUM, L) / PIVOT(I)
355 IF (M) 380, 380, 360
360 DO 370 L = 1, M
370 B(ICOLUM, L) = B(ICOLUM, L) / PIVOT(I)

```

C REDUCE NON-PIVOT ROWS

```

380 DO 550 L1 = 1, N
390 IF (L1 = ICOLUM) 400, 550, 400
400 T = A(L1, ICOLUM)
420 A(L1, ICOLUM) = 0,0
430 DO 450 L = 1, N
450 A(L1, L) = A(L1, L) - A(ICOLUM, L) * T
455 IF (M) 550, 550, 460
460 DO 500 L = 1, M
500 R(L1, L) = B(L1, L) - B(ICOLUM, L) * T
550 CONTINUE

```

C INTERCHANGE COLUMNS

```

600 DO 710 I = 1, N
610 L = N + 1 - I
620 IF (INDEX(L,1) = INDEX(L,2)) 630, 710, 630
630 JROW = INDEX(L,1)
640 JCOLUM = INDEX(L,2)
650 DO 705 R = 1, N
660 SWAP = A(K, JROW)
670 A(K, JROW) = A(K, JCOLUM)
700 A(K, JCOLUM) = SWAP
705 CONTINUE
710 CONTINUE
740 RETURN
750 END

```

DISCUSSION

D. Egle (Univ. of Okla.): There is one point on which I would like to disagree. I do not think it affects anything you did, it is just a statement. You said that if you worked this system of equations straightforwardly to get the eigenvalue, the highest eigenvalue would be infinite. That is not so because you have a finite matrix and the largest eigenvalue will be finite. In theory, anyway, you could start from the highest and work down.

Mr. Witte: That is right. We use a finite difference approximation and hence the largest eigenvalue has no meaning at all. We want to get down to the lowest eigenvalue where the accuracy is.

H. Saunders (G. E. Co.): Your explanation of the finite difference was good. But I think one of the better ways of doing it, if you take a

finite element approach, is to take sections and average them. You would probably get much better results for the frequency and mode shapes. Also, you have neglected a rotary inertia and shear deformation. At the higher frequencies that becomes important. Have you given any consideration to using the rotary inertia and shear deformation in your analysis?

Mr. Witte: Yes. It is a very complicated problem; that's why we stick to something simple. But I did do some work in averaging out. The frequencies came fairly close but the mode shapes did not. I found that there was considerable difference in averaging all these and obtaining the mode shape.

Mr. Saunders: Yes, that is using finite differences. If you try to use a finite element I believe the mode shapes would come out much better

* * *

SATURN V COMPONENT VIBRATION TESTS USING SEGMENTED SHELL SPECIMENS

Chintsun Hwang
Northrop Corporation, Norair Division
Hawthorne, California

and

Charles E. Lifer
NASA, Marshall Space Flight Center
Huntsville, Alabama

This paper describes an analytical and experimental program to develop and verify techniques for designing segmented shell specimens to be used in component vibration tests. The purpose of the program was to develop segmented shell test specimens of reasonable size that retain, as much as feasible, the dynamic characteristics of the complete shell structure. The analytical phase consisted of the development of a general shell analysis program in which the impedances of the ring stiffeners were considered. A finite difference computer program was applied to the modal analysis of the segmented shell specimen. The experimental phase included the evaluation of localized flexible supports, the development of Saturn V structure dynamic scale models, vibration tests of the complete and segmented shell models, and the vibration test of a full-scale segmented Saturn V shell specimen with mounted components.

INTRODUCTION

The shell structure in the various stages of the Saturn V system are large, massive, and intricate. To conduct vibration tests of the components that are mounted on the shell structure, correspondingly large and expensive facilities are needed. The conventional approach to the development and qualification vibration testing of equipment and subsystems, in which the item is attached to a rigid fixture and tied as directly as possible to an exciter, in most cases results in a poor reproduction of service loads and stresses. This is especially true for shell-structure mounted components (electronics packages) in which the impedance characteristics are not too greatly different from those of the mounting shell structure. A study was conducted by the Marshall Space Flight Center and Northrop Norair to develop techniques for designing relatively simple test fixtures which closely reproduce the significant response characteristics of the shell structure in the vibration test of components. The techniques could be used by a dynamicist to derive

(from component and structural design information) the appropriate dimensions and boundary restraints for a local section of shell structure, to which the component was attached during the test. By simple variation in fixity and attached masses, the same fixture could be used for tests of several items.

Vibration tests on equipment or systems mounted on shell structure segments are generally of two types, based on the method of excitation. In one case, the exciter is connected to a fixture which attaches to the boundaries of the shell segment, and test levels are controlled at the boundary or at some selected point on the specimen. In the other case, the exciter is connected to a selected point, or points, on the specimen, and the boundaries of the specimen are restrained by a passive fixture; test levels are controlled at the exciter attachment point or at some selected point on the specimen. Test level control may be through acceleration, displacement, or force measurement.

The techniques described in this paper are applicable to both of the above cases, assuming

that the exciter capabilities and specimen strength capabilities are not limiting factors. When very high test levels or unusually massive test specimens are involved, these limitations must be considered in the selection of the test approach.

The test design procedure involved a number of steps, starting with the analytical and experimental modal analysis of the complete and uncut shell structure. The analysis was followed by shell segmentation and edge condition evaluation. A parallel program evaluated the dynamic characteristics of the flexible supports to be applied to the segmented shell. After the test configuration was determined, a finite difference computer program was used to predict the modal data of the flexibly supported and segmented shell structure. The successful vibration test of a full scale Saturn V shell specimen concluded the procedure. In the following paragraphs, the important features of the test technique are described.

SHELL STRUCTURE ANALYSIS PROGRAMS

Two analytical programs were developed to predict and evaluate the shell dynamic behavior. For a complete shell of revolution, eight simultaneous linear differential equations are used in the standard manner [1]. Corresponding to a specific harmonic number, n , the dependent variables are the four displacement components (w_n, u_n, v_n, β_n) and the four stress components ($Q_n, N_{\phi n}, N_n, M_{\phi n}$). The stress components represent the transverse shear, the meridian membrane stress, the modified in-plane shear stress, and the bending along the meridian direction, respectively. The equations are integrated numerically in a segment-wise manner to minimize the accumulated errors. To accommodate the dynamic impedances of the ring stiffeners, the shell meridian is divided into segments in such a manner that all the stiffeners are located at the terminals of the segments. During the numerical integration process, the

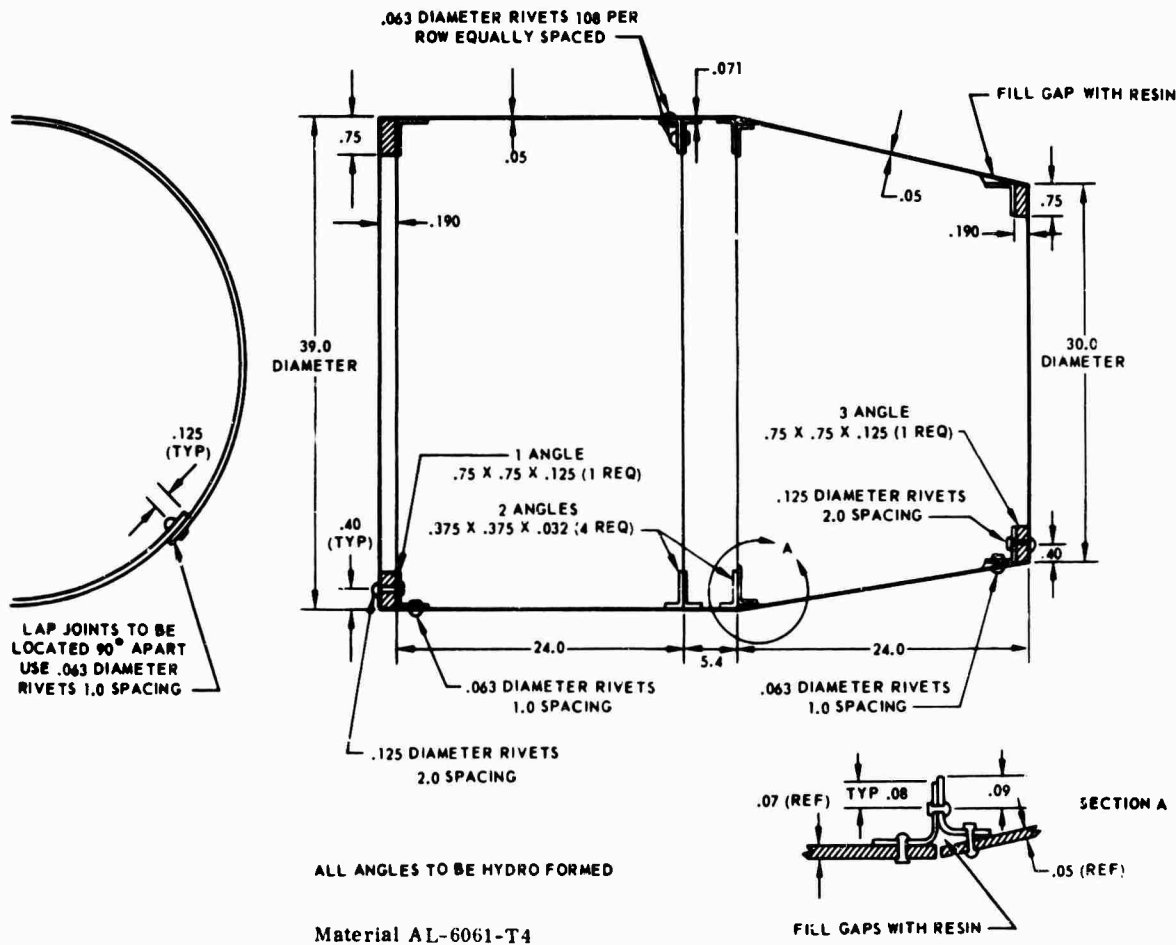


Fig. 1. Saturn V instrument unit scale model design drawing

four stress variables are modified, as shown below, when a ring stiffener is encountered.

$$\begin{Bmatrix} \Delta Q_n \\ \Delta N_{\phi n} \\ \Delta N_n \\ \Delta M_{\phi n} \end{Bmatrix} = \begin{bmatrix} Z_{11}(\omega) & Z_{12}(\omega) & Z_{13}(\omega) & Z_{14}(\omega) \\ & Z_{22}(\omega) & Z_{23}(\omega) & Z_{24}(\omega) \\ & & Z_{33}(\omega) & Z_{34}(\omega) \\ \text{(symmetric)} & & & Z_{44}(\omega) \end{bmatrix}$$

$$\times \begin{Bmatrix} w_n \\ u_n \\ v_n \\ \beta_n \end{Bmatrix}$$

where the left side column matrix indicates the increments in shell stresses owing to ring impedance components $Z_{11}(\omega)$, $Z_{12}(\omega)$, etc., corresponding to a circumferential harmonic number, n . The above formulation is mechanized in a computer program which has yielded consistently satisfactory modal information. Typical analytical data derived from a one-tenth scale Saturn V instrument unit shell structure (Fig. 1) are plotted in Fig. 2, together with the sinusoidal vibration test data.

For segmented shells with flexible point supports and attached masses, a finite difference

computer program was developed to generate the modal data. In this program, the segmented shell middle surface is divided into a grid pattern. A matrix equation is established, based on the shell dynamic equation and the boundary conditions of the shell specimen, considering the impedances of eccentrically located stringers and stiffeners. The matrix equation is reduced to an eigenvalue formulation in which the displacements at the grid points form the components of the eigenvector. The basic matrix formulation for this program is shown in Fig. 3. For a typical segmented shell (Fig. 4), the modal displacement data obtained by this program are plotted in Fig. 5.

The experimental program was divided into three major tasks: Modal and impedance surveys of shell structures, fixture parameter selection and evaluation, and segmented shell design and tests. The first two tasks were exploratory and preparatory in nature; the knowledge gained in the process was used in the final segmented shell design. The remainder of this paper describes the highlights of the experimental program.

MODAL AND IMPEDANCE SURVEYS OF SHELL STRUCTURES

To obtain Saturn V shell modal and impedance data and to check the validity of the analytical results, a number of one-tenth scale models were designed and fabricated. The shell structures chosen were those in which

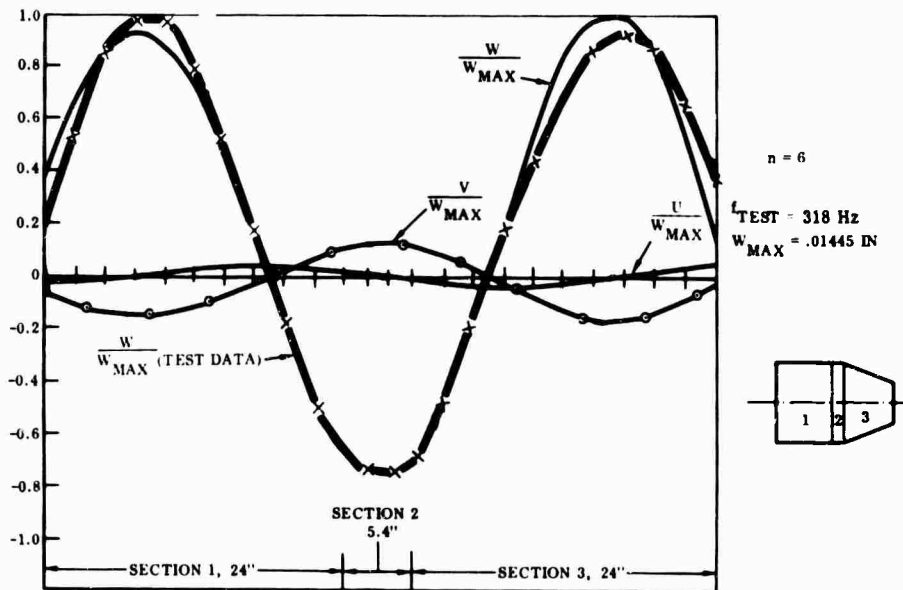


Fig. 2. Experimental and analytical deformation data along the meridian of the instrument unit scale model

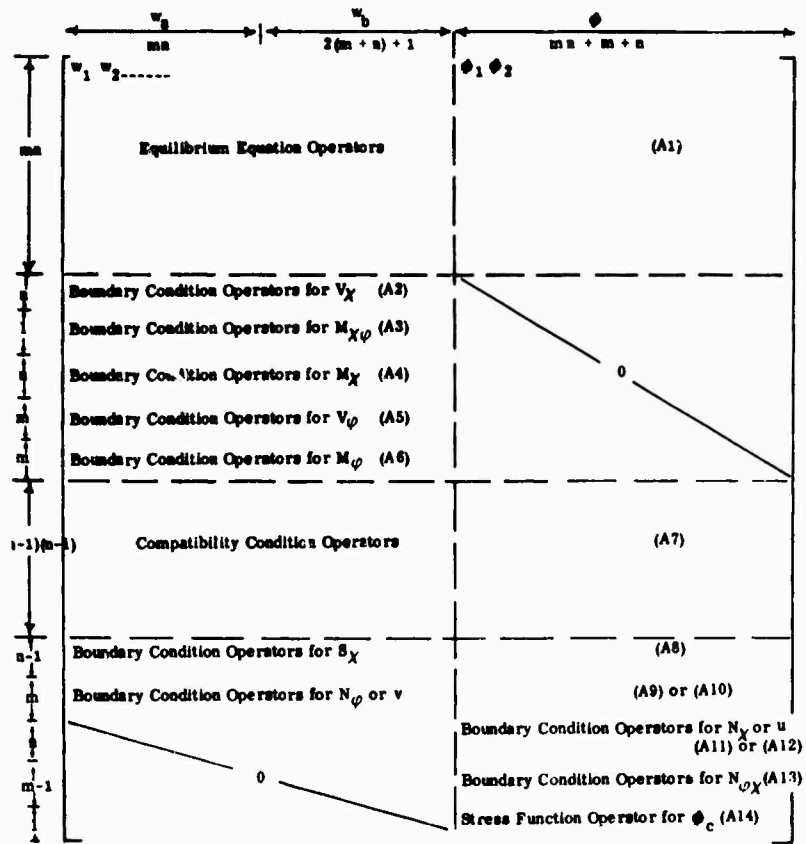


Fig. 3. Formulation of the coefficient matrix for the finite difference computer program



Fig. 4. Test setup of the instrument unit segmented model

3rd MODE $f = 518 \text{ Hz}$
 $K = 2430 \text{ lb./in.}$

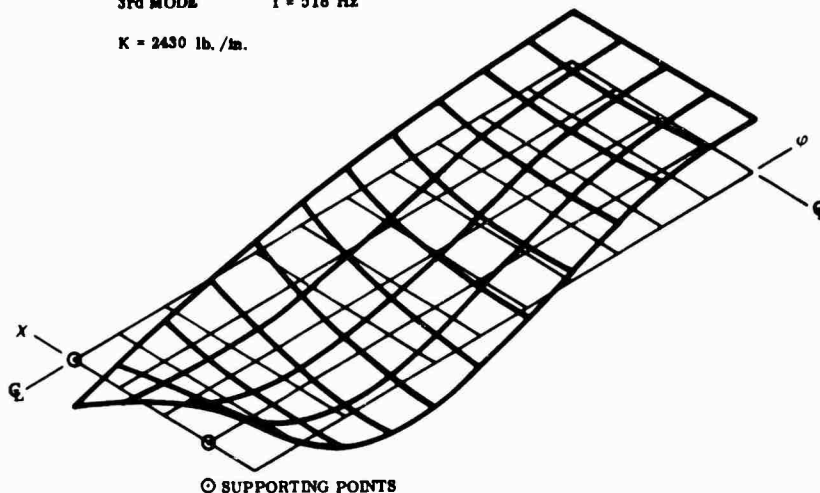


Fig. 5. Typical analytical modal pattern representing a quarter of the instrument unit panel

components were attached. Shell models of the Saturn V instrument unit and the S-II thrust cone structure are typical examples which are illustrated in Figs. 1 and 6. In designing the shell models, all the ring stiffeners were scaled down, based on dynamic similarity relations. The longitudinal stiffeners were not incorporated in the design. Their stiffness contribution was merged with the skin stiffness in choosing a proper shell model skin thickness.

The shell models were subjected to vibration tests to acquire the modal and impedance data for shell segmentation purposes. The data recorded included the response amplitude vs frequency, the impedance vs frequency, and detailed mode shapes corresponding to natural frequencies. Typical driving point impedance data is shown in Fig. 7 for the Saturn V instrument unit scale model (Fig. 1). Typical shell response data is shown in Fig. 8 for the S-II thrust cone shell structure model (Fig. 6).

TECHNIQUES OF FIXTURE PARAMETER SELECTION

Various types of flexible supports were fabricated and tested to evaluate their dynamic characteristics. Dashpot type dampers were tested and found ineffective in controlling the vibration amplitudes. For support evaluation purposes, a solid aluminum rectangular plate was used and tested. The use of a rectangular plate facilitated the dynamic analysis so that the flexible supports could be evaluated conveniently. Experimental modes of the rectangular

plate obtained during the support fixture evaluation phase are shown in Figs. 9 and 10. To predict and evaluate the experimental modal data, a simplified version of the finite difference computer program described previously was used to generate the analytical modes of the plate. The analytical technique facilitated the choice of support design parameters. It also served to interpret the main features and peculiarities of the plate dynamic behavior; for instance, the cantilever type vibrations of the unsupported corners of the rectangular plate (Fig. 9) were evaluated and controlled through the use of the finite difference computer program.

Based on the analytical and experimental modal data, a part of the component mounted shell was selected as the segmented specimen. The lines of segmentation were determined, based on the local displacements and shell stresses. These lines were usually located a fraction of a half of a wavelength away from the nodal lines of some major mode or modes.

A major criterion in shell segmentation was to retain as many as possible of the major vibration modes of the uncut shell structure. For this purpose, proper flexible supports were used at selected points along the edge of the shell. Weights of appropriate mass and mass inertia were attached to the edges to replace the edge stresses existing in the original uncut shell and to retain the modal patterns. Because of practical limitations in the degree of complexity of the supporting fixtures, it was not feasible to duplicate all the natural modes of

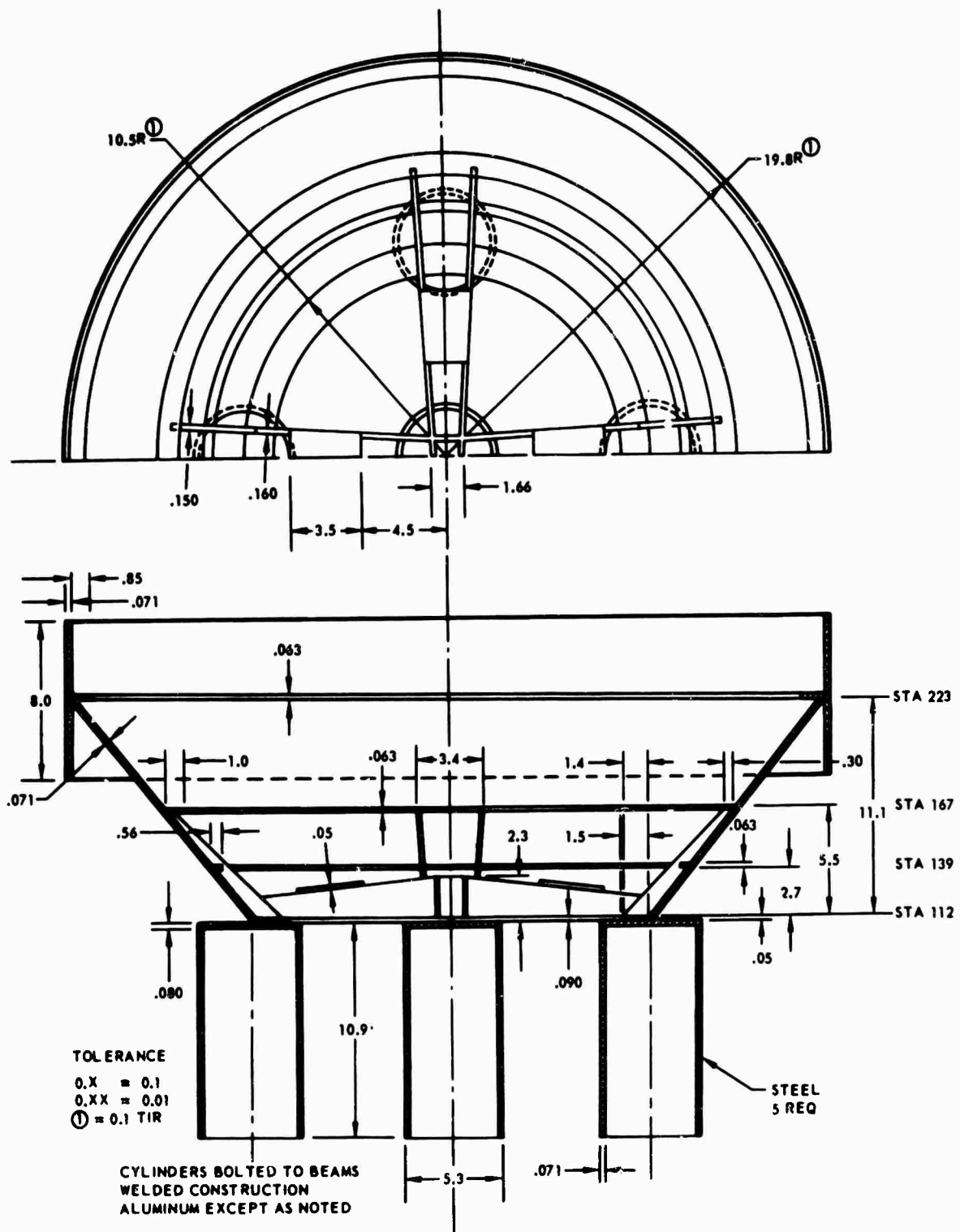


Fig. 6. S-II thrust cone scale model design drawing

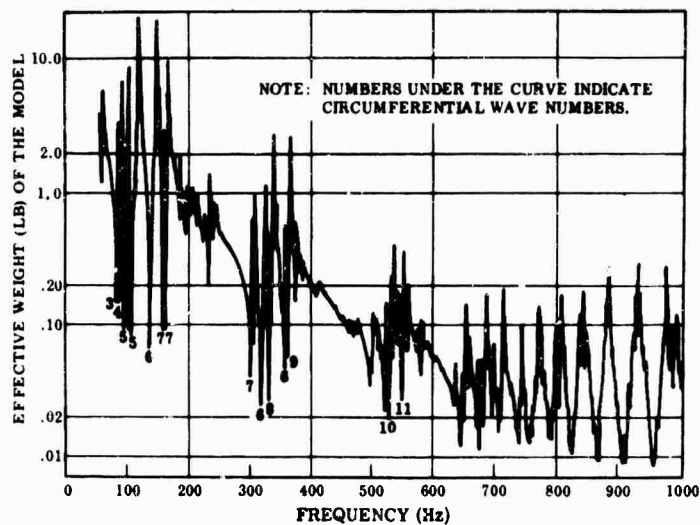


Fig. 7. Driving point impedance of the instrument unit shell model

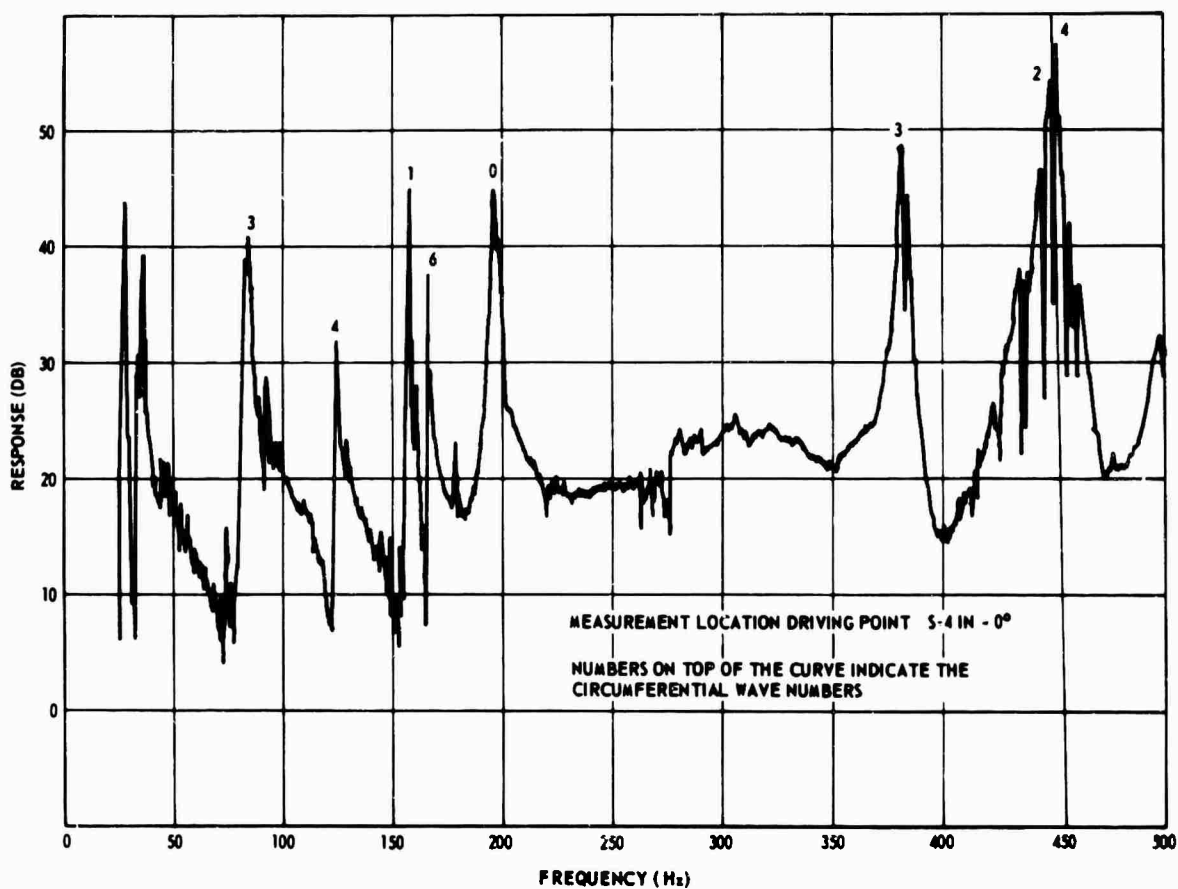


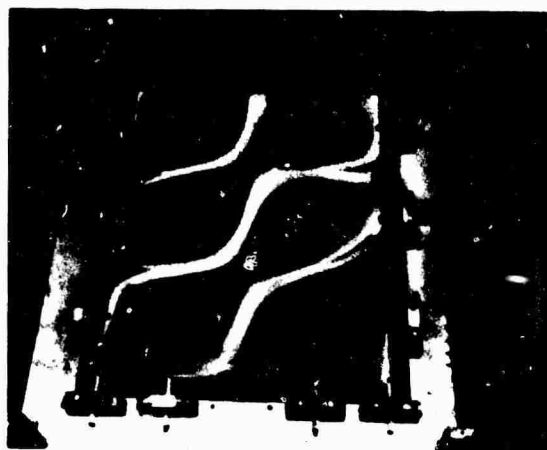
Fig. 8. Response of S-II thrust cone model with mass attachments



Fig. 9. Hard-spring testing, 295.2 Hz



(a) Intermediate supports on shorter sides, 126 Hz



(b) Intermediate supports on shorter sides, 291 Hz

Fig. 10. Corner-supported plate

the complete shell structure. The design criterion then was to retain the more significant modes in the segmented configuration. In some cases, it was found desirable to use different flexible supports for various frequency ranges. For different frequency ranges, the support and attached edge mass configuration may be modified to obtain a better match in the impedances between the complete and segmented shells; for instance, increasing the attached masses tends to tune down the frequencies of the natural modes of the segmented shell. The design configuration reached in this manner was further checked by an analytical investigation. A typical example of the analytical data was shown previously in Fig. 5.

A fixture design of the segmented and flexibly supported instrument unit shell model with

simulated component attachments is shown in Fig. 11. A photograph of the same structure was shown in Fig. 4, as mentioned previously. The corresponding impedance plot for the shell segment is shown as the dotted curve on Fig. 12. Note that the plot is for a full size shell specimen, as proper adjustments have been made for the impedance and the frequency according to scaling relations.

FULL SCALE SATURN V SHELL TEST

The shell segmentation technique was applied to the Saturn V instrument unit prototype (full-scale) structure. Vibration tests were successfully conducted on the full-scale segmented shell structure, with mounted components

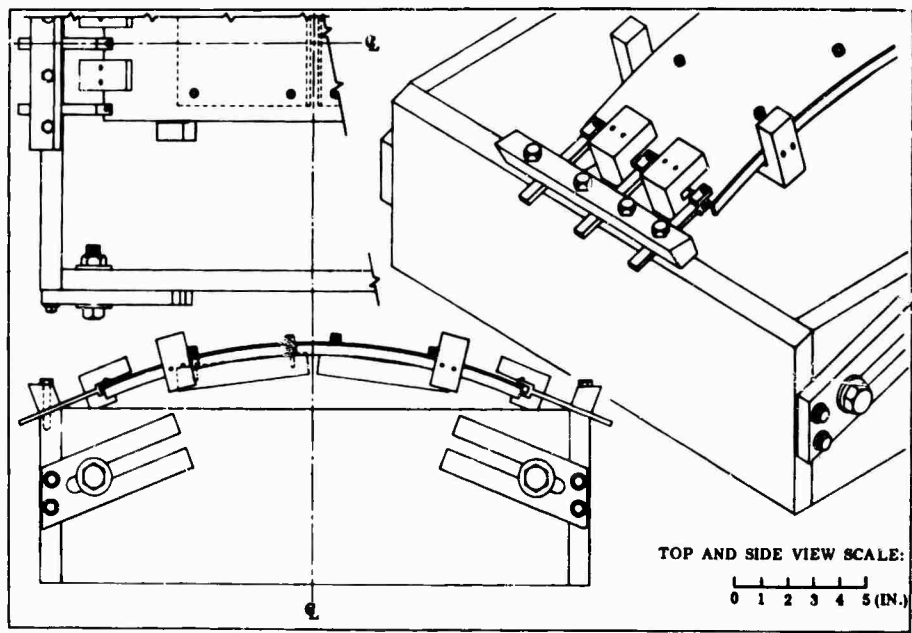


Fig. 11. Vibration fixture for the Saturn V instrument unit segment, one-tenth scale model

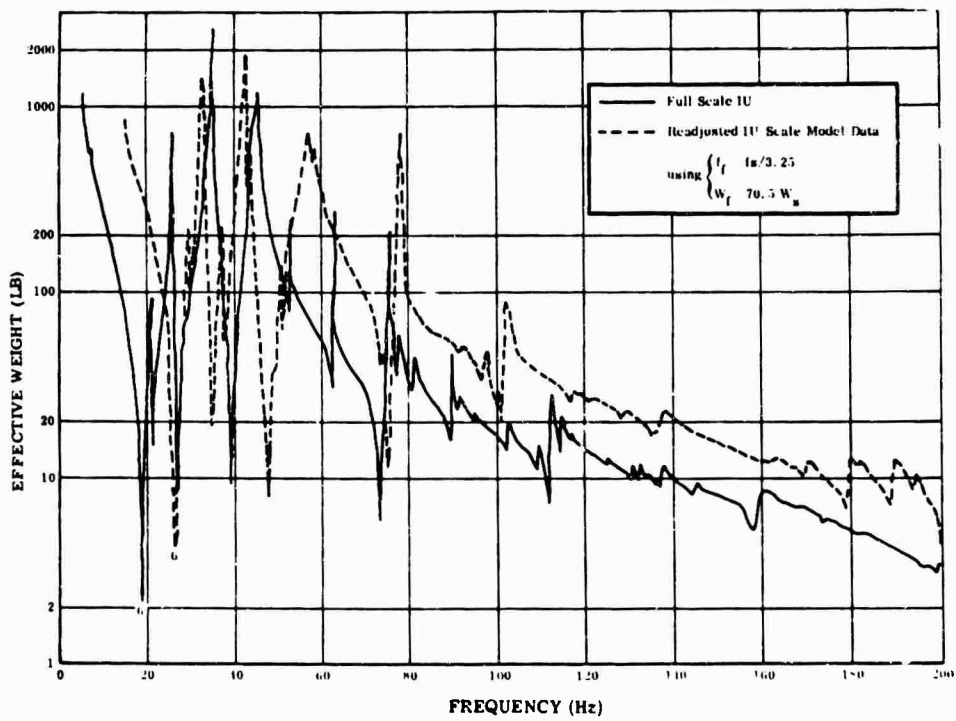


Fig. 12. Driving point impedance of the instrument unit segment with components attached, configuration 1

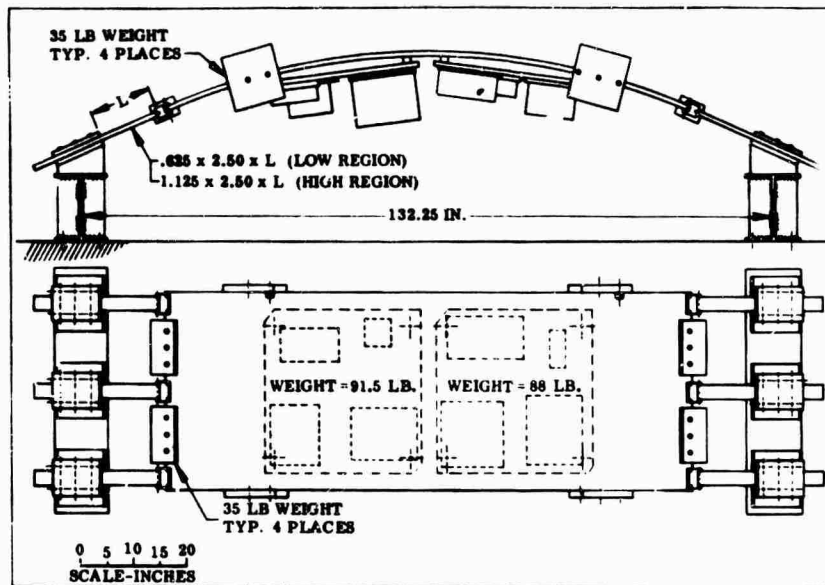


Fig. 13. Vibration jig for the Saturn V instrument unit shell segment

making use of the scale model data acquired previously. The test setup is shown in Figs. 13 and 14.

During the tests, accelerometers were mounted at a number of locations to monitor the vibration amplitudes. The vibration input was controlled so that the monitored acceleration level followed the NASA specification as a function of the excitation frequency. The driving point impedance data recorded during the test are plotted as a solid curve in Fig. 12. As the figure also shows the adjusted impedance data of the segmented scale model, a comparison of the two curves gives some indication as to the errors introduced in dynamic scaling of shell models.

CONCLUSIONS

The work described in this paper established the feasibility of and some guide rules for performing component qualification tests on segmented Saturn V shell structures. This application should result in a reduction of hardware failures because of unrealistic test conditions, and should eventually reduce the system weight. The increased cost of test fixtures should be more than offset by the reduction in redesign and retesting costs.



Fig. 14. Closeup of the Saturn V instrument unit shell segment with flexible supports

REFERENCE

1. C. Hwang and J. Brass, "Analytical and Experimental Determination of Localized Structure To Be Used in Laboratory Vibration Testing of Shell Structure-Mounted Components, Saturn V," NASA Contract NAS8-20025, Northrop Norair Progr. Rept. NOR 66-201, May 1966

BIBLIOGRAPHY

1. Hwang, C. and W. S. Pi, "Analytical and Experimental Determination of Localized Structure To Be Used in Laboratory Vibration Testing of Shell Structure-Mounted Components, Saturn V," NASA Contract NAS8-20025, Northrop Norair Progr. Rept. NOR 67-19, Jan. 1967
2. Hwang, C., W. S. Pi, and N. M. Bhatia, "Analytical and Experimental Determination of Localized Structure To Be Used in Laboratory Vibration Testing of Shell Structure-Mounted Components, Saturn V," NASA Contract NAS8-20025, Northrop Norair Final Rept. NOR 67-127, July 1967

DISCUSSION

F. Smith (Martin Marietta Corp.): I think the work you have done is very interesting. When you were exciting the full-scale specimen, were you attempting to simulate the response of the full shell to an acoustic driving function? In other words, was your shaker really attempting to simulate a point input?

Mr. Hwang: No, we were using a single frequency sweep. The spectrum amplitude at each frequency is in accord with the acceleration level specified by NASA.

Mr. Smith: Let me ask the question in reverse. Have you any relation between the response of the specimen owing to the shaker and what the response would be with acoustics, let us say during the launch phase?

Mr. Hwang: No, we do not have that. What we are given is the acceleration level which should be obtained at a certain point on the shell structure. That was used as a monitor or control point for the test.

Mr. Smith: Were you doing this in more than one axis?

Mr. Hwang: In the thrust cone it was done in quite a number of axes or directions normal to the conical shell structure and also in the thrust direction of the thrust cone.

Mr. Smith: So your test specimen really did not simulate three-axis response?

Mr. Hwang: No, it did not.

* * *

AN APPLICATION OF FLOWGRAPHS TO THE FREE VIBRATION OF STRUCTURES

Peter M. Wright
Department of Civil Engineering
University of Toronto
Toronto, Canada

and

Chuan C. Feng
Department of Civil Engineering
University of Colorado
Boulder, Colorado

This paper presents the application of linear flowgraphs to the free vibration analysis of structural systems. It is shown that the basic structural flowgraph can be formulated directly from an examination of the physical system under consideration. These flowgraphs are essentially independent of the type of loading, and the displacements at discrete points are represented by dependent nodes. In general, the dependent variables are vectors and the graph is referred to as a matrix flowgraph.

Following a brief discussion of the mathematical operations associated with flowgraphs, it is shown that the basic structural flowgraph can be easily transformed into the natural frequency flowgraph. In this latter graph, the branch transmission factors are in terms of both the stiffness properties of the members and the frequency of vibration. General expressions for the branch transmission matrices are derived by employing finite element techniques.

By employing the graph determinant, the values of the natural frequencies can be readily computed with a digital computer. Finally, a further simple transformation yields the eigenvector graph which is used to establish the elements of the eigenvector associated with each natural frequency.

INTRODUCTION

A systems-analysis approach to the formulation of the natural frequency equation and the determination of the eigenvectors for certain linear structural systems is presented in this paper. Developments in topology and systems analysis have revealed the existence of an isomorphism between oriented linear flowgraphs and structural systems [1]. These structural graphs have been used previously to a limited extent in studying the static and dynamic response of systems [2,3]. As a result of the work that has been done on static systems, it has become apparent that flowgraphs have specific advantages, particularly in seeking a better understanding of the design process.

Perhaps the most important technique developed for static systems analysis, using flowgraphs, is the concept of superimposing building-block flowgraphs to form the complete graph. This procedure is extended here to the case of the free vibration of discrete mass systems such as shear buildings, and continuous systems such as plane frames. As will be shown, the nodes of the flowgraph for discrete systems are the displacements of the masses, whereas for continuous systems, they are the displacements of the joints. In the latter case, the mathematical properties of the flowgraph are defined by the end properties of structural components derived from a finite element method [4].

A brief discussion about flowgraphs in general precedes the examination of their application to free vibration problems.

MATRIX AND SCALAR FLOWGRAPHS

In general, a flowgraph is a schematic representation of the interrelationships between the input to a system and the consequent behavior of the system. These same relationships can be expressed by simultaneous equations but not with the same clarity or ease of formulation. One advantage of flowgraphs is that their form can be deduced directly from the topology of the system under consideration. The fundamental concepts and mathematical operations associated with oriented linear structural flowgraphs are as follows [5].

A flowgraph consists of a network of directed branches connected to nodes in a manner that reflects the geometry of the system. To illustrate, Fig. 1 shows an oriented flowgraph. The variables that motivate a system are denoted by source nodes and represent independent inputs into the system. The dependent variables that represent the resultant behavior of the system are denoted by dependent nodes. In the figure the source nodes are lettered a, b, and c while the dependent nodes are numbered 1, 2, and 3.

These nodes are connected by directed lines or branches having associated transmission factors that relate the independent and dependent variables. In the case of structural

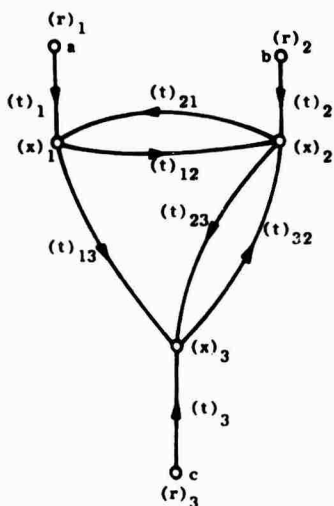


Fig. 1. Oriented flowgraph example

systems, these reflect the elastic properties of the components.

Generally, the variables are represented by vectors and the graph is referred to as a matrix flowgraph. The transmission factors for these graphs are then square matrices. In the special case where each node represents a single variable, the graph is referred to as a scalar graph, and the transmission factors are scalars. In this paper, matrices and vectors will be designated by the use of parentheses, i.e., $(t)_{32}$, while scalars will be designated without them, i.e., t_{32} .

The branches entering any node can be used to obtain the corresponding equation relating that variable to the others. For example, the dependent variable $(x)_1$ in Fig. 1 is related to the other variables by the expression

$$(x)_1 = (t)_{11}(r)_1 + (t)_{21}(x)_2 \quad (1)$$

The variable $(x)_3$ does not appear in this expression because there is no branch from that node.

Although of interest, equations of this form are not of any particular value because the flowgraph provides the same information pictorially. The more important equations are the solution equations that can be obtained from the flowgraph. These provide the solution of each dependent variable in terms of the independent inputs and the transmission factors.

To date, practical solution algorithms for multiple-connected matrix graphs have not been developed, although Kirchgessner [6] and Enger [7] have presented useful algorithms for series matrix graphs. As the examples to be considered in detail in this paper involve scalar flowgraphs, the solution algorithm for matrix graphs is reduced to the algorithm for scalar graphs presented by Mason [8,9]. Before considering his loop rule, the following further definitions are required.

A forward path is defined as any path originating at a source node and terminating at an interior node. Such a path can include any particular node only once. The associated forward transmittance, T , is the product of the transmission factors of the branches that constitute the path. Considering the figure, one of the two forward paths from the source node, a, to the dependent node, 2, is given by the path (a-1-3-2). The corresponding forward transmittance is

$$T_{a2} = t_1 t_{13} t_{32} \quad (2)$$

A loop is a series of branches that originate and terminate at the same node without encountering any particular node more than once. The product of the transmission factors of all the branches in the loop is defined as the loop transmittance, L . For example, in Fig. 1, there are three loops (1-2-1), (2-3-2), and (1-3-2-1). The corresponding loop transmittances are $(t_{12}t_{21})$, $(t_{23}t_{32})$, and $(t_{13}t_{32}t_{21})$. It is noted that loops cannot include source nodes.

The multiplication of scalar quantities is commutative and therefore the order of multiplication for loop transmittances and forward transmittances is immaterial. However, the noncommutative nature of matrix multiplication must be satisfied in arriving at solution algorithms for matrix graphs. This fact is responsible for their considerably more complex form.

The scalar graph determinant is defined as

$$\Delta = 1 - \Sigma L_p + \Sigma L_p L_q - \Sigma L_p L_q L_r \dots \quad (3)$$

in which L_p represents all the loops in the system, $L_p L_q$ all the pairs of nontouching loops, $L_p L_q L_r$ all the triplets of nontouching loops, etc. The algebraic sign is positive for an even number of loop products and negative for an odd number of loop products. Again considering the example, the graph determinant is

$$\begin{aligned} \Delta &= 1 - (L_{1-2-1} + L_{2-3-2} + L_{1-3-2-1}) \\ &= 1 - t_{12}t_{21} - t_{23}t_{32} - t_{13}t_{32}t_{21} \end{aligned} \quad (4)$$

The path determinant is a quantity associated with a forward path. It is obtained from the graph determinant by striking out all terms containing transmittances of loops that touch the path. For the forward path from the source node, a , to the dependent node, 2 , the path determinant is

$$\Delta_{a-1-3-2} = 1 - L_{1-2-1} - L_{2-3-2} - L_{1-3-2-1} = 1 \quad (5)$$

because this forward path touches all possible loops. On the other hand, the path determinant for the forward path from source node, a , to the dependent node, 1 , is

$$\begin{aligned} \Delta_{a-1} &= 1 - L_{1-2-1} - L_{2-3-2} - L_{1-3-2-1} \\ &= 1 - L_{2-3-2} = 1 - t_{23}t_{32} \end{aligned} \quad (6)$$

as the loop (2-3-2) does not touch this forward path.

Mason's loop rule states that the output, G_{pq} , at some specified dependent node, q , in terms of a unit input at the source node, p , is equal to the sum of the products of the forward transmittances, T_{pq} , and their corresponding path determinants, Δ_{pq} , divided by the graph determinant, Δ . Thus

$$G_{pq} = \frac{\Sigma T_{pq} \Delta_{pq}}{\Delta} \quad (7)$$

Considering all the inputs to source nodes, the final value of the dependent variable, x_q , is given by

$$x_q = \frac{\Sigma_r T_{rp} \Sigma T_{pq} \Delta_{pq}}{\Delta} \quad (8)$$

Thus each of the dependent variables can be solved individually by considering the scalar flowgraph only.

NATURAL FREQUENCY FLOWGRAPHS FOR DISCRETE SYSTEMS

In this section, a basic flowgraph is developed that can be used to represent a system made up of discrete masses and springs. It will be shown that this flowgraph is only a function of the geometry of the system. From this basic flowgraph, the natural frequency graph can be formulated and used to determine the natural frequencies of the system.

Consider the generalized three-mass system shown in Fig. 2. Let the displacements associated with mass m_i be given by the vector $(u)_i$ where

$$(u)_i = \begin{bmatrix} u_1 \\ u_2 \\ u_3 \end{bmatrix}_i \quad (9)$$

Assuming that these displacements are the dependent variables for the system, they can be represented by nodes of a flowgraph. From the connectivity of the masses in Fig. 2, it is apparent that the flowgraph in Fig. 3 does represent this system. The dependent nodes denote the dependent variables that, in this formulation, are the displacements of the masses. Any external static or dynamic loads applied to the masses would be denoted by inputs to the flowgraph at the source nodes. However, for

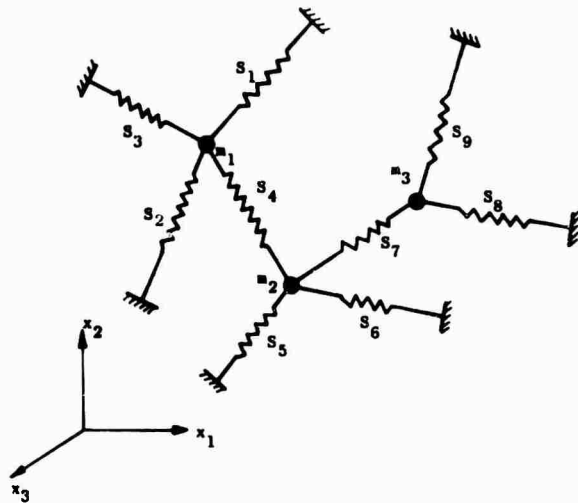


Fig. 2. Generalized three-mass system

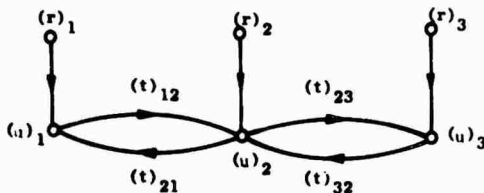


Fig. 3. Basic flowgraph for three-mass example system

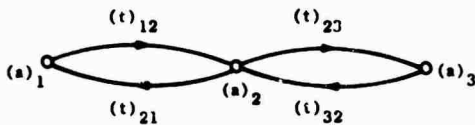


Fig. 4. Natural frequency graph for three-mass example system

free vibration, as there are no external actions, these source nodes can be deleted. The resultant graph is shown in Fig. 4 and is referred to as the natural frequency flowgraph. In this graph, the dependent variables are the amplitudes. Having established the form of the graph, the next step is to derive the transmission factors.

The stiffness of the n springs connecting to mass m_i are represented by an unassembled stiffness matrix, $(K_i)_m$, where m denotes member axis. This is an $(n \times n)$ diagonal matrix having elements S_j , $j = 1, \dots, n$, where S denotes spring stiffness. From basics, the direct, nodal, stiffness matrix, $(K)_{ii}$, in system coordinates is given by

$$(K)_{ii} = (R_i)(K_i)_m(R_i)^T \quad (10)$$

where

$$(R_i) = \begin{bmatrix} a_{11} & a_{12} & \dots & a_{1n} \\ a_{21} & a_{22} & \dots & a_{2n} \\ a_{31} & a_{32} & \dots & a_{3n} \end{bmatrix}$$

= rotation matrix for node i .

The columns of (R_i) are the direction cosines relating the spring axis to the system coordinates, assuming that the near end of the spring is at m_i .

Letting spring q connect the two masses, m_i and m_j , then the cross, nodal, stiffness matrix, $(K)_{ij}$, in system coordinates is given by

$$(K)_{ij} = -S_q \begin{bmatrix} a_{1q} \\ a_{2q} \\ a_{3q} \end{bmatrix} \begin{bmatrix} a_{1q} & a_{2q} & a_{3q} \end{bmatrix} = -S_q \begin{bmatrix} a_{1q}^2 & a_{1q}a_{2q} & a_{1q}a_{3q} \\ a_{2q}a_{1q} & a_{2q}^2 & a_{2q}a_{3q} \\ a_{3q}a_{1q} & a_{3q}a_{2q} & a_{3q}^2 \end{bmatrix} \quad (11)$$

It follows that for free vibration, the dynamic equilibrium of the forces acting on mass m_1 is given by:

$$(M)_i(\ddot{u})_i + (K)_{i1}(u)_i + \sum_j (K)_{ij}(u)_j = 0 \quad (12)$$

where $(M)_i$ is a diagonal matrix having elements equal to m_i .

For small displacements it is assumed that the displacements can be expressed by the product [10]:

$$\begin{bmatrix} u_1 \\ u_2 \\ u_3 \end{bmatrix}_i = \begin{bmatrix} a_1 \sin pt \\ a_2 \sin pt \\ a_3 \sin pt \end{bmatrix}_i \quad (13)$$

where p is the frequency of vibration in radians per second. Substituting this relationship into Eq. (12) yields

$$-p^2(M)_i(a)_i + (K)_{i1}(a)_i + \sum_j (K)_{ij}(a)_j = 0$$

or (14)

$$[(K)_{i1} - p^2(M)_i](a)_i + \sum_j (K)_{ij}(a)_j = 0.$$

For the usual case, the first matrix term is nonsingular. Then the amplitudes, $(a)_i$, can be expressed by the relationship

$$(a)_i = - [(K)_{i1} - p^2(M)_i]^{-1} \sum_j (K)_{ij}(a)_j \quad (15)$$

Thus a general expression for the branch transmission factors for the natural frequency flowgraph is

$$(t)_{ji} = - [(K)_{i1} - p^2(M)_i]^{-1} (K)_{ij} \quad (16)$$

Both the form of the natural frequency graph and the branch transmission factors can thus be derived directly from the physical system. As there are no inputs to the system, it can be shown that for a nontrivial solution for the natural frequencies, the graph determinant equals zero.

For series matrix graphs, the algorithm devised by Enger [2] is readily applicable. For the two-loop series matrix graph in Fig. 4, the graph determinant with respect to node 2 is given by

$$\Delta = |I - (t)_{21}(t)_{12} - (t)_{23}(t)_{32}| = 0 \quad (17)$$

where $(t)_{ji}$ is given by the preceding equation. In general, Eq. (17) is easily solved by using progressively increasing values for p^2 and then selecting those for which the graph determinant is zero.

For plane systems, the preceding development is equally valid. In this case the dependent variables are vectors having two elements and the transmission factors are (2×2) matrices. Finally, for one-dimensional systems, the matrix graph reduces to a scalar graph.

To illustrate the application of flowgraphs to the determination of the natural frequency of discrete systems, consider the mass-spring system shown in Fig. 5(a). The corresponding natural frequency flowgraph is shown in Fig. 5(b).

Using Eq. (16), the branch transmission factors are obtained directly from the physical system shown in Fig. 5(a).

$$\left. \begin{aligned} t_{12} &= -(S_2 + S_3 - m_2 p^2)^{-1} (-S_2) = \frac{S_2}{S_2 + S_3 - m_2 p^2} \\ t_{21} &= -(S_1 + S_2 - m_1 p^2)^{-1} (-S_2) = \frac{S_2}{S_1 + S_2 - m_1 p^2} \\ t_{23} &= -(S_3 - m_3 p^2)^{-1} (-S_3) = \frac{S_3}{S_3 - m_3 p^2} \\ t_{32} &= -(S_2 + S_3 - m_2 p^2)^{-1} (-S_3) = \frac{S_3}{S_2 + S_3 - m_2 p^2} \end{aligned} \right\} \quad (18)$$

The scalar graph determinant given by Eq. (3) can be formulated directly and equated to zero. Thus

$$\Delta = 1 - t_{12}t_{21} - t_{23}t_{32} = 0.$$

Although for this relatively simple example, the graph determinant can be expanded to yield the usual frequency equation, normally it is probably easier to evaluate the equation for successively larger values of p^2 .

For shear buildings, with the mass assumed to be concentrated at the floor levels as shown in Fig. 5(c), the preceding approach can be applied directly, as these constitute discrete systems [11].

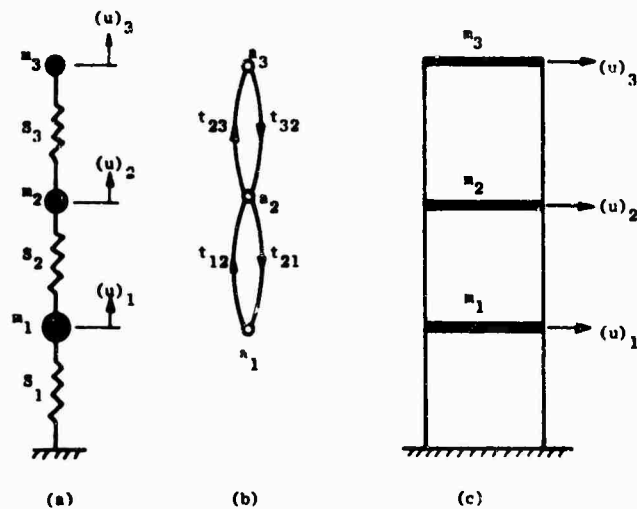


Fig. 5. Example three-mass system

EIGENVECTOR FLOWGRAPHS FOR DISCRETE SYSTEMS

For systems represented by scalar flowgraphs, the eigenvectors for each natural frequency can be obtained from an eigenvector flowgraph. One of the dependent nodes is selected to be transformed into a source node by deleting incoming branches. It is assumed here that the input to this source node is unity, i.e., the amplitude of the corresponding mass is unity. Using an eigenvector graph, the amplitudes of all other masses can be computed using Mason's loop rule as discussed previously.

These computations are illustrated for the one-dimensional, three-mass system shown in Fig. 5(a). The natural frequency graph for the system is reproduced in Fig. 6(a), and two of the possible eigenvector graphs are shown in Figs. 6(b) and 6(c). As seen, node 1 has been transformed into a source node by removing the incoming branch, 2-1.

The values of the relative amplitudes, a_2 and a_3 , are then given by

$$a_2 = \frac{(1) t_{12}}{\Delta_e}$$

$$a_3 = \frac{(1) t_{12} t_{23}}{\Delta_e}$$

where

$$\begin{aligned} \Delta_e &= \text{graph determinant for eigenvector graph} \\ &= 1 - t_{23} t_{32} \end{aligned}$$

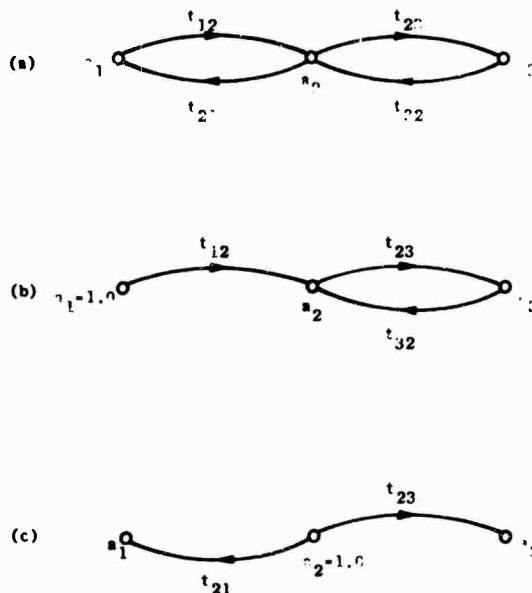


Fig. 6. Free vibration flowgraphs for three-mass system

It is noted that for this particular case it would have been simpler if node 2 had been transformed into the source node as shown in Fig. 6(c).

NATURAL FREQUENCY FLOWGRAPHS FOR PLANE FRAMES

In the preceding examples, each node of the flowgraph represented the displacements associated with one of the masses, and the springs were assumed to be weightless. Now

consider a system composed of axial-bending members connected to form a plane frame. Associated with each member, i , is a uniform distributed mass, m_i . In this type of system, flowgraphs are formulated for which the dependent nodes represent the displacements at discrete points. It is shown that the branch transmission factors, in general, include dynamic stiffness factors and that the natural frequencies for the system can be computed in a manner similar to that noted in the preceding section.

To illustrate the form of the flowgraphs for a plane frame, consider the structure in Fig. 7(a).

At each joint of a plane frame there are three possible displacements denoted by

$$(u)_i = \begin{bmatrix} u_x \\ u_y \\ u_\theta \end{bmatrix}_i$$

Thus the matrix flowgraph for the structure in Fig. 7(a) is as shown in Fig. 7(b). As joints 7 and 8 are fixed supports, they are excluded from the flowgraph. Inputs to the system in the form of either static or dynamic loads would be applied at the source nodes shown. In the case of free vibration, as there are no external loads, these source nodes are omitted and the resultant graph is referred to as a natural frequency flowgraph.

An alternate matrix flowgraph for this structure is shown in Fig. 7(c). In this formulation, the displacements for an entire level are represented by a single vector such that

$$(u)_A = \begin{bmatrix} (u)_1 \\ (u)_2 \end{bmatrix} = \begin{bmatrix} u_{x_1} \\ u_{y_1} \\ u_{\theta_1} \\ u_{x_2} \\ u_{y_2} \\ u_{\theta_2} \end{bmatrix}, \text{ etc.}$$

The branch transmission factors are now (6×6) matrices.

To derive expressions for the branch transmission factors for the flowgraph in Fig. 7(b), a member is considered as shown in Fig. 8. The member axes are $(x' - y')$ while the system axes are $(x - y)$. In the figure the near end is denoted by α and the far end by β . These subscripts also imply actions and displacements with respect to the member axis. The actions shown are the forces owing to displacements of the ends given by

$$(u)_\alpha = \begin{bmatrix} u_{x'} \\ u_{y'} \\ u_\theta \end{bmatrix}_\alpha \quad \text{and} \quad (u)_\beta = \begin{bmatrix} u_{x'} \\ u_{y'} \\ u_\theta \end{bmatrix}_\beta$$

The relationship between these displacements and the end actions $(b)_\alpha$ has been summarized by Ariaratnam [12] as follows:

$$\begin{bmatrix} b_1 \\ b_2 \\ b_3 \end{bmatrix}_\alpha = \begin{bmatrix} \frac{EA}{L} \psi_1 & 0 & 0 \\ 0 & \frac{EI}{L^3} \phi_5 & \frac{EI}{L^2} \phi_1 \\ 0 & \frac{EI}{L^2} \phi_1 & \frac{EI}{L} \phi_3 \end{bmatrix} \begin{bmatrix} u_{x'} \\ u_{y'} \\ u_\theta \end{bmatrix}_\alpha + \begin{bmatrix} -\frac{EA}{L} \psi_2 & 0 & 0 \\ 0 & \frac{-EI}{L^3} \phi_6 & \frac{EI}{L^2} \phi_2 \\ 0 & \frac{-EI}{L^2} \phi_2 & \frac{EI}{L} \phi_4 \end{bmatrix} \begin{bmatrix} u_{x'} \\ u_{y'} \\ u_\theta \end{bmatrix}_\beta \quad (19)$$

where

$$\psi_1 = \mu \cot \mu$$

$$\psi_2 = \mu \operatorname{cosec} \mu$$

$$\phi_1 = \lambda^2 \left(\frac{\sin \lambda \sinh \lambda}{1 - \cos \lambda \cosh \lambda} \right)$$

$$\phi_2 = \lambda^2 \left(\frac{\cosh \lambda - \cos \lambda}{1 - \cos \lambda \cosh \lambda} \right)$$

$$\phi_3 = \lambda \left(\frac{\sin \lambda \cosh \lambda - \cos \lambda \sinh \lambda}{1 - \cos \lambda \cosh \lambda} \right)$$

$$\phi_4 = \lambda \left(\frac{\sinh \lambda - \sin \lambda}{1 - \cos \lambda \cosh \lambda} \right)$$

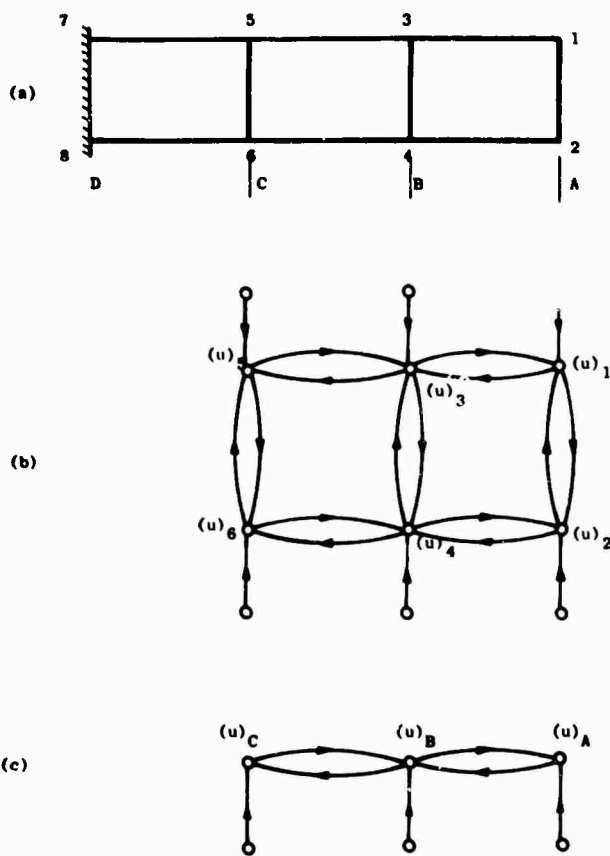


Fig. 7. Illustrative plane frame and flowgraphs

$$\phi_s = \lambda^3 \left(\frac{\sin \lambda \cosh \lambda + \cos \lambda \sinh \lambda}{1 - \cos \lambda \cosh \lambda} \right)$$

$$\lambda = L \left(\frac{mp^2}{EI} \right)^{1/4}$$

$$\phi_6 = \lambda^3 \left(\frac{\sinh \lambda + \sin \lambda}{1 - \cos \lambda \cosh \lambda} \right)$$

It is noted that when p equals zero, these dynamic stiffness factors reduce to the usual static ones. Equation (19) can be written simply as

$$\mu = L \left(\frac{mp^2}{EA} \right)^{1/2}$$

$$(b)_a = (K)_{aa}(u)_a + (K)_{a\beta}(u)_\beta \quad (20)$$

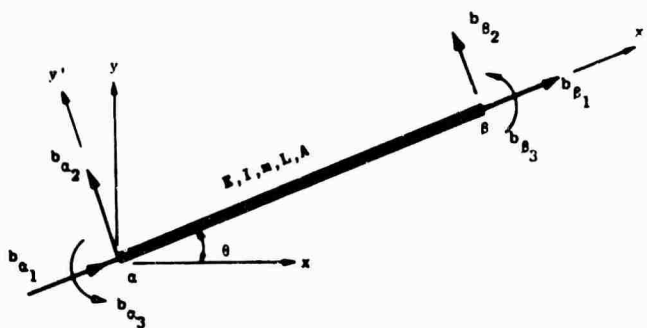


Fig. 8. Typical prismatic plane member

Thus the member end actions and the displacements are related by member stiffness matrices that include the frequency of vibration.

The stiffness of the n members framing into joint i are represented by an unassembled stiffness matrix, $(K_i)_m$, where m denotes member axes. This is a diagonal matrix having matrix subelements $(K)_{aa}$ as shown in Eq. (19). From basics, the direct nodal stiffness matrix, $(K)_{ii}$, in system coordinates is given by

$$(K)_{ii} = (R_i)(K_i)_m(R_i)^T \quad (21)$$

where

$$(R_i) = \begin{bmatrix} (T)_{i1} & (T)_{i2} & \dots & (T)_{in} \end{bmatrix}$$

and

$$(T)_{ij} = \begin{bmatrix} \cos \theta & -\sin \theta & 0 \\ \sin \theta & \cos \theta & 0 \\ 0 & 0 & L \end{bmatrix}$$

Assuming that member q connects the two joints, i and j , then the cross nodal stiffness matrix, $(K)_{ij}$, in system coordinates is given by

$$(K)_{ij} = (T)_{ij}(K)_{a\beta}(T)_{ij}^T \quad (22)$$

where $(K)_{a\beta}$ is given in Eq. (19) and is with respect to member q .

It follows that for free vibration the dynamic equilibrium of the forces acting at joint i is given by

$$(K)_{ii}(u)_i + \sum_j (K)_{ij}(u)_j = 0. \quad (23)$$

Again, for the usual case, the first matrix term is nonsingular and the displacements, $(u)_i$, can be expressed by

$$(u)_i = -(K)_{ii}^{-1} \sum_j (K)_{ij}(u)_j. \quad (24)$$

Thus a general expression for the branch transmission factors for the natural frequency flowgraph for plane frames with axial-bending members is given by

$$(t)_{ji} = -(K)_{ii}^{-1} (K)_{ij}. \quad (25)$$

Both the form of the natural frequency graph and the branch transmission factors have been derived directly from the physical system.

As there are no inputs to the system, it can be shown that for a nontrivial solution for the natural frequencies, the graph determinant equals zero.

To illustrate the application of flowgraphs to the determination of the free vibration of systems with distributed mass, consider the two-span continuous beam in Fig. 9(a). The natural frequency flowgraph is shown in Fig. 9(b) and an eigenvector graph in Fig. 9(c). For simplicity of presentation, consider transverse vibration only. As there is then only one displacement at each joint, the general matrix flowgraph reduces to a scalar one for this example. Using Eq. (25), the transmission factors are

$$\begin{aligned} t_{12} &= - \left[\left(\frac{EI}{L} \phi_3 \right)_a + \left(\frac{EI}{L} \phi_3 \right)_b \right]^{-1} \left(\frac{EI}{L} \phi_4 \right)_a \\ t_{21} &= - \left[\left(\frac{EI}{L} \phi_3 \right)_a \right]^{-1} \left(\frac{EI}{L} \phi_4 \right)_a \\ t_{23} &= - \left[\left(\frac{EI}{L} \phi_3 \right)_b \right]^{-1} \left(\frac{EI}{L} \phi_4 \right)_b \\ t_{32} &= - \left[\left(\frac{EI}{L} \phi_3 \right)_a + \left(\frac{EI}{L} \phi_3 \right)_b \right]^{-1} \left(\frac{EI}{L} \phi_4 \right)_b \end{aligned} \quad (26)$$

The scalar graph determinant can be formulated directly from the flowgraph and equated to zero. Thus

$$\Delta = 1 - t_{12}t_{21} - t_{23}t_{32} = 0. \quad (27)$$

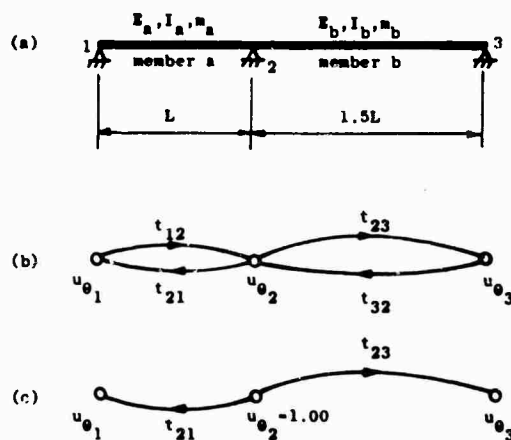


Fig. 9. Example beam vibration flowgraphs

As for discrete systems, the expression for the graph determinant can be expanded to yield the usual frequency equation. However, it is probably simpler for most continuous structures to evaluate the equation for successively larger values of p^2 . The eigenvector flowgraph shown in Fig. 9(c) can be solved using Mason's loop rule as shown in the preceding section.

CONCLUSIONS

An important characteristic of flowgraphs is that they can be formulated directly from the physical system under consideration. The consequent interrelationships are seen from the resultant loops and branches. In the case of linear structural systems, the nodes of the basic structural flowgraph represent the dependent displacements of discrete points and thus, in general, the variables are vector quantities.

Following a brief discussion of the mathematical operations associated with flowgraphs, it is shown that the basic structural flowgraph can be readily transformed into the natural frequency graph. In this latter graph, the branch transmission factors are in terms of both the member stiffnesses and the frequency

of vibration. Using the graph determinant, the natural frequencies can be computed using a digital computer. Finally, a further simple transformation yields the eigenvector flowgraph which can be utilized to determine the elements of the eigenvector for each natural frequency

This paper has demonstrated the feasibility of flowgraphs in the determination of the natural frequencies and eigenvectors of discrete and of continuous mass systems. It is concluded that this approach can be used effectively in the study of free vibration of structures.

It is hoped that this paper will provide new insights into the use of flowgraphs in correlating the physical system to its mathematical model. Flowgraphs have the advantage that the solution of the dependent variables is direct and does not involve mathematical solution processes that lead to the loss of the physical parameters.

ACKNOWLEDGMENTS

The research work leading to this paper was undertaken with the support of the National Science Foundation Grant No. GK 1636.

REFERENCES

1. H. M. Trent, "Isomorphisms Between Oriented Linear Graphs and Lumped Physical Systems," *J. Acoust. Soc. Am.*, 27(3):500-527, May 1955
2. Chuan C. Feng and Kenneth A. Stead, "Slope Deflection and Moment Flow Graphs," *J. Strl. Div., ASCE*, 93(ST3), 1967
3. G. Lasker and D. P. Brown, "Application of Linear Graph Theory to the Vibration Analysis of Frames," *Proc. of 6th Midwest Symp. on Circuit Theory*, Univ. of Wis., May 1963
4. H. Argyris and S. Kelsey, Energy Theorems and Structural Analysis (Butterworths, London), 1960
5. S. Seshu and M. B. Reed, Linear Graphs and Electrical Networks (Addison-Wesley Co., Reading, Mass.), 1961
6. Thomas E. Kirchgessner and Chuan C. Feng, "On a Solution Algorithm for Matrix Graphs," *Proc. of 1967 Natl. Symp. "Saturn V/Apollo and Beyond," Am. Astron. Soc.*, June 1967
7. Torliev Enger, "Notes for Solution of Series Matrix Flowgraphs," *Res. Rept.*, Univ. of Colo., Aug. 1967
8. S. J. Mason, "Feedback Theory: Some Properties of Signal Flow Graphs," *Proc. IRE*, 41(9):1144-1156, Sept. 1953
9. S. J. Mason, "Feedback Theory: Further Properties of Signal Flow Graphs," *Proc. IRE*, 44(7):920-926, July 1956
10. S. Timoshenko, Vibration Problems in Engineering (D. Van Nostrand Co., Princeton, N. J.), 1955, pp. 233-244
11. Grover L. Rogers, Dynamics of Framed Structures (John Wiley & Sons, Inc., New York), 1959, pp. 113-130
12. S. T. Ariaratnam, "The Vibration of Plane Frameworks," *Appl. Sci. Res.*, A XIII:249-259, 1964

* * *

DUAL SPECIFICATIONS IN VIBRATION TESTING*

Walter B. Murfin
Sandia Corporation
Albuquerque, New Mexico

A method of specifying vibration test inputs using both force and motion is shown to be superior to specification of either input alone.

INTRODUCTION

Vibration test levels may be given in two ways: by specifying an input motion or by specifying an input force.

Because motion (i.e., acceleration) is the quantity most often measured in the field, it might seem more logical to specify motion. However, such a specification is grossly over-conservative. Not only is the system drastically overdriven at some frequencies, but the wrong frequencies are emphasized. The specification of force is more logical, but the attainment of a realistic level is attended by great difficulties. Force is virtually unmeasurable under field conditions. Also, as shown by Otts [1], force-controlled vibration tests require the use of a "foundation mass"; realistic choice of this mass is generally impossible.

Many papers have been published suggesting exotic mechanical impedance methods for determining the proper test level. These methods are generally completely impracticable and are usually ignored.

DETERMINATION OF FORCE FROM MEASURED MOTION

If it is known that most of the vibration of the system results from input forces applied at a single, well-defined point, it is possible to compute appropriate forces from field-motion measurements and a laboratory measurement.

It is convenient to introduce the concept of driving point apparent weight. This is the ratio

of vibratory input force to vibratory input acceleration as a function of frequency, i.e., $W_a(\omega) = [F(\omega)]/[X(\omega)]$, where F is the force in pounds, \ddot{x} is the acceleration in g units, and ω is the circular frequency.

The apparent weight is then given in pounds. Apparent weight is related to mechanical impedance [2] by a factor of $j\omega$, where $j = \sqrt{-1}$. Although apparent weight is actually a complex quantity, only the absolute value is required here.

If field vibrations were known at discrete frequencies, it would be a simple matter to compute the forces, i.e., $F'(\omega) = W_a(\omega)\ddot{y}(\omega)$, where the \ddot{y} are measured field accelerations, and the $F'(\omega)$ are the computed field forces.

The field vibrations are measured, usually over a frequency interval for instance, as given by the Vibran [3,4] system. Although a certain level is reported for a frequency band, it must not be supposed that this vibration is uniform over the bandwidth. In fact, it will be obvious that if force is uniform over the band, almost all the vibration will take place at that frequency within the band where the apparent weight is a minimum.

One can choose an "average" value of apparent weight within a frequency band which is strongly biased toward the minimum value. Then the "average" force within a frequency band is $\bar{F} = \bar{W}_a \ddot{y}$, where \bar{W}_a is the "average" apparent weight. The method of choosing the average value is open to debate. The method used here is $\bar{W}_a = W_{\min} + 0.1(W_{\max} - W_{\min})$, where W_{\min} and W_{\max} are the minimum and

*This work was supported by the U.S. Atomic Energy Commission.

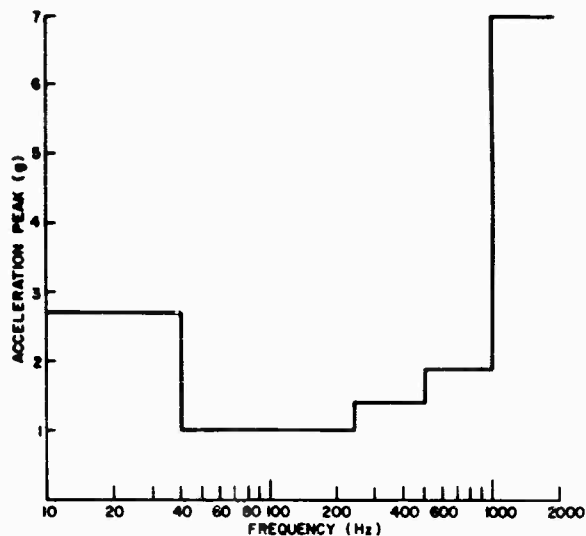


Fig. 1. Measured field vibration

maximum values of the apparent weight within the band.

Example

Analysis of many Vibran records of field measurements on a system showed that field vibrations were less than the levels shown in Fig. 1. Apparent weight of the same system was measured in the laboratory; the results are shown in Fig. 2. The product of measured vibration and average apparent weight is shown in Fig. 3. It will be seen that, although both field vibration amplitudes and apparent weight are fluctuating functions of frequency, the computed field forces are much smoother functions. This result is intuitively satisfying.

Combined Specifications

The requirement for foundation mass can be obviated by a simple limiting procedure. It is known that accelerations measured in the field will not exceed the levels shown in Fig. 1. It has been computed that force levels will not exceed those shown in Fig. 3. It is relatively simple to combine this information into a single test. The computed force of Fig. 3 is used as an input; however, the input acceleration is never allowed to exceed that of Fig. 1. At any frequency at which input accelerations would tend to exceed this limit, the force is suitably reduced so that the limit is not exceeded. It is exactly equivalent if acceleration is the specified input, and the force is limited.

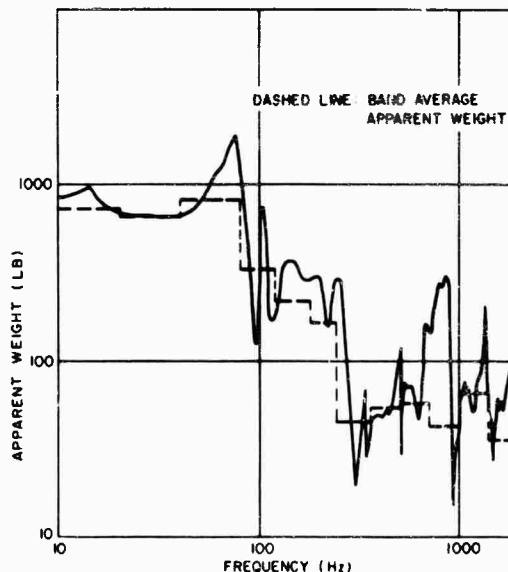


Fig. 2. Measured apparent weight

Both the force and vibration envelopes shown are rather complex, and it was not known that the measured field environment was the most severe that could ever be encountered. Therefore, for both conservatism and simplicity, the actual test specifications were as shown in Figs. 4 and 5. While this test is conservative, it is conservative by design and by a known amount. This is certainly preferable to the blind conservatism involved in motion specification.

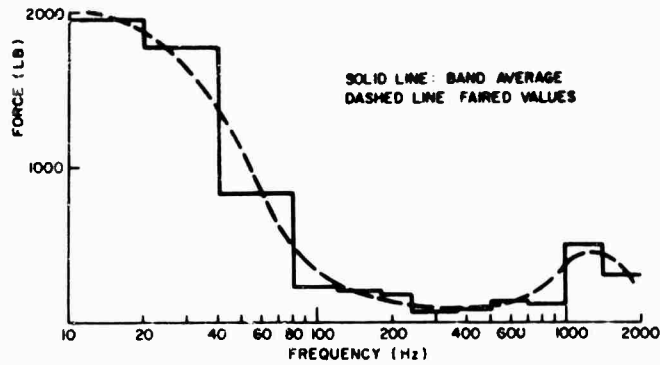


Fig. 3. Computed field forces

The results of this test were as shown in Figs. 6 and 7. It will be seen that at some frequency within each Vibran band (shown by heavy vertical lines), the amplitudes are as high as those shown in Fig. 4, and none are higher.

Random Testing

While the method is most easily applied to swept sinusoidal vibrations, it can also be used in random vibration testing. However, real-time limiting is very difficult in the random test. An alternative would be to shape the input, by suitable filters, in a preliminary low-level test. This can be done as part of the equalization procedure. It is hoped that the system is sufficiently linear to obtain the same shaping in the actual high-level test. If the system is

known to be very nonlinear, the method is more difficult to apply. (However, this is also true of the usual equalization procedure.)

RECOMMENDATIONS

To improve the method of specifying levels for vibration tests, one should have an extensive file of input forces computed for a wide variety of use and handling conditions. Normally, one has an adequate file of measured accelerations. In addition, there is a need for apparent weights of the structures on which these accelerations were measured, and, as pointed out by Foley [4], a rational method of averaging is required.

The following course of action is recommended to obtain the file of computed field forces:

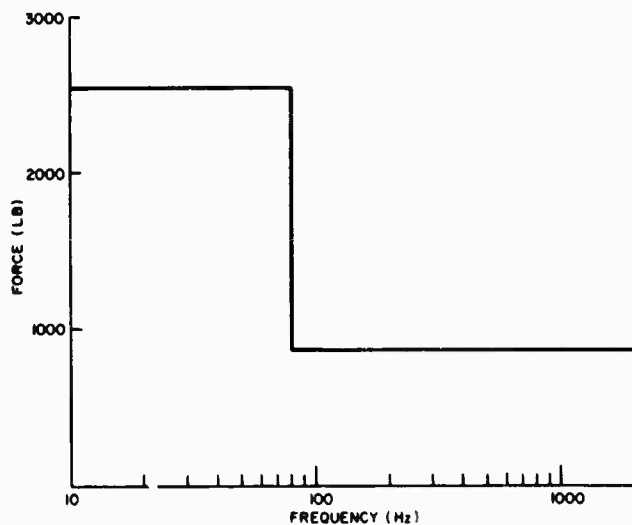


Fig. 4. Specified input force

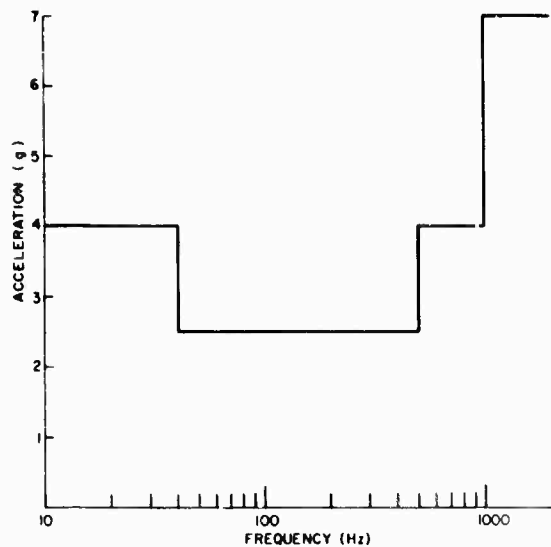


Fig. 5. Specified acceleration limit

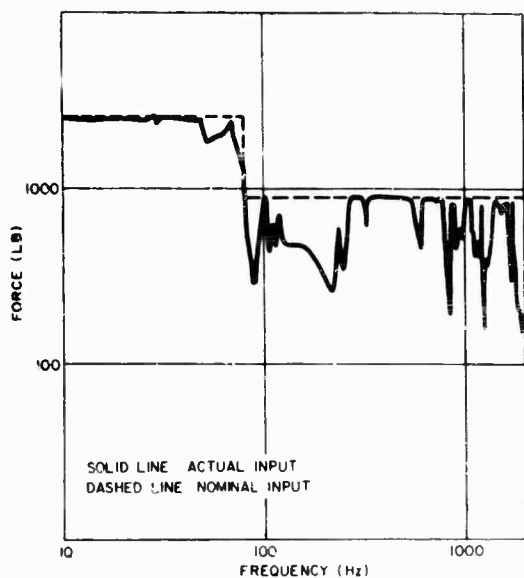


Fig. 6. Input force

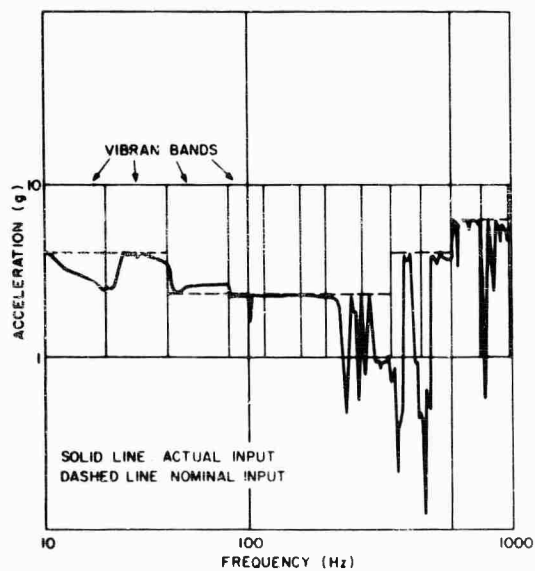


Fig. 7. Input acceleration

1. Design "universal" fixtures which could be used to measure apparent weights of many systems of the same general type.

2. Measure the apparent weight of all systems for which reliable field vibration data are available.

3. Compute field force inputs.

4. Compute average and peak force input envelopes.

Such a program can be of great value for all future systems.

CONCLUSIONS

Vibration tests in which a force input and an acceleration limit are specified have many advantages over those involving specification of either force or motion inputs. The method is feasible and only requires a knowledge of the system apparent weight in addition to the usual field data.

REFERENCES

1. J. V. Otts, Force Controlled Vibration Testing, Sandia Corp., SCTM-65-31, Feb. 1965
2. C. M. Harris and C. E. Crede, Shock and Vibration Handbook, I, Ch. 10 (McGraw-Hill), 1961
3. J. T. Foley, "Preliminary Analysis of Data Obtained in the Joint Army/AEC/Sandia Test of Truck Transport Environment," Shock and Vibration Bull., 35, Feb. 1966
4. J. T. Foley, "An Environmental Research Study," IES Proc., Apr. 1967

DISCUSSION

C. Smith (Bell Aerosystems Co.): I am a bit worried when you say that probably what you get in the end does not depend upon the foundation. Is it correct that the apparent field forces do not, in fact, depend on what the piece of equipment is attached to?

Mr. Murfin: Yes, but every foundation is different. What you want to do is give it the peaks that any foundation would give it, not the peaks that a particular foundation would give it.

Mr. Smith: Those peaks themselves are going to depend upon the foundation, are they not?

Mr. Murfin: They are dependent on the foundation, but if you want to demonstrate conservatively that the equipment that you are testing can survive any environment on any foundation, you want to require it to hit all the peaks of which it is capable, not simply those which would be transmitted by a particular foundation.

Mr. Smith: Would not a very low impedance foundation be effectively limited to an ability to input small forces, but a high impedance foundation be able to put in high input forces? I still cannot see why you apparently can completely disconnect the consideration of the two.

Mr. Murfin: Right. Forget about the foundation. You have a force that is being put in and whether it is being put in by a foundation or a shaker does not matter. If the equipment being tested wants to respond to that force at a particular frequency it will. Do not put it on a foundation that may obscure that peak. Do not put it on a foundation that may put in a spurious peak that could not really be there.

Mr. Smith: I still feel the two have to be connected. It seems to me that your system dynamics is somehow being considered independently of total dynamics. I feel this is a dangerous move.

Mr. Murfin: No, on the contrary, it is a dangerous move to attempt to measure a foundation that you can never measure exactly, and that will not be the same from day to day, and to assume that that foundation is putting the forces into the equipment.

Mr. Smith: But, if you do know enough about the foundation to which the equipment will be attached, the test specifications that you would like would be different on different foundations.

Mr. Murfin: They certainly would, but on the other hand, what you probably want is a test specification valid for any foundation, is it not?

Mr. Smith: I would not be that ambitious.

Mr. Murfin: I do not think that if a particular one is measured you can say that the equipment is always going to be on exactly that one.

Mr. Smith: I think I am getting my point across, nevertheless. You cannot be satisfied without some consideration of the foundation dynamics.

Mr. Murfin: Believe me, the foundation has nothing to do with it. There is so much force that it does not matter what is on the other side of the force -- it will create the same response.

* * *

SUBSTITUTE ACOUSTIC TESTS

Terry D. Scharton and Thomas M. Yang
Bolt, Beranek, and Newman, Inc.
Van Nuys, California

Experimental and analytical studies of idealized structures are presented to illustrate the use of multipoint mechanical excitation as a substitute for full-scale acoustic tests of large aerospace structures. The development of small vibration test fixtures that simulate the impedance of aerospace mounting structures is also discussed.

INTRODUCTION

In the environmental checkout of aerospace structures, components, and complete systems, it is becoming common practice to require full-scale prototype acoustical tests. These tests are justified by the argument that they can uncover effects that may not be seen in simplified analyses or less complete low-level tests. The usual approach in full-scale acoustical testing is to attempt to simulate the excitation by requiring that the pressure spectrum over some region of the test items is the same as that expected in the service environment. To fulfill this requirement, test facilities generating hundreds of kilowatts of acoustical power are being built. Because of the large costs of these highly specialized facilities, it appears worthwhile to examine the possibility of finding a more efficient substitute for full-scale acoustical tests. The results of an early study of acoustic and multishaker excitation of an electronic component box indicate that the concept of substitute acoustic tests deserves further attention [1].

The possibility of performing realistic substitute acoustical tests arises primarily as the result of recent advances in our ability to predict the vibration response of aerospace structures to acoustic and aerodynamic excitation fields, and recently developed concepts for utilizing multimodal vibration test fixtures that realistically simulate the impedance and vibration environment of aerospace mounting structures in the acoustic frequency range.

In "Spacecraft Model Experiments" (below) the results of acoustical and mechanical

excitation experiments involving a model spacecraft are presented to illustrate the accuracy with which the power that is transferred from an acoustic field to a vibrating structure can be analytically predicted, and to investigate the use of mechanical shakers to simulate acoustically induced power flow. Tests of a cylindrical structure are discussed in "Cylinder Experiments" (below) to show the feasibility of utilizing mechanical shakers to simulate the acoustically induced vibration environment on aerospace structures, such as a spacecraft shroud or the skin of a launch vehicle. "Impedance Simulation Tests" (below) discusses the development of small, multimodal, vibration test fixtures that simulate the impedance of typical aerospace mounting structures.

SPACECRAFT MODEL EXPERIMENTS

One method of performing a substitute acoustic test involves simulation of the power flow between an acoustic (or aerodynamic) pressure field and the vibrating structure. Consider, for example, the problem of testing a spacecraft that is excited in flight by the sound field inside the spacecraft shroud. Assuming that the pressure levels inside the shroud are known from previous measurements, we can calculate the power transferred to the important receiving elements of the spacecraft, such as the solar panels, the adapter, etc. The substitute acoustic test can then be performed by attaching a number of mechanical shakers to these receiving elements, and adjusting the power input to the calculated values.

Substitute acoustic tests based on the concept of simulating input power offer two advantages: the power transferred from an acoustic field to a vibrating structure can be calculated quite easily and reliably [2,3] and therefore low level acoustic tests or scaling techniques are not required to implement the concept, and calculation of the input power does not require a knowledge of the damping of the vibrating structure. However, tests based on the concept of simulating calculated input power are obviously not as accurate as tests based on the concept of simulating the measured response.

A series of tests was conducted utilizing the model spacecraft shown in Fig. 1. In the first test, the spacecraft was excited with a reverberant sound field with octave bands of random noise; the resulting space-average acceleration response of the solar panels, control box, and adapter are shown by the solid lines in Fig. 2.

The solar panels and adapter would appear to be the most important receivers of acoustic power. As the solar panels are un baffled, their response is governed by mass law and the power input can be calculated from Eq. (1),

$$P = \frac{4A^2}{M\omega} \langle p^2 \rangle_{s,t} \quad (1)$$

where A is the panel area, M is the panel mass, ω is the excitation frequency, and $\langle p^2 \rangle_{s,t}$ is the space-time average mean-square pressure in the reverberant field.

The response of the adapter to the sound field is complicated by its curvature, but the

input power at frequencies below the ring frequency of 2000 Hz (the ring frequency of a cylinder is given by $f_r = c_l/\pi d$, where c_l is the speed of sound and d is the diameter of the cylindrical shell) is given by the following equation:

$$P = \frac{2\pi c_0^2 AN_{af}}{M\omega^2} \langle p^2 \rangle_{s,t} \quad (2)$$

where c_0 is the speed of sound, and N_{af} is the modal density of acoustically fast modes in the adapter [4,5].

In the second test with the model spacecraft, two mechanical shakers were attached to the solar panels and one shaker was attached to the adapter as shown in Fig. 1. Accelerometers mounted at the shaker attachment points were used to control the power inputs according to the values calculated from Eqs. (1) and (2).

The power input to an infinite plate from a mechanical shaker is given in terms of the attachment point acceleration $\langle a^2 \rangle_t$ by

$$P = \frac{2\rho h^2 c_l}{\sqrt{3} \omega^2} \langle a^2 \rangle_t \quad (3)$$

where ρ is the density, h is the thickness, and c_l is the speed of sound in the plate. In calculating, it is assumed that Eq. (3) is valid for the solar panels and the adapter (this assumption is valid at high frequencies where the vibration wavelength is short compared to the structural dimensions), and Eq. (3) is combined with Eq.

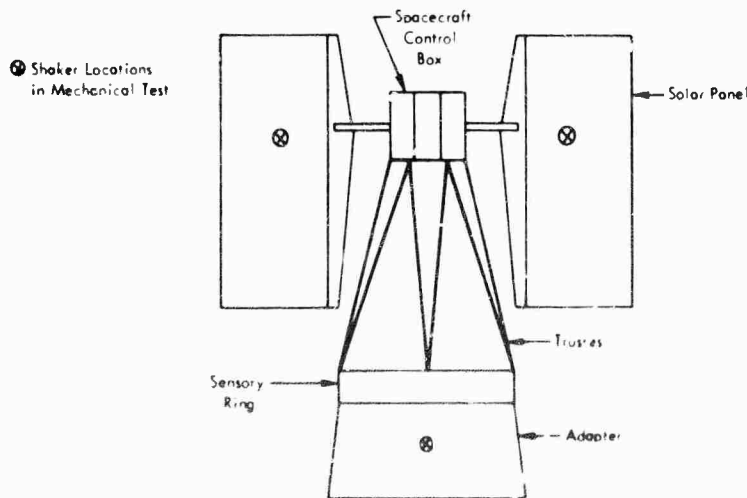


Fig. 1. Simplified view of the model spacecraft

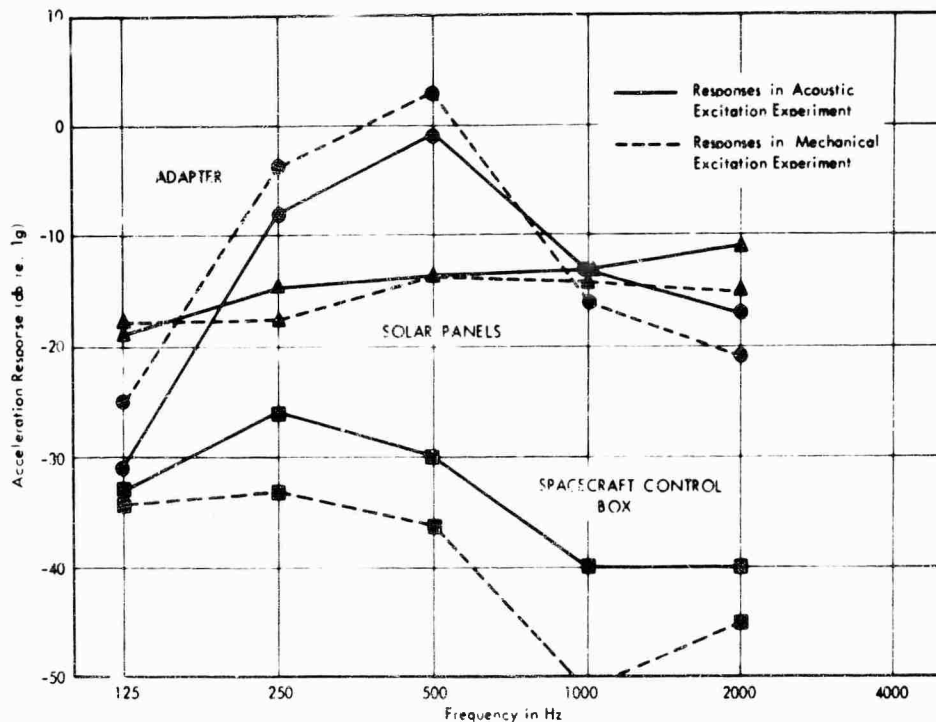


Fig. 2. Responses of spacecraft elements in acoustical and mechanical excitation experiments

(1) and Eq. (2) to obtain the desired relationships between acoustic pressure level and acceleration level at the attachment points.

The responses of the model spacecraft adapter, control box, and adapter are shown in Fig. 2 by the dashed lines. Notice that the responses of the solar panels and adapter are very similar in the acoustic and mechanical excitation experiments. However, the spacecraft control box response is considerably higher in the acoustic excitation experiment than in the mechanical excitation experiment, indicating that the control box is excited directly by the acoustic field rather than by mechanical coupling with the solar panels or the adapter in the acoustic excitation experiment.

The results of the spacecraft model experiments indicate that substitute acoustic tests based on power input simulation are feasible, provided that the shakers can be attached directly to each structural element in which the response is governed by direct acoustic excitation.

CYLINDER EXPERIMENTS

For many aerospace structures, an imaginary envelope of external structure can be

defined that responds directly to the acoustic or aerodynamic environment and subsequently transmits noise and vibration to the interior portions of the system; the shroud of a spacecraft or the skin of a launch vehicle are typical examples. In these cases, substitute acoustic tests can be performed by using mechanical shakers to simulate the desired vibration response of the envelope structure. The actual envelope vibration environment can be estimated by a combination of analytical methods, empirical scaling from existing data, and low-level acoustic tests.

Simulation of envelope response eliminates one of the problems associated with acoustic testing. It is well known that acoustical and aerodynamic environments with the same measured pressure spectra do not generally induce the same vibration response [6,7]. Thus, the use of acoustic tests to simulate aerodynamic environments can be very misleading if the pressure spectrum is simulated. It is more appropriate to simulate the response environment.

One may also question the validity of simulating the envelope response and ask whether the noise radiated by the envelope and the vibration transmission from the envelope to internal structure depends strongly on the nature

of the source used to excite the envelope vibration. For example, it can be argued that because of the wavelength matching of the exciting and radiated acoustic waves, in certain frequency ranges a structure excited acoustically will radiate sound more efficiently than a structure excited mechanically.

To investigate the validity of simulating envelope vibration response two series of experiments have been conducted with the sealed cylindrical structure shown in Fig. 3. In the first series, the noise radiated from the hollow cylinder to the interior acoustic field in acoustical and mechanical excitation tests was investigated; in the second series, we investigated the vibration transmitted from the cylinder to the instrument box attached to the cylinder was investigated. The sealed cylinder was placed in a reverberant sound field in the acoustic excitation tests, as shown in Fig. 3(a), and in the mechanical excitation tests two shakers were attached to the cylinder as shown in Fig. 3(b). In both the acoustic and mechanical excitation tests, the octave-band, random-noise excitation level was adjusted to establish a space-time average mean-square acceleration of 1 g on the cylinder.

The results of the first series of tests are given in Fig. 4, which shows the interior acoustic pressure levels for a given cylinder acceleration level in both acoustic and mechanical

excitation tests. Tests were conducted both with and without an acoustic liner inside the cylinder. The measured internal loss factor of the interior acoustic space was $\eta_2 = 2 \times 10^{-2}$ with the liner and $\eta_2 = 2 \times 10^{-3}$ without the liner. The data obtained, both with and without the liner, indicate that the interior acoustic pressure levels are approximately 3 db higher in the acoustic excitation tests than in the mechanical excitation tests.

The ratio of the interior acoustic pressure levels to the cylinder vibration levels can be calculated utilizing statistical energy analysis techniques [3]. At frequencies below the ring frequency ($f_r \approx 4000$ Hz for the test cylinder), the acoustic radiation is governed by resonant vibration modes of the cylinder, and the calculated pressure-acceleration ratio is the same for acoustic and mechanical excitation. For frequencies less than 4000 Hz, the pressure-acceleration ratio is given by

$$\frac{\langle p^2 \rangle_{s,t}}{\langle a^2 \rangle_{s,t}} = \frac{\rho_0^2 c_0^3 A}{(2\pi)^3 V_0} \frac{1}{f^3} \frac{1}{\eta_2} \left(\frac{N_{sf}}{N} \right) \quad (4)$$

where ρ_0 is the acoustic density, c_0 the acoustic speed of sound, V_0 the acoustic volume, and η_2 the internal loss factor of the interior acoustic space, A the cylinder interior surface area, and (N_{sf}/N) the ratio of modal density of acoustically fast cylinder vibration modes to the total

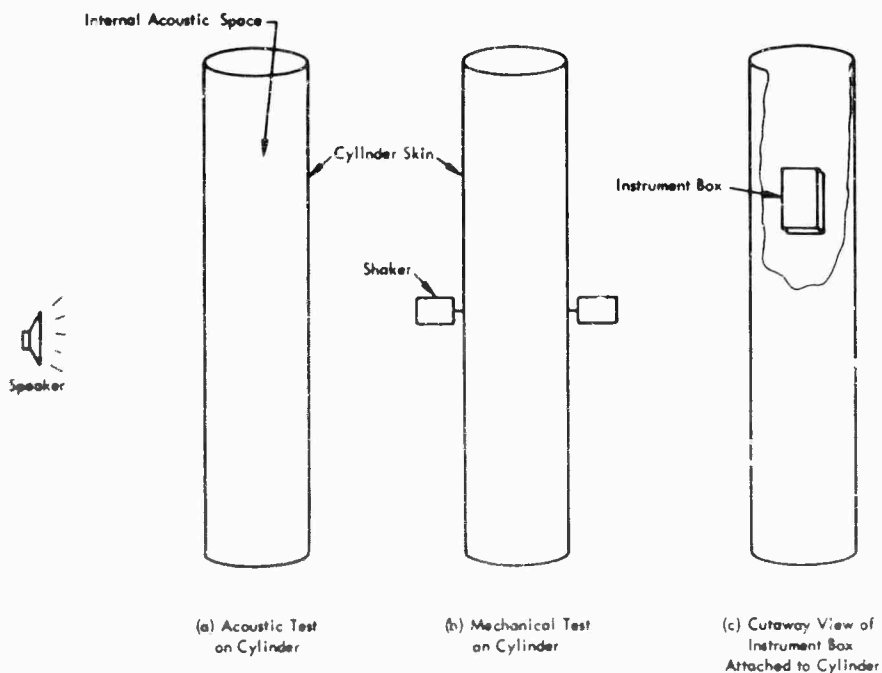


Fig. 3. Acoustic and mechanical tests on cylinder

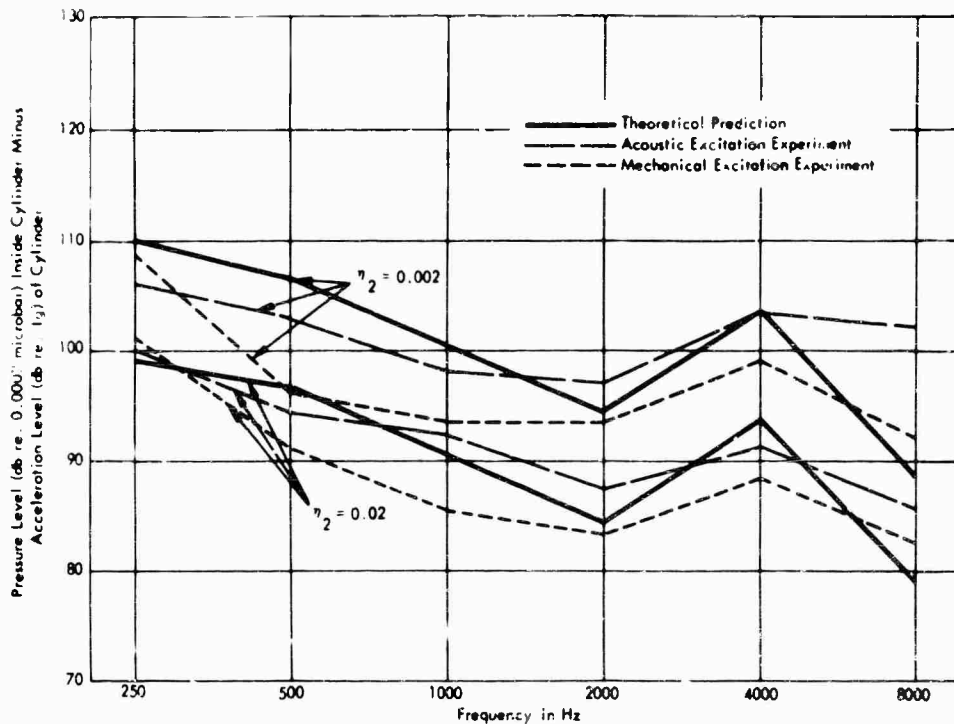


Fig. 4. Sound pressures generated inside a cylinder excited acoustically and mechanically

modal density of the cylinder [4]. The values of the pressure-acceleration ratio calculated from Eq. (4) are also shown in Fig. 4. The calculated values agree reasonably well with the values measured in acoustic and mechanical excitation experiments and predict measured 10-db difference in the interior acoustic levels with and without the liner.

The calculated ratio for the 8000-Hz octave band is obtained by considering radiation from the acoustically slow resonant vibration modes. That the measured interior pressure levels exceed the calculated levels in the 8000-Hz band indicates that above the ring frequency (but below the coincidence frequency) the nonresonant cylinder vibration modes govern the radiation. The sound radiated by the nonresonant cylinder motion depends on the details of the excitation; however, preliminary calculations indicate that the sound radiated is approximately the same for reverberant acoustic excitation and point mechanical excitation. Above the acoustic coincidence frequency ($f_c = \sqrt{3} c_0^2 / \pi c_p h$ where h is the cylinder thickness) of 16,000 Hz for the test cylinder, theoretical and experimental results again indicate that the resonant cylinder motion governs the radiation and the details of the excitation are not important.

The results of the second series of experiments (see Fig. 5) show that the acceleration transfer function from the cylinder to an instrument box, attached to the cylinder with four studs, is essentially the same in acoustic and mechanical excitation tests. The acceleration transfer function (defined as the ratio of the space-time mean-square cylinder acceleration to the space-time mean-square box acceleration) can also be calculated [8] using the following statistical energy analysis techniques:

$$\frac{\langle A_b^2 \rangle_{t,s}}{\langle A_c^2 \rangle_{t,s}} = \frac{\rho_c h_c^2}{\rho_b h_b^2} \left(\frac{f_r}{f} \right)^2 \frac{\eta_{bc}}{\eta_{bc} + \eta_b} \quad (5)$$

where the subscript b indicates the box and c the cylinder, η_b is the measured internal loss factor of the box, and η_{bc} is the coupling loss factor from the box to the cylinder given by [8]

$$\eta_{bc} = \frac{2R_c(Z_c)}{\pi f M_b |1 + Z_c Z_b^{-1}|^2} \quad (6)$$

where Z_c is the point force impedance of the cylinder, Z_b is the point force impedance of the box, and M_b is the mass of the box. In our evaluation of Eq. (6), we have used the equivalent infinite plate impedances given by

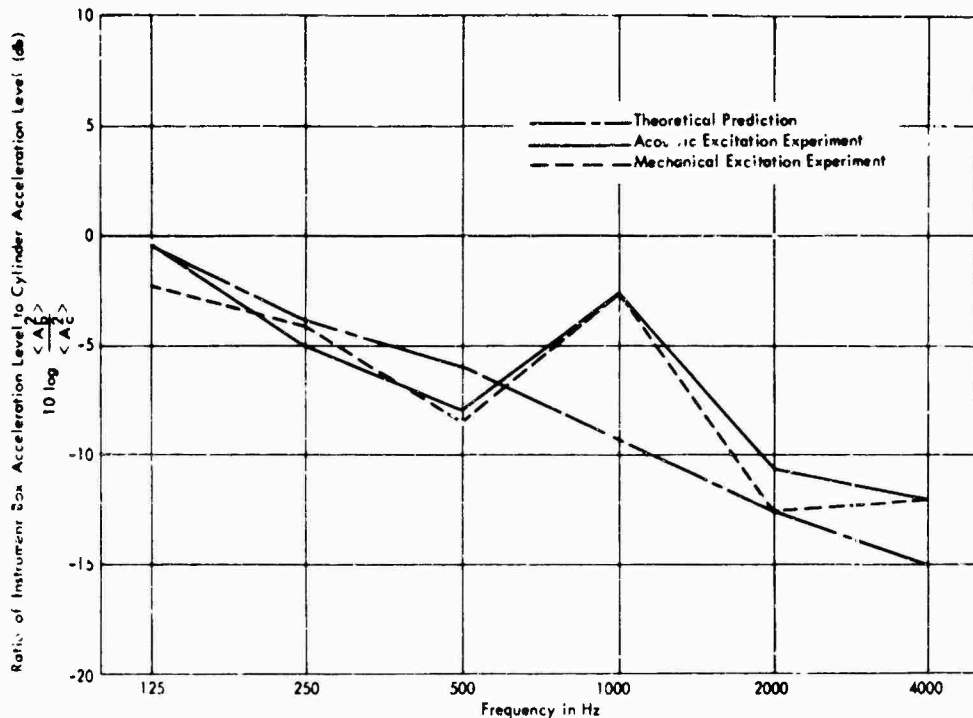


Fig. 5. Mechanical transfer function from a cylinder to instrument box

$$Z = 4\rho h^2 c_p / \sqrt{3} \quad (7)$$

The calculated values of the acceleration transfer function are also shown in Fig. 5. They agree very well with the values measured in the acoustic and mechanical excitation tests, except in the 1000-Hz octave band.

The results of these tests indicate that substitute acoustic testing based on simulating the vibration response of envelope structure gives realistic results for the noise radiated to the interior and for the vibration transmitted to skin-mounted equipment. In the case of large launch vehicles or spacecraft, however, it may be very costly and difficult to perform substitute acoustic tests using a large envelope section of structure; so we turn now to the problem of developing small vibration test fixtures for performing substitute acoustic tests of skin-mounted components.

IMPEDANCE SIMULATION TESTS

Acoustic testing has been advocated as a means of overcoming the problems associated with conventional vibration test fixtures in the high-frequency range [9]. In conventional vibration tests of large components, fixture

resonances inevitably occur within the frequency range of interest. These fixture resonances frustrate excitation and control problems and often render the high-frequency vibration data essentially useless. In addition, the use of rigid test fixtures often results in severe overtesting of instrument packages which in practice are attached to lightweight, acoustically susceptible structures and are subjected to a structurally reverberant vibration environment.

To avoid the problems associated with conventional vibration test fixtures and the inefficiencies associated with large-scale acoustic and multishaker testing, we are currently investigating the concept of utilizing light, flexible, multimodal vibration test fixtures that closely simulate the impedance of typical aerospace mounting configurations [10,11]. These fixtures have many resonances in any specific measurement bandwidth and result in a reverberant vibration field which is quite uniform over the fixture.

Theoretical considerations indicate that if the point impedance of the fixture simulates the point impedance of an actual mounting structure, then a realistic substitute acoustic test can be performed by using a number of small shakers to establish the inflight reverberant

vibration environment of the fixture. That is, if the space-average vibration of the fixture is adjusted to the space-average vibration level of a flight mounting structure, then the power flow into any test component attached to the fixture will be the same as the power flow under inflight conditions.

The technique for simulating the impedance of multimodal mounting structures, such as a spacecraft shroud or a vehicle skin, is illustrated in Fig. 6 which qualitatively shows the force admittance (reciprocal of impedance) of a finite plate. The real part of the admittance fluctuates with a peak-to-valley amplitude given by $1/M\omega\eta$ where M is the mass of the plate and η is the damping loss factor. The average frequency separation between peaks is given by the modal separation $\delta(\omega) = 2\pi h c_p / \sqrt{3} A$ where h is the plate thickness and A is the plate area. The spatial, frequency average of the real part of the admittance is equal to the admittance of an equivalent infinite plate, Y_0 , and is given by the reciprocal of the right-hand side of Eq. (7), and the spatial, frequency average of the imaginary part of the admittance is equal to zero. Thus the admittance of a finite plate is qualitatively described by the peak-to-valley amplitude, the modal separation, and the equivalent infinite plate admittance.

To illustrate the simulation of impedance, we have developed a small multimodal plate

(see Fig. 7) which simulates the impedance of a large plate. The plate shown in Fig. 7 is 6-in. square with 1-in. diameter coils of wire mesh attached to each edge. This small plate is designed to simulate the impedance of a 27- by 46-in. plate of the same thickness.

We have performed a series of experiments to evaluate the impedance simulation technique. In the first experiment, a 27- by 46-in. aluminum plate of 1/16-in. thickness was subjected to sine-sweep excitation of 20 to 20,000 Hz. The acceleration response measured approximately 2 in. from the shaker attachment point is shown in Fig. 8(a). The response shows approximately 80 resonance peaks below 1000 Hz, which agrees quite well with the theoretical modal separation of 10 Hz.

In the second experiment, the sine-sweep test was repeated for a small 6- by 6-in. plate that was cut from the original plate, and the results are shown in Fig. 8(b). The modal separation of the small plate (approximately one mode every 250 Hz, which is again quite close to the theoretical value of 300 Hz) is much less than the modal density of the large plate. The peak-to-valley amplitude of the response is also larger than for the large plate.

In the third experiment, the sine-sweep test was repeated for the 6- by 6-in. plate, modified as shown in Fig. 7, and the results

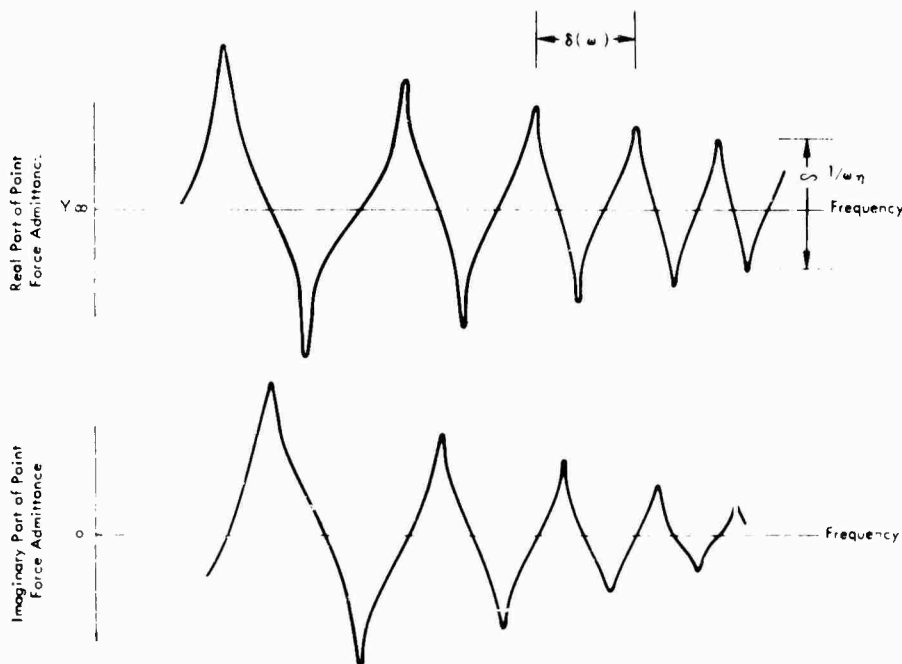


Fig. 6. Point force admittance of a finite plate

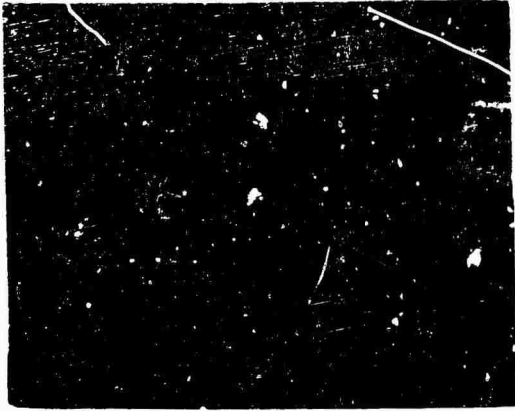


Fig. 7. Modification of a small plate to simulate a large plate impedance

are shown in Fig. 8(c). The modal separation and peak-to-valley amplitude of the modified 6- by 6-in. plate are very similar to those for the 27- by 46-in. plate. As the thickness and speed of sound in the modified plate are identical to the large plate parameters, the infinite plate impedances given by Eq. (7) are the same for each plate. It therefore follows that the point force impedance of the modified plate qualitatively simulates the point force impedance of the large plate. This example illustrates that in the high-frequency regime, small fixtures can be designed to simulate the point

impedance of a large aerospace mounting structure.

CONCLUSIONS

We have conducted a number of experiments and performed analyses to investigate the feasibility of using multishaker mechanical excitation tests as a substitute for high-level acoustic tests. The results of the investigation indicate that:

1. The power input from an acoustic field to an aerospace structure can be calculated and simulated with reasonable accuracy by attaching small shakers to each structural element that receives significant power from the acoustic field.

2. If an acoustically induced vibration environment on envelope structures, such as a spacecraft shroud or a vehicle skin, is simulated with small shakers, the acoustic radiation and the vibration transmission associated with the envelope structure will also be adequately simulated.

3. Small multimodal fixtures for performing vibration tests of aerospace components can be designed to simulate accurately the high-frequency impedance and vibration characteristics of large vehicle sections.

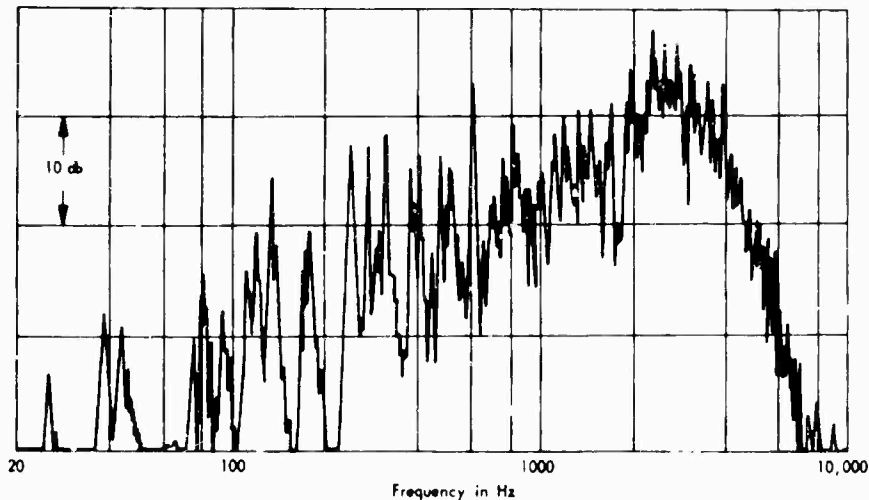


Fig. 8(a). Sine-sweep response of a 27- by 46- by 1/16-in. aluminum plate

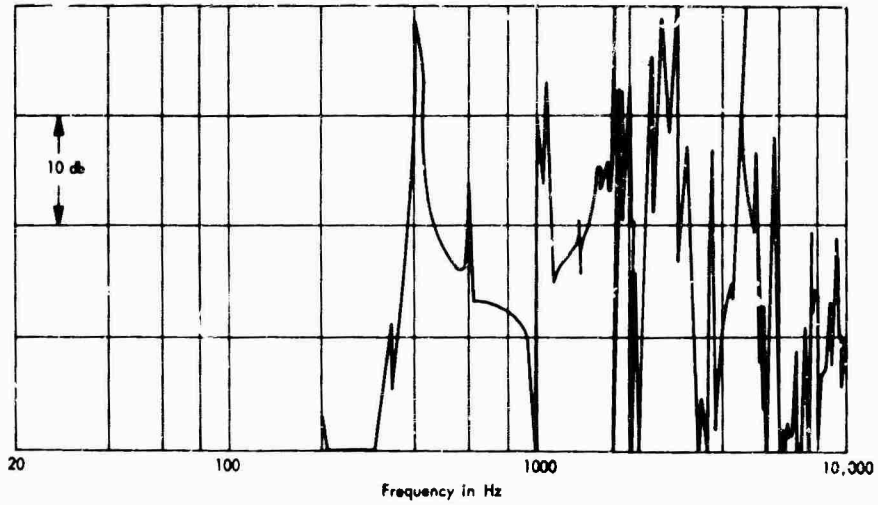


Fig. 8(b). Sine-sweep response of a 6- by 6- by 1/16-in. aluminum plate

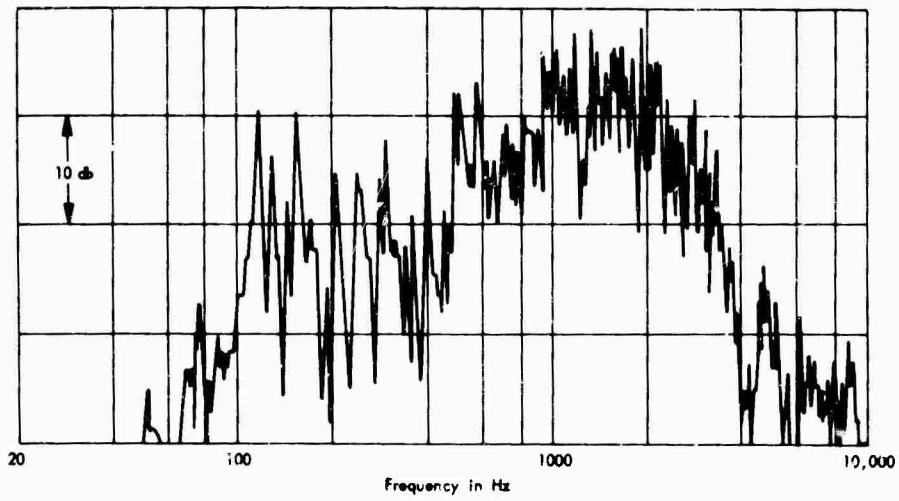


Fig. 8(c) Sine-sweep response of the 6- by 6- by 1/16-in. plate with boundary attachments to enrich modes

REFERENCES

1. D. U. Noiseux, C. W. Dietrich, E. Elchier, and R. H. Lyon, "Random Vibration Studies of Coupled Structures in Electronic Equipments," II, BBN Rpt. 1061, submitted to Wright-Patterson A.F.B., Oct. 1963
2. G. Maidanik, "Response of Ribbed Panels to Reverberant Acoustic Fields," J. Acoust. Soc. Am., 34:809-826, 1962
3. R. H. Lyon, Random Noise and Vibration in Space Vehicles, Shock and Vibration Monograph I, Shock and Vibration Info. Ctr., 1967
4. J. E. Manning, R. H. Lyon, and T. D. Schar-ton, "The Transmission of Sound and Vibration to a Shroud Enclosed Spacecraft," BBN Rept. 1431, submitted to NASA, Oct. 1966
5. R. H. Lyon et al., "Studies of Random Vibration of Coupled Structures," BBN Rept. 967, submitted to Wright-Patterson A.F.B., Nov. 1962
6. D. A. Bies, "Wind Tunnel Investigation of Panel Response to Boundary Layer Pressure Fluctuations," NASA-Cr-501, May 1966
7. "Summary of Random Vibration Prediction Procedures," prepared by the staff of the Measurement Analysis Corp., MAC Rept. 504-10, May 1967, p. 83
8. T. D. Schar-ton and T. M. Yang, "Statistical Energy Analysis of Vibration Transmission into an Instrument Package," Soc. Auto. Engrs. (670876), Oct. 6, 1967
9. R. W. Peverly, "Acoustically Induced Vibration Testing of Spacecraft Components," Shock and Vibration Bull. 36, Part 3, 1967
10. "Development of Improved Vibration Tests of Spacecraft Assemblies," Progr. Repts. 1-7, submitted to the Jet Propulsion Lab., Pasadena, Calif., by Bolt, Beranek, and Newman, Inc., under JPL Contract No. 951990, 1967
11. "Development of a Universal Multimodal Vibration Test Fixture," Progr. Repts. 1-7, submitted to NASA, Langley Res. Ctr., Hampton, Va., by Bolt, Beranek, and Newman, Inc., under Contract No. NAS1-7600

* * *

SIMPLIFIED METHOD OF CALCULATING NATURAL FREQUENCIES AND NORMAL MODES OF VIBRATION FOR SHIPS

Hassan B. Ali and Herbert F. Alma
Naval Ship Research and Development Center
Washington, D.C.

Methods currently used at the Naval Ship Research and Development Center (NSRDC) to calculate the natural frequencies and normal modes of vibration of ships use a lumped parameter approach based on a nonuniform free-free beam theory. The nonuniform beam theory considers elastic flexural and longitudinal deformations, including shear and torsion. Coupling between either vertical or athwartship flexural modes and torsional modes is also considered. The ship is divided into 20 sections of equal length. The total mass of a section is considered a point mass concentrated at the center of the section. The elastic properties are assigned to massless elastic members joining these mass points.

The evaluation of parameters requires not only time consuming calculations but also detailed ship section plans. The latter means that the ship is already in a stage of development where the results of the calculation of natural frequencies, normal modes, and vibration levels are of limited use to the designer. If the dynamic characteristics of the ship could be presented to the Naval Architect in the conceptual preliminary design stage, this would constitute a significant guide, as it would enable the designer to modify his design, if necessary.

With these considerations in mind, a simplified method was investigated. Using parameters calculated for only the center and quarter sections of the ship, curves were drawn over the whole ship length through these hull points, in a reasonable way, based on curves obtained from detailed calculations for a similar ship. The mass and stiffness parameters for the remaining 17 sections were obtained using values from the resulting curves.

The method was applied to a destroyer for vertical and horizontal vibration. Curves and tables are shown for the values obtained from the detailed and simplified methods. The results of the simplified method compare favorably with those of the conventional detailed method, the average percentage error in the calculated frequencies being 3.5 percent.

It is planned to check the accuracy of a more simplified method, namely, using only the center section parameters, and apply it to several ships for which detailed calculations and measurements are available.

INTRODUCTION

The ability to predict the dynamic response and the vibration characteristics of a ship's hull is an important input for the designer. It will enable him to prevent failure or malfunction of delicate instruments and to evaluate

vibration levels of shipboard machinery and equipment owing to resonance of a forcing frequency with a natural frequency of the hull. Calculations of hull vibration characteristics have therefore been requested for a considerable time during the construction of new ship classes.

MATHEMATICAL MODEL USED FOR PARAMETER CALCULATIONS

A free-free beam provides a basis for an understanding of the essential vibratory characteristics of a ship's hull at low frequencies. Calculations of lateral hull vibrations are, therefore, based on the Timoshenko equation for the free lateral vibration of a prismatic bar [1];

$$EI \frac{\partial^4 y}{\partial x^4} - I_{\mu z} \frac{\partial^4 y}{\partial x^2 \partial t^2} + \mu \frac{\partial^2 y}{\partial t^2} + \frac{I_{\mu z}}{KAG} \mu \frac{\partial^4 y}{\partial t^4} - \frac{EI}{KAG} \mu \frac{\partial^4 y}{\partial x^2 \partial t^2} = 0.$$

The differential equation for torsional vibrations about the longitudinal axis is

$$GJ \frac{\partial^2 \phi}{\partial x^2} - I_{\mu x} \frac{\partial^2 \phi}{\partial t^2} = 0$$

where

EI = bending rigidity

$I_{\mu z}$ = rotary inertia

μ = mass per unit length

KAG = shear rigidity

y = lateral deflection

x = distance from one end

t = time

GJ = torsional rigidity

ϕ = single amplitude in rotation about the longitudinal axis.

The coefficients expressed in these equations vary over the hull length, and cannot be expressed as continuous functions. Therefore, a numerical method must be applied, using finite-difference equations. For this purpose the ship is divided into a number of sections, the ends of which are called stations. For each section the mass is calculated and assumed to be lumped in the center of the section, which is called the half station. Shear, bending, and torsional stiffnesses are then calculated for each section. The finite difference method, with special equations for end conditions, is described in Ref. 2.

The number of stations used in calculations by different authors varies. NSRDC uses 20 equally spaced sections.

The parameters used for each section are obtained from tedious hand calculations requiring detailed ship section drawings that give weight distribution, inertia sections, body plans, lines, and molded offsets.

SIMPLIFIED METHOD OF PARAMETER CALCULATIONS

Calculations of parameter values for 20 stations is cumbersome and time consuming. Moreover, some of the required data are only available at a time when the ship design is already in a final stage of development, and are therefore only of limited value. Clearly, it would be preferable if the dynamic characteristics of the ship could be presented to the designer in the preliminary design stage. This would enable him to modify his design, if necessary.

With this consideration in mind, a simplified method was investigated. The parameters derived for digital computation of natural frequencies and mode shapes were calculated only for the center and the two quarter sections of the ship, for which early design plans are generally available. The three points are then connected by straight lines, the slopes being adjusted at the end sections to correspond to curves obtained for the respective parameters of similar ships. The parameters of the other 17 stations, or half stations, are scaled from these curves to obtain all parameters needed for a 20-mass system.

This simplified method was applied to a ship for which detailed calculations and measurements were available.

CONCLUSIONS

The motion equations of the hull, on which computations are based, and the parameters required for each station are as follows.

$$EI \frac{d^4 y}{dx^4} - I_{\mu z} \frac{d^4 y}{dx^2 dt^2} + \mu \frac{d^2 y}{dt^2} + \frac{I_{\mu z}}{KAG} \mu \frac{d^4 y}{dt^4} - \frac{\mu EI}{KAG} \frac{d^4 y}{dx^2 dt^2} = 0 \quad (a)$$

$$GJ \frac{d^2\phi}{dx^2} - I_{\mu x} \frac{d^2\phi}{dt^2} = 0 \quad (b)$$

where

EI = bending rigidity of the hull

$I_{\mu z}$ = rotary inertia of the hull per unit length

u = mass per unit length

KAG = shear rigidity of the hull

GJ = torsional rigidity of the hull

ϕ = single amplitude in rotation about the longitudinal axis

$I_{\mu x}$ = mass moment of inertia of the hull per unit length about the longitudinal axis.

Figure 1 shows distribution of the weights and the total masses (including the so-called virtual mass of the surrounding water). The three calculated points are marked with circles, and the assumed distribution is shown in dotted curves.

Figure 2 shows the two curves for the moment of inertia distribution about the vertical and horizontal axes, and Fig. 3 shows the shear area curves for vertical and horizontal vibration parameters.

Despite differences in mass and stiffness parameters, results of the simplified method compare favorably with those of the conventional method, as well as with measurements.

Figure 4 shows the small differences in mode shapes and frequencies obtained for the first four vertical modes. Differences for horizontal vibration calculations, not shown, are similarly small.

Table 1 is a tabulation of measured vertical natural frequencies and values obtained from detailed and simplified calculations. This shows that the simplified method may be confidently employed in the preliminary design stage.

TABLE 1
Measured and Calculated
Vertical Hull Resonances

Mode	Measured	Calculated	
		Detailed	Simplified
First	1.3	1.35	1.3
Second	3.0	2.88	2.82
Third	4.6	4.72	4.53
Fourth	6.5	6.71	6.5
Fifth	8.2	8.50	8.35

Studies are in progress to determine whether the method can be further simplified by calculating the center section parameters only and fairing the parameter curve to one of similar ship dimensions.

Further details, including figures and tables for horizontal vibration calculations, can be found in Ref. 3.

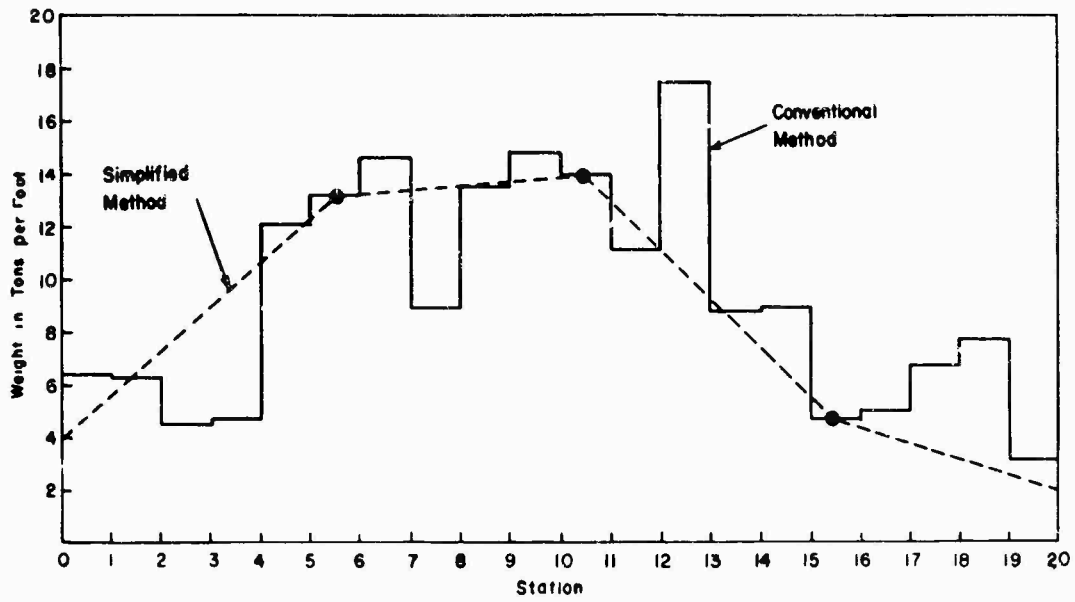
REFERENCES

1. S. Timoshenko, *Vibration Problems in Engineering* (D. Van Nostrand Co., New York), 1955
2. R. C. Leibowitz and E. H. Kennard, "Theory of Freely Vibrating Non-Uniform Beams, Including Methods of Solution and Application to Ships," David Taylor Model Basin Rept. 1317, May 1961
3. Hassan E. Ali, "Calculated Natural Frequencies and Normal Modes of Vibration of USS BRUMBY (DE-1044)," NSRDC Rept. 2619, March 1968

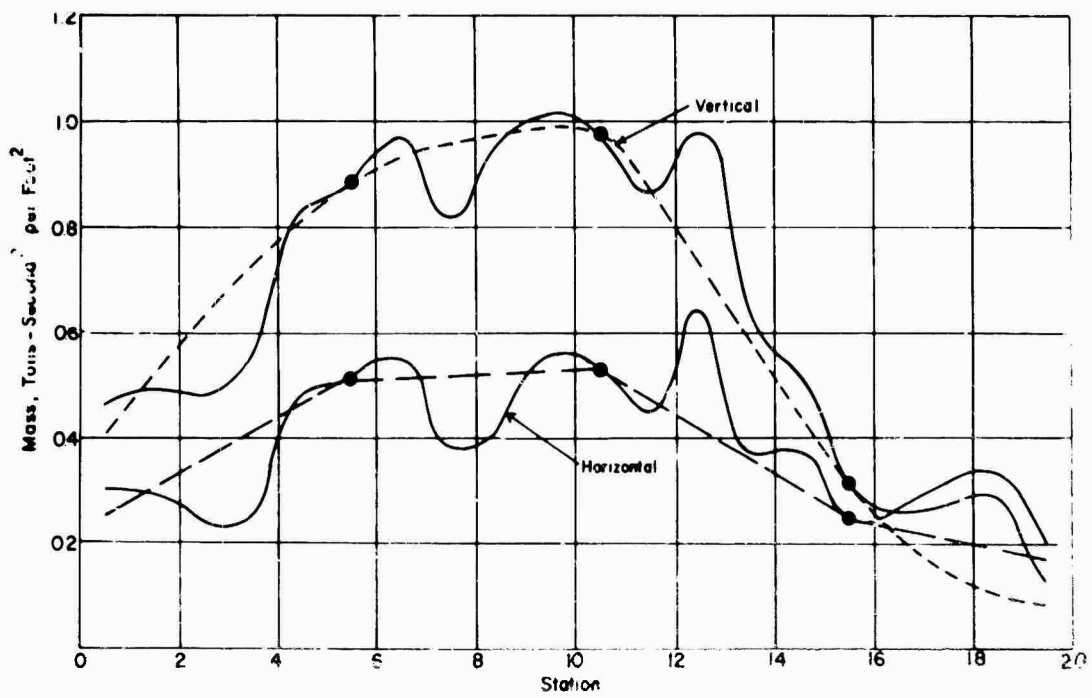
DISCUSSION

M. Pakstys (General Dynamics/Electric Boat): I noticed that your comparison between the experimental and the simplified method was better than that between the experimental and the full method. How do you explain that?

Mr. Ali: I cannot offer a scientific answer and I doubt if there is any significance to it. It is probably just a coincidence.



(a) Longitudinal weight



(b) Total mass

Fig. 1. Mass and weight distribution for detailed and simplified methods

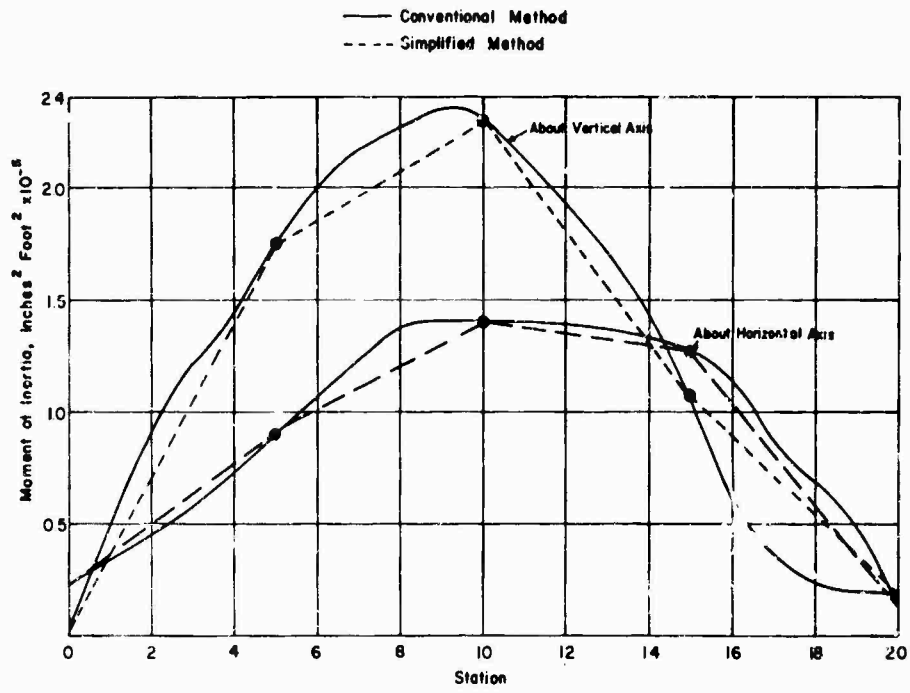


Fig. 2. Moments of inertia distribution

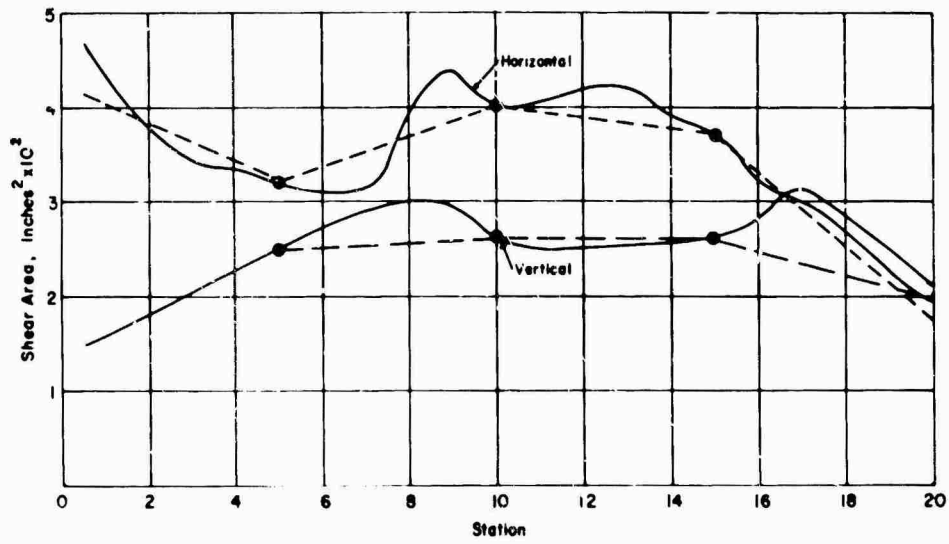


Fig. 3. Shear areas

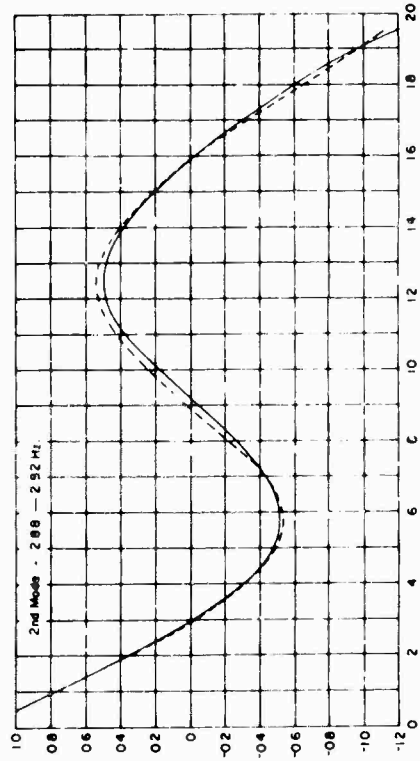
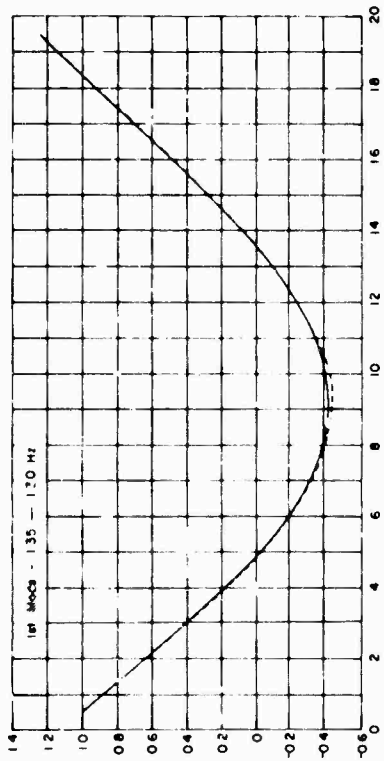
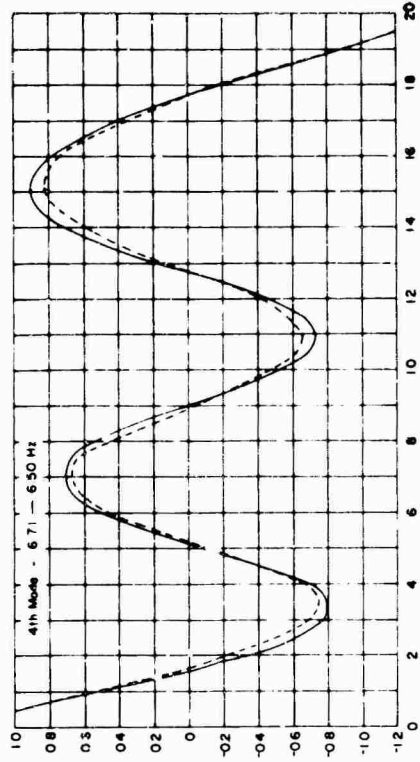
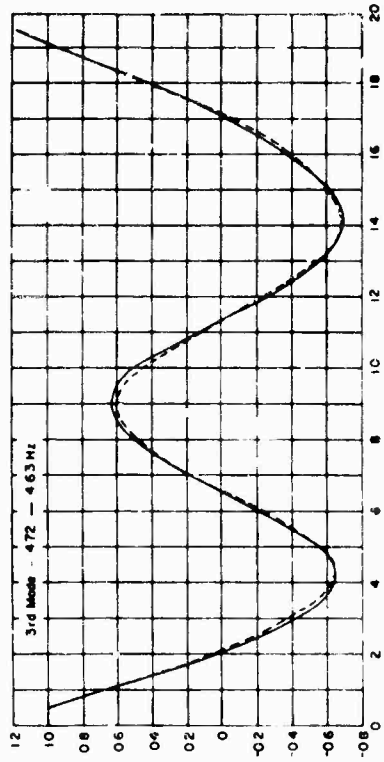


Fig. 4. Vertical normal modes

J. Weber (General Dynamics/Convair): How can you measure the natural frequencies of a ship's hull?

Mr. Ali: It is standard procedure. Normally, we perform a spectral analysis of recorded data from accelerometers, and from this we get the various frequencies. This has been done for several years, I understand.

Mr. Smith (Bell Aerosystems Co.): What sort of fundamental propeller frequency are you talking about, and what order of harmonics are you trying to avoid? I noticed your fourth frequency was about 6 Hz. Obviously, your luck runs out when the approximations to the mass and stiffness distributions are inadequate to calculate modes of an order sufficiently high to be within the order of propeller harmonics that you are trying to avoid. Could you relate propeller harmonics and their frequencies to the

modal number that you would have to know to avoid coincidence with these frequencies?

Mr. Ali: Anything beyond the fourth mode is of academic interest only. We are not particularly interested in the higher harmonics because we cannot measure them. Essentially, if this method is accurate for the first three or four modes, we are quite happy.

Mr. Noonan (NSRDC): The principal frequencies with which we would be concerned would be the fundamental blade frequencies and, on occasion, the shaft frequency. A particular example of difficulties along this line was the earlier class of destroyers that had a fundamental torsional mode of the hull at approximately 300 rpm of the shaft, and that was excited by unbalance in the propulsion system. No matter how much effort went into attempts to balance that, it was virtually impossible to have a vehicle which was satisfactory to the ship because that particular mode was so sensitive.

* * *

RESPONSE SPECTRA FOR SWEEPING SINUSOIDAL EXCITATIONS

Donald L. Cronin
TRW Systems Group
Redondo Beach, California

The amplification spectrum for a laboratory sinusoidal sweep test is often described as flat, with an amplitude equal to Q , the system quality factor. This description fails to account for two factors: (a) there is attenuation of system peak response as a consequence of sweeping, and (b) the spectrum approaches flatness only between the lower-frequency limit and upper-frequency limit of the sweep.

In this paper an approximate analytical description is derived for the amplification spectrum of a sweeping sinusoidal excitation which takes into account peak attenuation owing to sweeping and response outside the range of the sweep. The dependence of the spectrum upon sweep rate and system damping is discussed, and the results are extended to sinusoidal sweep tests wherein input acceleration levels are varied in discrete steps during the course of the test.

INTRODUCTION

Many environmental tests employ a slowly sweeping sinusoidal excitation. In these tests the excitation is started at some prescribed lower-frequency limit and is increased to some prescribed higher-frequency limit. The excitation frequency during testing depends exponentially on time, and the characteristic sweep parameter is the octave sweep rate, or the rate at which the excitation frequency is doubled. The tests generally consist of a collection of discrete frequency domains wherein the level of the excitation is controlled to provide shaker motion that has constant amplitude for displacement, velocity, or acceleration. Tests finding wide application consist, for the most part, of one or more constant acceleration domains. Tests falling into this category are discussed in the following paragraphs.

A convenient tool for visualizing the effect of an excitation is the response spectrum — a plot of the maximum response of a simple linear oscillator to the excitation in question as a function of oscillator frequency. An acceleration response spectrum or, more simply, an

amplification spectrum for a constant acceleration sweeping excitation is generally described as being flat, with an amplitude equal to Q . The spectrum for an undamped system is usually not defined.

This simplified view of the response spectrum fails to take into account two factors.

1. There is attenuation of system peak response, i.e., full resonant response is not always reached in testing owing to the effect of sweeping.

2. Relative flatness describes the spectrum only over the range of the sweep, i.e., only between the lower-frequency limit and upper-frequency limit of the sweep. It provides no information on the responses of systems having resonances outside the range of the sweep.

These two factors are discussed and analyzed separately in this paper. Results of analysis are then combined to provide a potentially useful and more accurate description, than heretofore available, of system response to sweeping excitations.

NOMENCLATURE

- A Amplification – ratio of response acceleration to input acceleration
- a_{max} Maximum oscillator acceleration
- B_i Input acceleration levels ($i = 1, 2, 3$)
- F Frequency as it pertains to the input (hertz)
- \dot{F} Time rate of change of input frequency (Hz/sec)
- f Frequency as it pertains to the oscillator (hertz)
- Q Quality factor ($Q = 1/2\zeta$)
- β Octave sweep rate (octaves per minute)
- ζ Fraction of critical damping
- η Sweep parameter
- τ Time required for excitation frequency to double ($\tau = 1/\beta$).

PEAK ATTENUATION

It has been widely recognized that peak response during a sine sweep test may be attenuated because the excitation, in passing through

resonance, provides the system with insufficient time to reach steady-state response. Analyses of this effect [1-3] have lacked generality owing to the fact that peak attenuation depends on several variables. These variables include system frequency, system damping, the rate of sweeping, and the method of sweeping, e.g., excitation frequency depending linearly on time, excitation frequency depending exponentially on time, etc.

During a recent study [4] consisting of analysis and analog computation, it was discovered that, to a good order of approximation, peak attenuation does not depend on the manner in which the sweeping takes place, nor on the direction of sweeping, i.e., on whether the excitation frequency increases or decreases in time. It was discovered, moreover, that peak attenuation, again to a good order of approximation, depends upon a single parameter which combines system damping, system natural frequency, and the absolute value of the time rate of change of excitation frequency as the excitation passes through system resonance:

$$\eta = \frac{Q^2 |\dot{F}|}{f^2} \quad (1)$$

Figure 1, adapted from Ref. 4, illustrates the fractional reduction of peak response as a function of the parameter η .

A fairly simple function may be fitted to the curve of Fig. 1 to provide a reasonable description of peak attenuation owing to sweeping:

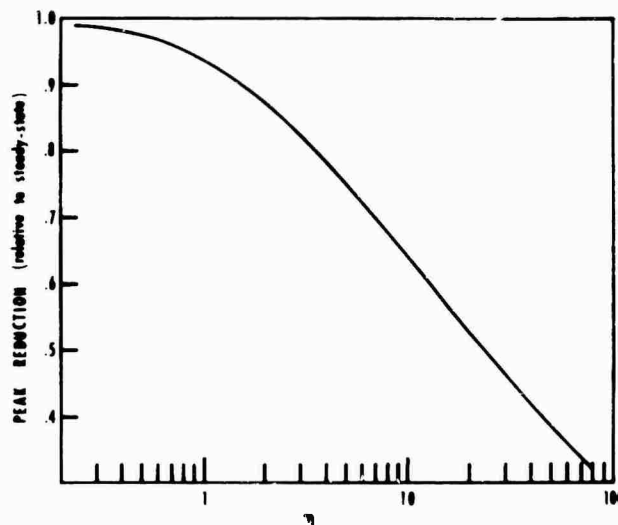


Fig. 1. Fraction of steady-state response attained by a mechanical oscillator as a function of the sweep parameter η

$$G = 1 - \exp(-2.86 \eta^{-0.445}). \quad (2)$$

As resonant response produces an amplification of Q , the system quality factor, the amplification produced by a sine sweep test will be given by

$$\left. \begin{aligned} A &\approx QG \\ A &\approx Q \left[1 - \exp(-2.86 \eta^{-0.445}) \right] \end{aligned} \right\} \quad (3)$$

When the excitation frequency depends exponentially on time, that is, when the sweep is logarithmic, the sweep parameter, η , may be written in terms of the octave sweep rate. For logarithmic sweeping, the frequency at any time is given by

$$F = F_0 e^{at}, \quad (4)$$

and the time, τ , required for the frequency to double is obtained as follows:

$$\begin{aligned} F_1 &= F_0 e^{a\tau} \\ F_2 &= 2F_1 = F_0 e^{a(\tau_1 + \tau)} \\ 2 &= e^{a\tau} \end{aligned}$$

Thus $\tau = [(\ln 2)/a]$, and the octave sweep rate is $\beta = (1/\tau) = [a/(\ln 2)]$. The frequency-time relation may then be written

$$F = F_0 \exp(\beta \ln 2t/60), \quad (5)$$

wherein the octave sweep rate is given in octaves per minute and time is expressed in seconds. The time rate of change of excitation frequency is then

$$\begin{aligned} \dot{F} &= \frac{\beta \ln 2}{60} F_0 \exp(\beta \ln 2t/60) \\ \dot{F} &= \frac{\beta \ln 2}{60} F \end{aligned} \quad (6)$$

When the excitation passes through system resonance, excitation frequency F becomes equal to resonant frequency f . The time rate of change of excitation frequency during the passage through system resonance is then

$$\dot{F}|_{F=f} = \frac{\beta \ln 2}{60} f. \quad (7)$$

Substitution of Eq. (7) into Eq. (1) produces the sweep parameter germane to logarithmic sweep testing:

$$\eta = \frac{\ln 2}{60} \times \frac{Q^2 |\beta|}{f}. \quad (8)$$

When Eq. (8) is substituted into Eq. (3), an approximate analytical expression is produced for the amplification spectrum of a constant acceleration, logarithmic sine sweep test:

$$A \approx Q \left\{ 1 - \exp \left[-20.75 \left(\frac{|\beta| Q^2}{f} \right)^{-0.445} \right] \right\}. \quad (9)$$

This expression is approximate because of its empirical origin and because it ignores the effects of starting transients on the spectrum, although starting transients will not be a particularly significant matter in a test involving several thousand stress reversals. Equation (9) also constitutes an incomplete picture of the requisite amplification spectrum, in that it describes response behavior only for systems having resonances within the range of the sweep, i.e., for the frequency range between the lower-frequency limit of the sweep and upper-frequency limit of the sweep. Response outside the range of the sweep will be discussed in the next section.

In Fig. 2 the dependence of the amplification spectrum upon octave sweep rate is illustrated for a Q of 25. It is seen, for example, that for a sweep ranging from 5 to 1000 Hz at 4β , a system having a resonance at 10 Hz will respond to a level of about 20 times the input level, or to about 80 percent of full resonant response.

In Fig. 3, the dependence of amplification spectrum on system damping is illustrated in a normalized plot for a sweep rate of 4β .

The spectrum for an undamped system will always be defined for nonzero sweep rates, as an undamped system requires an infinite time to build up to an unbounded response. For slow sweep rates, Lewis [5] noted that undamped system response may be approximated (in the present notation) by

$$A \approx 3.67 \sqrt{\frac{f^2}{|\beta|}}, \quad (10)$$

which, for logarithmic sweeping, may be written

$$A \approx 34.1 \sqrt{\frac{f}{|\beta|}}. \quad (11)$$

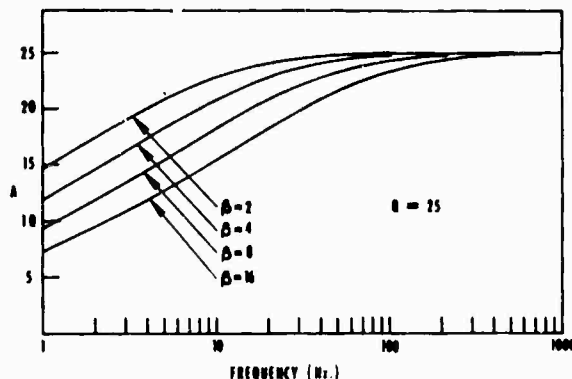


Fig. 2. Amplification spectra for several sweep rates and for a Q of 25

RESPONSE OUTSIDE THE SWEEP RANGE

To complete the definition of the response spectrum, it is necessary to describe how systems having resonances outside the range of the sweep respond, e.g., how a system having a 5-Hz resonance responds to an excitation sweeping from 10 Hz to 1000 Hz at 4β .

If peak attenuation owing to sweeping is ignored momentarily, the amplification for a system having a resonance lower than the lower-frequency limit of the sweep will be approximated by

$$A \approx \frac{f^2}{\sqrt{(f^2 - F_1^2)^2 + \frac{f^2 F_1^2}{Q^2}}} \quad (12)$$

where f is the system resonant frequency and where F_1 is the lower-frequency limit of the sweep.

The amplification for a system having a resonance higher than the higher-frequency limit of the sweep will be approximately

$$A \approx \frac{f^2}{\sqrt{(f^2 - F_2^2)^2 + \frac{f^2 F_2^2}{Q^2}}} \quad (13)$$

where F_2 is the upper-frequency limit of the sweep.

The application of Eqs. (12) and (13) to the present situation may be justified by physical argument. If, for example, the sweeping excitation is initiated at some low frequency, F_1 , a system having a resonance at $f < F_1$ will respond to a level approximating the steady-state response level for a sinusoidal input having a frequency F_1 (given by Eq. (12)). As the sweep progresses up the frequency scale, the response of the system having a natural frequency, f , will become smaller and smaller. The initial

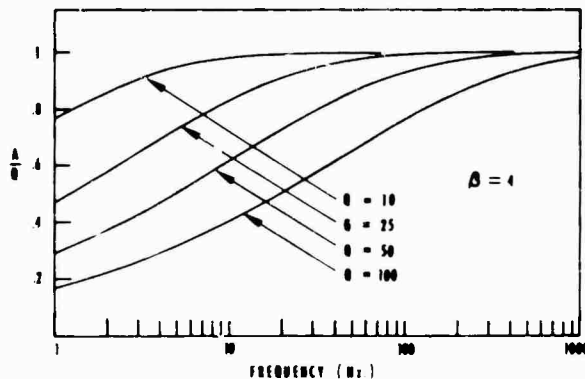


Fig. 3. Amplification spectra for several values of Q and for a sweep rate of 4β

level will then envelope all subsequent response peaks. Equation (12) therefore approximates the maximum response of the given oscillator to the specified input.

If, on the other hand, a system having a resonance at $f > F_2$ is influenced by the same sweeping excitation, the response will grow larger and larger as the sweep progresses up the frequency scale. The terminal value of the response (approximated by Eq. (13)) will envelope all previous response peaks and thus will be the maximum response for this oscillator. If peak reduction owing to sweeping is ignored, the amplification spectrum for the entire frequency range will appear as sketched in Fig. 4.

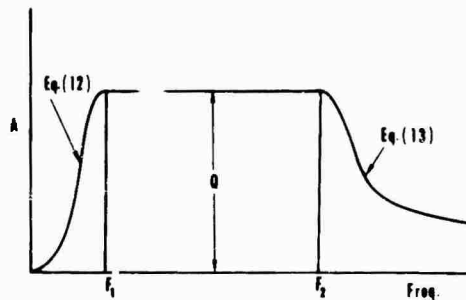


Fig. 4. Amplification spectrum for a constant acceleration sweep test

The notion of these approximations may be applied to tests made up of a collection of frequency domains wherein the level of the excitation is held at one or another constant acceleration level.

An example of this type of test is listed in Table 1.

TABLE 1
Representative Multilevel Test

Range	Level
$f < F_1$	0
$F_1 \leq f < F_2$	B_1
$F_2 \leq f < F_3$	B_2
$F_3 \leq f < F_4$	B_3
$F_4 < f$	0
$B_1 < B_2 < B_3$	

The test may be considered to be the sum of three constituent tests, each having an amplification spectrum as shown in Fig. 4. Maximum response vs frequency for each test may be plotted on a common set of axes (see Fig. 5).

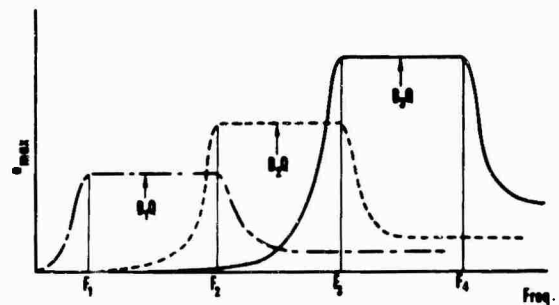


Fig. 5. Common plot for maximum response to constituent tests listed in Table 1

The maximum response plot for the entire test will, by definition, envelope the three constituent tests (see Fig. 6).

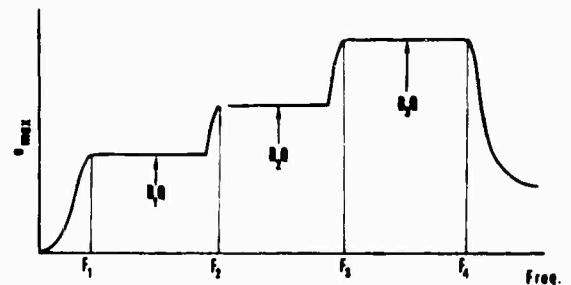


Fig. 6. Maximum response for test described in Table 1

In Fig. 6, the description of the maximum response plot is defined in terms of input levels multiplying Q or Eqs. (12) and (13).

CONCLUSIONS

In view of the work presented, approximate expressions may be formulated to describe response spectra for constant acceleration sweeping sinusoidal tests. These expressions will take into account peak reduction owing to sweeping and response of systems having resonances outside the range of the sweep.

TABLE 2
Analytic Description of Maximum Response
Plot Shown in Figs. 5 and 6

Range	Applicable Equation
$f < F_1$	$B_1 \times \text{Eq. (12)}$
$F_1 \leq f < F_2$	the greater of $B_1 Q$ and $B_2 \times \text{Eq. (12)}$ with $F_1 = F_2$
$F_2 \leq f < F_3$	the greater of $B_2 Q$ and $B_3 \times \text{Eq. (12)}$ with $F_1 = F_3$
$F_3 \leq f < F_4$	$B_3 \times Q$
$F_4 \leq f$	$B_3 \times \text{Eq. (13)}$ with $F_2 = F_4$

For a simple test embodying one acceleration level, the amplification spectrum for frequencies within the range of the sweep will be given by Eq. (9).

For frequencies lower than the lower-frequency limit of the sweep, the amplification spectrum may be approximated by combining Eqs. (9) and (12).

$$A \approx \frac{f^2 \left\{ 1 - \exp \left[-20.75 \left(\frac{|\beta| Q^2}{F_1} \right) \right] \right\}}{\sqrt{(f^2 - F_1^2)^2 + \frac{f^2 F_1^2}{Q^2}}}$$

For frequencies higher than the upper-frequency limit of the sweep, the amplification spectrum may be approximated by combining Eqs. (9) and (13), i.e.,

$$A \approx \frac{f^2 \left\{ 1 - \exp \left[-20.75 \left(\frac{|\beta| Q^2}{F_2} \right)^{-0.445} \right] \right\}}{\sqrt{(f^2 - F_2^2)^2 + \frac{f^2 F_2^2}{Q^2}}} \quad (13a)$$

The generalization to a plot of maximum oscillator response vs frequency for tests embodying several constant acceleration levels proceeds from the work presented in the last

section with Eq. (9) replacing Q , and Eqs. (12a) and (13a) replacing (12) and (13) in Table 1.

A parenthetical statement regarding Fig. 5 may be of interest here. When a sine sweep test has step changes in level, certain systems are excited to high levels at their resonant frequency, and are also excited to high levels at some frequency other than resonance. An example may be cited using the Atlas Agena spacecraft flight acceptance test (Y-Y) found in Table XX of Ref. 6. The test includes a 2-g input sweeping from 250 to 400 Hz, and a 5-g input sweeping from 400 to 2000 Hz. A system having a resonance at 375 Hz and Q of 10 will be tested to approximately 20g by the 2-g input. According to Eq. (12), this system will be tested to about 28g by the 5-g input sweeping up from 400 Hz. Figure 7 illustrates the amplitude of response for this system.

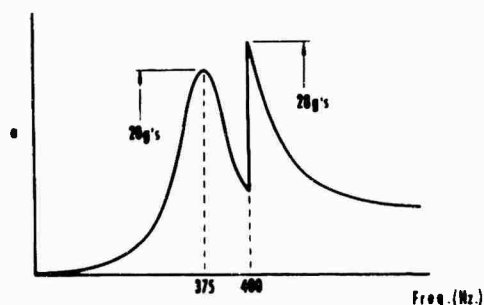


Fig. 7. Amplitude of response plot for a 375-Hz oscillator

It is seen in Figs. 5 and 7, that one portion of such a test may produce response levels which envelope resonant response levels produced by another portion of the test.

ACKNOWLEDGMENTS

The work reported herein was performed during a study for NASA Goddard Space Flight Center. The author wishes to acknowledge W. F. Bangs of Goddard and coworkers at TRW Systems Group for constructive criticism of portions of this work

REFERENCES

1. R. E. Morse, "The Relation Between a Logarithmically Swept Excitation and the Build-Up Steady-State Resonant Response," Shock and Vibration Bull., 35, Part 2
2. R. Hartenstein, "TR-10 Computer Solution to Q, Frequency Sweep Rate Problem," U.S. Govt. Memo., 6 Nov. 1962 (no other identification given)
3. P. Hawkes, "Response of a Single Degree of Freedom System to Exponential Sweep Rates (U)," LMSC (A/362881), Lockheed Missiles and Space Company, Sunnyvale, Calif., 1963
4. D. L. Cronin, "Response of Linear, Viscous Damped Systems to Excitations Having Time-Varying Frequency," Calif. Inst. Technol. Dynam. Lab. Rept., 1966
5. F. M. Lewis, "Vibration During Acceleration Through a Critical Speed," Trans. Am. Soc. Mech. Engrs., 54:253-261, 1932
6. "General Environmental Test Specification for Spacecraft and Components Using Launch Environments Dictated by Atlas-Agena, Thor-Agena, or Thrust-Augmented Thor-Agena Launch Vehicles" (S-320-A-1), NASA Goddard Space Flight Center, 1 Oct. 1965

DISCUSSION

Mr. Smith (Bell Aerosystems Co.): We got tangled on this sweep rate problem quite a number of years ago. I would like to bring to your attention a couple of papers that we found did not agree with the Lewis reference that you quoted. We looked into these, because we were not happy with Lewis's results. One was by a fellow named Hok — I think it was in the Journal of Applied Mathematics in 1948 — and Reed had an article in the Journal of Aerospace Sciences, in about 1959. For some time we have been using a little nomograph which relates permissible sweep rate to system natural frequency and system damping. I have never yet found a case where we had a problem with the normal sort of test specification for bands per octave per minute sweep rate. We felt that what Hok had done was not in agreement with what Lewis had done, and we felt that Hok's work was more nearly correct.

Mr. Cronin: It is hard to criticize Lewis. His work predated the digital computer. He performed an analysis that he integrated numerically. I find it difficult to believe that he would make a mistake. Perhaps the format was not acceptable to you.

Mr. Smith: Hok's work also pretty much predated computers. He actually solved the response of a system. His results are in terms of Fresnel functions. Then he carried out an analog experiment on a simple electrical oscillator in which he swept the frequency. He compared his theoretical and experimental results and got extremely good agreement.

Mr. Cronin: The results I have presented here today have been checked against many other results. The one equation I gave for the fraction of maximum response obtained can be used to evaluate a sweep test to determine if it is, indeed, acceptable. Just pick the lowest important frequency and the lowest damping ratio or the highest Q and plug it in. If you get something less than 99 percent or 95 percent you know the sweep rate, or whatever your criterion might be, should be reduced. People who work on structures having very low frequencies do see these effects creeping in. I have seen actual records where these effects show up.

Mr. Smith: I am a little unhappy because I think the criteria that we are using differ from the criteria that you are using. I would like to exchange information.

* * *